Commissioning of the high-resolution comb-calibrated spectrograph at the Wendelstein Observatory and development of calibration and fitting software packages for the hunt of exoplanets

Hanna Kellermann

München 2021

Commissioning of the high-resolution comb-calibrated spectrograph at the Wendelstein Observatory and development of calibration and fitting software packages for the hunt of exoplanets

Hanna Kellermann

Dissertation
an der Fakultät für Physik
der Ludwig-Maximilians-Universität
München

vorgelegt von
Hanna Kellermann
aus Dachau

München, den 30.08.2021

Erstgutachter: Prof. Dr. Ralf Bender
Zweitgutachter: Prof. Dr. Barbara Ercolano
Tag der mündlichen Prüfung: 20.12.2021

Abstract

In order to answer humanity's ancient question of other life within the Universe, a widely approved starting point is the search for planets in orbit around stars other than our Sun. The effort to find these so-called exoplanets has been steadily advancing throughout the last 25 years. Besides photometric instruments, high-resolution spectrographs are an essential tool in this search for these new worlds.
The Wendelstein Observatory in the Bavarian Alps in Germany is a facility which is excellently suited for the hunt of exoplanets, since the 2 m class telescope there is equipped with both photometric and spectroscopic instruments. In the scope of this thesis, the Échelle spectrograph *FOCES*, which was formerly located at the Calar Alto Observatory in southern Spain, was installed at the Wendelstein Observatory to serve as a planet hunter during a second life with the goal to achieve a m/s accuracy. This required extensive effort, starting with the temperature and pressure stabilization of its environment controlled in a slightly overpressured vessel. Further, the multi-fiber light input was designed and realized, which provides the possibility of simultaneous wavelength calibration during observations. Besides the standard ThAr calibration utilized in most spectrographs, *FOCES* is also equipped with a laser frequency comb, which is stabilized to an atomic clock and therefore the most precise wavelength calibration light source achievable today. During the assembly of the fiber connections, special emphasis was put to tailor them to the specific needs of astrophysical observations.
The evaluation software *GAMSE* for the recorded Échelle spectra was developed by Dr. Liang Wang with contributions made in the scope of this thesis, while the Python software package *MARMOT* was developed as a major part of this thesis. *MARMOT*'s application options include, but are not limited to, comb-wavelength calibration, b-spline template creation as well as several different choices of radial velocity estimation. Test observations of the well-known planetary host 51 Pegasi yielded an accuracy of around 3.5 m/s, satisfying the previously mentioned requirement.
Apart from the work in spectroscopic hardware and software development, a Python fitting tool called *multranfit*, with the option for MCMC sampling of the parameter space for multiband photometric observations, was created. This program is capable of fitting observations of not only different bands but even different instruments and times of observation, simultaneously. This software contributed significantly to the confirmation of three exoplanetary candidates, Wendelstein-1b, Wendelstein-2b and

TOI-1823, by combining all photometric data taken of the transits into one fit and thus constraining the parameters.

Zusammenfassung

Auf der Suche nach einer Antwort auf eine der wohl ältesten Fragen der Menschheit, ob Leben auch an anderen Orten im Universum existiert, ist die Erforschung von Planeten im Orbit um andere Sterne (Exoplaneten) eine relativ junge und gleichwohl vielversprechende Herangehensweise.
Die Bemühungen, diese Exoplaneten zu finden, sind in den letzten 25 Jahren stetig vorangeschritten. Neben photometrischen Instrumenten sind insbesondere hochauflösende Spektrographen ein wesentliches Werkzeug bei der Suche nach neuen Welten.
Das Wendelstein-Observatorium in den bayerischen Alpen mit seinem 2.1 m-Teleskop, ausgestattet mit photometrischen und spektroskopischen Instrumenten, ist hervorragend geeignet, um wesentlich zu diesen Entdeckungen beizutragen. Im Rahmen dieser Arbeit wurde der Échelle-Spektrograph *FOCES*, ehemals am Calar-Alto-Observatorium in Südspanien im Einsatz, umgerüstet, am Wendelstein-Observatorium installiert und in Betrieb genommen, um fortan dort die spektroskopische Suche nach Exoplaneten zu ermöglichen. Ziel hierbei war die Messung von Radialgeschwindigkeiten im m/s Bereich zu ermöglichen. Die dafür erforderlichen Umbauten und Optimierungen umfassten unter anderem eine Temperatur- und Druckstabilisierung des gesamten Spektrographen in einem temperaturstabilisierten Überdrucktank, sowie eine komplette Neukonzeptionierung der Lichteinkopplung in den Spektrographen. Diese ermöglicht eine simultane Wellenlängenkalibrierung während astronomischen Beobachtungen, was die Messgenauigkeit des gesamten Aufbaus zusätzlich verbessert. Neben der standardmäßigen ThAr-Kalibrierung, die in den meisten Spektrographen verwendet wird, ist *FOCES* zudem mit einem Laserfrequenzkamm ausgestattet. Durch seine Stabilisierung auf eine Atomuhr stellt er dabei die präziseste derzeit verfügbare Lichtquelle zur Wellenlängenkalibration dar. Der Spektrograph selbst kann über eine Vielzahl von optischen Fasern mit Licht gespeist werden. Bei Auslegung und Montage sämtlicher Faserverbindungen wurde besonderer Wert darauf gelegt, diese auf die speziellen Bedürfnisse astrophysikalischer Beobachtungen mit außerordentlichen Anforderungen an Präzision abzustimmen.
Darüber hinaus wurde im Rahmen dieser Arbeit die federführend von Dr. Liang Wang entwickelte Auswertungssoftware *GAMSE* für die Datenreduktion der aufgenommenen Échelle-Spektren um eine präzisere Fehlerfortpflanzung erweitert. Zusätzlich dazu wurde das Python-Softwarepaket *MARMOT* für die Analyse von Radialgeschwindigkeitsdaten als wesentlicher Bestandteil dieser Arbeit von Grund auf neu entwickelt. Zu den Anwendungsoptionen von *MARMOT* gehören unter anderem die Rekalibrierung von Spektren mit Frequenzkammdaten, die Erstellung von B-Spline-Templates sowie verschiedene Möglichkeiten der Radialgeschwindig-

keitsberechnung. Aus ersten Testbeobachtungen des bekannten Exoplanetensystems 51 Pegasi konnte eine Messgenauigkeit von ca. 3.5 m/s für das gesamte Instrument, einschließlich der Auswertungssoftware, ermittelt werden.
Neben der Arbeit an der spektroskopischen Hardware- und Softwareentwicklung wurde überdies eine weiteres Python-Analyse-Paket für photometrische Beobachtungen (*multranfit*) entwickelt. Dieses Programm ist in der Lage, photometrische Beobachtungen in verschiedenen Filterbändern, sowie darüber hinaus Daten verschiedener Instrumente simultan zu fitten und mit Hilfe von Markow-Chain-Monte-Carlo-Sampling Konfidenzintervalle im Parameterraum zu ermitteln. Die Software trug dabei wesentlich zur Bestätigung von drei Exoplaneten-Kandidaten, Wendelstein-1b, Wendelstein-2b und TOI-1823 bei, indem photometrische Daten der Transits von verschiedenen erdgebundenen, sowie Weltraumteleskopen simultan gefittet und analysiert werden konnten.

Contents

List of Acronyms

CCD	charge-coupled device
CCF	cross-correlation function
ELT	Extremely Large Telescope
ESO	European Southern Observatory
FFT	fast Fourier transform
FOCES	fibre optics Cassegrain Échelle spectrograph
FPC	Fabry-Pérot cavity
FRD	focal ratio degradation
FWT	Fraunhofer Wendelstein Telescope
GAMSE	**G**eneral **A**stronoMical **S**pectra **E**xtractor
LC	light curve
LCOS	liquid crystal on silicon
LFC	laser frequency comb
MaHPS	**Ma**nfred **H**irt **P**lanet **S**pectrograph
MARMOT	**M**unich **A**nalyzer for **R**adial velocity **M**easurements with b-spline **O**ptimized **T**emplates
MCMC	Markov-Chain Monte Carlo
MLE	maximum likelihood estimation
NOLM	non-linear optical loop mirror
PDF	probability density function
PID	proportional–integral–derivative
RMS	root mean square

RV radial velocity

SARS Simultaneous Additive and Relative Sysrem

SLM spacial light modulator

TESS Transiting Exoplanet Survey Satellite

ThAr thorium argon

UNe uranium neon

USM Universitätssternwarte München

UV ultra violet

WWFI Wendelstein Wide Field Imager

3KK 3-Kanal-Kamera

Structure and Contents of this Thesis

This thesis discusses software developments and hardware improvements developed for and dedicated to the search of exoplanets for two of the most successful methods (in terms of number of detected objects), the radial-velocity and the transit method. Furthermore, first observational results which could be obtained utilizing those developments are presented.

The content of this thesis is thereby organized in seven chapters. The first chapter provides a brief overview over the field of exoplanetary science, starting with a summary of observational techniques and concluding with a brief introduction of a number of instruments relevant for this thesis. Chapters 2 and 3 introduce the fundamentals of high-resolution optical spectrographs, in particular the *fibre optics Cassegrain Échelle spectrograph (FOCES)* at the Wendelstein Observatory. Chapter 3 documents in detail hardware upgrades and improvements that were implemented in the context of this thesis and that enabled the ongoing research with *FOCES*. Chapter 4 provides an in-depth introduction on the statistical and analysis methods that were implemented in the two data-analysis-software projects that are described in the following two chapters, which form the foundation of the scientific results presented at the end of this thesis. Chapter 5 introduces thereby the Python program *MARMOT* dedicated and developed to analyze high-resolution Échelle spectra. Furthermore, a detailed study of the performance of *MARMOT* including a comparison of different implemented software options and features is presented. Chapter 6 introduces the software package *multranfit* developed to simultaneously fit transit light curves from various instruments. The last chapter (Chapter 7) summarizes first scientific results that could be achieved by exploiting the improved hardware and new developments in software that are presented in the preceding chapters.

Part I

Exoplanets

1 Exoplanets

> *The universe is a pretty big place. If it's just us, seems like an awful waste of space.*
>
> **— Carl Sagan**
> (Astronomer, astrophysicist, cosmologist and author in his novel 'Contact')

1.1 Ancient questions and recent answers

There are several 100 billion stars within our galaxy and about the same number of galaxies within the observable universe. It was widely accepted, even long before the first observational evidence of a planet orbiting another star was found, that it would be extremely unlikely if our solar system were an extreme exception in this regard. The question that has always sparked discussions and speculation and still does so today, is how many stars have planets within the habitable zone, and how many of those actually do host forms of life. With the current generation of instruments and observational evidence, it is still too early to reach a definitive answer to that question, but the last decades have seen the biggest progress so far. As will become clear within this chapter it would be fair to call the 21st century the century of exoplanets. Never before in history has humanity been so close to actually answer the question: "Are we alone out there?". If progress continues at the current pace, it is not unlikely that observational evidence might be available for signs of life on another planet by the middle of this century.

1.2 Observing Exoplanets

One can argue that the fundamental technologies required for detecting exoplanets were already available before the 1990s. The probable reason why the rate of discoveries took off only in the new millennium, is that direct observation through astronomical imaging, with the exception of a few extreme cases, is hardly feasible and other techniques require dedicated instruments. Moreover, the theories on

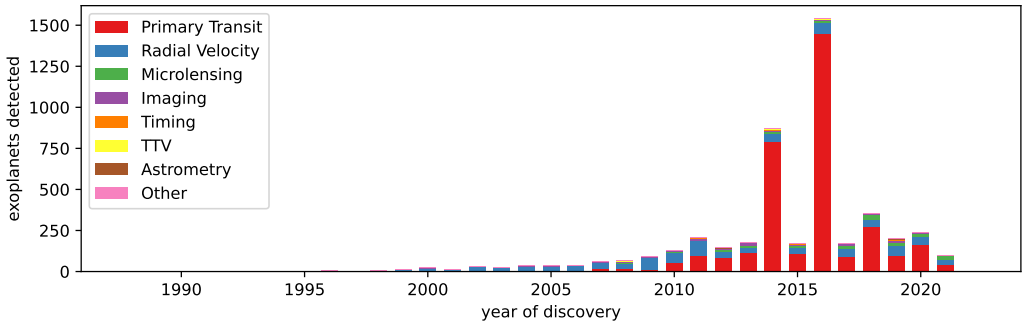

Fig. 1.1.: Statistical overview of all 4776 exoplanets discovered to date, with the different detection techniques highlighted. The two exceptional peaks in the displayed diagram are the result of a re-analysis of the existing *Kepler* data with new statistical analysis tools (Lissauer et al., 2014; Morton et al., 2016). Data taken from `http://exoplanet.eu/` accessed on 26.6.2021.

Jupiter-type planets on close orbits around their host star were not established knowledge (Mizuno, 1980) especially since our own solar system does not host such a type of planet[1]. With those instruments now available and the techniques maturing, at the time of writing this thesis, nearly 5000 exoplanets[2] have been discovered. In the following, important detection techniques will be discussed briefly. A statistical overview of planetary systems discovered to date of writing this thesis is shown in Figure 1.1.

1.2.1 Direct observation

As mentioned above, this method is by far not the most efficient or successful, and in most cases not feasible, even with unrealistically large telescopes[3]. The main problem of direct observations however is the extreme contrast in brightness between the host star and its companions. The only cases where such observations have been successful are such where a very large planet orbits its host star on a very large orbit (Chauvin et al., 2004; Deacon et al., 2016; Miles-Páez et al., 2017). In total, more than 140 exoplanets have been discovered using imaging techniques (Schneider et al., 2011). In some of those observations, the chemical composition of the atmosphere could already be analyzed (Swain et al., 2009). Still, the exoplanets

[1] Most current exoplanet evolution models indicate that such a planet would significantly reduce the probability of an Earth-like planet in that particular solar system (Steffen et al., 2012).

[2] There are 4776 confirmed exoplanets as of June 2021 (see also `http://exoplanet.eu/catalog/`).

[3] Interference techniques might help overcoming/resolving this obstacle, but carry the disadvantage that this method doesn't reveal detailed information about the properties of the discovered exoplanetary system compared to other detection methods.

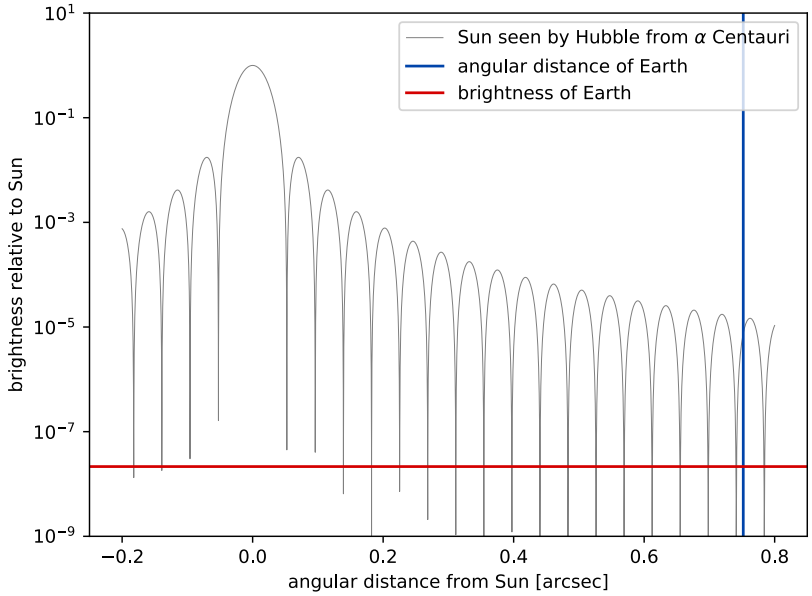

Fig. 1.2.: Hypothetical approximate cross-section of the visual diffraction pattern of the Sun imaged by the Hubble Space telescope on an orbit around Alpha Centauri. The red line indicates the expected brightness of the Earth, passively illuminated by the Sun. The blue line indicates the angular distance at which the Earth would appear relative to the Sun from Alpha Centauri. At this position, the Sun is still at least 1000 times brighter in the visual wavelength regime.

observable with this technique, at least to this date, are far from being considered habitable. They typically are super-Jupiter class objects, closer to brown dwarfs than to Earth-like planets (Schneider et al., 2011)[4].

If an Earth-like planet on its orbit around the Sun were to be observed from Alpha Centauri at a distance of 1.33 parsec, the main problem would be its extremely low brightness compared to its host star, at only 10^{-8} times its value. In this case, the Sun would roughly appear with magnitude 0 in the visible wavelength bands, putting the Earth at about magnitude 20. This would in principle be observable, even with medium-scale telescopes. Unfortunately, the diffraction pattern around the host star outshines the planet by several orders of magnitude. For an example of the *Hubble Space Telescope*, this is illustrated in Figure 1.2.

In recent years, a new idea that could overcome the problem outlined above has gained popularity. In this approach, the light of the host star is blocked by a suitable aperture, which also reduces the diffraction fringes by orders of magnitude utilizing a sophisticated flower-petal-like geometry. This method has for example been proposed by Turnbull et al. (2012) under the name *starshade*. The concept foresees

[4] `http://exoplanet.eu`, online accessed 2021-04-09

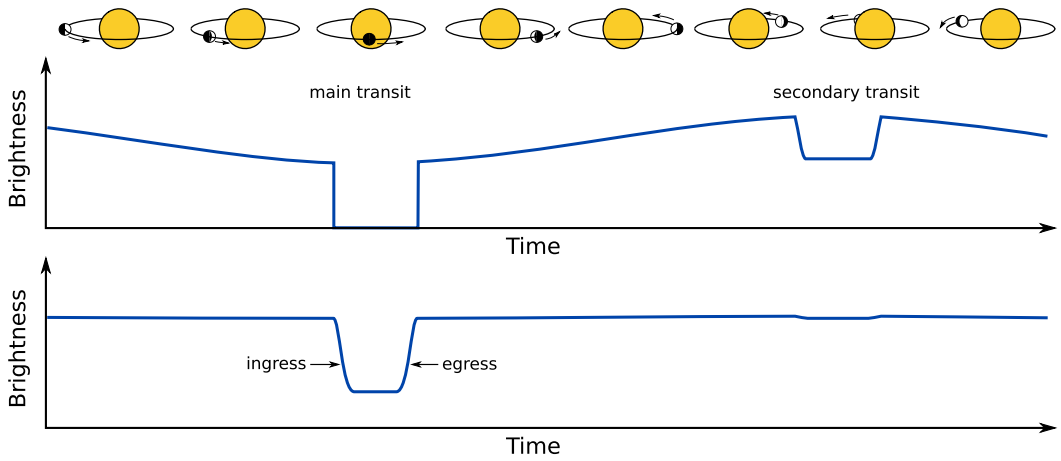

Fig. 1.3.: Illustration of how a typical transit light curve is generated when a planet passes in front of and behind its host star. The transition of the planet in front of the star is called main transit and leads to a much stronger dimming effect compared to the star passing in front of the planet (secondary transit). The phases in which the planet only partially overlaps with the stellar disk at the start or end of the transit are called ingress and egress, respectively. Inspired by and based on an illustration by Markus Kuhlberg.

to deploy a large, precisely shaped structure into space, together with a large space telescope. The *starshade* is then maneuvered into position in front of the host star of the planetary system in which one wishes to directly observe a planet.

1.2.2 Transit method

As discussed above, the amount of light reflected by a planet in comparison to the brightness of the host star is very unfavorable for direct observation. If on the other hand, the planetary orbit passes directly in front of the star, the amount of light blocked by the planet only depends on the ratio of the projected areas, independent of the orbital radius. This ratio - depending on the size of the planet and its host star - can still be several orders of magnitude. But with well calibrated photometric observations of sufficiently bright stars, this effect can be resolved relatively well, especially when using space telescopes that are not affected by the Earth's atmosphere. An advantage of the transit method is that it directly allows for the measurement of the planetary diameter, as long as the size of the star is known. A typical transit light curve is illustrated in Figure 1.3. For transits including a bright star with a close-by large planet, besides the main transit (planet passing in front of the star), the secondary transit (star obscuring the passively illuminated planet) can be observed as well. The fraction of the stellar surface that is obscured by the

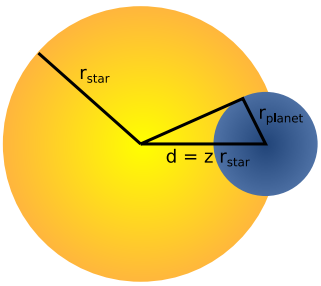

Fig. 1.4.: Parameterization of the obscuration of a star by a transiting planet. Image recreated from Mandel and Agol (2002).

planetary disk λ can be computed analytically which has been done so for example by Mandel and Agol (2002) (see Figure 1.4 for an illustration of the parametrization).

$$\lambda(p,z) = \begin{cases} 0 & 1+p < z \\ \frac{1}{\pi}\left[p^2\,\kappa_0 + \kappa_1 - \sqrt{\frac{4z^2-(1+z^2-p^2)^2}{4}}\right] & |1-p| < z < 1+p \\ p^2 & z \leq 1-p \\ 1 & z \leq p-1 \end{cases} \tag{1.1}$$

with $p = r_{\text{planet}}/r_{\text{star}}$, $z = d/r_{\text{star}}$, $\kappa_0 = \cos^{-1}[(p^2+z^2-1)/2pz]$ and $\kappa_1 = \cos^{-1}[(1-p^2+z^2)/2z]$. The maximum drop in brightness that can be observed would therefore be the ratio of the squares of the radii of the planet and the star. For the Earth, this drop results in $8 \cdot 10^{-5}$ and about 10^{-2} for Jupiter.

The first exoplanet observed this way was HD 209458 b by Charbonneau et al. (2000). At the time of writing this thesis, already more than 3400 exoplanets could be detected with this technique (Schneider et al., 2011)[5], making it the most successful method ever used. A major role in its success play the two large field of view space observatories Kepler and TESS (see Section 1.3).

The transit method leads to observational biases regarding the population of exoplanets. The most obvious one is that the vast majority of exoplanets remain hidden entirely, as their orbital plane does not align with the direction of the observer, resulting in only a fraction of these systems being at least theoretically observable. But the implications exceed further when taking into consideration that the subset of exoplanets which can be observed is not at all representative of the entire population. For statistical reasons, these observations strongly prefer planets on close orbits (something that is true for most detection techniques) but here, in particular, has to be factored in as an additional projection effect. This can be quantified in

[5] `http://exoplanet.eu`, online accessed 09.04.2021

terms of a probability Ω for an observable transit to occur (Charbonneau et al., 2006),(Perryman, 2018):

$$\Omega = 0.0045 \left(\frac{1\,\mathrm{A.U.}}{a}\right) \left(\frac{R_{\mathrm{star}} + R_{\mathrm{planet}}}{R_{\odot}}\right) \left(\frac{1 + e\,\cos(\pi/2 - \omega)}{1 - e^2}\right), \tag{1.2}$$

with the eccentricity e and the argument of the periastron (orientation of the major axis of the orbital ellipse with respect to the observer) ω. Concluding from Equation 1.2, a scenario closely resembling the properties of the Earth-Sun-system only has a 0.45% chance for a transit to be observable from a random direction without taking into account to miss the transit in time.

An additional effect that has not been mentioned is the fact that the stellar surface does not appear as of the same brightness when observed under different angles. This typically causes the star to appear dimmer towards the edge, an effect usually referred to as *limb darkening*. This effect is important for the precise modeling of transit light curves. The details are not discussed here, but some introduction is given in Chapter 6, when describing the multi-transit-fitting software that has been developed in the scope of this thesis.

An interesting prospect for future observations of transiting exoplanets is that these systems might also allow to measure spectral features with the light of the host star passing through the exoplanet atmospheres (transmission spectroscopy). First spectral measurements of transiting exoplanets are already available, mostly from hot-Jupiter type objects (McCullough et al., 2014; Bourrier et al., 2020; Beaulieu et al., 2010). It is likely that such observations will also be possible for Earth-like objects in the near future using large telescopes like the 39 m telescope Extremely Large Telescope (ELT) of the European Southern Observatory (ESO) (currently under construction).

Chapter 6 of this thesis is dedicated to the transit method. This chapter describes the concept and shows first applications of software tools for simultaneously fitting transit light curves from different instruments and different wavelength bands, which has been developed in the scope of this thesis.

1.2.3 Radial velocity method

The radial velocity technique has been used for analyzing observational data in the scope of this thesis and with the Munich Analyzer for Radial velocity Measurements with b-spline Optimized Templates (*MARMOT*), a dedicated software package has

been developed for this purpose. The following section, therefore, introduces the underlying principles in some detail.

Radial velocity measurements of stars that potentially host exoplanets exploit the optical Doppler effect that causes a shift in wavelength of a moving object that is emitting electromagnetic radiation. Fundamentally, two effects contribute to this shift in wavelength:

1. A moving source, velocity v, of a periodic signal, period T_λ, propagating at the speed of light c changes its location by a distance $s = v \cdot T_\lambda$ during one period, while the part of the signal emitted at the beginning of the period has traveled the distance $\lambda = c \cdot T_\lambda$. If the movement is constrained to the direction towards or from a resting observer, this observer will receive a signal with wavelength $\lambda' = \lambda + s = (v + c) \cdot T_\lambda = \lambda \cdot (v + c)/c$.
2. If the source is traveling at relativistic speed, an additional factor of $\frac{1}{\sqrt{1-(v/c)^2}}$ has to be considered that is caused by length contraction between the moving frame of reference in which the light is emitted and the observing system that is assumed to be at rest.

The overall relativistic Doppler effect for movements that take place along the line of sight can then be expressed as

$$\lambda' = \lambda \cdot \frac{1 + v/c}{\sqrt{1 - (v/c)^2}} = \sqrt{\frac{1 + v/c}{1 - v/c}}\,. \tag{1.3}$$

For radial velocities that occur when observing stars that are influenced by orbiting exoplanets it typically is absolutely sufficient to assume the non-relativistic approximation of the form

$$\lambda' = \lambda \cdot (1 + v/c)\,. \tag{1.4}$$

As dictated by Newton's third law, a star and its planetary companion orbit around their common center of gravity, such that the net momentum is constant (or zero if observed from the systems rest frame, as assumed in the following). Therefore, the orbital velocities distribute inversely proportional to the mass ratio of the two astrophysical bodies (stellar mass M, planetary mass m).

$$\begin{aligned} M \cdot \vec{v}_{\text{star}} + m \cdot \vec{v}_{\text{planet}} &= 0 \\ \Rightarrow M \cdot v_{\text{star}} &= m \cdot v_{\text{planet}} \\ \frac{v_{\text{star}}}{v_{\text{planet}}} &= \frac{m}{M}\,. \end{aligned} \tag{1.5}$$

Assuming circular orbits

$$v = \frac{2\pi\, a}{T}\,, \tag{1.6}$$

with the semi-major axis a and the orbital period T. Therefore also the semi-major axes a_{star} and a_{planet} behave in this manner.

$$\frac{a_{\mathrm{star}}}{a_{\mathrm{planet}}} = \frac{m}{M}\,. \tag{1.7}$$

From Kepler's third law and Newtonian gravity the following relation can be obtained,

$$\frac{(a_{\mathrm{star}} + a_{\mathrm{planet}})^3}{T^2} = \frac{G \cdot (M + m)}{4\,\pi^2}\,, \tag{1.8}$$

which can be further simplified to

$$\frac{a_{\mathrm{planet}}^3}{T^2} = \frac{G\,M}{4\,\pi^2}\,, \tag{1.9}$$

assuming that the mass of the planet and the semi-major axis of the star to not contribute significantly to the sums. Inserting Equation 1.6 and solving for v_{planet} gives

$$v_{\mathrm{planet}} = \sqrt[3]{\frac{2\pi\, G\, M}{T}}\,, \tag{1.10}$$

and after also inserting Equation 1.5 the velocity semi-amplitude of the star is obtained.

$$v_{\mathrm{star}} = \frac{m}{M} \cdot \sqrt[3]{\frac{2\pi\, G\, M}{T}}\,. \tag{1.11}$$

In practice, the planetary system is observed under an angle i (inclination) with respect to the surface normal to the orbital plane. Therefore, only the component projected onto the direction towards the observer $K = v_{\mathrm{star}} \cdot \sin i$ can be measured. The observed radial velocity then follows a sinusoidal curve with that semi-amplitude. One intrinsic disadvantage of radial velocity-based exoplanet studies is that the inclination and therefore also the true orbital velocity is not accessible to the observer. Without knowledge of the orientation of the orbital plane of such a system, the measured semi-amplitude K only serves as a lower limit for v_{star} and consequently, only a lower limit for the mass of the planetary companion can be obtained.

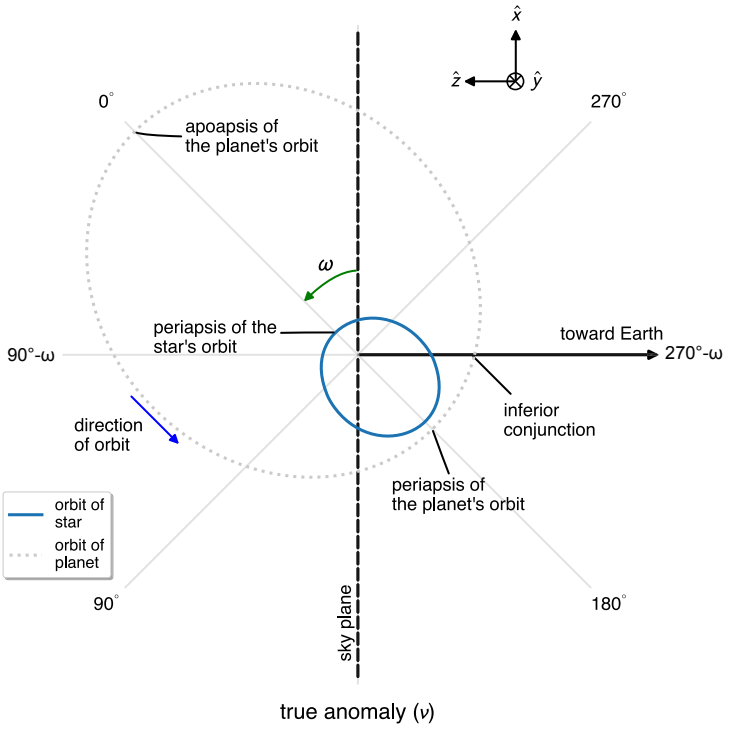

Fig. 1.5.: Parametrization for modeling radial velocity curves used by *RadVel*. Note that the inclination i (tilt of the orbital plane with respect to the direction to the observer) is not part of the model as this parameter is entirely inaccessible by the radial velocity method. Image taken from Fulton et al. (2018).

If the orbit is in addition elliptical, the situation is far more complex as also the orientation of the ellipse within the orbital plane determines the evolution of radial velocity signal with time. Modeling of the resulting radial velocity curves will not be discussed in detail in the scope of this thesis, but the parametrization of planetary orbits will be discussed at the example of the *RadVel*[6] fitting toolkit (Fulton et al., 2018). *RadVel* is used as a final analysis step after extracting radial velocity measurements from spectral measurements with the program *MARMOT*. The following parameters are used by *RadVel* for modeling radial velocity curves:

- orbital period P
- time of inferior conjunction (or transit) T_c
- time of periastron T_p
- eccentricity e
- argument of periapsis of the star's orbit ω
- velocity semi-amplitude K

[6] *RadVel* documentation: `https://radvel.readthedocs.io/`

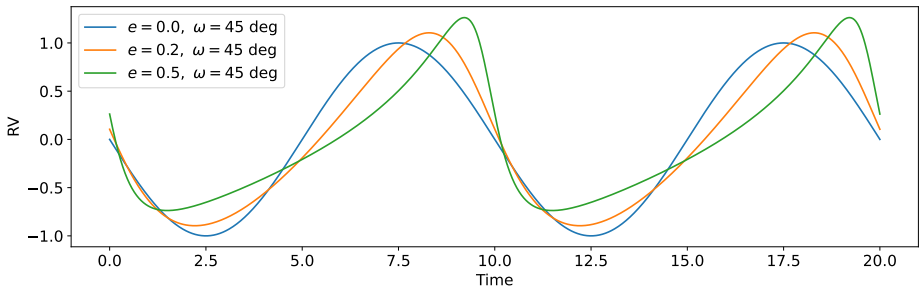

Fig. 1.6.: Three example radial velocity curves generated using *RadVel*, showing 2 orbital phases. With increasing eccentricity, the curves become more and more asymmetric, while of course also the orientation of the orbital ellipse with respect to the observer ω changes the actual shape. In this plot $\omega = 45$ deg has been chosen arbitrarily.

Some of those parameters are explained in the illustration shown in Figure 1.5 and three sample radial velocity curves are shown in Figure 1.6.

The following example is given in order to highlight the required spectral precision necessary, especially when searching for Earth-like worlds. In an Earth-like system, the planet orbits its host star with a velocity of 30 km/s, and a mass ratio of about $33 \cdot 10^4$. The resulting radial velocity of the star is about 0.1 m/s with respect to the speed of light. This corresponds to an optical Doppler shift of $3.3 \cdot 10^{-10}$, a very small value, but not entirely out of reach for modern highly stabilized spectrographs. Most of the modern instruments like *FOCES* can reach resolutions on the m/s level. In case of *FOCES*, as shown also in Chapter 3.1, the spatial precision that is required for maintaining a resolution of 1 m/s, corresponds to a relative precision of $3.3 \cdot 10^{-9}$. At a digitization resolution of 0.038 Å per pixel around 5500 Å this results in a shift that needs to be measured of only a 2000^{th} of a pixel.

For the radial velocity method to be feasible and achieve acceptable sensitivity, it is crucial that the observed star shows a sufficient amount (number density) of well defined spectral lines (sharp and deep absorption lines) in its spectrum. As shown on the left side of Figure 1.7 the number density of strong spectral lines depends significantly on the surface temperature of a star resulting in a drop of spectral lines from 1800 lines at 5000 K to less than 100 lines for early type stars (high temperature). The drop in the number density at lower temperature stem from the overpopulation of the spectrum with absorption lines resulting in unsolvable line blends and thus in a deterioration on the determination of the line center.
The table in Figure 1.7 (right side) lists the mean stellar rotation for different spectral types. The clear decrease starting around the mid-F type stars (so-called 'rotation break' (Kraft, 1967)) is the result of the development of a substantial convection in

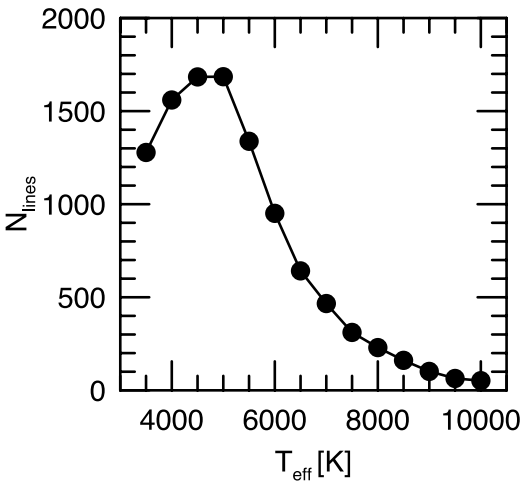

spectral type	v sin i [km/s]	spectral type	v sin i [km/s]
O4	110	G0	4
O9	105	G5	3
B5	108	K0	3
A0	82	K5	2
A5	80	M0	10
F0	44	M4	16
F5	11	M9	10

Fig. 1.7.: Number of strong absorption lines in stellar spectra as a function of surface temperature of the star. The term 'strong absorption line' refers here to a line having a depth deeper than 50% of the continuum value. Image taken from Hatzes (2019). Table on the right taken from Glebocki and Gnacinski (2005)

the outer star layers which leads in combination with the magnetic activity to a loss of angular momentum trough magnetic braking (Hatzes, 2019). These combined effects lead to a favored region of star types of $T_{eff} = 4500 - 6500K$ for the RV-hunt of exoplanets. This does not imply that planet-star systems outside of this temperature range can not be observed but that the achievable lower limit for the radial velocity signal is driven by the stellar properties and can dominate observed signals.

In statistical terms, the radial-velocity method is biased towards heavy planets and planets on close orbits, as those have much higher orbital velocities and are therefore easier to detect. With a total of nearly 1000 exoplanets discovered using this method at the time of writing this thesis, the radial velocity technique is the second most successful technique (Schneider et al., 2011)[7].

A large fraction of this thesis is dedicated to instrumentation and software that is required in order to achieve high precision measurements with the RV method. Chapter 2.2.2 introduces the *FOCES*, the instrument that was used for conducting the radial velocity measurements described in this thesis. This chapter also contains a detailed description of the installation, pressure and temperature stabilization, and laser-frequency-comb wavelength calibration of *FOCES*, conducted in the context of this thesis. Furthermore, Chapter 5.2 introduces and demonstrates the performance of the newly developed software *MARMOT* for precision calibration and radial velocity extraction from 1D Échelle spectra.

[7] `http://exoplanet.eu`, online accessed 2021.04.09

1.2.4 Other detection methods

The techniques mentioned above do not represent an exhaustive list of all detection methods for exoplanets which have been observed to date. Other known techniques are:

- Gravitational microlensing, where an exoplanet passing in front of a more distant star causes a short (selective) boost in brightness due to a light collection effect by the gravitational lens. This effect can reveal the presence of small, far-away, and non-transiting exoplanets that can not be detected with any other method. Unfortunately, those are by chance one-off observations that can not be repeated (e.g. (Beaulieu et al., 2006)).
- Pulsar timing is a special case of the radial velocity method that allows to observe exoplanets orbiting pulsars (e.g. Wolszczan and Frail (1992)). While pulsars do not possess spectral features in the optical wavelength regime that would allow to conduct precise radial velocity measurements, they emit pulsed radio signals with extraordinarily precise repetition rates. These frequencies can be measured with very high precision, allowing to measure even the smallest modulation due to Doppler shifts thereby being more sensitive to small planets than radial velocity measurements. Pulsars in general however are relatively rare and while it is of academic interest that these objects can also host planets orbiting them, those planets cannot be considered habitable, due to the little amount of thermal radiation emitted by pulsars and the strong high energy radiation they emit.
- Astrometry can also be used for detecting exoplanets (e.g. (Ranalli et al., 2018)). Similar to the radial velocity method, this technique exploits the fact that both, the planet and the star are affected by their corresponding gravitational pull, causing them to circle around their joint center of mass. For small, Earth-like exoplanets this effect is naturally quite small. The center of gravity of Earth and Sun lies at around 0.065% of the radius of the Sun from its center. In contrast to most other methods, the sensitivity, at least theoretically, increases with larger orbital radii since the distance between the barycenter of the planet star system and the star center grows, the further away the planet is located.
- Finally, there are a couple of additional methods that use timing of periodical events like planetary transits or eclipsing binaries in order to detect additional companions that might reside within the system.

With the scientific instrumentation available for the 2.1 m Fraunhofer Wendelstein Telescope (FWT) at the Wendelstein Observatory, radial-velocity as well as transit-based studies of exoplanet systems can be conducted. By combining both techniques it is not only possible to confirm the detection with different methods, but also narrowed down significantly the properties of the observed system. Such a combined observation has the potential to reveal information about the composition of the planet, as its radius, as well as the mass, can be measured this way.

1.3 Instruments

In this section, a selection of important instruments for the search of exoplanets utilizing photometric transits will be summarized. The data from some of those instruments have been employed for testing the *multranfit* software that is described in Chapter 6. Instruments for radial velocity measurements (high resolution Échelle spectrographs) are not introduced in this section as the entirety of Chapter 2 is dedicated to these devices and *FOCES* in particular.

1.3.1 Kepler

The Kepler satellite that was launched into a heliocentric orbit in 2009 and decommissioned in 2018, can be considered the most successful exoplanet mission to date, with a number of 2820 exoplanets detected in total[8]. This number is the sum of all exoplanets with a confirmed detection in both, the Kepler and the K2 phases of the mission. In 2013 the Kepler spacecraft lost two of its reaction wheels necessary for controlling its orientation. This terminated the original Kepler mission that was continuously monitoring a field of view of 110 square degrees in the Cygnus constellation and initiated a second phase in the operation of the Kepler satellite named K2, in which the instrument was forced to operate in a scanning mode (Howell et al., 2014).

With a primary mirror of 1.4 m diameter, Kepler is one of the largest optical space telescopes ever sent into orbit. The telescope follows a Schmidt design, with a single mirror and a Schmidt corrector plate. The science camera is located in the focal plane of the main mirror and consists of 42 individual CCD sensors with 2200 x 1024 pixels each, resulting in a total of 95 megapixels. The sensor surface is curved and follows

[8] `https://exoplanetarchive.ipac.caltech.edu/docs/counts_detail.html`, online accessed 2021-04-10

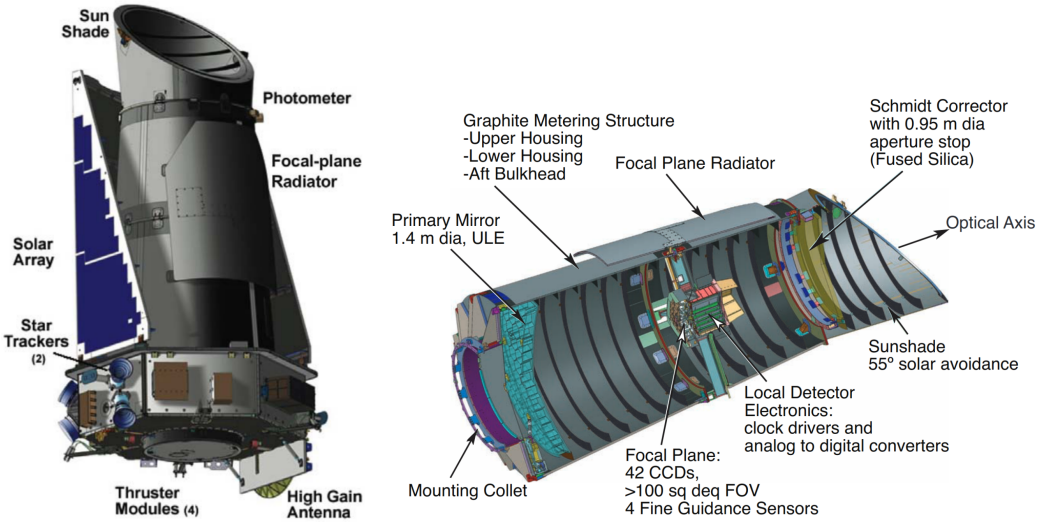

Fig. 1.8.: Main components of NASA's Kepler satellite (left) and cut view of the actual telescope (right). Image credit: NASA[9].

the field curvature of the optics. The camera itself is cooled to -85°C and covers a field of view of about 110 $\deg^2$. The CCD sensors are read out every 6 seconds, but the images are stacked for a total exposure of 30 minutes and then stored for transmission to Earth. This results in the finest available time binning in Kepler's standard operation mode to be 1800 s (Koch et al., 2010).

Despite covering only a quarter of a percent of the entire sky, Kepler detected nearly 2400 exoplanets during its first mission phase between 2009 and 2013. Petigura et al. (2013) argues that extrapolating from Kepler discoveries it is expected that within the entire Milky Way Galaxy about 17 million Earth-sized (1-2 $\times$ R_{earth}) planets are orbiting Sun-like (within a factor four of the Sun's energy output) stars.

1.3.2 TESS

The Transiting Exoplanet Survey Satellite (TESS) was launched into an elliptical orbit around Earth in 2018. TESS can be seen as the successor mission of Kepler, with however a quite different observation strategy. While Kepler was designed to conduct very deep observations of a relatively small field of view, TESS is scanning, with very small gaps, the entire sky. The main scientific instruments aboard of TESS are four 16.8 megapixel CCD cameras (mosaic of 2×2 2048×2048 sensors) equipped

[9] `https://www.nasa.gov/pdf/314125main_Kepler_presskit_2-19_smfile.pdf`, online accessed 2021-04-11

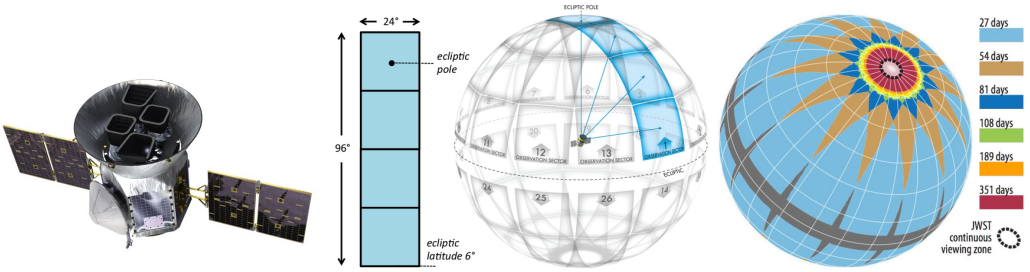

Fig. 1.9.: TESS with its four refracting telescopes, each covering $24 \times 24\,[\mathrm{deg}^2]$ (left). They are oriented such that they cover a field of view of $24 \times 96\,[\mathrm{deg}^2]$ (center). The sky-survey mode of TESS foresees to observe the same field of view for 27 days and then rotates around the ecliptic pole by about 28 degrees, and so on. The second hemisphere is observed after the first has completed a full rotation (right). Image credit: NASA[10].

with 10 cm aperture refracting telescopes. Each telescope has a $24 \times 24\,[\mathrm{deg}^2]$ field of view, and each individual telescopes points in a different direction, offset by 24 degrees. That results in a total field of view covered by a single exposure of $24 \times 96\,[\mathrm{deg}^2]$. The observational strategy of TESS foresees to continuously observe the same field of view for 27 days and then rotate by about 28 degrees and observe for the next 27 days this new field, and so on. The field of view is rotated around the ecliptic pole as indicated in Figure 1.9. This way, both the Sun and Moon are avoided while covering one hemisphere within one year. It is worth noting that the sky within a 12 degree radius field of view towards the ecliptic pole is observed continuously for the entire time window, which is in addition and by design the region of interest for the James Webb Space Telescope (to be launched in late 2021). After one year TESS repeats this procedure for the other hemisphere (Ricker et al., 2014).

1.3.3 3KK

3-Kanal-Kamera (3KK) is the optical-NIR multi-channel imager installed on the Nasmyth port[11] of the 2.1 m Wendelstein Fraunhofer telescope. The instrument allows to simultaneously record CCD images in up to two optical (CCD, Apogee ALTA F3041) and one NIR (CMOS, HAWAII-2RG) wavelength bands. An illustration of the optical setup alongside the dichroic beam splitters can be found in Figure 1.10. The optical channels have a field of view of 7 x 7 arcmin at a resolution of 0.2 arcsec/pixel while

[10] `https://heasarc.gsfc.nasa.gov/docs/tess/the-tess-space-telescope.html`, online accessed 2021-04-15

[11] Telescope port that couples the light along the elevation axis of an Alt-Az mounted telescope.

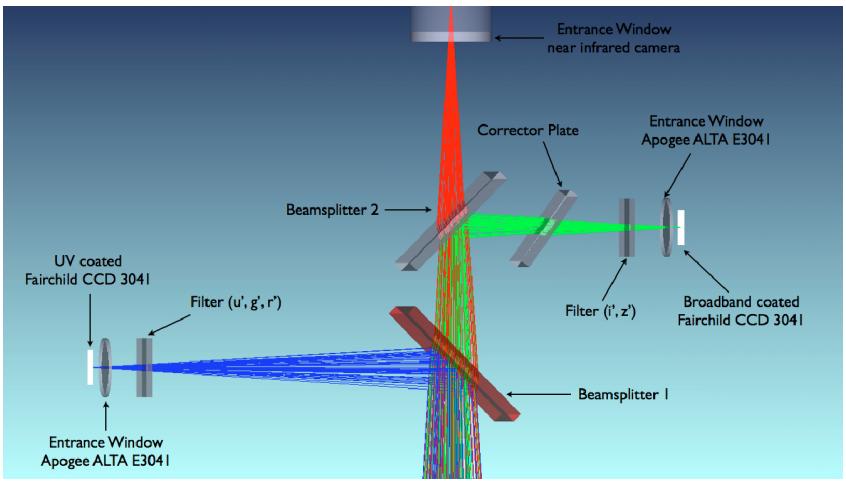

Fig. 1.10.: Top view of the optics inside the 3KK optical-NIR multi-channel imager. Several dichroic beamsplitters are used for separating parts of the optical and NIR spectrum of the light entering before filter wheels allow only wavelengths within the desired band to be recorded by the respective CCD cameras. Image taken from Lang-Bardl et al. (2010).

the NIR camera has a slightly wider field of view of 8 x 8 arcmin with 0.24 arcsec per pixel.

The 3KK is equipped with Sloan-like u', g' and r' filters to be utilized with the blue CCD and an i' as well as a z' filter for the red CCD. Furthermore, Y, J, H and a Ks filter are available for the CMOS camera. The wavelength filters, scaled with the overall optical efficiencies, are shown in Figure 1.11. The Ks filter was chosen over a K-band filter because the telescope optics are not optimized for infrared, causing self-emission from the structure to enter the camera, especially for the longest wavelengths. The Ks filter has an earlier cut-off wavelength compared to the K filter, reducing this effect. For a detailed overview of the instrument, the reader is referred to Lang-Bardl et al. (2010).

Such a 3-channel imager is advantageous for recording light curves of transiting exoplanets. Three spectrally disjunct channels allow for a better understanding and subsequently correction of atmospheric effects in the data, while at the same time also give a better handle on separating limb-darkening from orbital parameters. In the scope of this thesis, a dedicated software package *multranfit* (see Chapter 6) has been developed for simultaneously analyzing such multi-channel data. *multranfit* is not limited to the 3KK data but allows an arbitrary number of measurements from terrestrial and space-based instruments to be combined in a single fit to reveal the planetary and orbital parameters for such a planet-star-system. Such analyses have lead to the discovery/confirmation of three exoplanets (Wendelstein-1b, Wendelstein-

2b and TOI 1823) under the lead of Dr. Christian Obermeier and Jana Steuer, which are presented in Chapter 6.

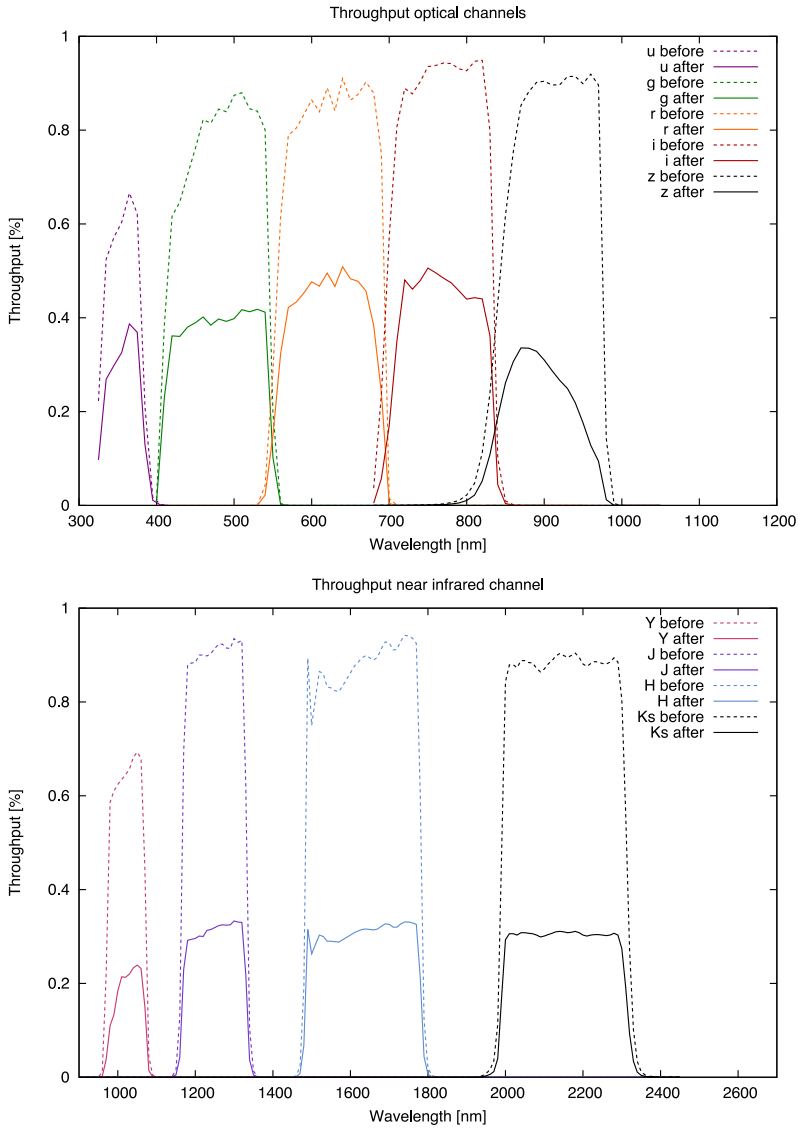

Fig. 1.11.: Band-pass filters available for the 3KK optical-NIR multi-channel imager, in optical (Top) and NIR wavelengths (Bottom). The upper curves correspond to the transmission curves of the optical filters, while the lower curves also factor in the overall efficiency of the optical system. Plot taken from Lang-Bardl et al. (2010).

Part II

Spectrographs

Spectrographs for astronomy

2

> *One can enjoy a rainbow without necessarily forgetting the forces that made it.*
>
> **— Mark Twain**

During the 17th century, Isaac Newton was for the first time able to prove that the white light from the sun is in fact a combination of light of different colors. Using a prism, it can be split into those components, revealing a rainbow-like spectrum, and subsequently re-combined into a white ray using a similar prism. Finally, at the beginning of the 19th century, utilizing narrower beams of light and higher quality prisms, scientists like William Hyde Wollaston and Joseph von Fraunhofer were able to resolve fine absorption lines in the solar spectrum. Fraunhofer introduced for the first time a labeling scheme that is still in use today, where the most prominent features are given capital roman letters (A, B, C, D, E, F, G, H, K) and fainter ones were assigned small letters. In total, he could identify more than 570 such dark features throughout the solar spectrum and even discovered absorption lines in the spectra of other stars, where he recognized differences to the solar spectrum. The dark lines in the solar spectrum, named after Fraunhofer himself, were then found by Gustav Robert Kirchhoff, Robert Bunsen and others to coincide with the emission lines of chemical elements, like the famous Na-doublet (D_1 and D_2) lines (Kitchin, 1995).

This kind of association of the properties of astrophysical objects with lab measurements was the second instance after Newtons *Philosophiæ Naturalis Principia Mathematica* that it could irrefutably be demonstrated that the cosmos and the Earth are subject to the same laws of nature. This finally gave rise to the field of science that we today refer to as astrophysics, meaning not only observing and describing the cosmos but also applying the laws of physics that are known and studied in laboratories here on Earth.

2.1 Motivation

As it has been demonstrated already in Chapter 1.2.3, the radial velocity method for detecting exoplanets imposes quite demanding requirements on the spectral accuracy for the observation of stellar spectra. In relative terms, an accuracy of about one in 300 million is required to reach the m/s regime, which is crucial for studying Earth-like objects inside the habitable zone around their host star. This level of accuracy does not only imply that the spectral resolution and photon statistics in the recorded spectra need to be sufficient in order to detect red/blue shifts on that level ($\lesssim 10^{-4}$ Å), but that the instrument needs to maintain such a level of stability over days, months or even years. Every apparent shift introduced by the instrument or the data analysis itself results in systematic errors of the radial velocity measurement and ultimately a decline of the RV-estimation properties. The following (non-exhaustive) list presents an overview of parameters that can influence the accuracy with which radial velocities can be measured based on stellar spectra:

- the resolving power of the spectrograph (spectral line resolution),
- the stability of the spectrograph (apparent shift of the spectral line),
- the uniformity of the entrance aperture illumination of the spectrograph (apparent shift of the spectral line),
- the amount of light per spectral bin (photon counting statistics),
- the wavelength calibration stability over at least one orbital period (apparent shift of the spectral line),
- the amount and magnitude of telluric lines in the observed spectrum,
- the number of absorption lines in the spectrum,
- the depth and sharpness/edge steepness of these spectral lines.

Of those parameters listed, the first five can be influenced by optical and mechanical design choices of the whole instrument while the latter three are intrinsic to the observed target and/or observatory site.
The setup of the high-resolution spectrograph *FOCES* at the Wendelstein Observatory is a typical example of a modern spectrograph. Connected via an optical fiber to the 2.1 m Fraunhofer telescope of the University Observatory is the spectrograph itself, housed in the basement in a temperate- and pressure-stabilized tank. The following

three sections provide an overview of the most essential components and design choices required to provide the option for m/s-measurements of exoplanets:

- the optical design of the spectrograph,
- the fiber connection between telescope and spectrograph and its implication on the hunt for exoplanets and
- the currently available wavelength calibration standard for high-resolution spectrographs, a frequency comb.

During the discussion, typical obstacles, their implication on the measured accuracy and solutions to these problems are presented.

2.2 Considerations on dispersive elements

Even though generations of scientists have improved measurement devices since the discovery of spectroscopy and wave optics, the same fundamental concepts are still used in spectrographs today. There are two basic physical principles that can be used for building optical spectrographs, refraction and diffraction.[1]

The two most important properties of these dispersive elements concerning spectroscopy in astronomy, and specifically for precise radial velocity measurements are: spectral resolution and total light yield (efficiency). Spectral resolution results in narrower lines being detectable/measurable in the spectrum which generally leads to a smaller uncertainty on the determined position of its central position. On the other hand, especially in astronomy, the actual limiting factor on the center-of-line-fit accuracy is determined by photon statistics. Therefore, light yield is commonly traded for spectral resolution by for example choosing a wider slit at the entrance of the spectrograph.

Refractive optical elements

Refractive elements are typically prisms made from refractive materials, showing dispersion. Dispersion, meaning a different (typically higher for normal dispersion) refractive index for blue light compared to red light, leads to different angles of deflection for different wavelengths when applying Snell's law. Dispersion can be understood as the increasing response of atomic oscillators to excitation frequencies as one approaches the resonance peak from lower frequencies (longer wavelengths), as

[1] As it will be shown later, high-resolution spectrographs like *FOCES* combine both effects.

described by the harmonic oscillator model (Jahns and Helfert, 2012). When guiding a narrow beam of light through such an apparatus and mapping the outgoing light onto a screen or CCD sensor, different wavelengths will be separated spatially. The maximum resolution in wavelength that can be achieved this way is fundamentally limited by the dispersion of the prism. This is usually not enough to serve as the main dispersive element in a high-resolution spectrograph and concatenating several prisms to combing their dispersion power leads to a number of disadvantages as for example increased surface losses.

Diffractive optical elements

The second fundamental concept of optics that is widely used in scientific spectrographs is diffraction, which can be exploited by utilizing diffraction gratings. Optical gratings introduce angle- and wavelength-dependent phase differences that are a multiple of $\Delta\phi$ between the different light paths (Figure 2.1, left side):

$$\Delta\phi = 2\pi \frac{d \sin\alpha}{\lambda}\,, \tag{2.1}$$

where α is the angle with respect to the direction normal to the grating, d is the distance between the slits of the grating and λ is the wavelength of the light hitting the grating. Whenever the different paths that the light can travel Δr differ by an integer multiple m of the wavelength, this leads to constructive interference for that wavelength at the given deflection angle α (Perpendicular incidence, $\beta = 0$, see Figure 2.4):

$$\Delta r = f = \pm m \cdot \lambda = d \cdot \sin\alpha, \quad m = 0, 1, 2... \tag{2.2}$$

2.2.1 Optical gratings: disambiguation and applications

The fundamental purpose of an optical grating is to create periodic phase differences in the outgoing light that depends on the angle α, under which the light is observed, ultimately leading to constructive or destructive interference depending on the direction or wavelength λ. This can be achieved in different ways, either by periodically blocking light from being transmitted (amplitude gratings) or transmitting all of the incident light, but periodically altering it's phase (phase gratings) whereby both types can be produced in both ways, as reflection or transmission grating, see also Figure 2.1, right side. As mentioned above, astronomical observations are typically limited in their sensitivity by the available amount of light, therefore amplitude gratings are usually not considered for astronomical spectroscopy. The intensity

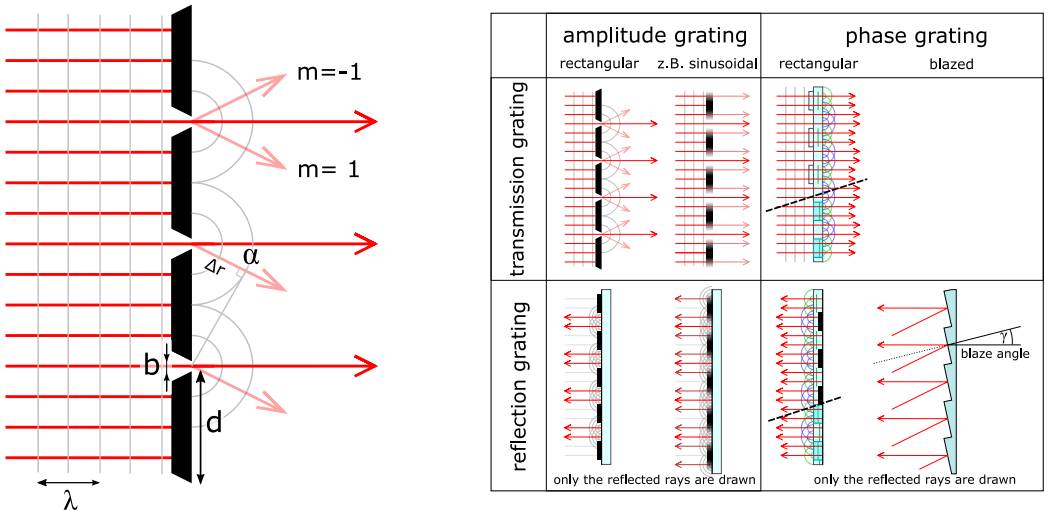

Fig. 2.1.: Left panel: Illustration of the condition for constructive interference of light interacting with an optical grating. Right panel: Disambiguation of different types of optical gratings[2].

pattern of a grating, for an incident angle $\beta = 0\,\text{deg}$ and with N lines illuminated, slit width b and spacing d, as a function of deflection angle α and wavelength λ is given by

$$
\begin{aligned}
I(\alpha,\lambda) &\propto \left\| \sum_{n=0}^{N-1} \left(\int_0^b e^{\frac{i2\pi(nd+x)\sin\alpha}{\lambda}} \mathrm{d}x \right) \right\|^2 \\
&= \left\| \sum_{n=0}^{N-1} \left(e^{\frac{i2\pi nd\sin\alpha}{\lambda}} \right) \cdot \int_0^b e^{\frac{i2\pi x\sin\alpha}{\lambda}} \mathrm{d}x \right\|^2 \\
&= \left\| \sum_{n=0}^{N-1} \left(e^{\frac{i2\pi nd\sin\alpha}{\lambda}} \right) \right\|^2 \cdot \left\| \frac{-i\,b\left(e^{\frac{i2\pi b\sin\alpha}{\lambda}} - 1 \right)}{\frac{2\pi b\sin\alpha}{\lambda}} \right\|^2 \\
&= \left\| \sum_{n=0}^{N-1} \left(e^{\frac{i2\pi nd\sin\alpha}{\lambda}} \right) \right\|^2 \cdot b^2 \frac{\left\| \sin\frac{i2\pi b\sin\alpha}{\lambda} - i\cos\frac{i2\pi b\sin\alpha}{\lambda} + i \right\|^2}{\left(\frac{2\pi b\sin\alpha}{\lambda} \right)^2} \\
&= \left\| \sum_{n=0}^{N-1} \left(e^{\frac{i2\pi nd\sin\alpha}{\lambda}} \right) \right\|^2 \\
&\cdot b^2 \frac{\left(\sin\frac{i2\pi b\sin\alpha}{\lambda} - i\cos\frac{i2\pi b\sin\alpha}{\lambda} + i \right)\left(\sin\frac{i2\pi b\sin\alpha}{\lambda} + i\cos\frac{i2\pi b\sin\alpha}{\lambda} - i \right)}{\left(\frac{2\pi b\sin\alpha}{\lambda} \right)^2}
\end{aligned}
$$

[2]Image source: Translated from `http://de.wikipedia.org/wiki/Optisches_Gitter`, accessed 20.01.2021

$$
\begin{aligned}
&= \left\| \sum_{n=0}^{N-1} \left(e^{\frac{i2\pi n d \sin\alpha}{\lambda}} \right) \right\|^2 \cdot b^2 \, \frac{2 - 2\cos\frac{i2\pi b \sin\alpha}{\lambda}}{\left(\frac{2\pi b \sin\alpha}{\lambda}\right)^2} \\
&= \left\| \sum_{n=0}^{N-1} \left(e^{\frac{i2\pi n d \sin\alpha}{\lambda}} \right) \right\|^2 \cdot b^2 \, \frac{4\sin^2\frac{i\pi b \sin\alpha}{\lambda}}{\left(\frac{2\pi b \sin\alpha}{\lambda}\right)^2} \\
&= \left\| \sum_{n=0}^{N-1} \left(e^{\frac{i2\pi n d \sin\alpha}{\lambda}} \right) \right\|^2 \cdot b^2 \, \mathrm{sinc}\left(\frac{\pi b \sin\alpha}{\lambda}\right)^2 , \qquad (2.3)
\end{aligned}
$$

Mathematically, the left side of Equation 2.3 describes the high-frequency interference pattern of all illuminated slits, whereas the right part of the equation represents the envelope function of a single slit of the grating. The intensity distribution $I(\alpha, \lambda)$ of a grating consists of a strongly structured function (the interference pattern of grating lines), the absolute intensity of which is superimposed by a sinc-function (single slit function of the grating) with a dominant central peak and smaller side maxima. Examples of the resulting intensity distribution are shown in Figure 2.2 for different numbers of contributing lines.

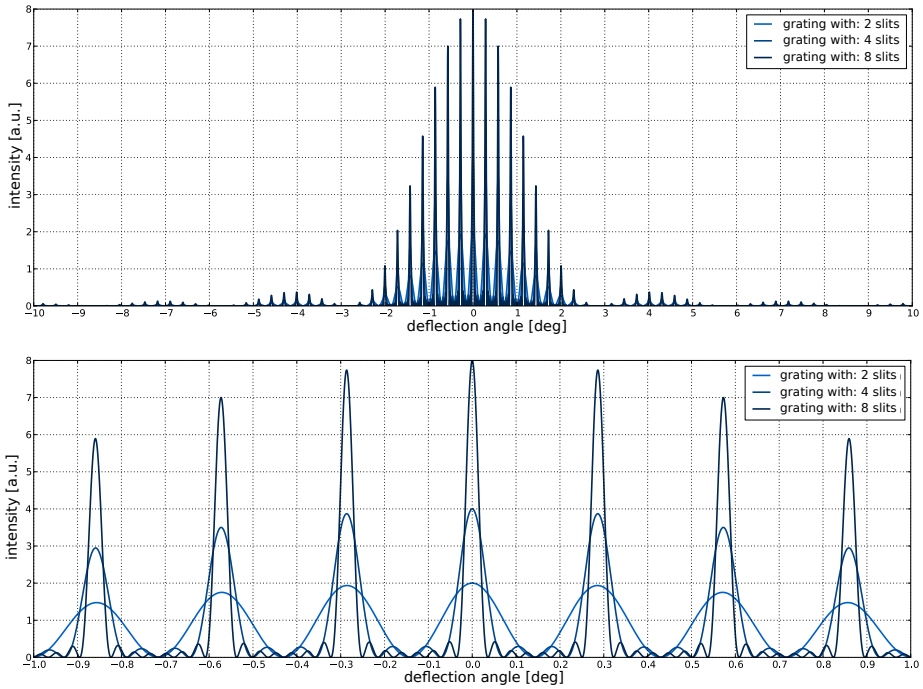

Fig. 2.2.: Diffraction pattern of an optical grating with increasing number of slits in terms of received optical power. The top panel highlights the diffraction pattern of a single slit, which acts as envelope function for the interference pattern formed by the grating. This pattern is better visible in the zoomed-in plot in the lower panel, which highlights the narrowing of the lines when adding more and more slits to the grating. The graph illustrates a grating with d=100μm, b=3.2μm illuminated by a wavelength of λ=500nm.

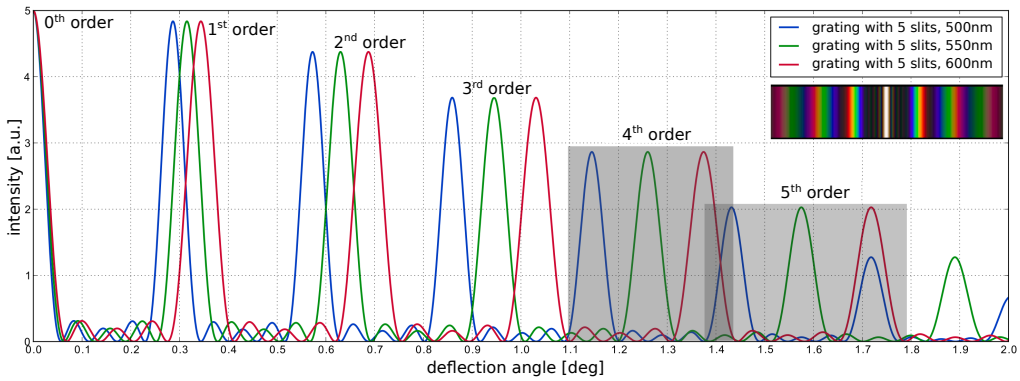

Fig. 2.3.: Illustration of the diffraction pattern of an optical grating for three different wavelengths. The individual wavelengths get thereby separated more and more with increasing order number, until they even start to overlap with lines from the adjacent orders. The graph illustrates a grating with d=100μm and b=3.2μm. Small inserted spectrum in the upper right corner: `http://www.vikdhillon.staff.shef.ac.uk/teaching/phy217/instruments/phy217_inst_grating.html` on the 18.12.2020 at 20:30.

The fact that the deflection angle of a grating is wavelength dependent leads to a wavelength-dependent separation when broadband light (e.g. starlight) is mapped through a spectrograph since every wavelength produces its own spacial separated interference pattern in the imaging plane. For higher orders of the grating, this results in an increased separation between the maxima corresponding to different wavelengths improving thereby the resolution which is usually desirable for exoplanet research. However, in this configuration, it is of tremendous disadvantage that the lower grating orders due to the enveloping sinc-function combine a substantial amount of light which is unacceptable in a low-light research field like astronomy. Blaze gratings however overcome this disadvantage by a saw-tooth-like structure which reflects, depending on the blaze angle, light to a higher-order or, in other words, introduces a shift into the envelope function. Based on Figure 2.4, the total path difference is represented as the difference between $e = \sin(\beta) \cdot d$ and $f = \sin(\alpha) \cdot d$, resulting in:

$$\Delta r = \pm m \cdot \lambda = e + f = \sin(\beta) \cdot d + \sin(\alpha) \cdot d = d \cdot (\sin(\alpha) + \sin(\beta)) \tag{2.4}$$

whereby an additional degree of freedom β compared to Equation 2.2 is introduced. In the depicted example, peaks from the fourth-order onward are completely disjunct. Indicated by the gray area, however, the interference maxima of different colors and different diffraction orders increasingly overlap. For such an optical setup, these higher diffraction orders would render completely useless as soon as the observed spectrum exceeds a certain spectral width.

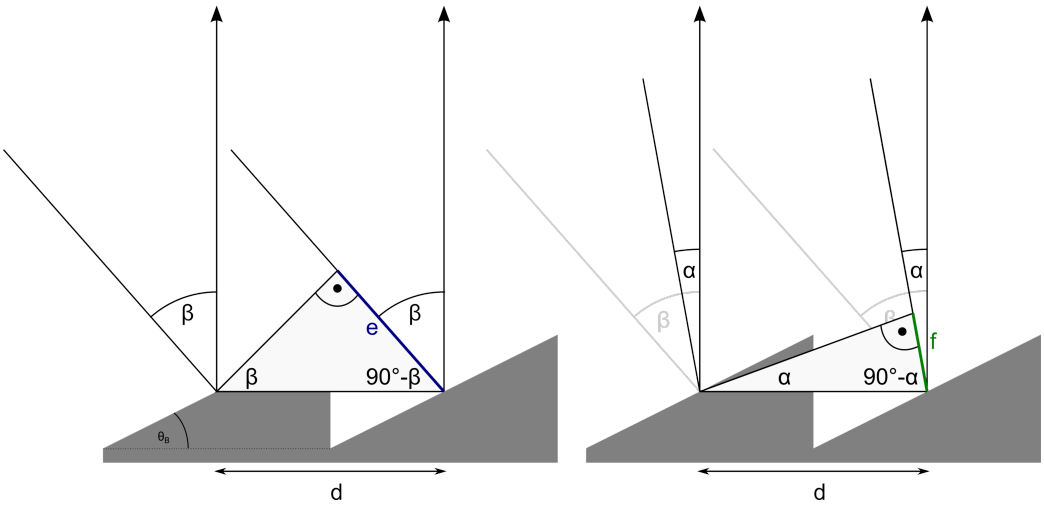

Fig. 2.4.: Illustration of the working principle of a blaze grating. By tilting the reflecting surfaces of a reflection grating, the single-slit diffraction peak can be moved in any direction. This way, high diffraction orders can be utilized with high efficiency. The sum of the distances e and f is thereby the optical path difference that needs to match an integer multiple of the wavelength in order to produce an interference maximum.

2.2.2 Composition of a high-resolution spectrograph

For optical high-resolution astronomical spectroscopy, mainly Échelle spectrographs are being used, as is the case for *FOCES*. From Equation 2.3 it can be deduced that for a given wavelength there are two ways to improve the resolution of a grating spectrograph: either by a reduction of the slit/line width d or by the choice of a higher-order m. High-resolution spectrographs usually exploit the second method, since the technical challenges are ever increasing with further decreasing grating line widths. Échelle spectrographs are therefore operated at very high orders of 80 and higher. However, at such a high-order number, individual orders substantially overlap each other in the image plane (see also Figure 2.3, gray shaded area). In order to avoid this obstacle, Échelle spectrographs consist of two concatenated spectrographs, namely:

- a high-resolution (e.g. using a blazed grating)
- and a low resolution (e.g. with the help of a prism).

Whereby the *high-resolution* part of the spectrograph is responsible for the separation of the light into its spectral components. In order to obtain analyzable data, despite the overlapping orders, an additional low-resolution spectrograph - also called a cross-disperser - separates the orders from another. This low dispersive element is introduced perpendicular to the high dispersive element and separates the individual

diffraction orders, such that they appear like "lines in a book". A visualization of this configuration can be found in Figure 2.5. A beneficial side effect of such an instrument is that it is well suited for being operated with an off-the-shelf rectangular charge-coupled device (CCD) sensor. For illustration, the length of the entire spectrum folded onto the CCD sensor of *FOCES* is more than a meter.

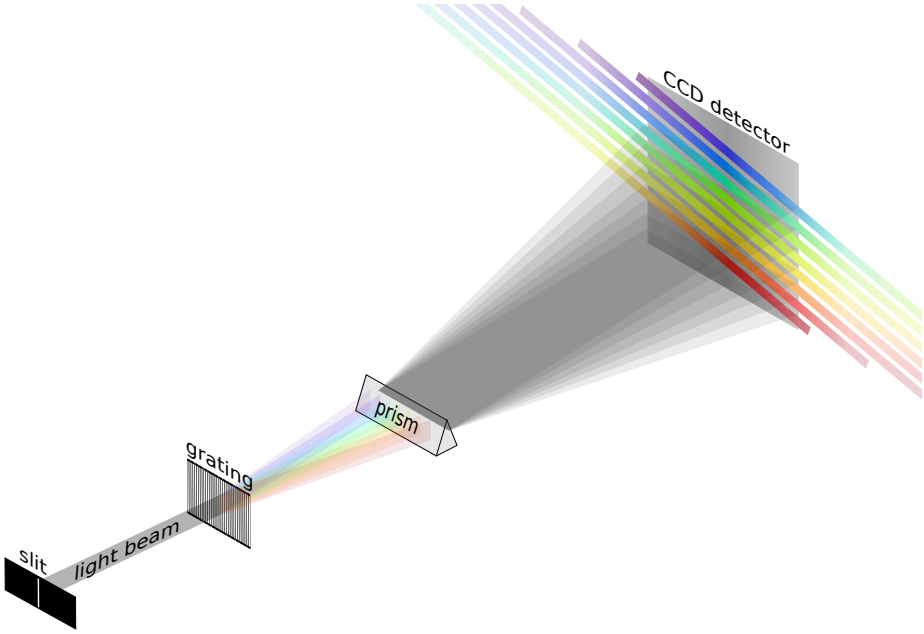

Fig. 2.5.: Illustration of the working principle of an Échelle spectrograph. Light enters into the spectrograph through a slit and falls onto the first dispersive element. This is an optical grating, which is used in a configuration that utilizes high diffraction orders. This would result in many of those diffraction orders overlapping in the main dispersion direction. This overlap is resolved by a second dispersive element, represented here by a prism, which acts perpendicular to the main dispersion direction and is thereby "pulling apart" the individual orders. This way the spectrum can be imaged line-by-line onto a screen or camera. Those order traces exhibit a natural tilt, which is the ratio between the dispersion of the cross disperser over the dispersion of the main disperser.

2.3 Optical fibers

High-resolution spectrographs installed in nowadays observatories are specially designed for dim astronomical objects and are typically of the size of meters and far too heavy to be mounted directly onto telescope ports. The ever changing g-vector which would arise due to the de-rotation movements of the telescope and the temperature changes in the dome would adversely influence the achievable stability of such an instrument. To overcome this problem, optical fibers are used and have become one

of the crucial elements to characterize, treat and handle correctly for astronomical applications.

Optical step-index fibers consist of concentric glass layers with different refractive indices. The innermost layer is called the core and has the highest refractive index, which is surrounded by the cladding, which has a slightly lower refractive index. Through total internal reflection at the transition between core and cladding material, light can be guided in these fibers with extremely low attenuation. This section will give a short overview of the most essential properties of optical glass fibers and some challenges which may and often do arise with this tool.

2.3.1 Attenuation and dispersion

The first two characterizing properties of optical fibers that will be discussed are damping/attenuation and dispersion. Spectral attenuation is the wavelength-dependent reduction of the light intensity while passing through a fiber. This is described mathematically by the Lambert-Beer extinction law, $P_{out} = P_{in} \cdot 10^{-\alpha L}$. The absorption coefficient α is usually expressed in dB/km (Jahns, 2001). Attenuation is a combination of several different physical causes that dominate in different wavelength ranges. In the infrared, above 1.6 μm, oscillation transitions of the quartz glass itself absorb a significant part of the light guided through the fiber. In the ultra violet (UV) range, electron transitions and mainly Rayleigh scattering are responsible for the increasing absorption coefficients. In addition, hydroxyl ions dissolved and/or diffusing into the glass provide the OH-absorption peaks (e.g. 950 nm, 1,25 μm, 1,4 μm) (Jahns, 2001).
Fiber curvatures, coupling and splicing are likewise non-negligible contributors to light losses, however, these effects are not intrinsic properties of the fiber, but effects that occur while handling fibers.

An exemplary spectral attenuation curve of the glass material which is used in the fibers connecting the telescope and the spectrograph at the Wendelstein Observatory can be found in Figure 2.6. The steep rise in the shorter wavelength regime (for optical astronomy the part from 350 - 550 nm) is one additional contributor to the low light sensitivity of typical optical high-resolution spectrographs in the bluer parts of their spectrum (see also Section 5.1 and Figure 5.2). Due to the relatively short distances of a few tens of meters, which are to be bridged, these comparably higher absorption coefficients are still acceptable, however not desired.

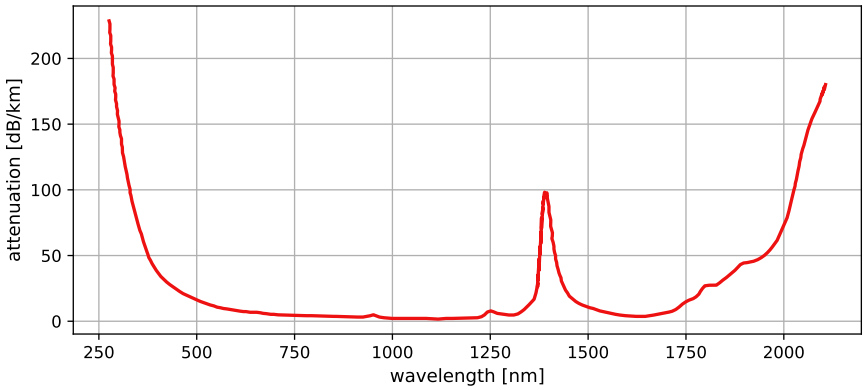

Fig. 2.6.: Example of the spectral attenuation curve of the glass used for fiber FBP100120140 which is used at the Wendelstein Observatory to guide the light from the telescope to the spectrograph. The steep rise in the bluer regime of the spectrum, for optical astronomy the part from 350 - 550 nm, is one additional contributor to the low light sensitivity in the blue regime of typical optical high-resolution spectrographs. Data points extracted from the datasheet of FBP fiber: `www.cmscientific.com/info-sheets/fbp.pdf`

Dispersion is the superordinate term for effects that contribute to pulse widening, such as for example *mode dispersion*, *chromatic dispersion* and polarisation mode dispersion (no claim for completeness). Pulse widening itself only plays a minor role for astronomical spectrographs since starlight is usually observed in a continuous mode. Figure 2.7 visualizes the two effects, mode and chromatic dispersion. While mode dispersion itself has a negligible effect for astronomy, the visualization of different fiber modes represented as beams traveling under a variety of paths through the fiber is beneficial and will be referred back to in the following sections. The understanding of chromatic dispersion however is of fundamental importance for the creation of frequency combs, the gold standard of astronomical wavelength calibration of high-resolution spectrographs (see Section 2.4.2).

2.3.2 Numerical aperture and f-number

In addition to attenuation, the numerical aperture and the associated F-number, as well as the far and near field of a fiber, play an important role in astronomy. The numerical aperture is a measure of the limiting angle at which light can be coupled into the fiber. The limiting angle is determined by the law for total internal reflection at the boundary surface of the core and cladding of a fiber and is therefore dependent on their refractive indices.

$$NA = n_{env.} \cdot \sin(\alpha) = n_{env.} \cdot \sqrt{n_{core}^2 - n_{cladding}^2}\,. \tag{2.5}$$

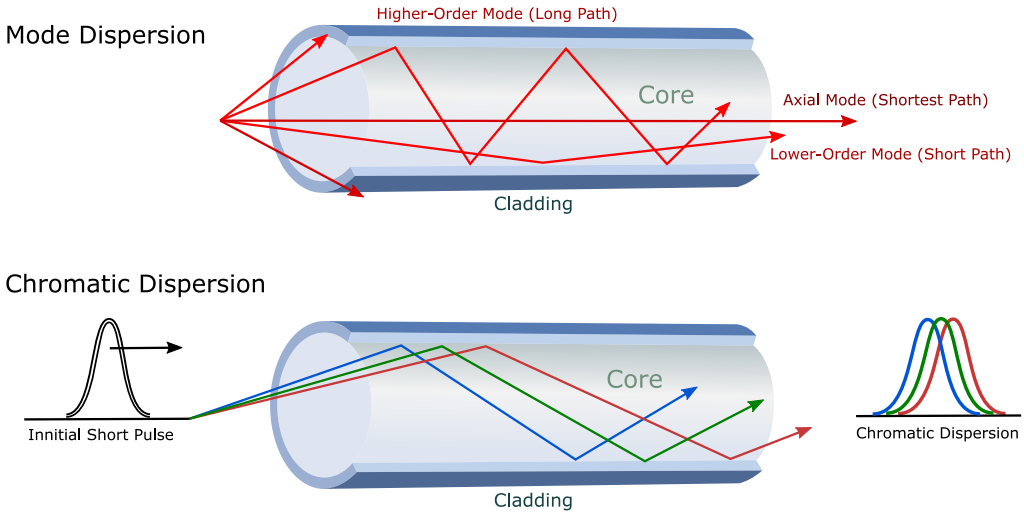

Fig. 2.7.: Visualisation of different causes of dispersion, specifically here, mode and chromatic dispersion explained by the beam model. Images inspired by: `https://community.fs.com/blog/types-of-optical-fiber-dispersion-and-compensation-strategies.html` on the 22.4.2021 at 14:20.

In astronomy, and especially in telescope development and design, a related parameter is common: the so-called F-number (f/#). This parameter is also a measure of the angles at which light passing through the optical elements is accepted. Since both terms are used synonymously, especially in fiber-fed spectrographs, Equations 2.6 & 2.7 depict the mathematical relationship between these two quantities.

$$NA = n_{env.} \cdot \sin\left(\arctan\left(\frac{1}{2} \cdot \frac{1}{f/\#}\right)\right) \tag{2.6}$$

$$f/\# = \frac{1}{2 \cdot \tan\left(\arcsin\left(\frac{NA}{n_{env.}}\right)\right)} \tag{2.7}$$

Considering that under reasonably small angles the approximation $\sin\alpha \approx \tan\alpha$ applies, Equations 2.6 and 2.7 can be described as small-angle approximations:

$$NA = n_{env.} \cdot \frac{1}{2 \cdot f/\#} \quad \text{and} \quad f/\# = n_{env.} \cdot \frac{1}{2 \cdot NA} \tag{2.8}$$

2.3.3 Near-and far-field

Optics defines the near- and the far-field of a system as the distance where either Fraunhofer or Fresnel diffraction dominates. In astronomy, the near-field of a fiber is usually referred to as the distribution of light at the end of the fiber. It is a measure

of the light distributed over the cross-section of the fiber end. The far-field however describes the angular distribution through which the light leaves the fiber (beam model). Both the near-field and the far-field of a glass fiber are created by the superposition of the fundamental modes, which form the solution space of the wave equation under the boundary conditions of the fiber properties. As the starting point of the calculation of these modes serves the time-independent wave equation (Helmholtz equation) in cylinder coordinates:

$$\frac{\partial^2}{\partial r^2} \cdot U + \frac{1}{r}\frac{\partial}{\partial r} \cdot U + \frac{1}{r^2}\frac{\partial^2}{\partial \varphi^2} \cdot U + \frac{\partial^2}{\partial z^2} \cdot U + n(r)^2 k^2 U = 0\,, \tag{2.9}$$

where $n(r)$ is the refractive index as a function of the radius, k is the wavenumber and U represents either the electric or magnetic field strength. Figure 2.8 is an illustration of the employed coordinate system.

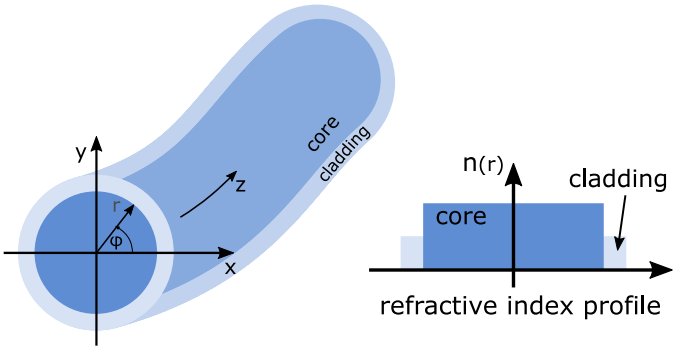

Fig. 2.8.: Illustration of the coordinate system that serves for the discussion of optical fiber modes. The light propagates in z direction, while the transverse distribution in the x/y plane is described using polar coordinates θ, r.

Using a suitable Ansatz (see e.g. Jahns (2001)),

$$U(r, \varphi, z) = U_{l,m}(r) \cdot e^{-i \cdot l\varphi} \cdot e^{-i \cdot \beta z}\,, \tag{2.10}$$

the dependencies in radial and tangential direction can be separated mathematically. The result for the radial direction is then

$$\frac{\partial^2}{\partial r^2} \cdot U_{l,m} + \frac{1}{r}\frac{\partial}{\partial r} \cdot U_{l,m} + \left(n(r)^2 k^2 - \beta^2 - \frac{l^2}{r^2}\right) U_{l,m} = 0\,, \tag{2.11}$$

where β is the phase constant and $l = 0, 1, 2, ...,\ m = 1, 2, 3, ...$ are the mode numbers. This equation is solved by the *Bessel functions of first kind* and order l for the fiber core J_l and the *modified Bessel functions of second kind* and order l inside the cladding K_l. At the boundary, the solutions need to match in value and first

derivative. The following Figures 2.9 and 2.10 depict a variety of selected examples of such solutions.

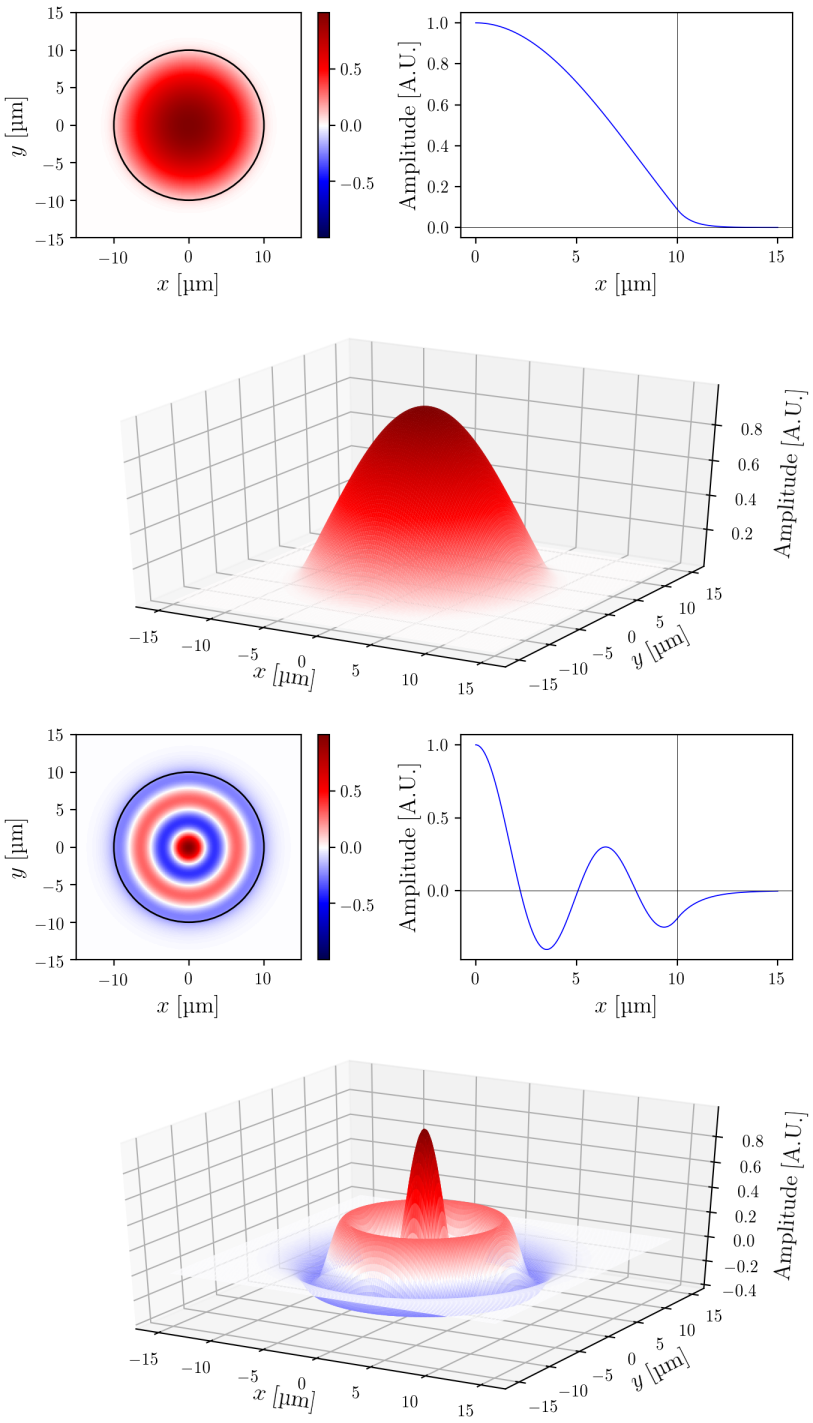

Fig. 2.9.: Solutions to the transverse part of the time-independent Maxwell equations within a step-index optical fiber. The upper solution corresponds to $m = 1$ and $l = 0$. The lower solution corresponds to $m = 4$ and $l = 0$.

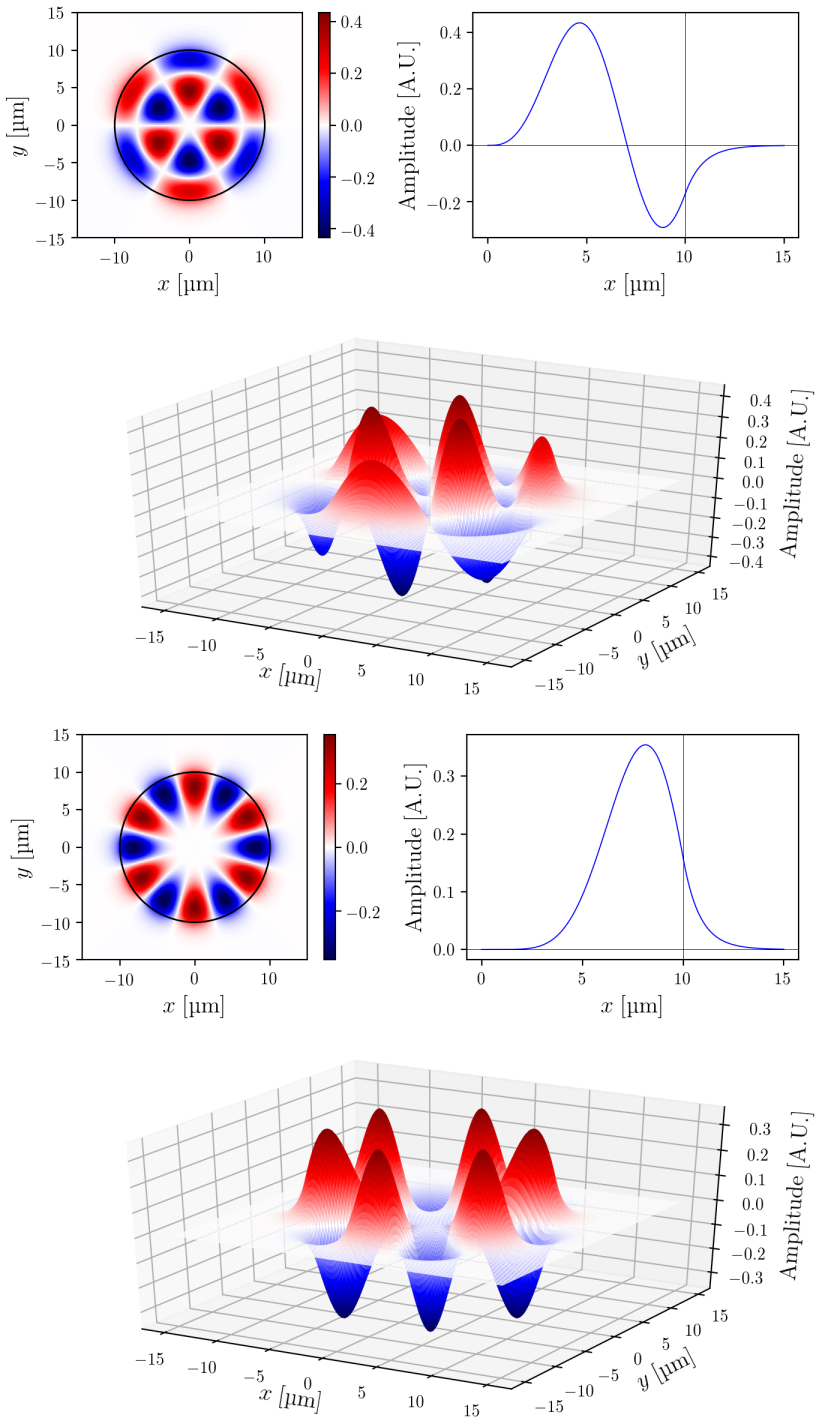

Fig. 2.10.: Solutions to the transverse part of the time-independent Maxwell equations within a step-index optical fiber. The upper solution corresponds to $m = 2$ and $l = 3$. The lower solution corresponds to $m = 1$ and $l = 6$.

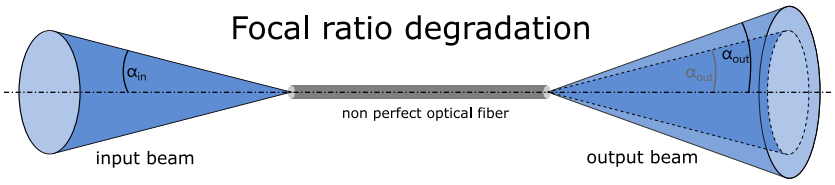

Fig. 2.11.: This sketch illustrates the effect of focal ratio degradation. When light is fed into a fiber non-perfect optical fiber under a specified angle α_{in} it can suffer from focal ratio degradation (due to e.g. micro-bending) resulting in a wider cone at the output α_{out} leading finally to a non-negligible light loss. Image inspired by: `https://astrospectroscopy.wordpress.com/frd-tests/`

2.3.4 Adverse effects in optical fibers

After the previous sections, focusing on disambiguation, this part will provide a short overview of the problems and challenges which arise utilizing optical fibers for astronomy. The three of the most influential obstacles are *focal ratio degradation (FRD)* (see for example Ramsey (1988)), *fiber noise* (e.g. Grupp (2003)) and the fact that fibers do not act as perfect homogenizers sometimes called *'photometric shift'* (e.g. Eversberg and Vollmann (2015)). While the first results in elevated light loss, the latter two effects act on the precision to determine the line center, resulting ultimately in a decreased precision on radial velocity data.

FRD

Considering the beam model of light guided in an optical fiber, there is a minimum f-number (maximum acceptance angle) for every fiber type which is set by the total internal reflection condition. Glass impurities and imperfections (e.g. due to fiber splicing or insufficient polishing of the end face of a fiber) and handling error such as harsh bends (even well below the critical bending radius of the fiber) lead to an inadvertently increase of the light cone guided inside the fiber and ultimately to an effective loss of light (see also Figure 2.11). Even in cases where the maximum acceptance angle of the fiber is not exceeded this results in a decrease in f-number and eventually in the combination with further optics (e.g. a spectrograph) to light loss due to étendue[3].

Light guided under high f-numbers (shallow angle with respect to the rotation axis of the fiber) is more vulnerable to FRD, leading to higher overall light losses (Eversberg and Vollmann (2015), Avila et al. (2011)). A light loss of 50% and more

[3] Étendue describes the product of cross-section and extension in terms of solid angle of a beam of light. It is a conserved quantity in geometrical optics and can be understood as a volume in phase space.

is not uncommon for input f-numbers of f/8 as could be demonstrated by Avila et al. (2011). Typical f-numbers of telescopes are rather large (e.g. f/7.8 at the Fraunhofer telescope, Wendelstein Observatory or f/15 at the Very Large Telescope (VLT, Paranal ESO) and it is therefore recommended and good practice to convert maximum mode angle transported in an optical fiber to a f-number between 3.5 and 4 to reduce light losses (Eversberg and Vollmann, 2015). This however results in the need for f-number adaption optics on both ends of the fiber, from the telescope to the transport fiber and from the fiber to the spectrograph (see also Section 3.3)

Fiber noise

Fiber noise however can best be explained exploiting the wave model. To optimize/-maximize the light throughput, the size of the connection fiber between telescope and spectrograph is almost exclusively implemented as multimode fibers with typical core diameters around 80 - 100 μm. The diameter of the core is thereby adapted to the average respective seeing disk of the telescope. These large core diameters permit the formation of a variety of modes with shorter wavelengths exciting significantly more modes than longer wavelengths for the same maximal input angle :

$$M = 2\pi^2 \left(\frac{r}{\lambda}\right)^2 \cdot \sin^2\left(\arctan\left(\frac{1}{2 \cdot \frac{\#}{f}}\right)\right) , \tag{2.12}$$

where r represents the radius of the fiber core, λ is the wavelength of interest and $f/\#$ represents the desired maximum entrance angle (Sharma et al., 1981)[4]. Guiding white light results in a homogeneous light cone at the exit of the fiber since this represents the superposition of all exited modes over the whole guided wavelength range. However, by selecting a small wavelength band, a speckle pattern is visible which is the superposition of all excited modes of the selected wavelength. This is due to the fundamental nature of the fiber and *not* an error of the fiber. Due to the entrance slit of a spectrograph, however, only a small section of the full speckle pattern is transmitted into the spectrograph, illustrated in Figure 2.12).

The speckle pattern itself is stationary as long as the fiber does not change/move in any way, which is impossible for astronomical observations where the telescope has to track the object of interest. These movements lead to changes in the effective path length of the individual fiber modes, resulting in an ever changing speckle pattern. In combination with the entrance aperture of the spectrograph, this results in small

[4] A f-number of 2 (which is a typical minimal f-number of optical multimode fibers) and a core diameter of 100 μm lead for a wavelength of 400 nm to approximately 250,000 modes while for longer wavelengths around 800 nm only around 60,000 modes are exited.

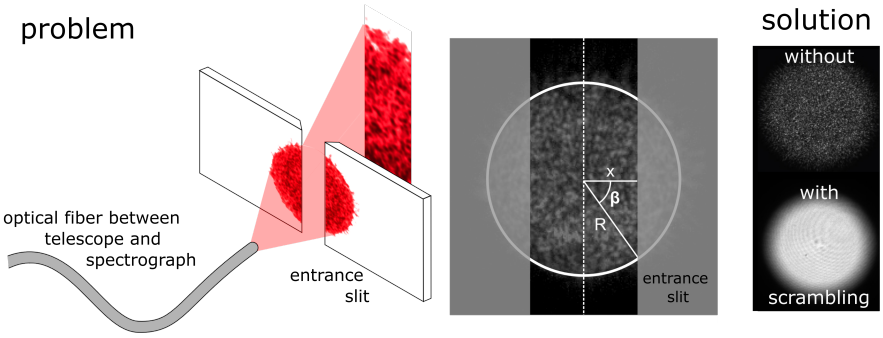

Fig. 2.12.: Visualization of the impact of fiber noise on the slit image and ultimately the determination of its centroid position. The reason for this problem is a slowly changing speckle pattern (= superposition of the contributing modes) at the exit of the optical fiber in combination with the entrance aperture of the spectrograph. The interference of these modes leads to darker and brighter regions that partially get blocked by the entrance slit of the spectrograph. This speckle pattern does vary with time due to movements of the telescope resulting in movements of the fiber. Mode scrambling can solve this problem by accelerating the process of changes in the mode pattern relative to the exposure time of the spectrograph, averaging out the inhomogeneities in the fiber image (see right image, credit for the speckle pattern: ESO).

intensity variation in the transmitted light, further resulting in a non-negligible shift of the center of gravity of the absorption lines. Since it is not possible to inhibit the change of the speckle pattern, the solution for this obstacle is to change the pattern fast enough during an exposure of the spectrograph so that the resulting mean speckle pattern appears to be homogeneous. This can be done with a vast variety of setups like small vibrating motors (e.g. unbalanced motors like the buzzing motor in mobile phones), mechanical setups that move the fiber several centimeters (similar to windshield wiper) or even by hand (Eversberg and Vollmann, 2015). For *FOCES*, a dedicated fiber-shaker was designed and build (Kellermann, 2015).

Non-perfect homogenizer

The second effect influencing the precision of the determination of the line center is the fact that fibers do not act as perfect homogenizers. A perfect fiber would produce a homogeneous output at the fiber end regardless of the light input, but this is not the case in practice. In the extreme (exaggerated)[5] case when a spot with a diameter significantly smaller then the fiber's core diameter is illuminated on an optical fiber, the near field of the light exiting the fiber is in no way homogeneous. While light travels through the fiber, it is redistributed concentrically to the fiber core, leading

[5]The images in Figure 2.13 exaggerate the problem since in reality the spot size is determined by the seeing profile and the fiber diameter is adjusted accordingly to e.g. 80 % encircled energy of the seeing profiles Moffat distribution (Moffat, 1969).

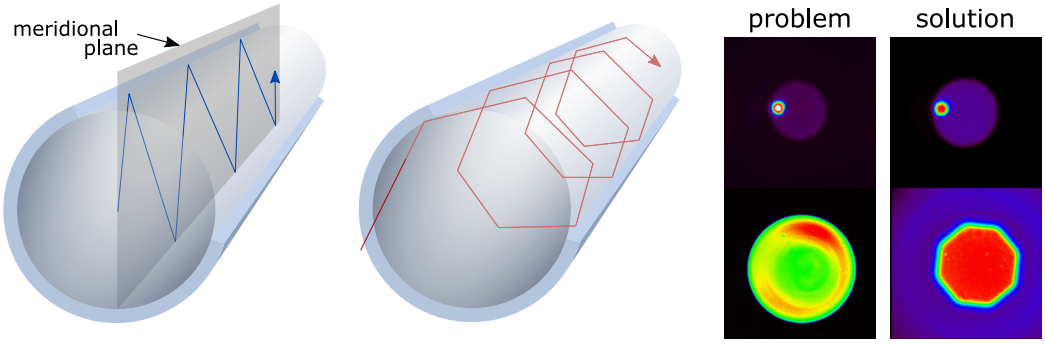

Fig. 2.13.: The left side of the illustrations depicts a sketch of different types of modes traveling in a fiber (beam model). It is possible to predominantly excite skewed modes (hexagon-shaped spiral) which never cross the fiber center. This leads to the ring-like structure which is depicted in the image on the right and ultimately to an apparent shift of the line center in the spectrograph. The remedy for this obstacle can be found in the rightmost image where an octagonal fiber was used. Sketch on the left inspired by Feger (2012). Images on the right: Credit to the McDonald Observatory of the Austin University in Texas.

to a ring-like structure at the fiber exit as shown in Figure 2.13. Although this would lead to light loss when combined with the entrance aperture of a spectrograph it could be acceptable in a static case. However, time-variant effects like seeing and/or the telescope and subsequently the fiber moving result in an ever-changing pattern at the fiber end, appearing as undesirable shift in the line center in the spectrograph. The remedy for this problem are so-called *non-circular fibers* and here in particular *octagonal fibers* (Figure 2.13, rightmost). This type of optical fiber prevents light from traveling in a spiraling pattern that at all times avoids for example the center of the fiber. In contrast, the reflections from the sides of the octagon lead to a much more erratic scattering throughout the fiber core and after a not too long distance a complete homogenization of the near field (see also Stürmer et al. (2016)). Feger et al. (2012) could prove that it is superior to combine octagonal (good near-field properties) and circular fibers (good far-field properties) in a concatenated way, which is now the desired standard for high-resolution spectrographs.

2.3.5 Fiber splitter

Optical fiber splitters are devices that allow to transfer optical power that is guided in one fiber over to another optical fiber. This transfer can be partial or, depending on the conditions, up to 100 %. An analogue in free-beam optics for such a device is a beam splitter. The most common design used in fiber optics is a so-called *fused optical fiber coupler/splitter*, for which two optical fibers are tapered down and fused

together in a way that allows the evanescent field, which extends into the cladding of one fiber, to "leak" into the adjacent fiber. By this process, energy is transferred from one fiber into the other, up to the point where 100 % is guided in the new fiber and the process reverses, leading to an oscillation back and forth between the fibers (Paschotta, 2008). The desired splitting ratio can be established by controlling the length over which the fibers are in contact, but also depends on the wavelength of the light. Such coupler devices are typically at least to some degree of dichroic nature, implying that the mixing ratio at the fiber end is wavelength-dependent.

Figure 2.14, left side, shows a simulation of the light distribution inside a fiber splitter. The right panel of the figure illustrates that for three different mode types of the same wavelength 580 nm (p=1,l=3; p=1,l=7; p=3,l=3), the evanescent field varies with mode number. The evanescent fields of higher mode numbers increasingly expand into the cladding. In addition, a set of three different wavelengths ($\lambda = 380\,nm$, $580\,nm$, $780\,nm$) with the same mode number is depicted, illustrating that for longer wavelengths, the evanescent fields increase, resulting in the aforementioned dichroic effect. It is also worth mentioning that this kind of optical splitter is always a four-way device where one end can be disabled during manufacturing if desired. Not relevant for astronomy but crucial for the manufacturing of fiber frequency combs is the fact that feeding light from two input fibers with a certain phase offset also influences the splitting ratio at the output which is exploited for the commonly utilized *figure-8*-laser and the novel invention by *MenloSystems* the *figure-9*-laser[6] (see also Appendix 9.1).

[6]The *figure-8*- and *figure-9*-laser are both types of fiber lasers where the fundamental setup of the fiber mimics the numbers eight or nine

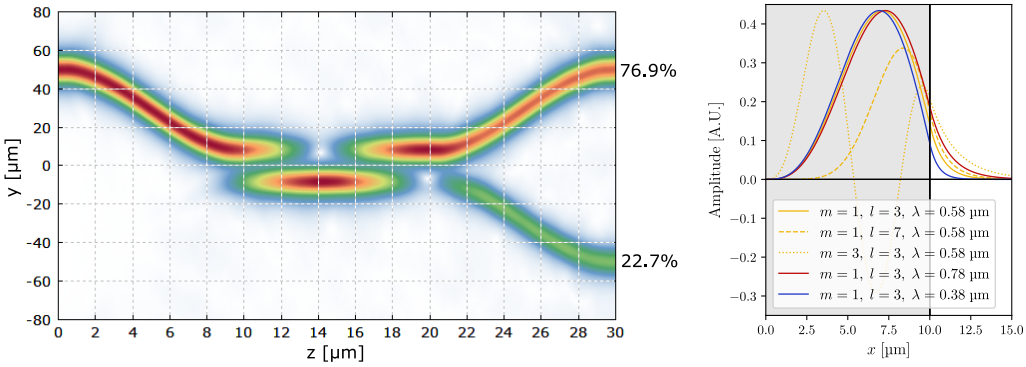

Fig. 2.14.: Illustration of the working principle of an optical fiber coupler. The left panel shows how the light intensity oscillating between two optical fibers that have been brought into close contact with one another. (Image taken from Paschotta (2008)). This continues as long as they stay close and enabling the construction of fiber couplers with arbitrary splitting ratios. The reason for this transfer of energy is the evanescent field that extends from the core of one fiber into the cladding or even the core of the adjacent fiber, exciting a resonant oscillation there. This is highlighted by the cross-section of simulated fiber modes shown on the right, illustrating that higher modes and longer wavelengths do extend further into the cladding and are therefore easier to couple.

2.4 Wavelength calibration

Every spectrum of an astronomical object needs to be wavelength calibrated, whether it will be used for radial velocity studies or to learn more about stellar atmosphere physics. There are different types of calibration light sources in active use in astronomy, for example:

- hollow cathode lamps and here especially ThAr and UNe lamps (*FOCES*, *HARPS*, *CARMENES*),
- Iodine cells (Tautenburg-Spectrograph),
- Fabry-Pérot etalons (*CARMENES*) and/or
- an astronomical laser frequency comb (LFC) (*FOCES*, *HARPS*, *ESPRESSO*),

to name a few, which are also the most common ones. Behind each type of calibration light source examples of well-established instruments which utilize these technologies are listed.

A spectrum can also be calibrated using the so-called *telluric lines* (Griffin and Griffin, 1973). These lines are always imprinted on every spectrum taken on Earth (hence the name 'telluric') and originate from the absorption and emission of mostly water vapor and oxygen in the atmosphere (Osterbrock et al., 1997). However, due to temperature and pressure changes (winds) in the different layers of the atmosphere,

the exact line positions are varying, which is why this type of calibration is usually not considered for high-resolution spectroscopy.

Since the wavelength calibration is one of the most crucial parts of the data reduction, it is worthwhile to invest in the understanding of the different ways they work, their advantages and limitations. The following two sections give an overview of the two different types of wavelength calibration light sources available at the Wendelstein Observatory, namely hollow cathode lamps and laser frequency combs.

The primary requirement for every wavelength calibration light source is to produce a spectrum which covers the whole region of interest with narrow lines, meaning that the detected line width in the spectrograph is dominated by the resolution of the spectrograph and not by the natural linewidth of the emission line itself (e.g. blend of lines). These lines should be dense enough to provide sufficient calibration anchor points for the pixel to wavelength conversion. In the best case, this would be realized with all lines at almost equal strength to avoid saturation and equally spaced with no line blended with a neighboring line. In addition, the wavelength of each line has to be known accurately and should not change with time, in order to be able to calibrate spectra taken years apart with the same precision.

2.4.1 Hollow cathode lamps

By far the most widely and longest used of the aforementioned calibration light source in high-resolution spectroscopy are hollow cathode lamps. A hollow cathode lamp is a specific type of cold cathode device filled with a low-pressure gas. The cathode material, and in some cases the filling gas as well, emit the desired emission lines. The cathode has a particular geometry, in this case, the shape of a small pot with the cathode material chosen for the application case. A typical setup of such a lamp can be found in Figure 2.15 .[7]

[7]Note that the metallic dark spot found in almost all hollow cathode lamps at one side of the glass cylinder is not a sign of bad production or indicating a soon to be expected end of the lifetime of this lamp, but the so-called ‘getter’. This area is usually made of Zirconium (Zr) and traps any impurities which might be in the lamp.

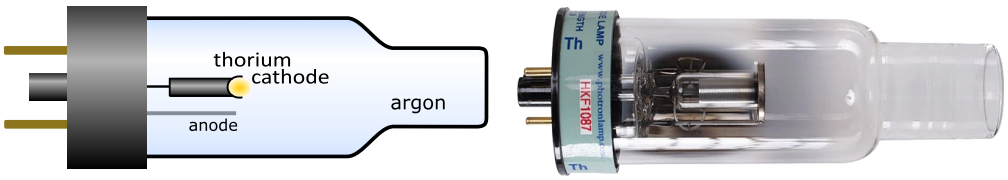

Fig. 2.15.: Illustration of a ThAr hollow cathode lamp, similar to the one that is installed inside the calibration unit of *FOCES*. Right image is taken from *Photron*: `https://www.photronlamp.com/` on the 14.3.2021 at 14:40.

The emission line spectrum itself is generated in a three-step process (Shrader et al., 2010) via:

- ionization of the filling gas,
- sputtering of the cathode material, and
- excitation of the sputtered particles.

To start the lamp, a high voltage is applied between the anode and the cathode, which causes parts of the filling gas to become ionized. The filling gas itself needs to be a single atom gas to avoid the very dense 'line forests', which arise in general with excited molecules and contamination. This is achieved by filling the lamp with a noble gas like neon or argon. This ionized gas is then accelerated in the high electrical field between the electrodes in the direction of the cathode while gaining enough energy along the way to eject particles of the cathode material during impact. These (generally neutral) particles are subsequently excited by collisions with other atoms. Over time, the excited cathode-, as well as filling gas atoms, relax back to their ground state by emitting photons which generate the desired line spectrum as a result. In astronomy, the most commonly used type of hollow cathode lamp is the Thorium-Argon-lamp (ThAr-lamp; Cathode = Th, filling gas = Argon) which is specifically chosen to cover fairly evenly the entire visible wavelength range[8]. Due to the relatively low costs, their turn-key availability and their low maintenance, ThAr lamps are mainly considered the de facto standard for wavelength calibration, for which several catalogues providing the corresponding wavelength lists in high precision exist. However, there are several drawbacks concerning these lamps which drive the spectroscopy community to consider and explore new wavelength calibration light sources. These drawbacks include, but

[8]Here, thorium provides the emission lines in the blue part (< 400 nm) of the spectrum whereas argon dominates in the red part (> 800 nm), gradually changing over the wavelength range in between.

are not limited to, material contaminants resulting in far too dense 'line forests'[9], aging over time which averts long-term surveys and the need of a high-voltage power supply. One of the best replacements are laser frequency combs which will be discussed in the next section.

2.4.2 Laser frequency combs

Laser frequency combs are the most precise and accurate wavelength standards known to date, leading to a Nobel price in physics 2005[10]. This makes them ideal calibration light sources for stabilizing/correcting high-resolution optical spectra when searching for exoplanets and resulted in LFCs becoming the gold standard for this technique. There are several ways how a frequency comb can be realized in practice.

However, building a frequency comb with suitable properties for optical astronomy requires a few technical adjustments:

- Due to technological reasons, the natural wavelength regime of such lasers is usually around 1000 nm (ytterbium-laser) or 1550 nm (erbium laser) being far too red for most visible spectrographs like *FOCES* (spectral range: 380 - 900 nm).
- Adding to the aforementioned problem is the fact that the line density is far too high to be resolved with a typical astronomical spectrograph (high-resolution: R=∼60.00 - 120.000).
- The spectrum itself is highly structured, which leads to saturation in parts of the detector whereas other parts lack light.

Therefore, the requirements for astro frequency combs can be summarized as follows:

- visible in the wavelength region of interest,
- a resolvable line spacing,
- a flat spectrum.

[9] World wide restrictions on the retail of thorium due to its radioactive nature led lately even vendors which were widely known for their high quality astronomy grade ThAr-lamps to change their cathode materials, resulting in the aforementioned 'line forests' (Nave et al., 2018).

[10] For this concept, the 2005 Nobel prize for physics was awarded to T. Hänsch and J. Hall along with R. Glauber for his contribution to the quantum theory of optical coherence (*The Nobel Prize in Physics* 2005)

At the Wendelstein Observatory, an astronomical frequency comb - or astro-comb - is one of the available wavelength calibration options for the high-resolution optical spectrograph *FOCES*.

This section will not provide a comprehensive overview of all the different aspects and options regarding frequency combs or astro-combs. Instead, only the basic concepts are introduced, followed up by a technical description of the astro-comb by *MenloSystems*[11], operated at the Wendelstein Observatory. A more detailed overview of frequency combs can for example be found in Udem (2002) and Probst (2015). For applications of frequency combs in astronomy, it is referred to Steinmetz et al. (2008) and Probst et al. (2020)

Figure 2.16 shows a photograph of the FOCES-LFC at the Wendelstein Observatory. The overall setup consists of two electronic racks and two optical breadboards

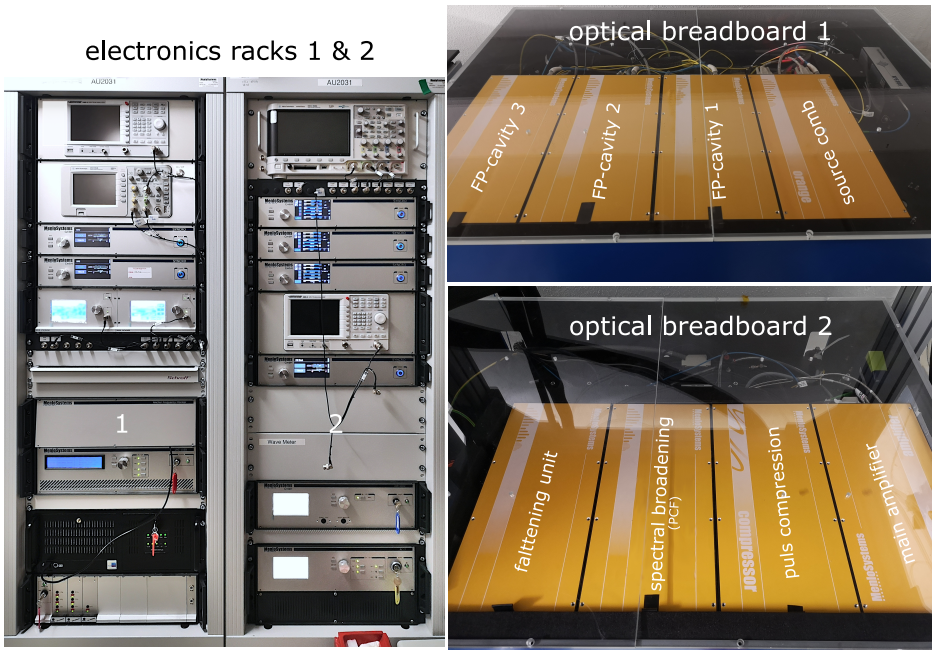

Fig. 2.16.: Photograph of the laser frequency comb of *FOCES*, which consists of two electronic racks and two optical breadboards. Each breadboard contains four boxes (the size of a shoebox) housing the equipment for the different optical transformations found in Table 2.1.

while each breadboard contains four smaller optical boxes. The initial source comb is housed in only the first small optical box while all the other boxes house the equipment to prepare the comb light to fit the needs of astronomers. The individual steps to generate an astro comb spectrum are listed in Table 2.1.

[11] *MenloSystems* webpage: https://www.menlosystems.com/

Tab. 2.1.: Overview of the individual steps performed in the astro frequency comb of *FOCES*. Steps written not in bold indicate a preparation step for the following stage

optical box	purpose
1	**source LFC**
2-4	**mode filtering**
5	pulse amplification
6	pulse compression
7	**spectral broadening**
8	**spectral flattening**

An illustration of the individual steps and their influence on the spectrum can be found in Figure 2.17.

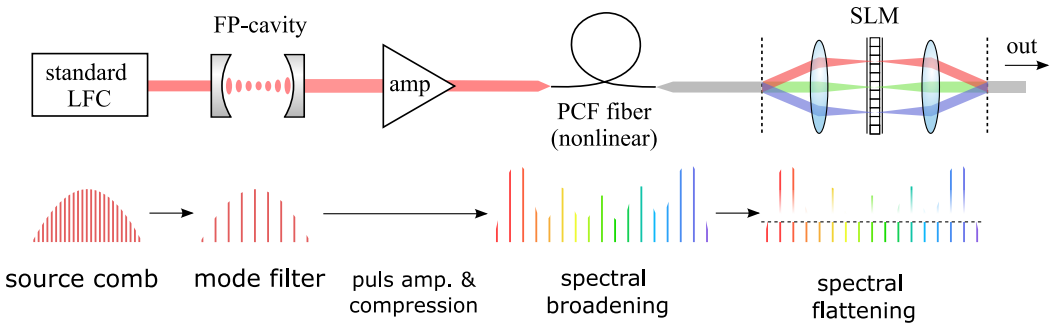

Fig. 2.17.: Schematic illustration of the individual optical transformation steps in an astro frequency comb and their influence on the spectrum. FPC: Fabry-Pérot cavity, SLM: spatial light modulator, PCF: photonic crystal fiber. Illustration kindly provided by Dr. Rafael Probst and modified by me.

2.4.2.1 Source comb

Most of the important concepts regarding LFCs are deeply linked to the theory of Fourier transformations. Utilizing this relation, it is possible to explain how the most important spectral properties of a frequency comb are linked to technical aspects of the laser required to build such a comb. Generally speaking, only three key 'ingredients' are necessary to create a frequency comb whereby the first two of them are of structural components and the last is an applied technique:

- a stabilized laser resonator,
- a broadband laser material and
- mode-locking needs to be favoured.

The starting point for the creation of a frequency comb for applications in optical astronomy is a stabilized femtosecond mode-locked laser, that by itself already has a comb-like spectrum (Short pulses in the time domain result in a comb-like structure in the frequency domain). The excited laser material emits light which can, e.g. for *Ti:sapphire lasers*, span a spectral range of around 400 nm (670 to 1070nm) (see for example Withnall (2005)). Within any laser resonator, only modes fulfilling the resonator condition:

$$f = \frac{c}{2 \cdot l \cdot n} = \frac{c}{m \cdot n \cdot \lambda}\,, \tag{2.13}$$

can exist, whereby l is the length of the resonator, n the refractive index inside the cavity, λ represents the wavelength and m is an integer[12].
To generate the ultra-short pulses of a femtosecond laser, the individual modes of the laser need to be mode-locked. This condition is satisfied when the individual modes have a fixed phase relation to one another, creating constructive interference of all the involved laser modes[13], and thereby generating ultra-short pulses[14]. To establish and maintain these short pulses long-term, the natural dispersion of the resonator has to be compensated while the continuous-wave-mode (cw-mode) of the laser has to be suppressed. Femtosecond pulsed lasers, therefore, use non-linear optical effects in order to create a soliton[15]. This leads to the more efficient amplification of these short pulse, which oscillates inside the laser cavity. As the amplification progresses, all other modes quickly become negligible compared to the main pulse. Such a femtosecond laser is already represented by a comb-like structure in the frequency domain, see Figure 2.18 as an illustration.

The modes of a frequency comb are defined as (see e.g. Udem (2002)):

$$f_n = f_{CEO} + n \cdot f_{rep}\,, \tag{2.14}$$

[12]For the sake of this consideration only longitudinal modes are discussed.

[13]In a laser with a broad spectrum, normally two modes are possible: the *continuous wave*-mode (cw-mode) and the *pulsed*-mode. The pulsed-mode can be established via mode-locking which itself can be generated in two ways: either active or passive. For the active case, mode-locking is usually only suitable for up to picosecond lasers (Paschotta, 2008). For femtosecond lasers, a passive mode-locking is generally required whereby different techniques can be exploited to suppress the cw-mode, so that only the pulsed-mode is sustainable. In one of the simplest examples, the Ti:sapphire femtosecond laser, this can be accomplished via the self-focusing property of the Kerr-effect and an aperture (Paschotta, 2008). When a pulse is formed by chance the higher local field strengths are affected significantly stronger by non-linear optical effects, like the aforementioned Kerr lens effect, and lead in case of the Ti:sapphire to self-focusing of the laser inside the resonator. By placing an aperture in the laser cavity, the pulse-mode is favoured since it is substantially less altered by the aperture than the cw-mode.

[14]Therefore, an ultra-short pulse (fs) in the time domain translates into a broad spectral range in Fourier space and vice versa.

[15]A soliton is a self-reinforcing wave packet which can establish when the dispersive effects of the material, in which the wave packet is traveling, are compensated (Udem, 2002).

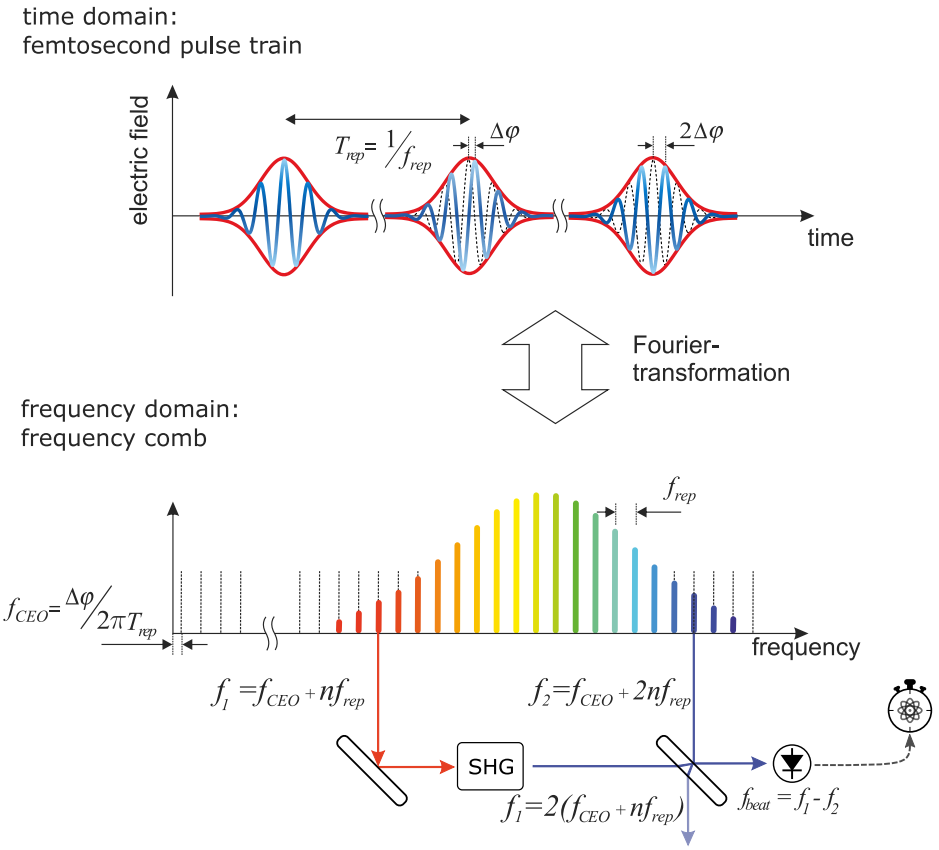

Fig. 2.18.: Illustration of the source comb in time and frequency domain. The lower half of the sketch depicts the process necessary to stabilise the frequency comb to an atomic clock. A lower frequency of the broadened spectrum is frequency-doubled (second-harmonic generation (SHG)) and a beat signal is created. This beat signal is then stabilized to an atomic clock. The idea of the beat signal is to convert the ultra-fast frequency of optical light to a frequency (the beat signal) which is easily manageable with current electronics whereby the optical frequency can be stabilized. Upper part taken from Probst (2015) and modified by me with inspiration taken from Samoudi (2017).

whereby f_{rep} is the repetition rate of the laser which is determined by the optical length of the laser cavity for the circulating soliton. The so-called *carrier–envelope offset frequency* f_{CEO} can be understood in the time domain as the difference between the optical phase of the carrier wave and its envelope function, which is the difference between phase and group velocity. In the frequency domain, this translates to the deviation from 0 when extrapolating the comb spectrum to lower frequencies.[16] The deviation stems from the refractive index in the laser itself.

[16]Note that these frequencies (represented by dotted black lines in Figure 2.18) are only of theoretical nature and can not be observed by a spectrograph since they do not lie in the wavelength regime of the laser material and have a far too long wavelength to satisfy the resonator condition for presumable all current practical laser.

Although the dispersion needs to be zero to form a soliton, the overall refractive index is not necessarily 1, which results in the offset f_{CEO}. Changes in the refractive index due to e.g. acoustic waves or thermal expansion, lead to slightly different resonator condition, thereby changing f_{rep} and subsequently f_{CEO}, which results in a different type of comb-like spectrum with slightly different mode spacing. The goal of a frequency comb is to measure and stabilize the aforementioned setup in order to maintain the same frequency comb over a long period of time.

The most difficult aspect in this regard for a long time was the measurement of frequencies, since frequencies of optical light are in the THz regime, being hardly measurable with electronic equipment. The working group around T. Hänsch was able to resolve this problem by using an optical interferometic setup. By broadening the initial comb spectrum (see also Section 2.4.2.3) to span at least one octave and subsequently frequency doubling[17] a selected frequency of the comb, a beat signal can be created. The frequency of a beat signal is defined as $f_{beat} = f_1 - f_2$, resulting in a frequency range which can easily be measured with current electronics. Changes in the beat signal are a measure for changes in the comb structure and can thereby be compensated e.g. by adjusting the length of the cavity via a piezo or the adjustments of the pump power of the laser which results ultimately in a change of the refractive index. Referencing this beat signal to a long-term stable frequency normal like an atomic clock results in an absolute referenced signal. This opens the possibility to produce a long-term stable measure for wavelength calibration in astronomy.

Although it is possible to create optical frequency combs utilizing e.g. Ti:sapphire lasers, they are predominantly implemented as free beam optics, which is disadvantageous for most astronomical observatories due to their vulnerability to environmental changes. Since most observatories are in quite remote places, a dedicated optical laboratory can often not be provided. Fiber lasers on the other hand are much less susceptible under such conditions, but are predominantly operating in the infrared regime for technical reasons. A description of the actual source comb utilized in the astro comb of *FOCES* can be found in Appendix 9.1.

[17] Frequency doubling or second-harmonic generation (SHG) is an effect that occurs in nonlinear-optical media whenever the Fourier expansion of the polarization as a function of the electrical field contains a quadratic term. In this case, when a sine wave excites the medium, the reaction of the polarization also contains a $\sin^2$ contribution, which oscillates at double the exciting frequency. This effect typically occurs for high electric field strengths, like it is the case in laser beams with high power density.

2.4.2.2 Mode filtering

As already mentioned before, the density of the source comb modes is far too high to be resolved with a typical resolution of an astronomical spectrograph. Therefore, this step is dedicated to filter out/suppress a significant number of these superfluous modes. The filtering process exploits the same physical processes as the initial laser resonator in a so-called Fabry-Pérot cavity (FPC) (see also Steinmetz et al. (2008)). To act as an effective mode filter, the free spectral range of the FPC must be chosen to be an integer multiplicator m of the initial source comb f_{rep}, see also Figure 2.19 a) where $m = 4$. The amount of suppression is determined by the cavity's finesse. Since the side modes can not be resolved in a typical astronomical spectrograph, a sufficient and equal suppression of the side modes is a crucial step, since failures to meet this requirement would lead to the center of the comb line appearing to be shifted. The frequency comb of *FOCES* therefore uses three concatenated identical cavities with an average suppression of 33 dB, leading to an overall attenuation of almost 100 dB (a factor of 10^{-10}) of the unwanted side modes.[18]

For the FOCES-LFC, a line spacing of 25 GHz is sufficient, leading to only every

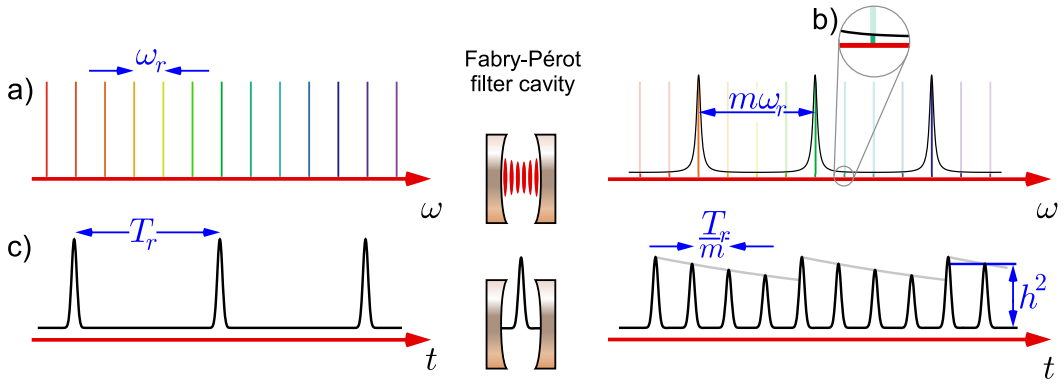

Fig. 2.19.: Schematic sketch of the principle of operation for mode filtering via a Fabry-Pérot cavity performed by the FOCES-LFC. Image taken from Probst (2015).

100$^{\text{th}}$ comb mode of the 250 MHz initial source comb passing the cavities. Since the working principle of the cavities is closely tied to the actual length of the Fabry-Pérot resonator, it is crucial to actively control this measure, which is done in a two-step manner - fast and slow, as shown in Figure 2.20. The slow mode controls the length via the temperature of the overall brass cavity while the fast mode adjusts the length via a piezo. The whole setup is actively adjusted via the Pound-Drever-Hall technique using a CW-laser[19] ((Pound, 1947) and (Drever et al., 1983)).

[18] This strong suppression is needed since the following processes in the astro comb amplify them again and even in this amplified status they must be weak enough to not shift the center of the unresolved line in the spectrograph.

[19] CW-laser = continuous-wave laser

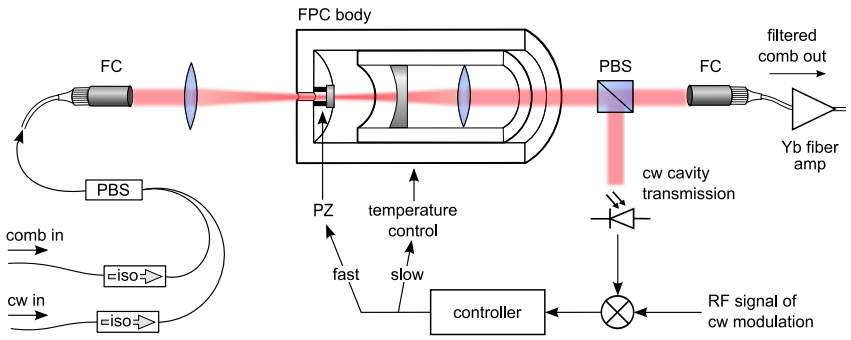

Fig. 2.20.: Setup of the Fabry-Pérot cavity (FPC) inside the FOCES-LFC. The cavity length is actively controlled in a two-stage mechanism. The fast stage is controlled via a piezo actuator (PZ), while the slow stage compensates temperature effects via heating the brass housing. Yb: ytterbium, RF: radio frequency, PBS: polarizing beam splitter, FC: fiber collimator, iso: optical isolator. Image taken from Probst (2015).

2.4.2.3 Spectral broadening via a photonic crystal fiber

Spectral broadening, which describes in this context the extensive expansion of the comb spectrum, is one of the key technologies needed in frequency combs. The FOCES-LFC exploits this technology at two points: as broadening for the absolute referencing of the source comb and for the final broadening of the spectrum to convert/adapt the infrared source comb to the wavelength range needs of astronomers.

For the actual broadening of the spectrum a *photonic crystal fiber* (PCF) (Russell, 2003) is used. These are a special type of fiber, which instead of consisting of a (typically round) core and a surrounding cladding, they are an assembly of holes (which are usually air filled but can also be flooded with different gasses) with different sizes and arrangements, whereby the relative position of the holes to each other can shape and engineer the properties of the fiber. Their overall configuration can either feature a glass core or a hole in the center of the fiber (see also Figure 2.21). With those fibers, one either strives to exploit non-linear effects by strongly confining the light in a small area in the core by the comparably large refractive index difference ($n_{glass,1}$=1.463, $n_{glass,2}$=1.458 vs. $n_{glass,1}$, n_{air} ≈1.0003 (Jahns, 2001), endlessly single mode fibers) or in the latter case tries to achieve the exact opposite by guiding light in the hollow hole core, as can be seen in the photographs shown in Figure 2.21. A more comprehensive overview over the different types of photonic crystal fibers and their classification can be found in Delcourt et al. (2020).

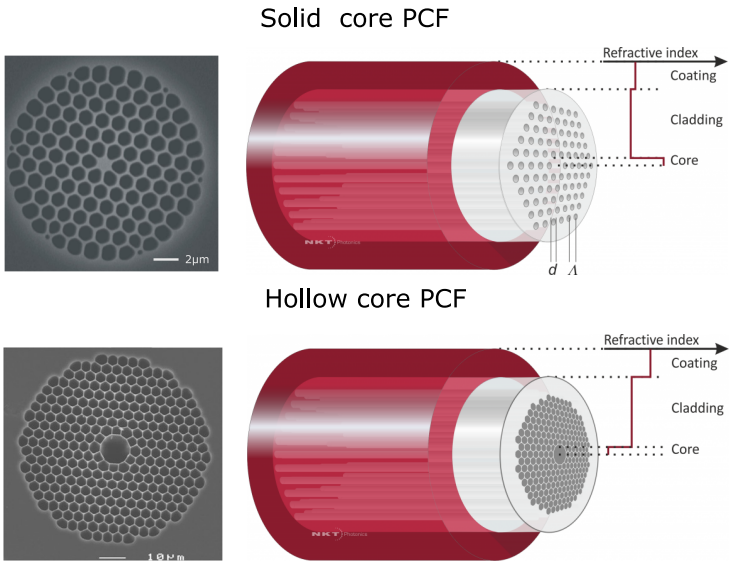

Fig. 2.21.: Visualization of the different groups of photonic crystal fibers (PCF). Left image taken from: `https://slideplayer.com/slide/4427942/`, slide 2 on 4.4.2021 at 11:50. Images on the right taken from: `https://www.nktphotonics.com/lasers-fibers/technology/photonic-crystal-fibers/` on 13.4.2021 at 20:30.

For the broadening of the spectrum, the femtosecond pulses are guided through a specially engineered PCF (configuration of the holes) which in addition is tailored down to a core size of around 550 nm to enhance strong non-linear optical effects in the fiber core (Figure 2.22, right side)[20]. The super-continuum generation is mainly driven by self-phase modulation while other non-optical spectral broadening effects play only a minor role[21] ((Paschotta, 2008), (Karlsson, 1994)). Traveling trough the tailored PCF, the femtosecond pulses experience a time-dependent phase shift according to the time-dependent pulse intensity via the Kerr-effect, which is naturally accompanied by a shortening of the pulses which results in a broadening of the spectrum. In Figure 2.22 on the left side, a simulation of the broadening process via a tapered PCF is depicted. The resulting spectrum is highly structured, which would lead to saturation in parts of the CCD. To overcome this obstacle, the final step in an astro-comb flattens the spectrum and can even be adjusted to the overall wavelength-dependent efficiency of the spectrograph. It is worth noting that

[20]The tailoring is necessary, since the mode filtering greatly reduces the power yielded in a single pulse. The tailoring itself is performed by heating the PCF to a temperature where the glass is already plyable but not yet molten, while pulling the fiber ends apart.

[21]The electronic Kerr-effect acts extremely fast since it is the polarization of the electron cloud around the individual atoms and can therefore respond fast enough to femtosecond pulses. The Raman-effect however, has only negligible effects on the spectral broadening for femtosecond pulses, since it is driven by the interaction of the electric field transversal oscillations between molecular vibration modes in the medium, which have a much slower response time (Karlsson, 1994).

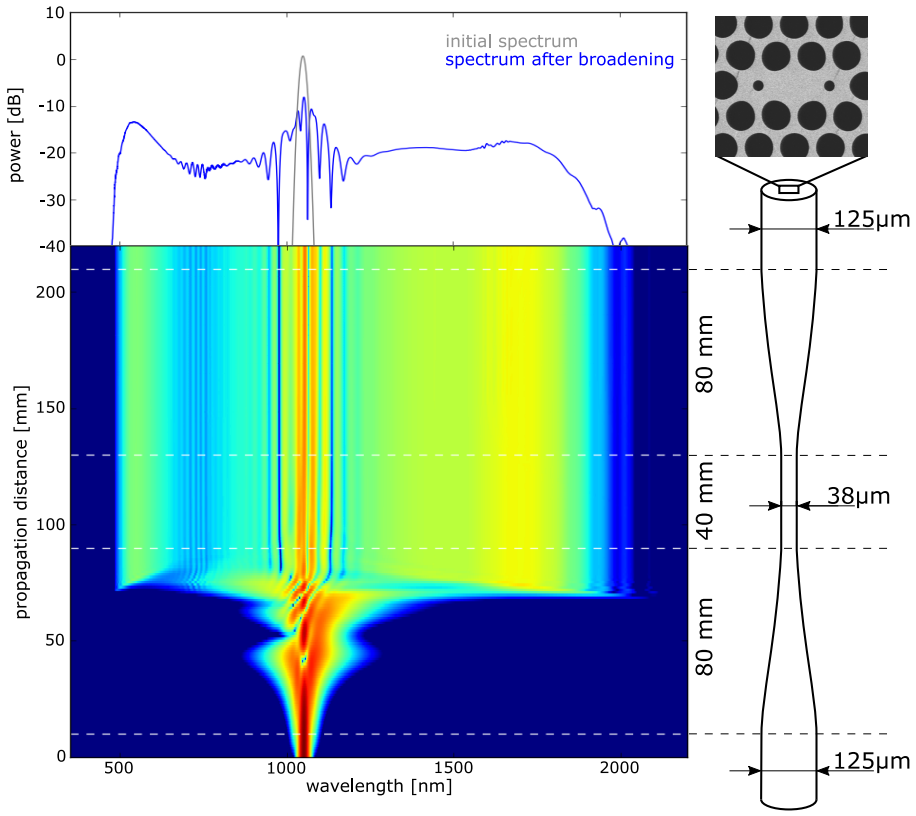

Fig. 2.22.: Numerical simulation (left side) of the super-continuum generation in a tapered photonic crystal fiber (right side). Image kindly provided by Dr. Yuanjie Wu and modified by me.

the high power density necessary to exploit the non-linear effects needed for the super-continuum generation, however, are harmful for the fiber material itself which leads over time to defects in the fiber core matrix and ultimately to its destruction. During an average use at the observatory, weeks before the final destruction happens, a degradation of the spectrum can be noted, with narrow dips in the spectrum that vary in depth and position and can not be eliminated with adjustments of the comb flattening due to their extend/depth.

2.4.2.4 Spectral flattening

The strong modulation in the brightness of the resulting spectrum is highly disadvantageous for practical purposes. This problem is solved in the so-called 'flattening unit', exploiting a reflective spacial light modulator (SLM). This SLM is an array of individually computer controllable pixels which can affect/change the phase of the incident light. After passing through a polarization filter, the light is split via a grating, so that different parts of the spectrum reach the SLM at different spatial

positions where the SLM - through a feedback loop - can change the phase of the light which in combination with the second polarisation filter acts as an amplitude modulator (see also Figure 2.23). A small percentage of the light is afterwards separated and fed to a spectrum analyser determining the relative brightness and adjusting the phase shift while closing the feedback loop. The remaining light can finally be fed to the astronomical spectrograph satisfying all the aforementioned requirements.

The SLM itself is a liquid crystal on silicon (LCOS) in which via the liquid crystal layer[22] the phase can be changed in 256 increments resulting in equally as many brightness attenuating steps (also known as gray values). For the FOCES-LFC, the LCOS (Zhang et al., 2014) is configured in a stripe-like pattern where the strip width corresponds to the width of a pixel which equals approximately 0.2 nm.

[22] A liquid crystal is a material combining its two eponymous structure properties. The material is birefringent and this property can be controlled via an applied voltage which is heavily exploited in a large variety of display technologies.

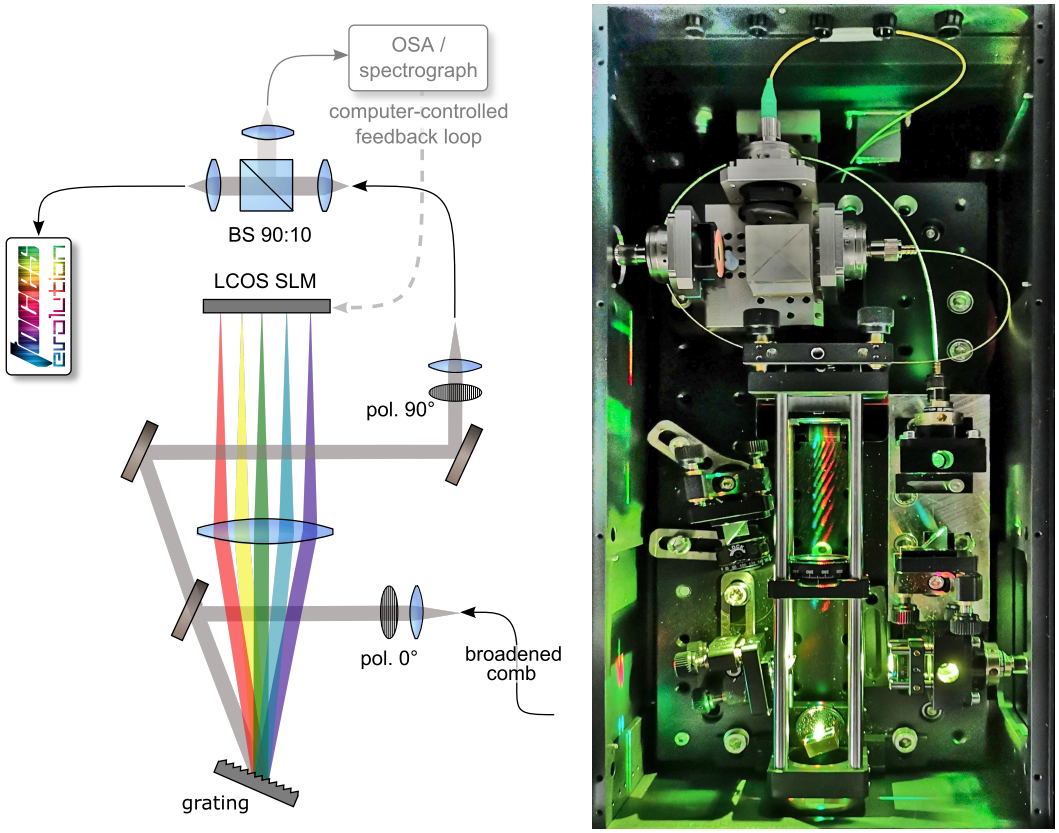

Fig. 2.23.: Illustration of the light path inside the spectral flattening unit besides a photograph of the setup. The core of the flattening process is formed by a spatial light modulator (SLM) (specifically by a Liquid Crystal on Silicon (LCOS)), which acts as a variable controllable wave plate that allows to rotate the polarization angle of the light being reflected on its way from a polarizer to an analyzer. This modifies the amount of light that passes through the system, depending on its position/wavelength on the SLM. Illustration on the left taken from Probst (2015) and modified by me.

3 The Manfred Hirt Planet Spectrograph

> *Pain is temporary. Glory is forever!*
>
> — **the angle grinder of Martin Molin**
> (Wintergatan, the Marble Machine X)

In 1939 a solar observatory was founded in the Bavarian Alps on top of Mt. Wendelstein ($47° 42' 10''$ N, $12°0' 44''$ E, 1838 m) by Karl-Otto Kiepenheuer. Since 1949 the observatory is associated and operated by the Ludwig-Maximilians-University of Munich. Over the years and due to the increasing air pollution, which made solar observations more and more difficult if not impossible, the research focus of the whole observatory shifted to nighttime observations. In the years between 1988 and 2008, the Observatory was equipped with an 80 cm telescope onto which different scientific instruments could be mounted. Starting in the year 2008 the whole observatory facility was upgraded to meet nowadays standards by a complete reconstruction of the observatory building and culminated in 2009 in the construction and installation of a modern 2.1 m telescope replacing the older 80 cm one.

Nowadays the observatory operates three telescopes (see also Figure 3.1):

- one choronograph (*Zeiss*)
  build in the 1960ies for Sun observations and now used for public outreach,
- a 43 cm telescope (student telescope)
  for teaching, student lab courses and scientific long-term observations[1] and
- a 2.1 m telescope (Fraunhofer-Wendelstein-Telescope) for a variety of different scientific observations and worldwide collaborations.

The so-called FWT is with its 2.1 m mirror the biggest and most modern optical telescope located in Germany to date. It offers currently three main instruments to the observer:

[1] For example observations of potential exoplanets for which the period could not be determined with high enough accuracy so that the expected transits period spans several days. Such observations are much more suitable to be performed with the smaller 43 cm-telescope than potentially wasting precious observation time at the larger 2.1 m telescope.

Fig. 3.1.: View of the Wendelstein Observatory taken by Andreas Leder with its three domes housing the coronograph, the 43 cm student telescope and the 2.1 m Fraunhofer-Wendelstein-Telescope. Inserts in the lower right corner taken by Matthias Kluge.

- a Wide-Field-Imager, Wendelstein Wide Field Imager (WWFI)
- a 3-channel-camera, 3KK
- a stabilized high-resolution spectrograph, ***Ma**nfred **H**irt **P**lanet **S**pectrograph (MaHPS)*[2]

The whole setup of *MaHPS* is a combination of two subsystems: the spectrograph *FOCES* and its ultra-stable calibration light source an LFC. The instrument is since its upgrade dedicated and optimized for radial velocity measurements with precision on the $\sim 1\,\mathrm{m/s}$ scale.

Considering that the main focus of the presented thesis evolves around the high-resolution spectrograph the whole next chapter describes in detail its physical properties and efforts taken to prepare the instrument for the hunt of exoplanets.

[2] *MaHPS* was named in honor of Professor Manfred Hirt, president of the association of friends of the Munich University Observatory, who played a key role in the upgrade of the Wendelstein Observatory including the Fraunhofer telescope. (Webpage of Prof. Manfred Hirt: `https://www.professoren.tum.de/honorarprofessoren/h/hirt-manfred`)

3.1 *FOCES* - An overview

FOCES was designed and built at the Universitätssternwarte München (USM) in 1997, as a high-resolution optical Échelle spectrograph. The spectrograph was originally build to be operated at the 2.2 m as well as the 3.5 m telescope of the Calar Alto Observatory ($37^\circ\,13'\,2''$ N, $2^\circ 32'\,46''$ W, 2168 m) in southern Spain. After its successful operation at the Calar Alto Observatory for more than 14 years, *FOCES* was brought back to Munich for a major upgrade and to serve its second lifetime at the 2.1 m telescope at the Wendelstein Observatory as a dedicated planet hunting instrument. The following sections will give an overview of the optical design and its implications on the recorded data and data analysis.

3.1.1 Optical design considerations

Even though not specifically designed for the hunt of exoplanets, the particular emphasis of the spectrograph was set on a high throughput, low stray-light optical design including already a passive thermal enclosure. Due to these considerations, *FOCES* operates in a *near-Littrow-configuration*[3] (with an incident angle of $\gamma = 0.7^\circ$) with an overall *white-pupil-design* (Baranne and Duchesne, 1972). The advantage of such a configuration is its intermediate image (re-image of the entrance aperture but already separated spectrally by the Échelle grating) offering the possibility to filter with an intermediate slit most of the stray-light emerging from the Échelle grating. This design choice implies a horizontal orientation of the entrance slit of *FOCES*, something that will become relevant in the following sections. As cross-disperser, a concatenation of two prisms was chosen to again avoid stray-light contributions from gratings or grisms (=grating prism). Figure 3.2 shows a top view of the optical design and the relative positions of the optical elements to each other on the optical bench inside a thermal wooden enclosure. The specifications of the optical elements can be found in Table 3.1. An in-depth discussion and a detailed technical description of the instrument can be found in Pfeiffer et al. (1998).

The resolution of an Échelle spectrograph in general and of *FOCES* in particular is subject to several limiting factors, where the worst component dictates the actual spectral resolution of the entire instrument. The three most important aspects to be considered are:

[3] Littrow configuration describes a choice of spectrograph geometry in which the incident angle, the blaze angle and subsequently also the outgoing angle are chosen to be all identical. In this configuration, the diffracted, outgoing light beam points back into the direction of the incident beam.

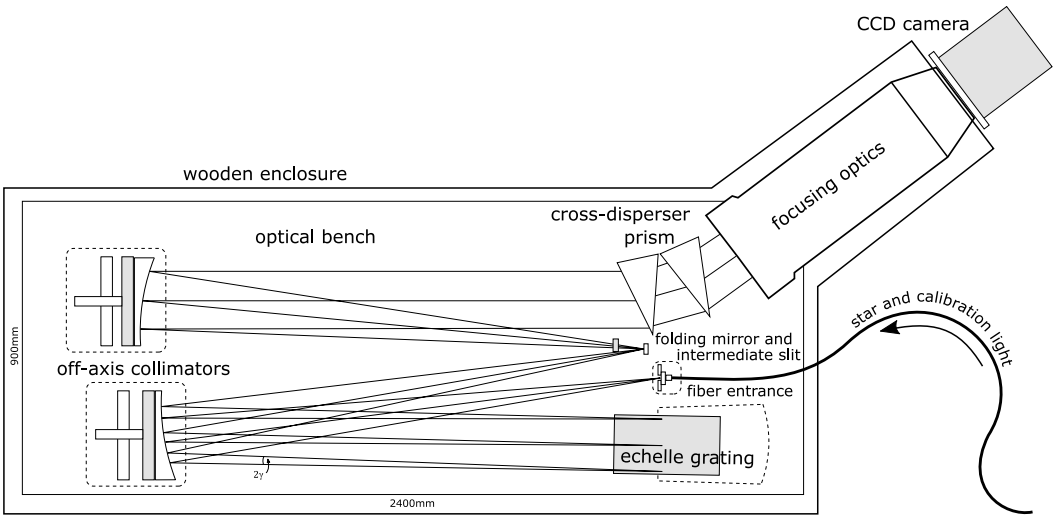

Fig. 3.2.: Top view of the optical design of the high-resolution spectrograph *FOCES* inside its wooden thermal enclosure. Note that the entrance slit to the spectrograph at the end of the optical fiber is oriented horizontally (aligned with the image plane in this sketch). Image parts taken from Pfeiffer et al. (1998).

- the intrinsic spectral resolution of the Échelle grating
- the imaged size of the entrance slit onto the CCD sensor
- the resolution of the CCD sensor itself.

The relevant components have to be chosen in a way, such that the overall resolution, which is dominated by the weakest link in the chain, is as good as dictated by the needs of the scientific goal, while still optimizing other parameters, such as light throughput. In case of *FOCES*, the intrinsic resolution $R_{\mathrm{intr.}}$ of the grating can be calculated as

$$R_{\mathrm{intr.}} = \frac{\lambda}{\Delta\lambda} = m \cdot N \,, \tag{3.1}$$

where N is the number of illuminated grating lines and m is the diffraction order. The value of $R_{\mathrm{intr.}}$ is on the order of 120000 to 220000, depending on the observed order (between orders $m = 64 \,..\, 114$). The width of the entrance aperture is ultimately defined by the typical dimension of the star in the focal plane of the telescope. Considering that a smaller entrance slit would indeed increase the resolution of the spectrograph but at the same time result in a higher light loss at the entrance aperture, a balanced approach has to be found. Derived by the image of the entrance aperture (100 x 280 μm) in the focal plane of the spectrograph, when imaging a narrow spectral line like e.g. a line of the frequency comb, it can be concluded that for *FOCES* the resolution limiting factor is the entrance slit (which leads to the somewhat boxy shaped images of the entrance slit $\neq$ diffraction-limited). The last contributor, the CCD sensor, was chosen to follow at least the sampling criterion,

Tab. 3.1.: Table of the optical elements of *FOCES*. Information taken from Pfeiffer et al. (1998) and the camera vendor Andor

optical element	**property**	
optical table:		
	dimensions	2400 x 900 x 203 mm
collimator:		
	focal length	1524 mm
	diameter	254 mm
Échelle grating:		
	dimensions	165 x 320 x 50 mm
	blaze angle	63.4°(R2)[4]
	grating constant	31.6 lines/mm
cross-disperser:		
	dimensions	190 x 160 x 112.6 mm
	deflection angle	≈ 42°(both prisms combined)
entrance apertures:		
science	dimensions	100 x 280 μm
calibration	dimensions	100 x 180 μm
camera:		
(Andor: iKon-L 936)	number of pixel	2088 x 2048
	active pixel	2048 x 2048
	pixel size	13.5 x 13.5 μm
	active sensor size	27.6 x 27.6 mm

which allows to map the image of the entrance aperture onto approximately 2.5 pixel. Derived from frequency comb observations the resolution of *FOCES* was measured to be around 60000.

3.1.2 Properties of Échelle spectrograph images

This section takes a closer look at the properties of Échelle spectrograph images (Échellogramm). The physical effects discussed below have implications for the data extraction from CCD-imaged Échelle spectra. The combination of using an Échelle grating with its high spectral resolution potential, together with a cross disperser that helps to separate the diffraction orders, in principle allows to image an optical spectrum such that it can be read like the "lines in a book" (Appendix 9.5 lists the individual Échelle orders and their corresponding wavelength coverage). An example of such an Échelle pattern of a wavelength calibration light source is shown in Figure 3.3. This image reveals that the orders traced on the imaging plane

[4]Échelle grating and being more precise their blaze angles can be specified by their R-number. This equals their tangent, e.g. R2 $\arctan(2) = 63.43°$

of *FOCES* are neither straight and perfectly horizontal, nor are the spectral lines perpendicular to these orders. In the next two sections it will be established that this is *not* due to a poor optical design of the spectrograph, but rooted in much more fundamental properties of such optical systems.

The more prominent observable effects in Échelle image of *FOCES* are:

- the tilted spectral lines and
- the curved order traces.

Both effects will be discussed in the following sections.

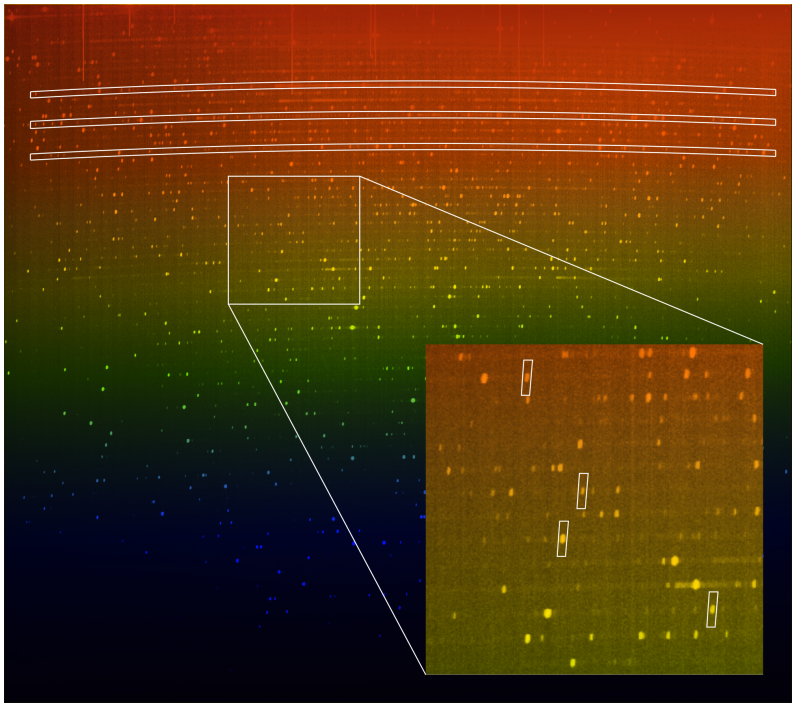

Fig. 3.3.: This illustration is based on an actual ThAr calibration frame taken with *FOCES* that has been artificially colorized in order to highlight regions of certain wavelengths. Three Échelle orders have been traced with a white outline in order to highlight the curvature on the CCD image. Similarly, inside the zoom-in of the marked region, four individual spectral lines have been highlighted with an outline that indicates the tilt of those lines.

3.1.2.1 Tilted lines in an Échelle order

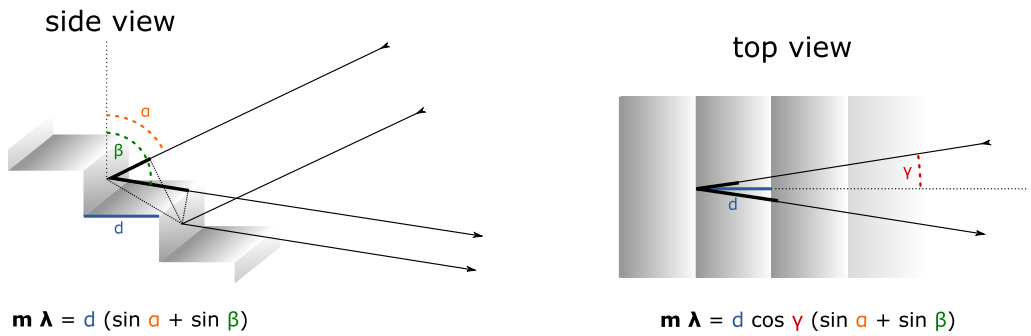

Fig. 3.4.: Illustration of the path difference in Échelle gratings as a function of the angles. α and β in the *side view* are angles in the plane of diffraction. In the *top view* the off-axis angle γ is introduced. Even though γ has no own component inside the plane of dispersion caused by the grating, it still influences the path difference d and therefore the interference condition.

The effect of tilted lines versus the order normal in an Échelle spectrograph only appears in one of the possible types of layout for such a device, the so-called γ configuration, in which the off-axis angle $\gamma \neq 0$. The derivation of the grating equation is illustrated in Figure 3.4. The left panel depicts the plane of dispersion of the Échelle grating. Light arrives at an incident angle α and leaving at an angle β. The condition for constructive interference already introduced in Section 2.2 is therefore:

$$m\,\lambda = d\,(\sin\alpha + \sin\beta)\,, \tag{3.2}$$

where the path difference $d\,(\sin\alpha + \sin\beta)$ is highlighted by the bold black line. Échelle spectrographs can be built in a configuration where the optical axes entirely lie inside this plane, meaning that Equation 3.2 sufficiently describes the setup. For practical reasons however, often a configuration is chosen where $\alpha = \beta = \Theta_B$, which requires the introduction of a so-called off-axis angle γ, such that the two collimators can still be installed in spatially disjunct positions. A top view of this described configuration is illustrated in the right panel of Figure 3.4. This angle γ modifies the grating equation, resulting in the following condition:

$$m\,\lambda = d\,\cos\gamma\,(\sin\alpha + \sin\beta)\,. \tag{3.3}$$

The entrance slit of a spectrograph has a finite extension in values of γ if it is oriented horizontally, meaning that it lies within the image plane of the right side of Figure 3.4. This implies that in cases where the grating equation is fulfilled for a certain wavelength λ (imagine a narrow spectral line), the "deflection angle" β for

that wavelength is fully defined by α and γ. In cases where γ differs from one end of the entrance slit to the other end, this leads to a different "deflection angle" β for different positions on the slit and ultimately to a tilted line in the Échelle pattern.

It is demonstrated by Eversberg and Vollmann, 2015 that the line tilt χ can be calculated by solving for and computing the derivative of β with respect to γ. Making the above assumption that $\alpha = \beta = \Theta_B$, this results in

$$\tan \chi = 2 \tan \gamma \cdot \tan \Theta_B. \tag{3.4}$$

It is worth noting that this tilt angle is wavelength-independent, but will slightly vary across the Échelle pattern as the assumption $\alpha = \beta = \Theta_B$ cannot be exactly met for the entire spectrum as β naturally has to vary across each spectral order. Inserting the numbers for *FOCES* ($\gamma = 0.7°$ and $\Theta_B = 63.4°$) a line tilt of $\chi \approx 2.8°$ is expected, which is in good agreement with the observed tilt of around $3°$.

3.1.2.2 Curved Échelle orders

The fundamental concept behind the tilted lines in an Échelle spectrum, as described in the previous section, is also partially responsible for another phenomenon that can typically be observed in Échelle spectra. The spatially disjunct Échelle orders in the imaging plane, that are a result of combining the main dispersive element (Échelle grating) and a cross-disperser with dispersion direction perpendicular to each other, appear not only tilted[5] but curved. In cases where a low dispersive grating serves as cross-disperser, the main dispersion direction of the Échelle grating acts as off-axis angle γ (see last section) for the cross disperser. This implies that similar to the tilted lines mentioned earlier, the deflection angle depends on the off-axis angle. The deflection is less prominent for large absolute values of γ, which typically occurs at the edges of an Échelle orders. This finally leads to the often noticeably curved shape of Échelle orders.

When utilizing a prism instead of a grating, a similar effect occurs that will not be discussed in detail here. Additionally, varying dispersion of a prism with wavelength can contribute to the curvature of orders. Typically the dispersion of a prism is stronger for shorter than for red wavelengths which causes the blue Échelle orders to be wider spaced than the red ones. In addition, this results in an increase of the slope with which the orders appear across the CCD towards bluer wavelengths,

[5] The tilt angle is simply the fraction between the dispersion powers of the two dispersive elements. Usually, the main dispersive element is much stronger than the cross disperser, leading to tilted, but still relatively flat orders.

resulting in a certain degree of curvature too. The combined effect observed in *FOCES* data is a change of slope of the Échelle order from the left to right end of the order by about $5°$.

It is worth noting that the curvature of the Échelle orders on the CCD is an effect of the dispersion properties of the cross disperser (for different wavelengths and different off-axis angles) and is in no way directly related to the tilted lines discussed in the previous section. In the detector plane, spectral lines are essentially monochromatic images of the slit and their shape is therefore not influenced by the cross-disperser. The effect that causes the lines to be tilted in the first place is the fact that the extension of the slit on the longer side acts as different off-axis angles on the main dispersion element. For the cross-disperser, the extension of the slit in either direction can be neglected. In summary, the tilt of the lines should not follow the curvature of the orders but should, in the absence of additional adverse optical effects, stay relatively constant across the image recorded in the CCD.

For the extraction of Échelle spectra from 2D CCD images, this implies that each spectral order needs to be traced individually, in order to correctly extract the proper region of the cross-order profile. Although the everywhere constant line tilt could be considered as well in the extraction of 1D spectra, usually the image resolution is not high enough for this to be possible. Instead, also in the case of *FOCES*, the extraction is performed by simply following the pixel grid and accepting the somewhat decreased spectral resolution that is caused by the line tilt.

3.2 *FOCES* - Upgrade and implementation at the Wendelstein Observatory

For its deployment at the 2.1 m telescope at the Wendelstein Observatory, the main scientific purpose of *FOCES* has shifted to exoplanet hunting and verification via the radial velocity method on the meter per second level. Demanding to measure line shifts in the order of a 2000th of a pixel (see also Section 1.2.3) over a time span of weeks or months, this new task comes with much stricter requirements for the stabilization and wavelength calibration compared to other fields in astronomy. *FOCES* is therefore housed in the basement of the observatory, several floors below the telescope and the incoming light is guided via optical fibers to feed the spectrograph. Figure 3.5 provides an overview of the architectural layout of the telescope and the spectrograph at the observatory. This setup already has the advantage of thermal and mechanical decoupling of both components, which has a number of positive implications for the overall stability.

In addition, several upgrades and modifications were performed during the installation of *FOCES*, which include but are not limited to:

- a multi-fiber light input to enable simultaneous wavelength calibration (Section 3.2.1),
- a new wavelength calibration light source (laser frequency comb) (Section 3.4),
- a new pressure stabilized and thermally insulated tank and a multi-stage active temperature stabilization system (Section 3.5),
- carefully considered connections of the fibers feeding the spectrograph (Section 3.3),
- an in-situ exposure time measurement unit (mini-spectrograph called FOX) (Appendix 9.4)
- a new camera (*Andor iKon-L 936*[6]),
- the removal of all potential heat sources (motors etc.),
- the removal of all moving parts (e.g. adjustable entrance aperture).

The following chapters describe hardware upgrades and implementations of which a substantial amount was already published in a series of conference proceedings, many of which with major contributions during the scope of this thesis (*Hardware:* Grupp et al. (2009), Grupp et al. (2010), Grupp et al. (2011), Feger et al. (2012),

[6] *Andor* webpage: `https://andor.oxinst.com/products/ikon-xl-and-ikon-large-ccd-series/ikon-l-936`

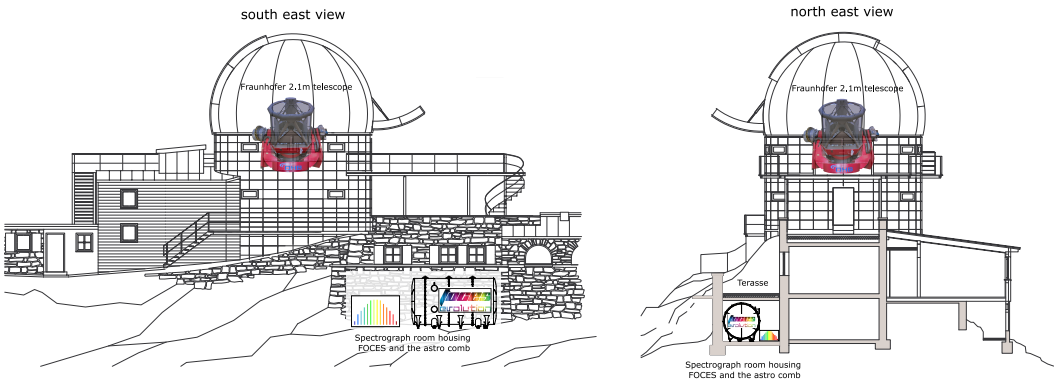

Fig. 3.5.: Architectural drawings of the Wendelstein Observatory building highlighting the locations of the 2.1 m Fraunhofer telescope inside the main dome as well as *FOCES* in the basement. Illustration not to scale.

Brucalassi et al. (2012), Brucalassi et al. (2013), Kellermann et al. (2015), Brucalassi et al. (2016), Kellermann et al. (2016), Kellermann et al. (2019), Krecker et al. (2020), and Fahrenschon et al. (2020), *Software:* Wang et al. (2017), Wang et al. (2016), and Kellermann et al. (2020)).

The next sections follow the path of the light backward from the spectrograph to the telescope, starting with a detailed description of the new light-injection system (i.e. the new entrance slit unit) of the spectrograph, developed entirely in the scope of this thesis, followed by an overview of all the fiber connections and their properties installed at the observatory to guide light into *FOCES*. Closing this chapter, an overview of all the auxiliary installations including the calibration unit and the temperature- and pressure-control system is given.
Due to its exposed location on top of Mount Wendelstein and frequently occurring thunderstorms in the German Alps, *FOCES* is at an elevated risk to be affected by lightning. Appendix 9.3 provides therefore an overview of measures taken to prevent damage to the system.

3.2.1 New multi-fiber-light-injection system

As already addressed in Section 2.4, the most important component in the hunt for exoplanets is the stabilization of the whole measurement setup to such a degree that it is possible to measure the small shifts in the spectrum introduced by exoplanets orbiting their host stars. Besides stabilization efforts, it is also possible (and practiced by all major planet hunting spectrographs) to measure instrumental shifts as accurately as possible to eliminate/subtract these drifts during data reduction, which is done via simultaneous calibration. The main purpose of the new

multi-fiber-light-injection system described in detail in this chapter is to offer this simultaneous calibration mode by recording science light and light from the LFC or other calibration light sources at the same time. Different technical approaches for this technique are used with instruments around the globe. The goal can be achieved by guiding the light from different sources (star & calibration light) in at least two distinct fibers into the spectrograph (*double-* or *multi-fiber-mode*) and mapping them onto the CCD in spatially separated locations. Otherwise, the light can be guided in one fiber, which results in light of both light sources overlaying each other in the image plane of the spectrograph (*single-fiber-mode*). Traditionally, the second option is utilized when spectrographs are calibrated via the iodine method[7]. While the first method is significantly easier with regard to data reduction, it has the disadvantage that differences arising from the two distinct fibers cannot be eliminated with this approach. Therefore, special emphasis is usually put on treating both fibers as equally as possible (same type of fiber from the same fiber coil, same length, same manufacturer, same routing through the observatory etc.). The setup of *FOCES* offers both options to the user, however, only the double-fiber option could be tested to date due to time limitations. It is also worth noting that the single-fiber method proposed here is in contrast to the iodine cell additive, i.e. the comb light is added to the starlight and not subtracted due to absorption like it would be the case for the iodine method. Figure 3.6 depicts possible light paths for the two simultaneous calibration modes and shows a 2d spectrum of the double-fiber method recorded with *FOCES*.

To enable the double-fiber option, the light input of *FOCES* had to be modified to accommodate two instead of one single input fiber. In addition, and to be able to perform tests in the future without changing hardware, it was decided to implement four fibers in total into a single setup. In this approach, two multi-mode fibers enable feeding the spectrograph with science (star) and calibration light during normal operation. The other two fibers are mono-mode fibers and are to date installed purely for academic purposes, as test instruments to study the effect of differences in mono and multi-mode behavior, particularly regarding comb light. Due to their substantially smaller core diameter (multi-mode: 100μm, mono-mode: 3μm), the

[7]For the iodine method, a cylinder containing iodine gas is placed into the light path from the telescope to the spectrograph. The thermally stabilized gas has a well-defined absorption spectrum which is thereby imprinted onto the star spectrum (subtractive process) in the wavelength range from 490-650 nm. Although high precision RV measurements are possible in this way (e.g. see also the Tautenburg spectrograph `http://www.tls-tautenburg.de/TLS/index.php?id=31`) it is not the most common method of choice due to challenging software demands to disentangle starlight and iodine absorption imprint as well as hardware requirements concerning the stabilization of the iodine cell itself.

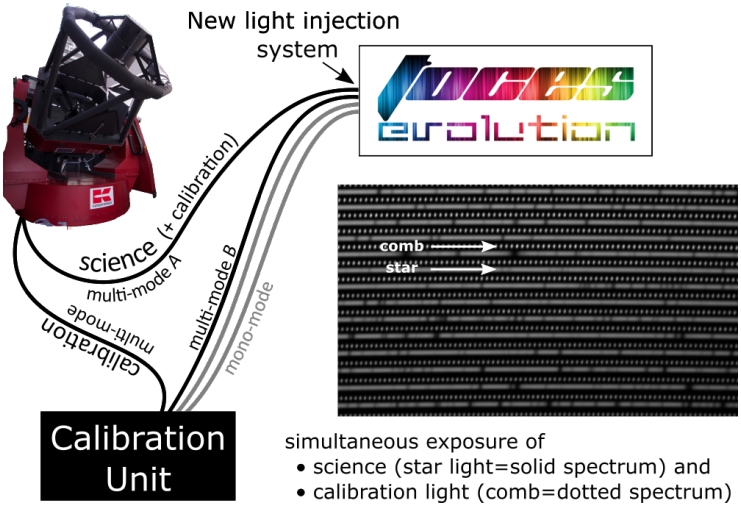

Fig. 3.6.: Illustration of the simultaneous calibration concept of *FOCES*. Light is fed into the spectrograph from the telescope (science), but also from calibration light sources, through the 4-fiber-slit assembly, resulting in the line-by-line pattern depicted on the right, with science and calibration spectra alternating.

amount of light guided by these fibers is limited compared to multi-mode fibers. This is the reason why they are not foreseen to be used during normal operation.

To accommodate this modernized approach derived from the new stability requirements, and to reduce the amount of movable components (entrance slit), the entire light injection into the spectrograph needed alterations. The new multi-fiber-light-injection system has been designed, built and tested in the context of this thesis. A substantial amount of the technical details have already been published in Kellermann et al. (2015), Kellermann et al. (2016), and Kellermann et al. (2019).

The multi-fiber-light-injection system for *FOCES* can be divided into the following three components:

- the **4-fiber-slit assembly**
  which physically combines four individual optical fibers and keeps them precisely aligned in close proximity in the object plane of the spectrograph,
- the **miniature lens system**
  that performs the re-imaging of the fiber ends and the focal ratio adoption of the exiting transport beam (f/#=3.6) of to the beam expected by the spectrograph (f/#=10.0),
- and the **slit mask**
  that serves as entrance slit for *FOCES*.

An overview of the components and their physical arrangement can be found in Figure 3.7. In the following sections, each of the three components and their design considerations are described, followed by a summary of the assembling process and an evaluation of the whole setup.

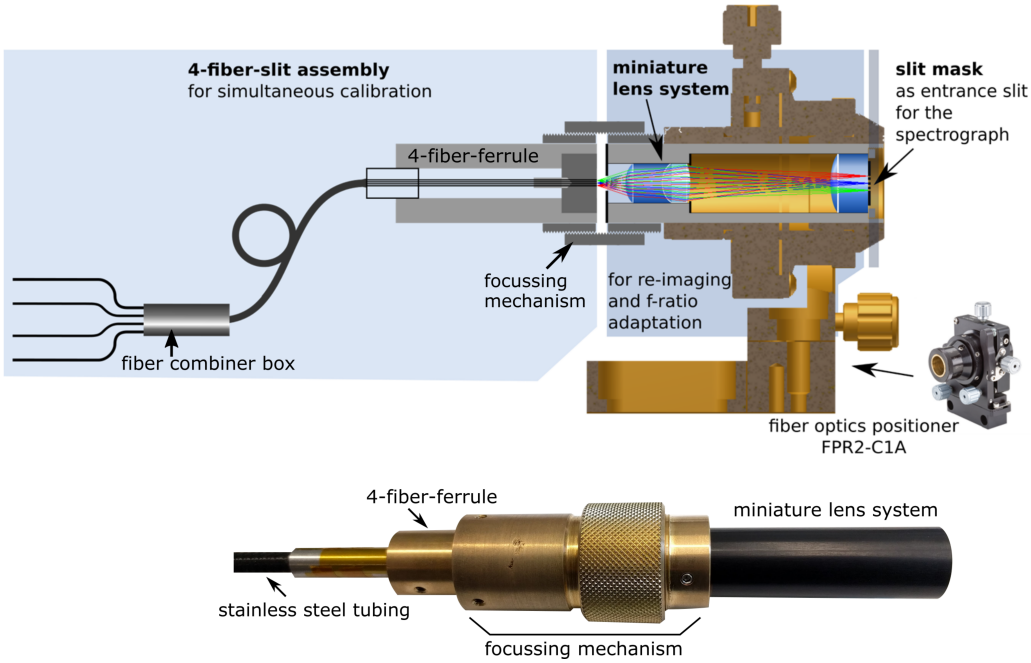

Fig. 3.7.: Illustration of the components of the new multi-fiber-light-injection system for facilitating simultaneous calibration during scientific observations with *FOCES* (top). Annotated photograph of the miniature lens system that serves for focal-ratio adaptation and re-imaging (bottom).

3.2.1.1 4-fiber-slit assembly

The 4-fiber-slit assembly serves the purpose of combining optical fibers of various types, carrying light from different sources. The individual fibers on the input side are guided in their own protection tubes that are terminated inside a *combiner box*, from where on they are guided in the same protection tubing. This protection tube leads to a custom-designed *4-fiber-ferrule*, which keeps the fiber centers aligned and at a defined distance. See also the Figure 3.7 upper left corner and Figure 3.8 for illustration. Throughout the next paragraphs, the different aspects of the 4-fiber-slit assembly are described in detail.

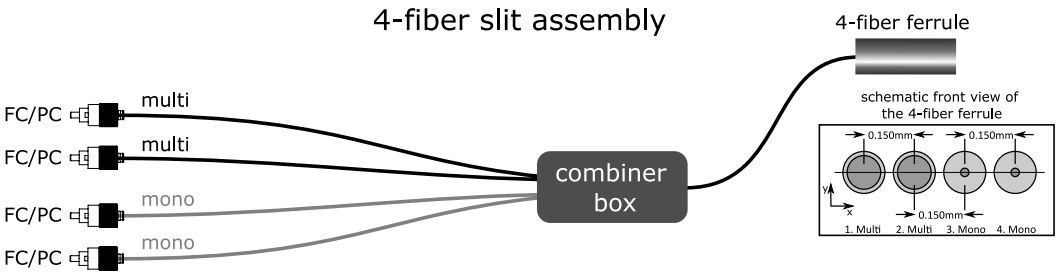

Fig. 3.8.: The 4-fiber-slit assembly consists of four separately enclosed and guided optical fibers (two multi-mode and two single-mode fibers). After passing through the *combiner box* they are joined in a common tubing and guided towards the 4-fiber-ferrule. This specially designed ferrule keeps the fibers in a well-defined configuration and acts as part of the entrance slit of the spectrograph. In its final installation in *FOCES* the *combiner box*, as well as the 4-fiber ferrule, are installed inside the *FOCES* tank while the four individual fibers are guided through an airtight sealing to the outside of the tank.

Optical fibers, connectors and fiber glue

For the 4-fiber-slit assembly, different fiber options were explored by Tobias Feger (Feger, 2012). The fiber type of the multi-mode fibers was selected to be *Polymicro* FBP100120140. For the mono-mode option, the choice fell on *Thorlabs* S405-XP to match the fiber type exiting the LFC. The properties of these fibers are listed in Table 3.2.

Tab. 3.2.: Optical fibers and their properties used in the 4-fiber assembly (clad.=cladding, jack.=jacket).

no.	fiber	type	purpose	diameter [μm]		
				core	clad.	jack.
1	FBP100120140	multi	calibration	100	120	140
2	FBP100120140	multi	science	100	120	140
3	S405-XP	mono	test	3	125	245
4	S405-XP	mono	test	3	125	245

Bare fibers are extremely fragile and impractical to handle, which is why they are usually covered in protective tubing and equipped with fiber connectors. The optical fibers themselves are thereby moving freely inside their tubing, while both ends of the fibers are glued into the so-called ferrules of their individual fiber connectors. Subsequently, the end faces of these fibers need to be polished to optical quality to minimize scattering losses. The connectors themselves consist of two main components: a ferrule - holding the optical fiber itself - and a mounting system which varies widely between connector types. The most commonly used connectors types

for astronomical purposes are FSMA and FC/PC[8]. All fibers related to *FOCES* are equipped with FC/PC connectors since this type of connector offers rotation protection via a key when fibers are connected to each other, which improves repeatability when coupling optical fibers. Every fiber connector has to be chosen according to the dimensions of the optical fiber intended to be used (outer diameter of the fiber + 1-5μm = inner ferrule diameter). Thereby different connector implementation options offer different accuracy choices.

For the ferrules inside these connectors, two different types are commonly available: either stainless steel or ceramic ferrules. Due to their production process, stainless steel ferrules usually provide only in the first 1-2 mm the narrow hole to guide the fiber, making the expected angle tolerance (combination of the ferrule hole tolerance and fiber diameter tolerance) significantly larger. Ceramic ferrules on the other hand provide holes with tight tolerances over a much longer length of usually 10-12 mm, thus administering far tighter tolerances on the angle of the fiber (see also Figure 3.9). This in fact can reduce FRD originating from fibers which are unintentionally polished under an angle because of too large ferrule borehole tolerances. As an additional advantage, ceramic ferrules produce less abrasion during the polishing process, which considerably simplifies the entire polishing procedure.

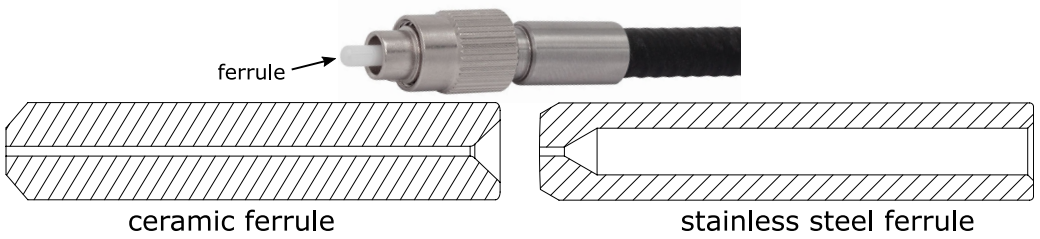

Fig. 3.9.: Two main types/materials of optical-fiber ferrules are available, ceramic and stainless steel. The ceramic ferrules usually guide the fiber inside a much longer hole (about 1 cm in length) with precise tolerances, leading to higher angular accuracy of the fiber orientation. Stainless steel ferrules on the other hand only guide the fiber for a length of about 1 mm, resulting in a higher possibility of misalignment of the fiber axis. Image taken from *Thorlabs* and modified by me.

Fiber Protection

For *FOCES*, each fiber is protected in a two-layered structure consisting of a ca. 3mm (outside diameter) furcation tubing, which is in turn inside a ca. 6mm (inside diameter) stainless steel tubing, further illustrated in Figure 3.10.

[8]Due to the relatively large footprint of those connectors they are no longer commonly used for telecommunication but are quite frequently seen in laser setups and lab applications due to their ruggedness.

The stainless steel spiral tubing safeguards the fiber against all high-stress impacts, like sharp edges and people or equipment crushing the fiber. It is covered in black plastic coating to prevent any visible or near-infrared light from entering the fiber and protects the inside of the tube from moisture. Besides that, the coating reduces stretching of the metal spiral and friction during the installation process, which lowers the stress to and the risk of breaking the fiber.

The inner furcation tubing serves two purposes: It protects the optical fiber against any sharp edges, which might appear inside the steel tubing, and restricts length changes of the outer tubing that would put stress on the fiber. Since the fiber has to be installed hanging freely, at least for a few meters, there is a risk of the metal spiral changing its length under its own weight. To prevent this source of potential stress on the fiber, the installed furcation tubing is lined with protective Kevlar threads[9] that prevent this behavior. This two-layered approach creates, in addition, a more

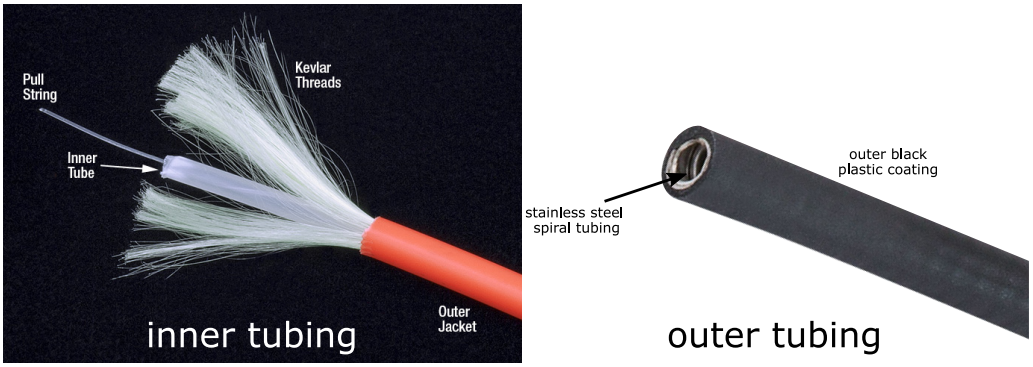

Fig. 3.10.: Left panel: Structural layout of the inner furcation tubing where the outer jacket protects the optical fiber from sharp edges, the Kevlar threads prevent length changes, while the inner tube houses the fiber itself which can be installed using the pull string.
Right panel: Stainless steel spiral tubing for protection against high-stress impacts. The black plastic coating prevents light and moisture from entering the fiber and reduces friction during the installation process. Both images taken from `https://www.thorlabs.com/newgrouppage9.cfm?objectgroup_id=312` on 7.1.2021 at 16:35.

rigid fiber assembly, which reduces the chances of the fiber being too tightly rolled up in its final position and/or during installation. Although the fiber could in theory be bent to a radius of 2 cm without permanent damage, it is not advised to do so. The recommended manufacturer radius for storage and long-term installation is a minimum of 20 cm which was purposefully exceeded to ensure optimal FRD. Figure 3.11 depicts the schematic structure of an optical fiber assembly as produced for *FOCES* with its double-layered structure, which is inserted by pushing the inner

[9]The Kevlar threads have to be cut with special dedicated scissors since they will damage and dull normal scissors.

tubing into the outer tubing while agitating the metal tubing[10]. The white inner tubing, shown in Figure 3.10, left side, directly safeguarding the optical fiber is thereby glued into the back end of the connector itself (*not* the ferrule) to ensure full protective coverage over the whole fiber length. The Kevlar threads are folded over, glued[11] and clamped between spiral tubing and tube connector to ensure the proper long-term alignment of inner (plastic) and outer (metal) tubing. The polishing of these fibers is described in Section 3.2.2.

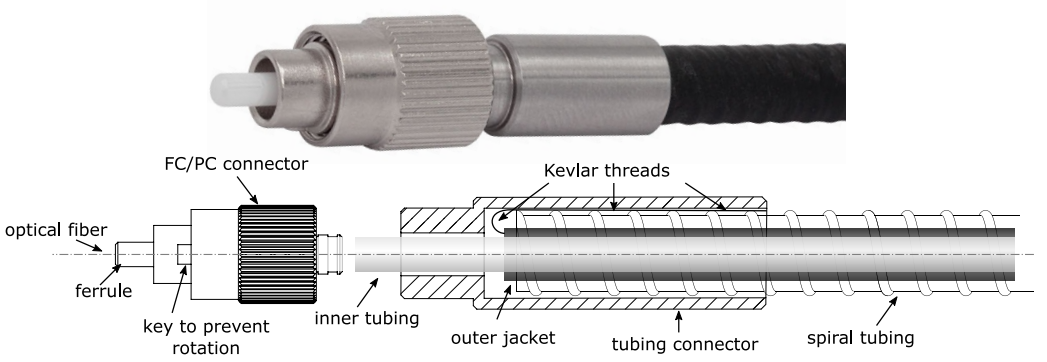

Fig. 3.11.: Illustration of the fiber protection concept and fiber connectors on the single-fiber end. An outer spiral tubing assures a secure bending radius, while an inner tubing lined with Kevlar threads prevents the optical fiber from receiving stress due to tension from stretching. Parts of the image were taken from *Thorlabs* and modified by me.

Combiner Box

The *combiner box* is an about 20 cm long metal box where four individual fibers enter at one side and exit the box on the other side through one single protection tube (see also Figure 3.12). This box serves two purposes: it allows for the combination of the fibers in a protected setting and offers a possibility for length compensation of the optical fiber in regards to their protection tubing caused by length differences arising when bending the protection tubing since the fibers can move freely in the inner volume of the box. The length of the box and the arrangement of the fibers help to avoid sharp kinks or excessive bending. To be able to do so, the fibers are left bare without metal or plastic tubing, only protected by their jacket to move as unrestricted as possible. All fibers enter and exit the combiner box conveniently through off-the-shelf fiber connectors with an inner diameter of 1580 μm[12], offering

[10] In this configuration and the mentioned procedure only fiber lengths up to 12-15 m can be assembled.

[11] For this task *UHU Plus Endfest universeller starker 2K Epoxidharz Klebstoff* was used after consulting with the fiber expert of ESO Dr. Gerardo Avila due to being slightly flexible even after being fully cured which is beneficial considering the flexible black outer plastic covering.

[12] *Thorlabs* fiber connector: 30126G2-1580

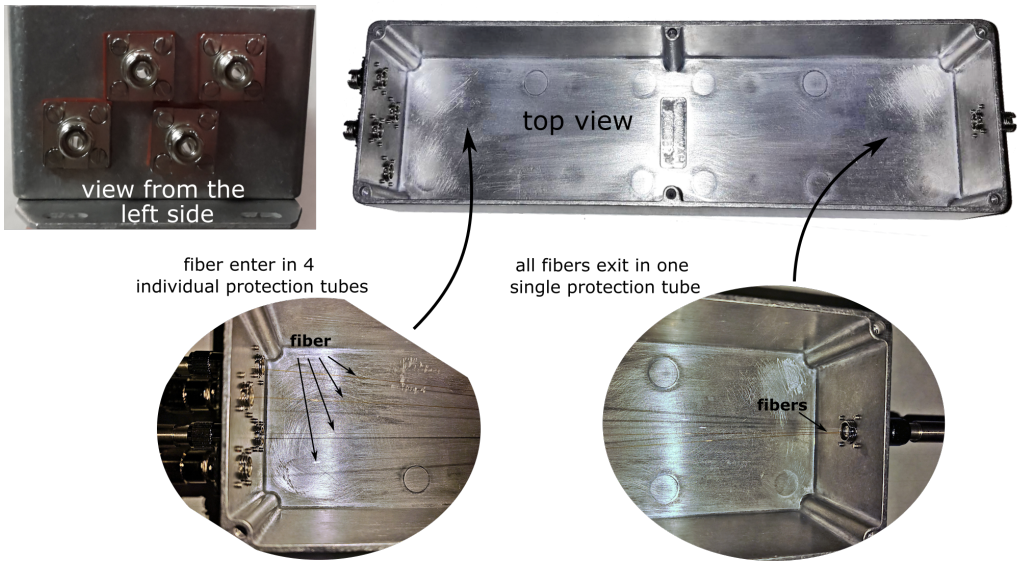

Fig. 3.12.: Image of the Combiner Box that guides the four optical fibers from their separate tubings into one. It also serves for providing minimal amount of slack, avoiding stress on the optical fibers at all costs.

as few restrictions as possible on the fiber movement. The metal box itself has a plastic sealing to protect the fibers from dust and humidity entering the box.

4-fiber-ferrule

The 4-fiber-ferrule is designed to accommodate two multi-mode and two mono-mode fibers that can be used to guide light into the spectrograph.

The optical design of the spectrograph dictates a maximum distance between the fiber centers of 150 μm, leaving only a gap of 10 μm between the multi-mode fibers due to their outer diameter of 140 μm. This configuration ensures that spectra guided in both fibers do not overlap in the imaging plane. To avoid different light paths through the spectrograph[13] due to misalignment of the fibers to each other, the requirement for the 4-fiber-ferrule was to achieve a comparable angular-alignment accuracy of the fibers to that of an off-the-shelf ceramic ferrule. Different designs have been evaluated for the 4-fiber-ferrule, including through-holes and V-grooves. In terms of materials, glass and metal options have been explored. Due to the high aspect ratio originating from the angle requirement, classical drilling in metal could be ruled out. An interesting approach that was investigated in some detail

[13]Misalignment of the fibers could result in a different number of lines illuminated at the Échelle grating leading to a variation in the resolution of the science and calibration light or in light loss when the optical components of the spectrograph are (partially) missed by the light beam coming from the two different multi-mode fibers.

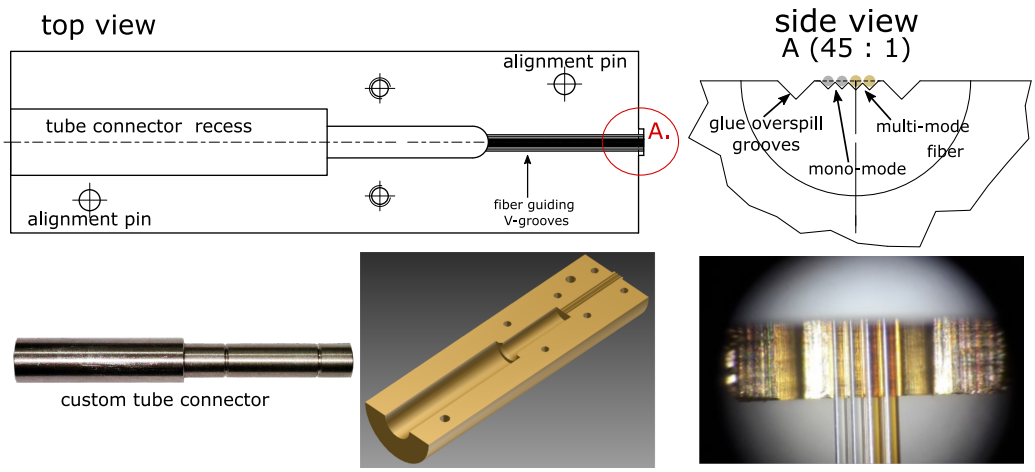

Fig. 3.13.: Simplified CAD drawing of the 4-fiber-ferrule design (top) with 3d illustration (bottom middle). On the bottom right, a microscope image of the tip of the ferrule with all 4 fibers in their dedicated V-grooves can be found. The bigger V-grooves on the left and right from the optical fibers act as overflow reservoirs to pick up glue that might spill over during the production process. The bottom left depicts the custom tube connector attaching the fiber tube to the 4-fiber ferrule.

were laser-drilled holes in glass, utilizing dissolvent solutions to create the holes. Although very attractive due to the simple installation process of the fibers, similar to off-the-shelf fiber ferrules, and therein especially the simplicity of the polishing process of the same, this approach had to be discarded due to the infeasibly large hole depths required. Finally, the choice fell to a V-groove design manufactured from brass (see Figure 3.13 and Figure 9.2) manufactured by *Zilske Präzisionsmechanik GmbH*[14].

The fiber ferrule consists of a 60mm long cylinder that was cut in two halves along its length and an outer diameter of 17.2 mm to dictated by the width of the 5-axis fiber positioner (*Newport* FPR2-C1A) installed in *FOCES*. The lower half-cylinder represents the actual ferrule with four 15 mm long V-grooves of two different depths to accommodate the two different fiber types and to align their center on a straight line. In addition, two wider V-grooves are intentionally placed beside the fiber-guiding grooves to serve as a possible over-spill reservoir for the fiber glue. The alignment of the upper and lower half of the ferrule is ensured by positioning pins and fixed via sunk screws. The material was chosen to be brass on the recommendation of the manufacturer. To minimize problems during the fiber polishing originating from the wide front surface (⌀17.2mm) manufactured in

[14]Zilske Präzisionsmechanik GmbH, Hochstr. 37, 82024 Taufkirchen, Germany; webpage: `http://www.a-zilske.de/`

brass, a protrusion of ⌀2.5mm[15] was requested, reducing the contact surface during polishing significantly. See Figure 3.13 and Appendix 9.2, *Section A*). The upper half-cylinder does not at all come into contact with the optical fibers themselves, in order to avoid mechanical stress. It merely serves for mechanical protection and facilitates mounting the whole 4-fiber-ferrule in its holding structure.

3.2.2 Assembling and evaluation of the 4-fiber assembly

Following the overview of the individual components in the last section, this section describes in detail the assembly process, followed by the last paragraph reporting the evaluation of the finished assembly. All the details described in the following paragraph are the result of a trial-and-error process, yielding a very specific method that proved to be suitable for manufacturing the 4-fiber assembly.

Assembling the 4-fiber assembly

The fibers were threaded into their individual tubing by gluing them to their so-called pull-string delivered in every protection tubing with superglue (see also Figure 3.10), re-attaching them in a staggered manner to the pull-string of the single protective tubing in the combiner box[16]. The fibers were thereby pulled with as little as possible tension through cotton swabs slightly moistened with distilled water and isopropyl alcohol which acted as dust scraper. This eliminates the chance of sharp dust particles entering the tubing and over time scratching the optical fibers, which could lead to a decline in the performance of the fiber.

The two multi-mode fibers with an outer diameter of 140 μm fit directly into the foreseen grooves, while the two single-mode fibers with an outer jacket of 245 μm had to be stripped using a razor blade. There are different ways to strip a fiber of its jacket, the most commonly used techniques are mechanical stripping, striping with a solvent and heat stripping (burning the jacket of). The risk of damaging or changing the optical properties of the fiber utilizing an aggressive solvent or a heat source was considered to be too high. Therefore, the fibers were stripped mechanically with a razor blade holding the blade under an angle of 30 degrees during the procedure. While this method is not entirely without risk, especially of breaking the fiber, it has the advantage that this kind of damage can be detected very easily.

[15] As 2.5mm is the usual diameter of a commercial fiber ferrule for FC/PC connectors.

[16] Around 20-30 cm at every superglued fiber end was removed after pulling the fibers to eliminate potential damaged fiber ends.

As preparation for the gluing process, the 4-fiber-ferrule was cleaned with an ultrasonic cleaner, which's cleaning solution was removed by a bath in isopropyl alcohol and rinsed with distilled water before being dried off by clean pressurized air in order to avoid stains. Subsequently, the four fibers were positioned into their individual grooves, placing the mono-mode fibers in a staggered manner to reduce stress points on all fibers which would arise when both mono-mode fibers transition from 245 μm jacket diameter to 125 μm cladding diameter at the same height. During the gluing process, the fibers were weighted down by a 3 mm Teflon strip to avoid self-attachment of the fibers via capillary forces once the glue was applied. For the glue itself, the aforementioned *EPO-TEK 301-2* was specifically chosen for its low shrinkage rate and low viscosity. Small bubbles originating from the mixing process (*EPO-TEK 301-2* is a two-component glue) were removed by applying a vacuum before applying the glue to the fibers via a syringe. Subsequently, the fibers were cured over 48 h on a heating plate stabilized at 24°C ($\pm$1.5°C) under a glass dome ensuring a constant humidity of 60-75%. The whole gluing process was monitored under a microscope with LED lighting to avoid heating the brass ferrule while moving and arranging everything with tweezers to avoid heat transfer to the ferrule. The tube connector was likewise glued in place but only the installation of the upper half of the ferrule ensures the final mechanical stability of the connector.

As already mentioned in the previous sections, the fibers are intentionally barely covered in glue to avoid stress to the fibers originating from the curing process. However, for the polishing process, this is a disadvantage especially considering that the ferrule material is brass. From experience, it can be stated that polishing metal ferrules (especially materials which are not specifically dedicated as ferrule materials) is challenging since metal abrasions created in the polishing process jeopardize the entire polishing process either by scratching the freshly polished fiber surface or by creating pressure points which together with the rotating disc of the polishing machine can even rip the whole fiber out of its gluing (thereby destroying the whole 4-fiber assembly). To avoid this scenario, a glue support (similar to a neck brace) was built upon the lower side of the fiber utilizing the surface tension of the glue. With this technique the brass material does not come into contact with the polishing disc, avoiding all the aforementioned risks. The glue support itself is thereby (almost) entirely removed during the polishing process.

The fibers inside the 4-fiber-ferrule were polished with the *Buehler FiberMet* polishing machine, explicitly choosing the direction of rotation of the polishing pads to work against the small support structure made from glue. After cleaving the excess fiber ends with a sapphire blade, the wet polishing was started utilizing a 3 μm pre-polishing paper and distilled water. It was finished with 0.3 μm finishing paper,

cleaning everything extensively with a lint-free paper, isopropyl alcohol and distilled water between each polishing pass. Figure 3.14 illustrates the gluing and polishing process.

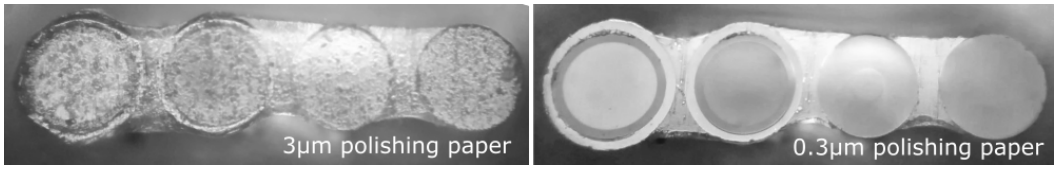

Fig. 3.14.: Gluing and polishing process of the 4-fiber-ferrule. The gluing process and formation of a "neck brace" below the fibers are illustrated in the two upper rows. The lowest row depicts microscope images showing the end surface of all four fibers at different stages of the polishing process.

Evaluation of the alignment of all four fibers with respect to each other

To validate and evaluate the positioning of all four fibers with respect to each other, the setup described in detail in Section 3.2.3 was utilized. The measurement was conducted while all 4 fibers were homogeneously illuminated. By extracting the center of gravity of all four fibers of the recorded CCD image (Figure 3.15, left) and subsequently fitting a straight line to them, a position error could be evaluated. Finally, a good result of no individual deviation of more than 2 μm and a maximum offset between two fibers of 3.5 μm could be measured (Figure 3.15, right).

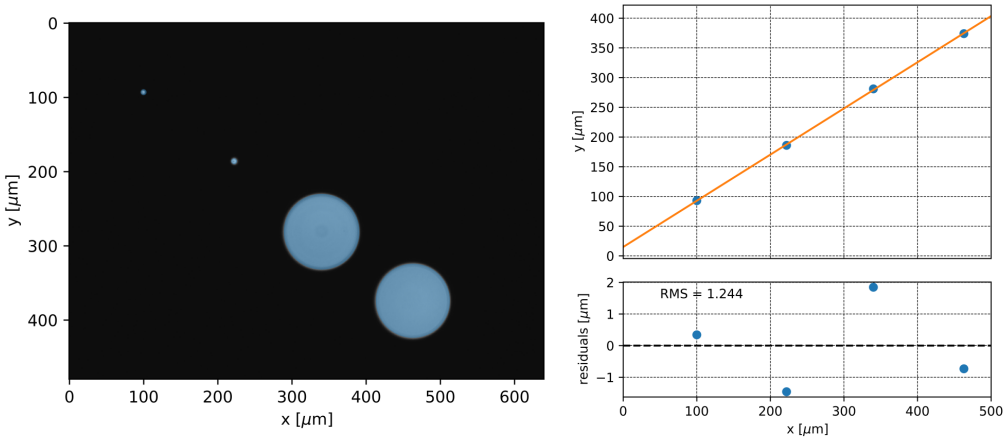

Fig. 3.15.: Evaluation of the positioning and alignment of the fibers in the 4-fiber assembly. The left panel shows a CCD image of the fibers that are all illuminated with diffuse light from the backside. Based on this image the center of gravity of each fiber has been calculated and the resulting coordinates fitted with a straight line (shown in the upper panel on the right side). The residuals in the lower right panel show no deviation of more than 2 μm from perfect alignment.

3.2.2.1 Miniature lens system for f-ratio adoption

The miniature lens system for re-imaging and focal ratio adoption is a custom in-house design (by Dr. Frank Grupp) that was manufactured by the company Präzisionsoptik Gera[17].

The f-number at the output of the 2.1 m Fraunhofer telescope is f/#=7.8 (see also Section 3.1). This is adapted to a value of f/#≈4 for optimal guidance inside the optical fiber delivering the light to *FOCES*, utilizing a small achromatic lens[18] (ø=3mm, f=5mm) at the telescope. *FOCES* on the other hand is designed to be fed with a focal ratio of f/#=10. This final adjustment of the focal ratio is performed by the so-called *miniature lens system* where the image plane of the lens assembly is modeled to be the surface of the last lens. Furthermore, the last surface of the lens system is intentionally designed to be flat and simultaneously represents the image plane of the lens system. This opens the possibility of exploiting this surface as the mechanical holder for the entrance slit mask of *FOCES*. By eliminating one degree of freedom during the alignment of the miniature lens system with respect to the slit mask, the whole procedure is greatly simplified and it is conveniently possible to glue the slit mask directly onto the flat surface of the miniature lens system. A schematic drawing and the optical design in *ZEMAX* can be found in Figure 3.16. The mechanical and optical design parameters of the system are listed in Table 3.3. The performance of the miniature lens system was evaluated by

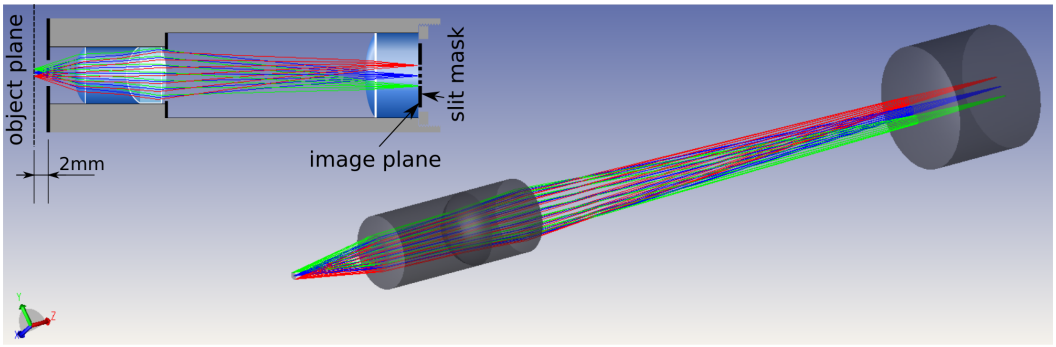

Fig. 3.16.: Schematic drawing of the miniature lens system (top left) and 3d ray-tracing simulation performed with *ZEMAX*. The object plane is located 2mm outside of the mechanical mount. The image plane is located on the last optical surface, onto which the slit mask is finally attached. Optical simulation provided by Dr. Frank Grupp.

[17] Präzisionsoptik Gera (POG): Alte Str. 3, 04626 Löbichau, Germany; webpage:`https://www.pog.eu/de/`

[18] *Qioptiq* achromatic lens: G052002000; Achromat, VIS, ARB2, D=3, F=5

Tab. 3.3.: Technical specifications of the miniature lens system

Optical specifications	
Magnification:	2.81
both sides telecentric:	yes
polish:	laser polish (P4; mean roughness $<=0.001\mu$m; number of micro defects per 10mm <3)
Image Space NA:	0.05 (f/#=10.0)
Object Space NA:	0.14 (f/#=3.6)
Wavelength range:	400 - 800 nm
Mechanical specifications	
Mechanical length:	71.60 mm
Mechanical diameter:	17.20 mm

measuring the edge spread function. For this test, an Apogee A340 CCD-Camera equipped with an infinity-corrected, long working distance apochromatic microscope lens with a magnification of 7.55 ± 0.04 and a visibility of $\sim 60\%$ for 228 l/mm (Feger, 2012) was utilized. The vendor's data sheet specifies a resolution of 1.1 μm for the microscope objective[19]. The test was performed on a standard USAF resolution chart. The result of this measurement can be found in Figure 3.17 and demonstrate the excellent quality of the miniature lens system which is in good agreement with simulations performed by Dr. Frank Grupp. Figure 3.18 shows that the lens system is even able to resolve the smallest pattern (Group: 7, Element: 6) on the USAF resolution chart.

[19] *Qioptiq* part number: R282110000: Optem long working distance, infinity corrected objectives

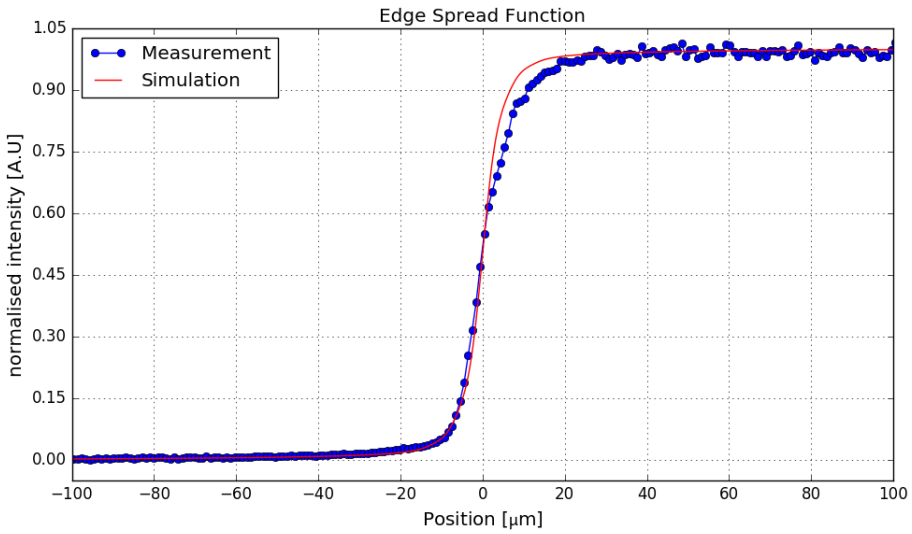

Fig. 3.17.: Edge Spread Function of the miniature lens system in simulation and actual measurement. Both are in good agreement, proving the performance to be within specifications. Optical simulation in *ZEMAX* provided by Dr. Frank Grupp.

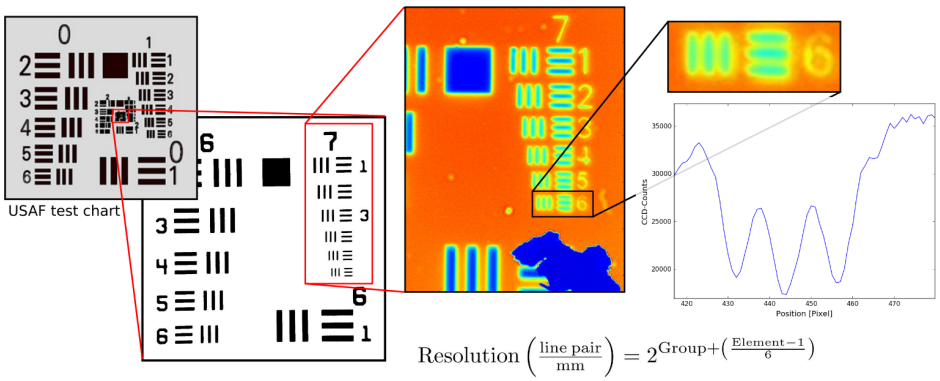

Fig. 3.18.: Evaluation of the miniature lens system using the USAF test chart (magnified by 2.81 by the lens system). All patterns of the smallest group (7) are well resolved. The irregularly shaped dark blue spot below group 7 is the dust particle that was used for focusing the test setup to the last optical surface of the miniature lens system which also serves as the image plane of the lens system.

3.2.2.2 Slit mask - new entrance slit of the spectrograph

To further enhance the stability of the whole spectrograph setup, the adjustable slit was replaced to eliminate an additional source of possible inaccuracies. It was replaced by a custom-designed slit mask that also adjusts the setup to the new simultaneous calibration mode. The final design as well as the overall specifications of the new entrance aperture for all four fibers feeding the spectrograph can be found in Figure 3.19. The length of entrance slits corresponding to both multi-mode fibers is deliberately chosen to be different even though both are fed by optical fibers with identical core diameters to accommodate for the fact that *FOCES* was initially not designed to be served by two optical fibers. By choosing different slit lengths (so-called *decker* width), an overlap of Échelle orders recorded by the spectrograph CCD is avoided, at the same time giving preference to the more precious science light by adjusting the slit length to its maximal dimension[20]. The apertures corresponding to the two mono-mode fibers will not entirely be illuminated by the light guided in that fiber but predominately serve as stray light protection when operating in this mode. To avoid reflections, the mask was coated black on both sides by the

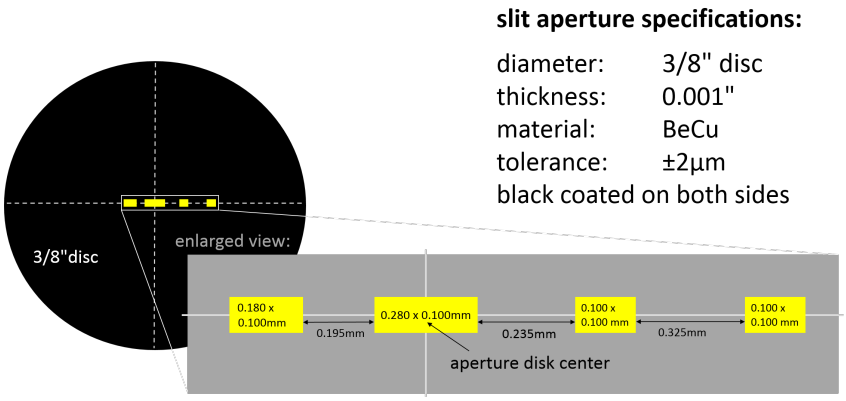

Fig. 3.19.: Dimensions of the slit mask of the new light injection system.

manufacturer *National Aperture Inc.*[21]. Figure 3.20 shows images of the slit mask recorded with the digital microscope ocular CMOS camera DCM-130 whereby all four individual slits were illuminated with a diffuse light source to check particularly the corners for inaccuracies.

[20] The maximal slit length is 280 μm since the 100 μm fiber core is re-imaged with a magnification of 2.8 by the mini-lens system

[21] National Aperture Inc.: 5 Northwestern Drive Salem, NH 03079, USA; webpage:`https://www.nationalaperture.com/`

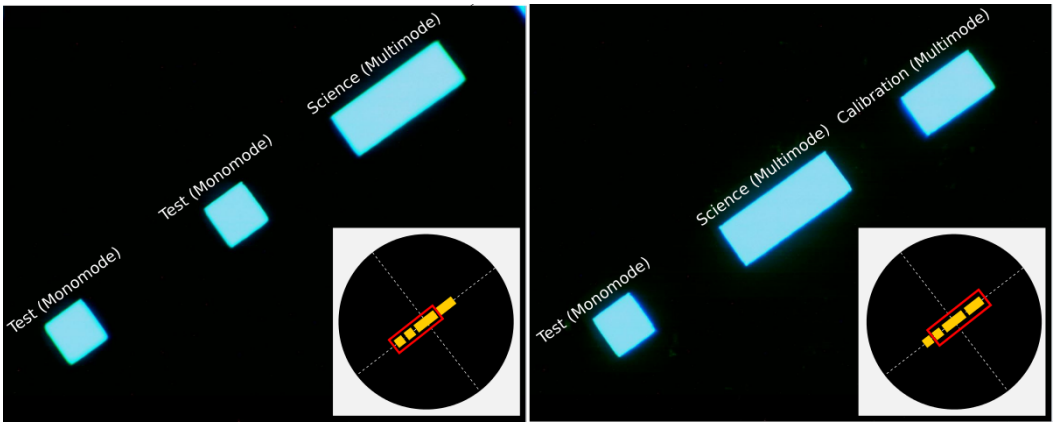

Fig. 3.20.: Microscope images confirming the dimensions of the new slit mask for the 4-fiber slit assembly which serves as entrance aperture of the spectrograph. The microscope field of view is too small to fit all four individual slits, therefore two separate images are shown. The inserts in the lower right corners indicate the section depicted.

3.2.3 Assembly, alignment and performance evaluation of the new light-injection system

This last section describes the procedure of assembling the individual elements of the new light-injection system. Furthermore, a couple of final tests for qualification conducted during and after the assembly are presented.

3.2.3.1 Assembly and alignment of the new light-injection system

The assembly and alignment of the new light injection system for *FOCES* was conducted in a two-step process. First, the 4-fiber-ferrule was joined with the miniature lens system and adjusted for the fibers to be re-imaged exactly on the last optical surface of the lens system via the focusing mechanism which was afterward locked in place. Thereafter, the slit mask was aligned to the magnified image of the four fibers and glued into place. Especially for the second step, it is advantageous to have the light injection system aligned vertically, with the slit mask being mounted from the top, and therefore not adversely affected by gravity. The required precision (in the order of a few μm) is too small for adjustment by the naked eye or with bare hands. Therefore, the same Apogee A340 CCD-Camera equipped with the infinity-corrected, long working distance apochromatic microscope lens, which has already been used for the evaluation of the miniature lens system, was utilized to monitor the procedure from above. As the very first step, before starting the actual assembly and alignment, the CCD camera was focused on the last optical surface

of the miniature lens system and all four fibers were illuminated by diffuse light to be able to accurately adjust the mask position. For manipulating the slit mask on top of the lens system, two jointed arms with attached needle tips were fixed to an outer holding structure while the entire light-injection system is mounted on an XY-stage that itself was fixed on top of a rotational stage at a distance of 40 cm from the optical bench. This was done to allow for a reasonable bending radius of the optical fibers. To prevent scratches to the slit mask during the alignment, the needles were deliberately chosen to be soft and flexible and their tips were dipped in glue which covered them in a slightly sticky film after they were cured, which made the handling of the slit mask easier.

Figure 3.21 illustrates the concept and components of the alignment setup. This way, the entire light-injection system can be positioned and aligned exactly below the slit mask. It is crucial that the centers of the respective optical fiber images are perfectly aligned with the centers of the holes of the slit mask, reducing the illuminated surfaces of the multi-mode fibers to near-perfect rectangles.

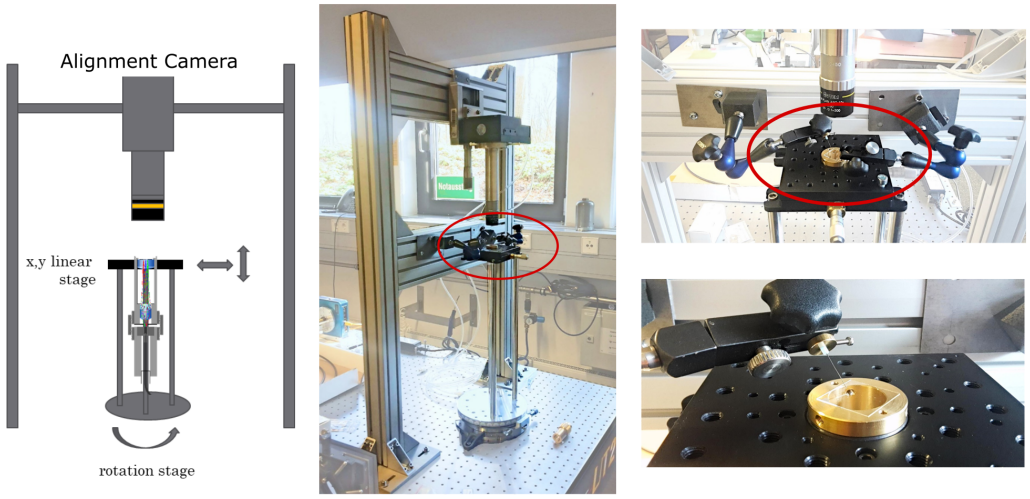

Fig. 3.21.: Setup for aligning the slit mask on top of the miniature lens system with μm precision. The basic principle is illustrated on the left. The optical axis of the light-injection system is mounted vertically, inside an XY stage that is mounted to a rotation stage, which sits 40 cm below. A CCD camera equipped with a microscope lens is used for monitoring the surface of the lens system, onto which the slit mask is being glued from above. The photograph in the center depicts the entire setup. The right side shows two close-up pictures of the jointed arms that hold the slit mask (not in the image) in place while the light-injection system can be manipulated from below.

As the final evaluation Figure 3.22 presents the result of the alignment and gluing process in form of a CCD image taken through the microscope objective described above. The image shows the mono-mode fibers perfectly centered inside their

respective slits and the calibration and science multi-mode fibers abstracted to their individual rectangular profile. The alignment of the slit mask to the fiber images could be determined to be better than 5 μm.

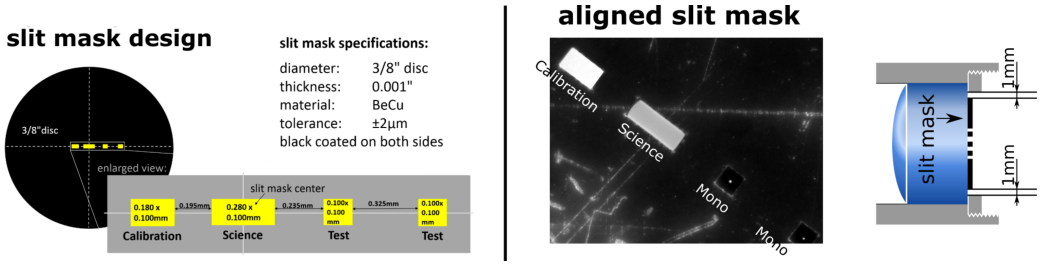

Fig. 3.22.: Schematic drawing of the slit mask (left) to be compared to the microscope image of the slit mask. All four fibers of the light-injection system were illuminated and a schematic drawing of the last lens of the miniature lens system with the slit mask (right).

3.2.3.2 Performance evaluation of the new light-injection system

The following subsections summarize the methods and results of the tests that were conducted to evaluate the quality and performance of the new light-injection system for *FOCES*.

Cross-talk evaluation

Another crucial concern for the design of the 4-fiber assembly was potential cross-talk between the fibers, as they come into relatively close proximity and are only separated by transparent glue. Other causes like scattered light inside the lens system from imperfections or dust on the lenses might cause this effect. Contamination between light sources guided in different fibers is highly disadvantageous and can affect the RV measurements.

To test this cross-talk effect, one fiber at a given time was illuminated by an f/#=3.5 beam thereby evaluating the slit regions of the other fibers on the slit mask for excess CCD counts in the image. These tests did not reveal cross-talk above a level of 0.03% (see also Figure 3.23).

First test results of simultaneously recorded comb spectra

After installing the new light-injection system inside *FOCES* and tuning the temperature and pressure control system, first simultaneous calibration runs could be

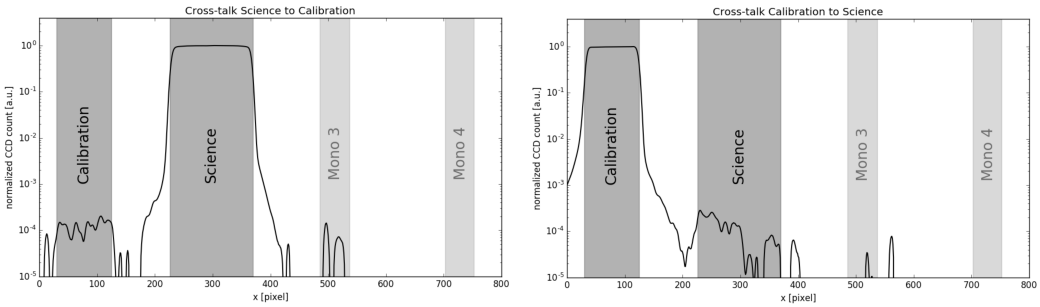

Fig. 3.23.: Cross-talk measurement of the science fiber (left) and the calibration fiber (right) including their neighboring fibers. Both plots show histograms of CCD counts, resulting from projecting the CCD images onto the direction of the slit. No cross-talk above a level of 0.03% was found.

performed, utilizing the science and calibration fiber at the same time. These tests serve as a proof of principle that remaining radial velocity (RV) drifts, which were not entirely eliminated by all the other efforts, can be corrected for by simultaneous corrections using LFC light fed through the calibration fiber. The measurement presented is the result of a 24 h test run recorded in summer 2019, with 2 min exposures taken every 5 minutes and light of the astro comb guided into both fibers. During the whole test run, the fiber shaker was dynamically scrambling both fibers. The data was reduced using *GAMSE* (see Chapter 5.1) and examined for RV drifts by Dr. Liang Wang. Figure 3.24 shows that both channels follow the same overall trend. By correcting the science channel with the information extracted from the calibration fiber, only fluctuations with an root mean square (RMS) of about 2 m/s remain. The situation seems to even improve further after some initial oscillations. From these data, reaching an RV precision on the order of ∼1-4 m/s with *FOCES* seems feasible.

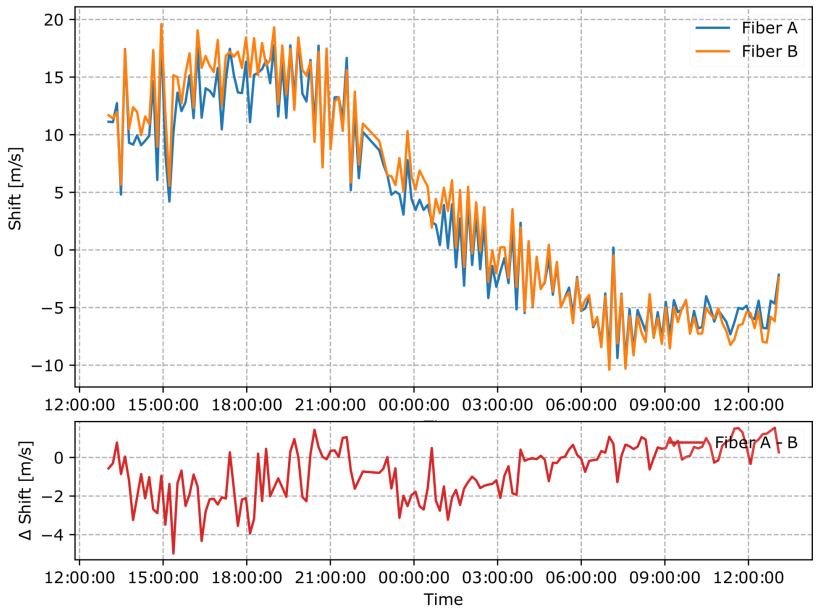

Fig. 3.24.: 24 h measurement with light from the frequency comb guided in both, the calibration and science fiber of the new light injection system. This measurement was conducted with the light-injection system already installed inside *FOCES*. The top panel shows the RV drift of both individual channels. The bottom panel shows the residual fluctuations after correcting channel A with the drift of channel B.

3.3 Fiber connections and fiber scramblers

Besides all the positive possibilities optical fibers provide, they can also introduce non-negligible adverse effects, which can prohibit the m/s measurement goal on the hunt for exoplanets. To reduce or even eliminate these effects, several different approaches were combined. As introduced in Section 2.3.4, there are three main effects which interfere with the science goals of *FOCES*: light loss due to too high FRD and shifts in the wavelength calibration due to fiber noise or photometric fiber shift. For the selection and the assembly of the fiber connection, special care was taken to avoid or at least minimize these problems.

Fiber connections feeding *FOCES*

A listing of all fibers providing possible ways to feed light into *FOCES* can be found in Table 3.4, while Figure 3.25 illustrates all fiber connections and depicts the pathways light can travel. For all fiber connections which transport starlight, special emphasis was put on the selection of fiber types with low intrinsic FRD. All starlight guiding fibers are custom ordered fiber assemblies utilizing the fiber glue *EPO-TEK 301-2*,

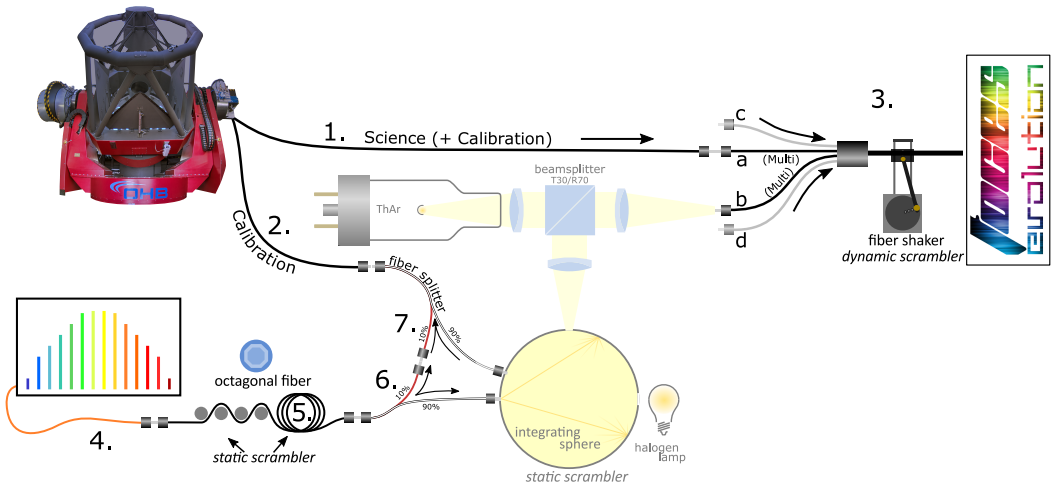

Fig. 3.25.: Illustration of all fiber connections serving *FOCES*. To better visualize the light pick-up at the telescope Figure 3.26 depicts a detailed view of the *FOCES* pick-up module (called *FOCES Kuchenstück*).

slowly cured at 24°C over a time span of 48 h to prevent stress during the curing process.

Light pick-up at telescope and guiding

Figure 3.26 (left) provides an overview of the location of three main instruments on the 2.1 m Fraunhofer telescope. As indicated share the instruments 3KK and *FOCES* one common Nasmyth port where the light of the telescope can be redirected to the *FOCES* pick-up module (designed and build by Florian Schlagintweit (Schlagintweit, 2015)) by the means of the M4 pick-off mirror mounted on a manually operated sliding stage (right panel). The light of the telescope is thereby focused onto a tilted pinhole mirror allowing the majority of the star light to be passed onto fiber path *1.-3a.* feeding FOCES (see also Figure 3.27). Behind the tilted pinhole mirror a small lens serves as re-imaging and f-ratio adoption (f/#=7.8 to approximately 4) to focus light onto transport fiber *1.* (yellow light path in Figure 3.26, right). The guiding itself is executed on the parts of the Moffat profile (ring-like structure) which is not passed through the pinhole mirror and subsequently guided to be fed into FOCES. This is enabled by a dedicated guiding camera[22] which is mounted and focused to face the pinhole mirror (blue light path in Figure 3.26, left). In order to enable precise pinhole guiding even when observing at different elevation angles,

[21] The whole pick-up module was designed as temporary solution and will soon be replaced by a new light distribution setup called 'Erster Ring' which will provide much higher long-term stability especially for the calibration light path which right now suffers from instabilities in the manually operated folding mirror.

[22] *FLI* Hyperion HPx285 interline CCD equipped with a telecentric lens *EHD* EHD50TC (f=50mm).

Tab. 3.4.: Listing of all fiber connections enabling light input into *FOCES*. The shaded gray area indicates fibers inside the 4-fiber assembly.

no.	fiber name (manufacturer)	type	core ⌀	purpose	connector
1.	FBP100120140 (*Polymicro*)	multi	100μm	connection fiber telescope - spectograph	FC/PC
2.	FPB100120140 (*Polymicro*)	multi	100μm	connection fiber calibration unit - telescope	FC/PC
3.	4-fiber assembly				
a	FBP100120140 (*Polymicro*)	multi	100μm	**science fiber**	FC/PC
b	FBP100120140 (*Polymicro*)	multi	100μm	**calibration fiber**	FC/PC
c	S405-XP (*Thorlabs*)	mono	3μm	test fiber	FCPC
d	S405-XP (*Thorlabs*)	mono	3μm	test fiber	FCPC
4.	FG105LCA (*Thorlabs*)	multi	105μm	transport fiber	FC/APC
5.	OCT WF 67/125 (*CeramOptec*)	multi	67μm	static scrambler	FC/PC
6.	TM105R2F1B (*Thorlabs*)	multi	105μm	fiber splitter (comb/comb)	FC/PC
7.	TM105R2F1B (*Thorlabs*)	multi	105μm	fiber combiner (comb/flat)	FC/PC

the camera is equipped with a red-band filter (*Baader Planetarium*: 2459422R), which reduces the effects of atmospheric dispersion. In addition, the pick-up unit offers the option to re-image calibration light guided in fiber *2.* from the basement to the telescope to be injected into the science channel (fiber 1.-3a.) for calibration purposes (red light path in Figure 3.26, right).

Fiber scrambling options

The various fiber paths at the Wendelstein Observatory feeding light into *FOCES* provide different static and dynamic scrambling options, adapted to their different needs. The fiber path *1.-3a.* is actively scrambled (0.3-0.5Hz), utilizing an in-house build fiber shaker designed during my master thesis (Kellermann, 2015) and further optimized during this project. Fiber *1.* will be upgraded in the near future to an octagonal fiber offering additional passive scrambling properties to further prevent photometric shifts such as for example guiding errors and/or clouds passing the FoV of the Fraunhofer telescope.

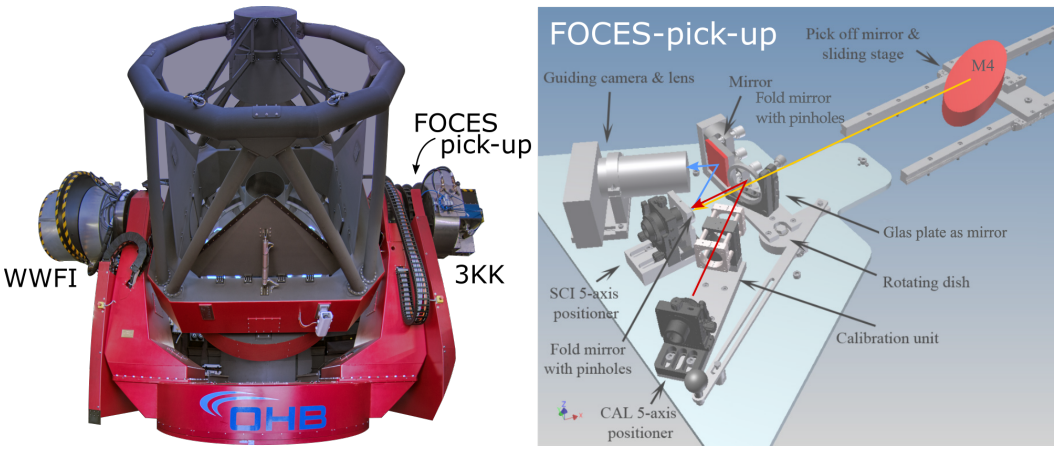

Fig. 3.26.: The left panel provides an overview of the location of the instruments on the 2.1 m Fraunhofer telescope. The 3KK and *FOCES* share one common Nasmyth port where the light of the telescope can be redirected to the *FOCES* pick-up module by the means of a pick-off mirror (M4) mounted on a manually operated sliding stage (right panel). On the pick-up module three different light paths are available indicated be the yellow, blue and red arrows. The yellow arrow illustrated the path of the light guided from the telescope via the M4 mirror to the pinhole via a re-imaging optic into *fiber 1.*. Highlighted in blue the light path to the guiding camera used for pinhole guiding is shown. In addition, the pick-up module offers the option to re-image calibration light guided in fiber *2.* from the basement to the telescope to be injected into the science channel for calibration purposes (red light path). Image on the left kindly provided by Dr. Matthias Kluge. Image on the right taken from Schlagintweit (2015) and modified by me.

For comb light, there are two possibilities to be guided into *FOCES*: either via the fiber path option I (*4.-5.-6.-7.-2.-telescope* FOCES *module: calibration imaging optics-1.-3a.*) or via option II (*4.-5.-6.-integration sphere-imaging optics-3b.*). Starting inside the comb itself, the comb light is focused using free-beam optics onto the fiber entrance of fiber *4.*. At this location, the beam diameter is only 3-5 μm entering a 105μm multi-mode fiber. Temperature changes in the comb unit (due to temperature changes in the basement), transfer to the mounting of the free-beam optics inside the comb and trigger the beam to undergo small meandering motions on the entrance surface of fiber *4.*, leading to photometric shifts when traveling through pathway option I. To avoid this behavior and to prevent temperature drifts to be reflected in calibration data, two passive scrambling measures were installed. The light is guided through an octagonal fiber (acting as the first passive scrambler), which is tightly woven through five rods (2.5 cm apart) by which an even distribution of the fiber modes over the whole core diameter of the fiber can be achieved at all times. This is also relevant as the light is subsequently guided through fiber splitter *6.*, which is sensitive to the mode pattern inside the fiber. The splitting ratio of a fiber splitter depends on the evanescent fields that transfer energy between the fibers.

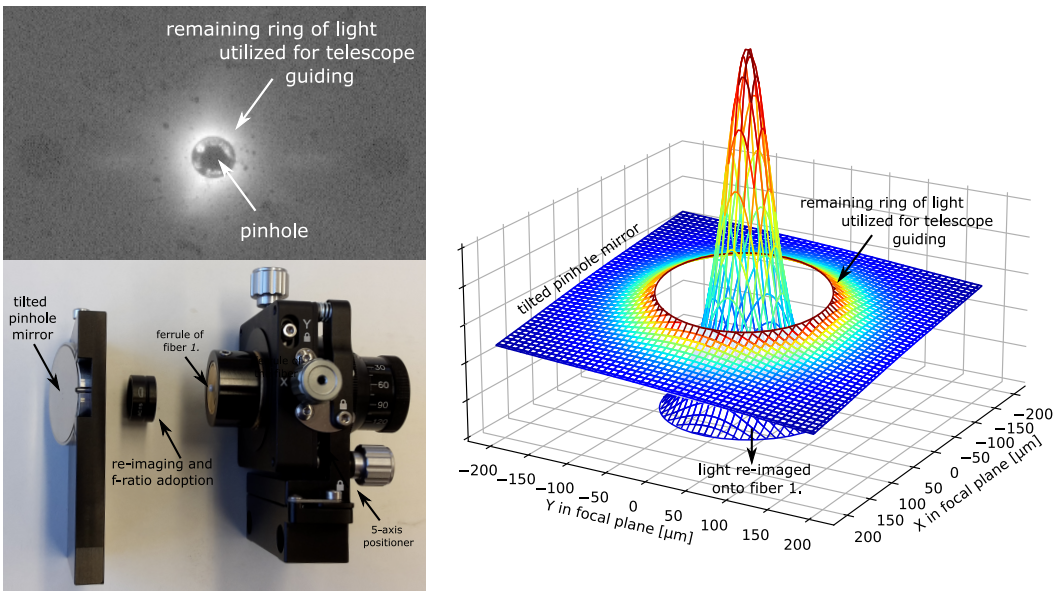

Fig. 3.27.: Upper left panel: Image of the pinhole mirror take by the guiding camera of *FOCES*. In this image are star is focused on the pinhole and the reaming ring of light is utilized to guide the telescope. The penumbra-like structure (double ring structure) of the pinhole is a remnant of the manufacturing process by means of wire eroding. The lower left panel depicts in an exploded view like manner the tilted pinhole mirror, the re-imaging and f-ratio adoption lens and the 5-axis positioner folding the fiber. On the right side the operating principle of the pinhole guiding is illustrated on a simulated 2D Moffat profile.

A varying mode distribution in the fiber means varying evanescent field strengths and therefore varying splitting ratios of the fiber splitter. This uniforming setup has the additional advantage of ensuring a consistent light pickup at the fiber splitter to provide a coherent splitting ratio to both fiber outputs of fiber *6*. at all times. Option II furthermore offers additional passive scrambling, since the light is guided through an integrating sphere, therefore eliminating/equalizing all possible adverse photometric shifts. Directly before entering the spectrograph, fiber *3b*. is finally dynamically scrambled by the aforementioned fiber shaker, since fiber *3a*. and *3b*. are installed on the same fiber shaker.

3.4 Calibration Unit

One of the most important parts of *FOCES* is not the spectrograph itself or parts of it, but its calibration unit, which provides the light for different calibration purposes. Without this, all the previous efforts may to some extend be pointless as sufficient stability cannot be maintained long term without precise calibration.

Since it is of such crucial importance, this chapter will provide a short overview of essential components and their application in the context of *FOCES*. The overall goal of this assembly was to combine all necessary light sources preferably without, but at least with as few as possible, moving elements. In addition, the option to easily incorporate new calibration light sources for tests was strongly favored. As was introduced before, one of the new options for observations with *FOCES* is the double-fiber-mode by which light from a wavelength calibration light source is directly recorded alongside the science light of the star. To enable this type of observation, it is necessary to finely adapt the attenuation of the used light sources to avoid overexposure for faint star observations.

Figure 3.28 illustrates the design and layout of the different components and the necessary fiber connections between telescope, calibration unit and *FOCES*. The unit itself houses light sources for different types of calibration needs, specifically for flat fielding and wavelength calibration, including combining optics. Traditionally, flat fielding is understood as the correction process by which the pixel-to-pixel-variations of a CCD-sensor can be measured and during data reduction be eliminated. For this purpose, usually flat images are recorded using a white light source (incandescent lamp) without any prominent spectral features and by illuminating the CCD as homogeneously as possible. Since light can only enter *FOCES* through its entrance aperture, it is not possible to homogeneously illuminate the CCD-sensor. The flat fielding, therefore, serves two slightly different purposes in *FOCES*, namely order-tracing and a novel and specifically developed for spectrographs type of flat fielding (developed by Dr. Liang Wang), which is described in detail in Section 5.1.2.

There are a variety of different options available for the wavelength calibration of spectrographs of which two are implemented for *FOCES* observations: either a hollow cathode lamp or an astro frequency comb. As already established in the general overview of wavelength calibration light sources, the first offers a relatively cheap solution with the downside of sparsely distributed emission lines with enormous brightness differences and a long-term stability of only meter per second in the best possible cases[23] (Pepe et al., 2014).The latter on the other hand, while far more costly and high-maintenance, provides a densely sampled emission-line spectrum of equal brightness with absolute wavelengths attributed to every line which is even long-term stable on the centimeter per second level.

[23]This is accomplished by calibrating the drifts of the lamps that are used during operation by means of a dedicated master lamp that serves as reference and is used only rarely for this purpose.

These calibration options are implemented as three different wavelength calibration light sources, namely:

- for the long-term stable and high precision calibration
  - *an astro frequency comb*,
- for the short-term stable and lower precision calibration
  - *two hollow-cathode lamps*[24],
    one thorium-argon-lamp (ThAr-lamp) and one uranium-neon-lamp (UNe-lamp).

When choosing the high stability option for observation (the frequency comb) it is still necessary to administer at least some type of low precision calibration with ThAr or UNe light in order to obtain a coarse preliminary wavelength calibration which serves as the starting point for the refined comb wavelength calibration. Figure 3.28 depicts a sketch of the calibration unit with all its optical components and fiber connections. The aperture at the output of the calibration unit ensures an input beam for the calibration fiber *3b.* of f/#≈4 to match the light beam guided in the science fiber.

The two brightest light sources, comb and flat lamp, are combined via an integration sphere while the others - the hollow cathode lamps - are combined through a beam splitter or a manually insertable mirror. The integration sphere offers the additional option to easily add guest light sources, if necessary, and acts as pick-up for the flat light for the science channel via the fiber path *(7.-2.-telescope* FOCES *module: calibration imaging optics-1.-3a.)*, depicted in Figure 3.28. For the high precision mode (simultaneous wavelength calibration mode) the light of the calibration source needs to be adjusted accordingly to avoid overexposure while taking the simultaneous calibration. This can be done by utilizing one or two concatenated neutral reflective density filters housed in two automated filter wheels (*Thorlabs*: FW212C). The individual optical density of the filters can be found in Table 3.5.

[24] *Photron* P858A (ThAr) and P863 (UNe) powered by the remote controllable hollow cathode power supply P209.

Tab. 3.5.: Listing of the reflective neutral density filters installed in the calibration unit of *FOCES* to attenuate the calibration light.

comb - filter wheel	
pos.	throughput
1	40%
2	32%
3	25%
4	10%
5	5%
6	1.0%
7	0.1%
8	0.01%
9	blocked
10	empty
11	empty
12	empty

ThAr - filter wheel	
pos.	throughput
1	10%
2	0.1%
3	0.4%
4	0.2%
5	0.1%
6	empty

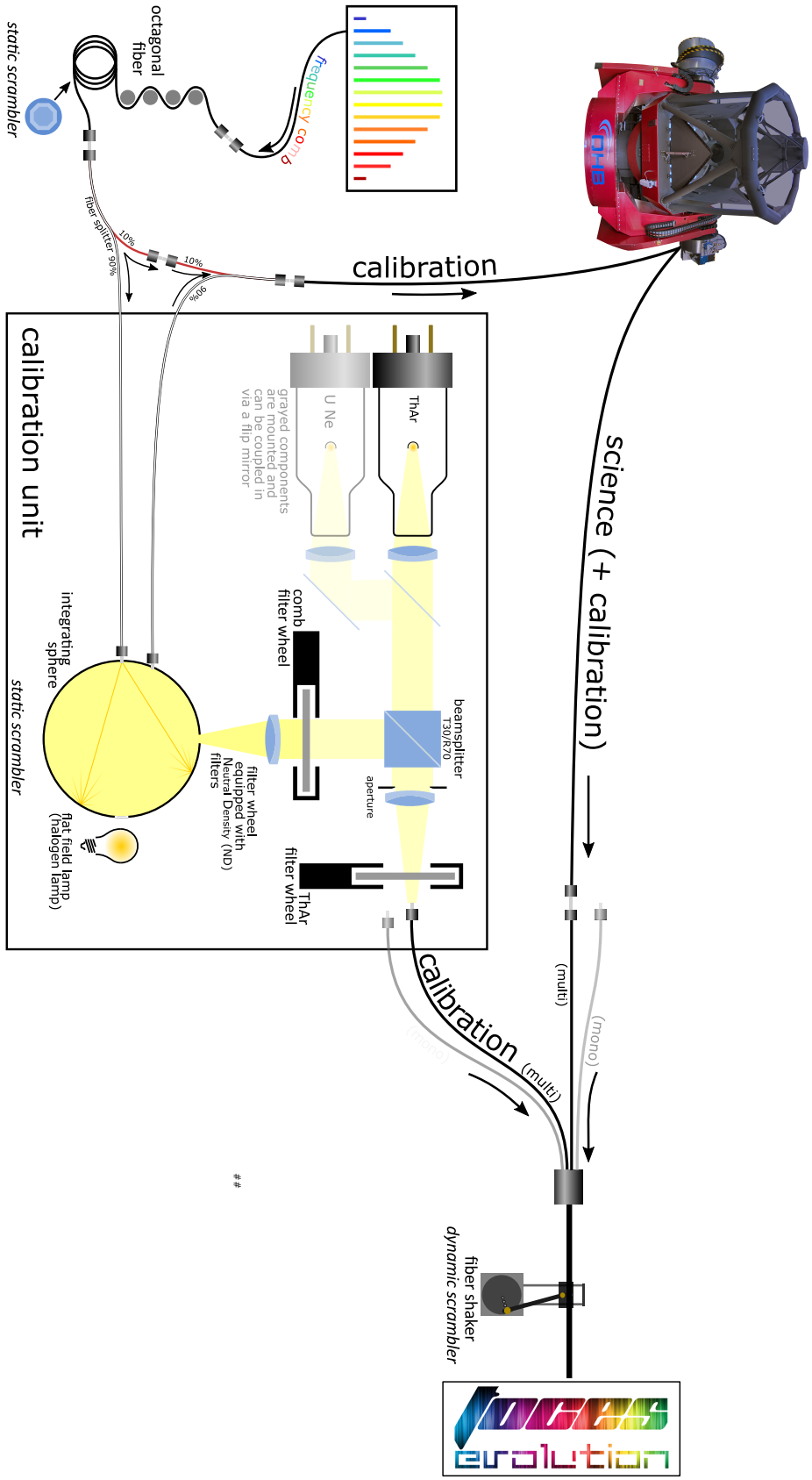

Fig. 3.28.: Illustration of the calibration unit and its fiber connections

3.5 Temperature and pressure stabilization

Precisely controlling the pressure and temperature of the environment *FOCES* is operated in is crucial for even getting close to the m/s regime in terms of radial velocity accuracy. As it has already been outlined in the previous sections, an RV resolution of 1 m/s corresponds to about $1/2000^{\text{th}}$ of a single CCD pixel in spatial terms in the image plane. Small changes of any of the optomechanical components due to thermal expansion can lead to spectral shifts much more severe than that. Changes in pressure can in some cases lead to mechanical deformations while temperature changes also directly affect the refractive index of the air in between optical components.

The aspired precision in terms of temperature and pressure stability are motivated in detail in Grupp et al. (2009). With applied safety margins to account for imperfect modeling this leads to the following requirements:

- Δ **temperature** $< 0.01\,\mathrm{K}$,
- Δ **pressure** $< 0.1\,\mathrm{hPa}$.

The following paragraphs describe the applied design and implemented approaches to reach these goals.

Temperature stabilization

The key aspect of the pressure and temperature stabilization concept of *FOCES* is a large cylindrical 3.2 m long and 1.75 m wide insulated and pressurized tank design by Dr. Anna Brucalassi and Florian Lang-Bardl[25] (Figure 3.29).

For the temperature stabilization, a three-layer approach was chosen whereby every shell should roughly be 10 times more stable compared to its predecessor. In this concept, the temperature of the room in which *FOCES* is operated already represents the first shell of the temperature-controlled environment. It is followed by the *FOCES* tank itself in which a wooden insulated box is nested, housing the optical components of the spectrograph. Figure 3.30 illustrates the multi-layer approach in the basement of the Wendelstein Observatory where *FOCES* is operated.

The *FOCES* room itself is housed in the basement of the observatory beneath the terrace and one wall directly faces the environment. Due to the exposed position, temperature changes of 50°K and more over the course of a year are not uncommon,

[25] The full evolution and test on the tank are published in the following proceedings: Grupp et al. (2010), Grupp et al. (2011), Brucalassi et al. (2012), Brucalassi et al. (2013), Brucalassi et al. (2016), and Fahrenschon et al. (2020)

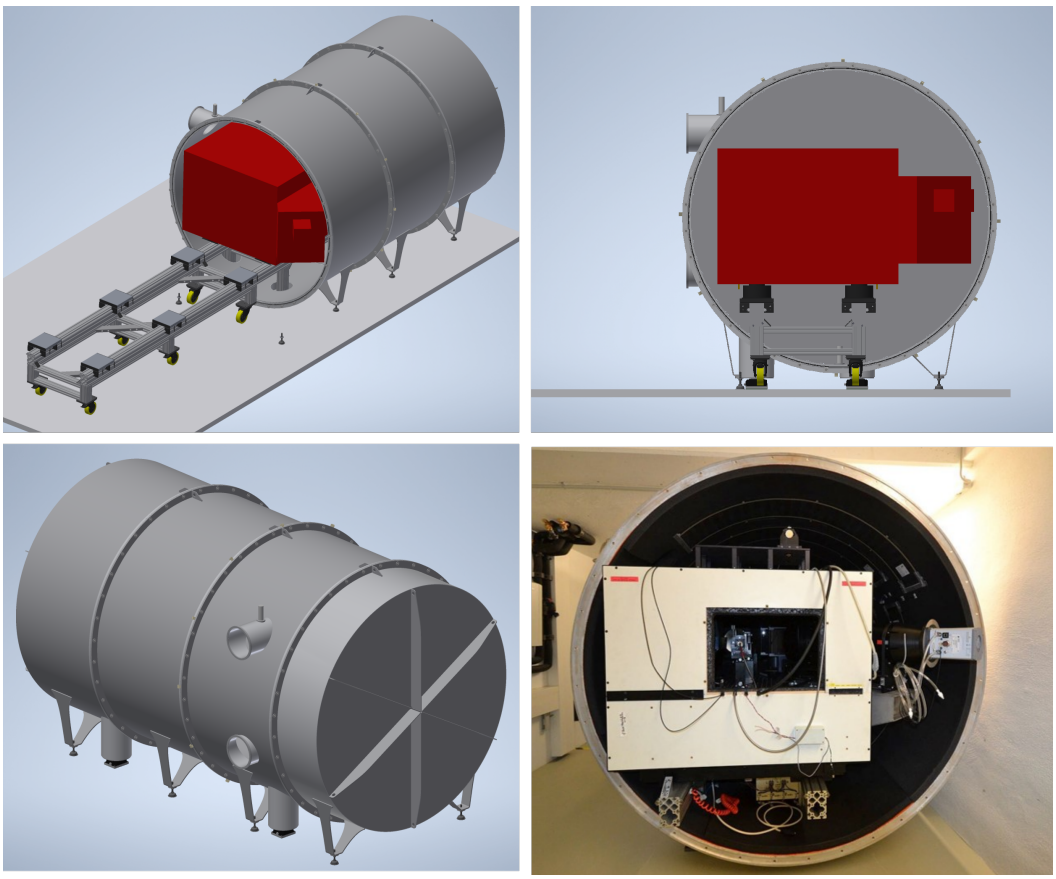

Fig. 3.29.: 3d CAD drawings of the overpressure vessel of *FOCES*. The red indicated areas outline the volume of the innermost temperature shell inside the wooden enclosure housing the optical components of *FOCES*. The bottom left image depicts both flanges for the cable throughput sealed via the *VARIOZELL* VARIOSOLID rubber modules. On the bottom right, a photograph of the open tank with *FOCES* already installed inside its wooden enclosure is shown. For a better view of the optical components, the front entrance to the wooden box was opened. In the upper half of the tank, some of the 14 heating mats evenly lining the whole interior can be found. 3d CAD drawings kindly provided by Florian Lang-Bardl.

which poses challenges to the temperature control of the room. The upgraded air-condition (AC) (*Panasonic*: CS-Z50TKEA) is able to achieve short-term temperature stabilization of 1.0-1.5 K over the course of a day-night cycle (with short term stability over a half-hour cooling cycle of 0.5-0.8 K). Slow temperature drifts of less than 5°K between summer and winter can be countered with additional heating (heat load enhancer). To avoid strong gradients inside the room (temperature differences of more than 5°K could be measured), the new AC control is equipped with a ventilation system to quickly distribute the air in the tightly packed *FOCES* room.

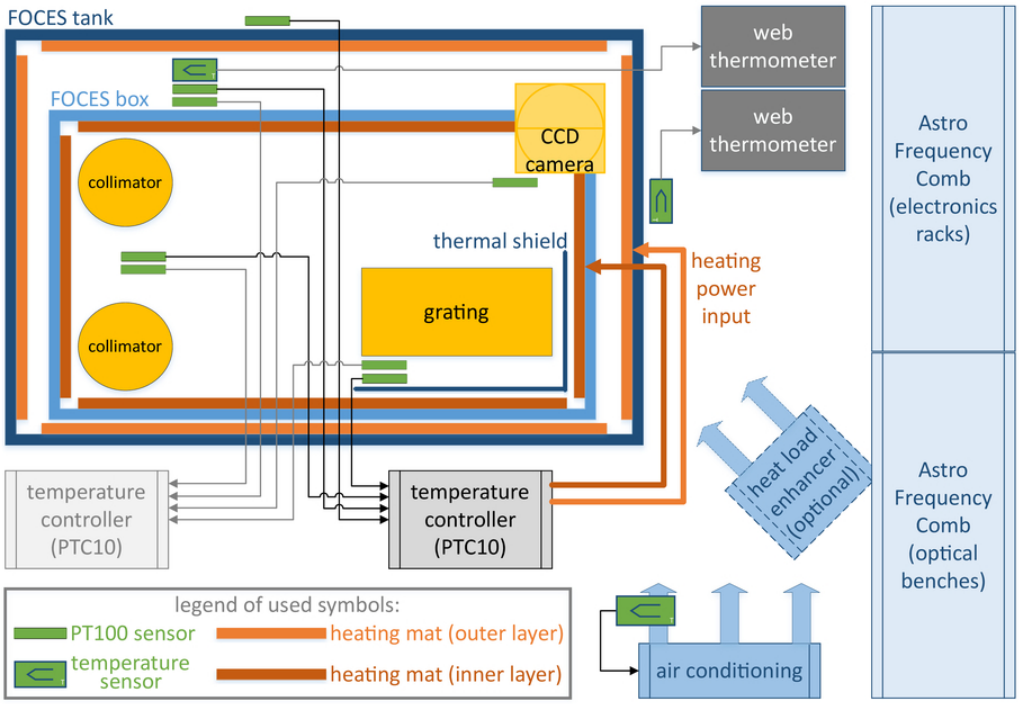

Fig. 3.30.: Schematic drawing of the temperature control system of *FOCES*. The blue rectangles represent the outer (dark blue) and inner shell (light blue), the corresponding heating mats for the temperature control are indicated in orange. Temperature sensors and their positions are shown in green. The L-shaped structure next to the grating depicts the thermal shield utilized to protect the grating from immediate irradiation from the nearby heating mats. The outermost layer of the heating concept is the room itself containing all electronics as possible heat sources (e.g. exhaust heat from the LFC) plus additional heating and air conditioning to counteract and control the room's temperature. Drawing kindly provided by Vanessa Fahrenschon.

Both inner shells (tank and wooden box) follow a slightly different approach. Each layer is equipped with insulation which itself provides the surface for a dedicated number of heating mats. No cooling option is installed inside the tank. In order to nevertheless be able to actively stabilize these shells, a temperature difference of around 1-2°K is aimed for. Figure 3.31 illustrates the different insulation approaches for the tank and the wooden box. The inside of the pressure vessel is lined with 3 cm of black *ARMAFLEX*™, followed by a layer of 14 evenly distributed electric heating mats that can be regulated via an external PID controller (proportional–integral–derivative controller). The heating mats are glued to the insulation material and additionally secured by drywall dowels which were screwed into the *ARMAFLEX*™ layer (Figure 3.31, left side). Opening the vessel for maintenance purposes is not foreseen due to the long-term science goals of *FOCES*. The drywall dowels are therefore installed to prevent the heating foils from detaching and falling

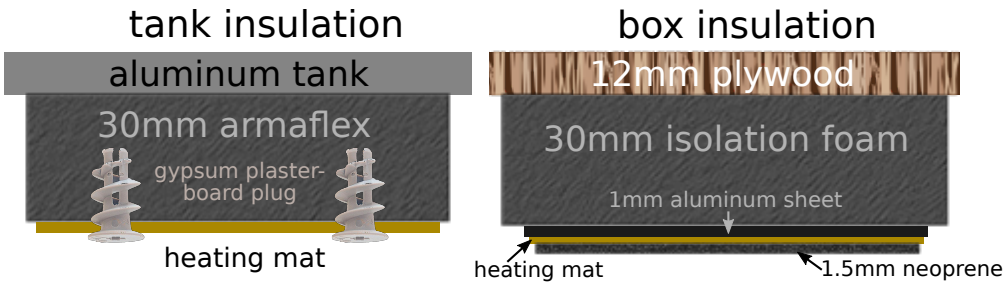

Fig. 3.31.: Thermal insulation of the multi-layer insulation approach of *FOCES*. Left: layers of the tank, from outside to inside: aluminum hull of the overpressure vessel, *ARMAFLEX*™, heating mats; Right: layers of the wooden box, from outside to inside: plywood board, insulation foam, aluminum foil, heating mats, neoprene.

onto the wooden spectrograph enclosure in case of glue failure which might occur over time due to the low humidity in the vessel (<5 %).

The inner layer that surrounds the actual optical components of *FOCES* consists of a wooden box, which is lined with a 3 cm layer of Styrofoam. Inside, 11 heating tiles with a total power of 50 W which can be adjusted via an external PID control loop are installed. These inner heating mats are in close proximity (< 10 cm) of the optical components and their mechanical structure. To ensure an as even as possible heat distribution, the heating mats are mounted on 1 mm aluminum sheets and covered in a 1.5 mm thick layer of neoprene to prevent direct radiative heating of the optical components and heating hot-spots (Figure 3.31, right side). The angle of the Échelle grating can be adjusted via a micrometer screw. This design has the adverse effect that the micrometer screw can act as a thermometer, translating temperature changes to changes in the grating angle. To inhibit this behavior, a protective heat shield was installed. The heat shield consists of an aluminum frame structure on which on three sides a black coated Aluminum foil is mounted using magnet strips. The outer side of the heat shield is covered in multiple layers of Mylar film to prevent direct radiative heat input to the Échelle grating and its mechanics.

Pressure stabilization

In terms of pressure stabilization, the best possible option to avoid influence due to temperature changes within an Échelle spectrograph would be to operate the entire instrument in vacuum. However, this would require a vacuum vessel of considerable volume (⌀ 1.75 x 3.2 m) and would put special constraints on all the utilized components of the spectrograph. Since almost all components of *FOCES* stem from an earlier phase of operation during which the instrument was not pressure controlled,

they are not at all suited for operation in vacuum. Therefore, an overpressure approach was chosen by which *FOCES* is operated inside an overpressure vessel, which is operated at a PID loop stabilized pressure of 833 hPa. This setpoint was chosen as it represents an upper limit to naturally occurring ambient pressures, exceeded only once within 12 years. An overpressure as low as possible is desirable for several reasons, among which are the lower consumption of pressurized air[26] as well as the reduced structural loads on the vessel. The pressurized air is produced by a compressor within the observatory, filtered[27] and temperature stabilized before entering the *FOCES* tank. The air is released into the tank through an electronically controlled valve (coupled to the PID controller unit) and into the vessel through a two-layer sound-suppression system, one professional suppressor and a canister with holes drilled into the walls to further disperse the air.
Besides this, the pressurized air is flushing all three Fabry-Pérot cavities of the LFC to prevent humidity condensation on the cavity mirrors which would lead to significant degradation of the LFC performance and the frequent need of manufacturer maintenance.

Water cooling

The CCD camera of *FOCES* is kept at -80°C[28], which is achieved by a 5-stage Peltier cooling inside the camera resulting in dark rates of less than $0.5 e^-$/h/pixel. To eliminate excess heat and to avoid the vibrations of an air cooling via ventilators, a water cooling system was installed. This so-called liquid-to-liquid water-cooling system (*Solid State*: ThermoCube)[29] circulates the temperature-controlled cooling liquid (*innovatek*: Protect IP)[30] to enter the camera at a temperature of 16°C to avoid condensation on all water pipes. The cooling liquid returning from *FOCES* is subsequently circulated through a heat exchanger to passively pre-heat the pressurized air input before it is passed through the optical benches of the LFC and the small auxiliary spectrograph, *FOX*, to likewise temperature stabilize them. The LFC racks are thereby purely passively stabilized.

[26] Pressurized air is directly produced at the observatory but has to be shared with all other consumers like for example the telescope's brakes and is therefore not indefinitely available.

[27] The filtering process is performed via a four step concatenated filter battery: an activated carbon filter to eliminate possible oil contamination originating from the compressor, followed by three filters with a filter grain size of 5 μm, 1 μm, 0.01 μm.

[28] Temperatures as low as -100°C are technically possible, but traded for a longer lifetime of the instrument and an expectedly higher precision when operating the cooling system, not at the absolute limit of its capability.

[29] *Solid State* ThermoCube: `https://www.sscooling.com/product/thermocube-liquid-to-liquid/`

[30] The cooling liquid acts thereby as buffer solution in order to avoid corrosion on the different materials introduced into the cooling circle.

All input tubes guiding water or air into the pressure vessel are insulated to prevent condensation and to minimize stress to the PID loops by pre-stabilizing the tank intake.

Temperature and pressure control units

The temperature is monitored via *Stanford Research Systems* PTC10 controllers with a precision of approximately 2 mK utilizing eight high-resolution PT100 (Class AA/10) sensors. The location of these sensors can be found in Figure 3.31. The temperature is read via two PTC10 controllers whereby one is dedicated to actively control the temperature and the other serves as monitoring unit. In case of a failure in the control unit the monitoring unit can serve as backup but needs to be manually started to do so. In addition, four inline temperature sensors monitor the input air and the in- and output temperature of the cooling liquid. The temperature controllers are decoupled from the power grid by an isolation transformer (*polyMIT*: 1700e) to prevent power spikes to jeopardize the temperature stability. Two web-thermo-hygrobarometers (*Wiesemann & Theis*: 57713) continuously track the humidity in the room and the *FOCES* tank. The overpressure in the vessel is stabilized via a PID loop controlled valve (*Bronkhorst*: EL-FLOW F-201AV-50K-RAD-33-V) while two high precision pressure sensors monitor the pressure in the tank (Control: *GE* DPI142[31], Monitor: *MENSOR* CPG2500). To prevent damage and as safety features, over- and underpressure valves were installed which mechanically open once predefined thresholds are surpassed.

An in-depth description of the whole setup including all liquid and air connections and a detailed overview of the PID-loop tuning process can be found in Fahrenschon (2021).

[31] Soon to be replaced by a *GE* Pace1000.

Part III

Analysis Software

4 Statistics, fitting tools and error estimation

> *If you thought that science was certain — well, that is just an error on your part.*
>
> — **Richard P. Feynman**

The scientific results presented in this work and the underlying data analysis software, which has been developed to determine those results, rely heavily on a variety of statistical tools and minimization techniques. The most relevant mathematical concepts are summarized in this chapter.

First, the two fundamental frameworks of statistical inference are introduced, the frequentist approach and the Bayesian approach. Then, the concepts for parameter and error estimation for both frameworks are described, alongside the numerical tools required for the process.

4.1 Frequentist vs. Bayesian approach to statistics

One of the most common problems throughout the evaluation of astronomical data, and in quantitative science in general, is adjusting model parameters to fit the measurements. In such a situation one typically defines a so-called figure-of-merit (or merit function) which quantifies the agreement between model and data. Then, usually a numeric optimization algorithm is used in order to determine these optimal parameters. Subsequently, the uncertainties associated with those optimal parameters need to be quantified. Another aspect worth considering at this point is the overall plausibility of the measurement in question, given the model.

Generally, there are two different approaches, or philosophies, regarding probability and statistics and their role in scientific inference. These two are commonly referred to as the frequentist school and the Bayesian school of statistics. Those concepts will be explained here briefly as the differences between them have some implications regarding the terminology and the type of questions asked and answered by the method.

Frequentist school of statistics

The key concept of the frequentist approach is to regard the model and its parameters as constants, something that is fixed and given by nature, although not known with certainty to the observer. The observed data, on the other hand, is the outcome of a random process, caused by measurement errors or more fundamental randomness, e.g. quantum processes. Those data can now be used in order to compute certain estimates for the values of the model parameters. The figure-of-merit function that is used for this estimate, should ideally be formulated in a way, so it converges towards the true value of the parameters (best-fit parameters) in the limit of an infinitely large data set as does for example the likelihood function (see Section 4.2.1.2). In addition, it is important to state a region of uncertainty, in order to present the quality of the best-fit parameters. The frequentist approach to this problem is to define a confidence interval for the best-fit parameters that is designed in such a way that it would contain the parameter estimate in, for example, 68.3%[1] of the cases, when repeating the experiment infinite time, assuming that the estimated parameter value is the true value.

Bayesian school of statistics

The Bayesian view on statistical inference expresses the limited knowledge about a certain parameter value as probability distribution or probability density function (PDF). The data on the other hand is the unchangeable result of a measurement that may have underlying randomness, but stand as they are. The goal of the Bayesian method of statistical inference is now to use the fixed outcome of the measurement in order to update the PDF that assigns a (posterior) probability to each possible parameter value. Uncertainty intervals given in this framework are simply ranges that when integrating the PDF yield a certain probability, like the 68.3% of the previous example. An established convention is to state the median value of the posterior distribution (the value that splits the distribution into two equally likely intervals) as an estimator for the parameters. The uncertainty is then expressed in terms of intervals left and right of the median with equal integral probability, which sums up, for example, to 68.3% integral probability.

In the scope of this thesis, the main focus regarding these two concepts is on determining optimal parameters and providing reasonable and justified uncertainty intervals for them. Therefore, these aspects will be further explored in the next sections.

[1] Typically confidence intervals are expressed in terms of multiples of sigma (and the corresponding containment fraction) of a one-dimensional Gaussian function: $1\sigma \approx 68.3\%$, $2\sigma \approx 95.5\%$, $3\sigma \approx 99.7\%$

4.2 Frequentist tools for parameter estimation

In order to find optimal parameter values for a model to describe a measurement, a so-called estimator is used. Estimators are rules of computation that lead to parameter values that have a high chance of reproducing the outcome of the measurement. In some cases, those estimators can be computed purely analytically, as is the case with linear regression. Most practical applications however involve numeric optimization algorithms.

4.2.1 Figure-of-merit

Both approaches - the frequentist and the Bayesian - rely on methods that define merit functions to determine the best parameter values. Examples for such estimators are the parameters that minimize the sum of least squares of the residuals, maximize the likelihood or minimize χ^2, which is a special case of both of the two other estimators[2]. The latter two are among the most common parameter estimators used in astronomy. As they are also relevant in the scope of this work, they are briefly introduced in the following.

4.2.1.1 χ^2

A commonly used estimator for fitting a theoretical model to measured data points (in order to determine the values of best-fit parameters) in astronomy and other fields of quantitative science is χ^2 . This estimator can in fact be seen as a special case within the more general concept of likelihood maximization, which will be covered later. χ^2 is defined as

$$\chi^2 = \sum_{i=1}^{N} \frac{(y_i - f(x_i, \boldsymbol{\theta}))^2}{\sigma_i^2} \,, \tag{4.1}$$

with y_i being the i$^{\text{th}}$ measurement with error σ_i, and $f(x_i, \boldsymbol{\theta})$ the model prediction at the corresponding point x_i with model parameters $\boldsymbol{\theta}$.

For a χ^2 fit to produce valid results for the model parameters and their statistical uncertainties, the data points and their respective errors need to fulfill the following properties:

[2] χ^2 minimization yields identical results to likelihood maximization in case of Gaussian errors. At the same time, χ^2 is the special case of a sum of weighted least squares, in which the weights are the inverse of the squared Gaussian errors.

- the statistical errors of the measurements have to follow a normal distribution
- the measurements/data points and their errors need to be uncorrelated

Nevertheless, in practice the χ^2 approach is also applied in situations where the statistical uncertainties of the measurement are only approximately following a Gaussian distribution (for example Poisson distributed random numbers with high mean value μ). However, in case the exact shape of the distribution of the measurement errors and/or the correlation between the measurements is not available or known, this may lead to biased results for the best-fit parameter values and the error estimation for those parameters.

A very convenient property of using χ^2 as a figure-of-merit function is that it allows to make a statement about the quality of the model in general. If the data are correctly described by the model function $f(x_i, \boldsymbol{\theta})$, then for repeated measurements the values of χ^2 follow a χ^2 distribution with $k = N - P$ degrees of freedom, where N is the number of independent data points and P is the effective number of free parameters[3]. See Andrae et al. (2010) for a detailed discussion of how to correctly determine the number of degrees of freedom. k is also the expectation value of the χ^2 distribution, meaning that if the model is suited to describe the measurements and the errors assigned to the data points are Gaussian distributed in nature and estimated correctly, the minimal value of χ^2 should be of the order of k. Strong deviations can be regarded as a clear hint that either the model is not describing the data properly or the errors are wrongly estimated.

If the measurement errors are truly Gaussian distributed, the parameter values that minimize χ^2 automatically also represent the maximum-likelihood solution to the problem, which is a more general approach to a merit function and is therefore covered in the next section.

4.2.1.2 Likelihood function

A practical example for a situation in which the χ^2 approach definitely fails to provide correct results is a scenario where a discrete observable yields a very low number of counts per measurement (e.g. measuring CCD counts in a low light-background scenario). For an average number of counts observed in a detector λ the Poisson distribution,

$$P_\lambda(k) = \frac{\lambda^k}{k!} \exp(-\lambda)\,, \tag{4.2}$$

[3] Strictly speaking this is only true if the model has a linear dependence on the parameters, but also holds as a good estimate in other cases Press, 2007

describes the probability of finding a specific number of counts k in a single measurement. For large λ this can be approximated with a Gaussian normal distribution with mean λ and $\sigma = \sqrt{\lambda}$, this approximation fails if λ is of the order of 10 or less especially when $\lambda \ll 1$ and thus the Gaussian distribution would predict negative values for the number of counts with high probability. In this case, one can instead use the maximum-likelihood approach; for this example more specifically a Poissonian likelihood is used. The likelihood in this context describes the probability of measuring a certain set of data $\boldsymbol{y}$ under the assumption of a specific model $f(\boldsymbol{x}, \boldsymbol{\theta})$ with a given set of parameters $\boldsymbol{\theta}$:

$$\mathfrak{L}(\boldsymbol{\theta}) = P(\boldsymbol{y}|f(\boldsymbol{x}, \boldsymbol{\theta}))\,. \tag{4.3}$$

For the Poissonian case, this is

$$\begin{aligned}\mathfrak{L}(\boldsymbol{\theta}) &= \prod_{i=1}^{N} P_{\lambda_i}(y_i), \text{ where } \lambda_i = f(\boldsymbol{\theta}) \\ &= \prod_{i=0}^{N} \frac{f(\boldsymbol{\theta})^{y_i}}{y_i!} \exp(-f(\boldsymbol{\theta}))\,,\end{aligned} \tag{4.4}$$

where the $\boldsymbol{y}$ represent the N individual measurements in the form of discrete numbers of counts. By maximizing $\mathfrak{L}$, an estimator is obtained for the most likely values of $\boldsymbol{\theta}$. In practice, it is advantageous to maximize $\log(\mathfrak{L})$ instead, as especially for large numbers of measurements, $\mathfrak{L}$ may change over many orders of magnitude, when varying $\boldsymbol{\theta}$, which may lead to problems with numerical calculations.

Both of the above described merit functions need to be minimized/maximized by optimizing the parameter values. This optimization can only in simple cases be achieved by analytically solving a set of equations. Often, one has to rely on numerical optimization algorithms, some of which are described in the next section.

4.2.2 Minimization algorithms

This section gives a very brief overview of the vast topic of minimization techniques used in computer-aided data analysis. Only the fundamental concepts and differences will be highlighted in order to motivate some of the choices made while developing the software packages *MARMOT* and *multi-transit-fitter* that are described in the following chapters. The focus here will be on techniques for solving χ^2 minimization or likelihood maximization problems. In addition, techniques and/or

concepts of how to determine realistic uncertainties for the best-fit parameters are presented. As it is impossible to cover all the different algorithms, only three relatively common representatives of certain classes of minimizers will be summarized hereinafter. A much more comprehensive overview can be found for example in Press (2007). The classification chosen in this thesis, without claim of completeness, is the following:

- "Calculus-free" methods, for example the *downhill simplex method* used in the software *Exostriker* by Trifonov, 2019
- Newton-type methods, for example the *variable metric method* widely used in particle physics for example in Vovk, I. et al. (2018) and also used in this thesis
- Gauss-Newton-type methods, for example the *Levenberg–Marquardt algorithm*

4.2.2.1 Downhill simplex method

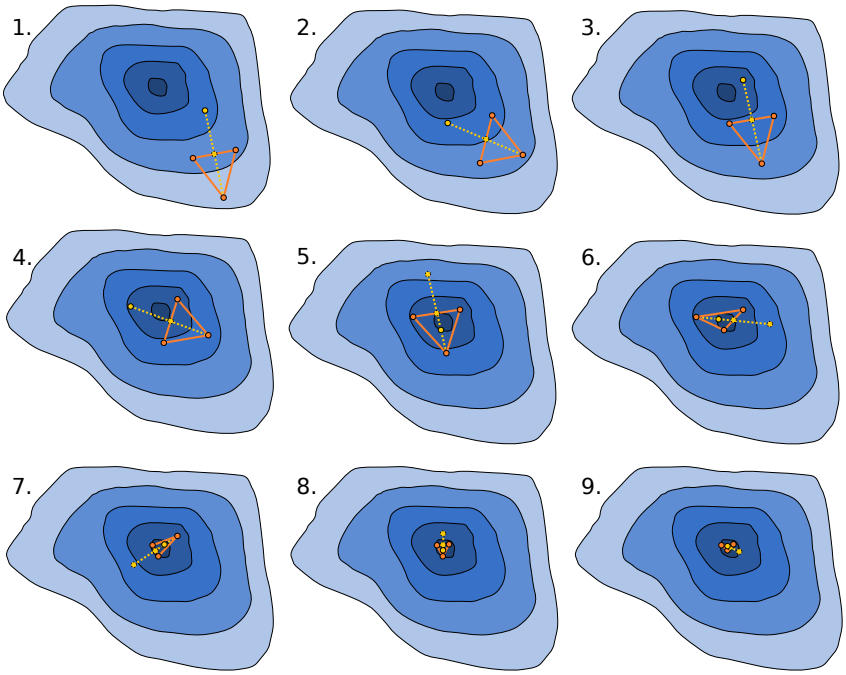

Fig. 4.1.: Illustration of the working principle of the downhill simplex method in 2D. Three initial points forming a triangle are chosen in the 2D parameter space. In each step, the algorithm seeks to replace the point with the highest function value with a new point. This is achieved by choosing a new candidate along the line from the highest point through the center of gravity of the remaining points. The first candidate lies outside the triangle, behind the center of gravity of the remaining points (works for steps 1-4). If this point turns out to result in a higher function value, the "half-way" point inside the triangle is chosen instead (from step 5 on).

This method works entirely without derivatives of the function to be minimized and was first proposed by Nelder and Mead (1965). The term "simplex" refers to a geometric object with flat sides formed by $M + 1$ points in M-dimensional space (simplest possible polytope)[4]. The method utilizes such a polytope in the parameter space, where the function is evaluated on each of the points. The relative function values on all $M + 1$ points are used to decide how to select a new point and discard one of the original points. This process is repeated iteratively until it converges to a local minimum (for an illustration of the method see also Figure 4.1). This process can be relatively slow and it is not trivial to find a stopping condition. Apart from that, the simplex method does not offer a possibility for estimating parameter errors.

4.2.2.2 Variable metric method

A detailed description of the algorithm first proposed by Fletcher (1970) can also be found in Press (2007). The basic concept of the method is to approximate the scalar-valued merit function (depending on M to-be-determined parameters) by an M-dimensional parabola using 'local' information. The algorithm is also known as "quasi-Newton" method as it falls into a class of minimizers that try to determine the roots of the first derivative (gradient) of a function. If the first and second-order derivatives are exactly known for any given point on an M-dimensional parabola, its vertex can also be computed exactly. Quasi-Newton methods compute the gradient numerically using finite differences and start with some initial guess for the Hesse matrix[5]. In an iterative procedure, the algorithm then jumps to the "would-be vertex" and uses the deviation from the predicted function value to the actual one in order to improve the guess for the Hessian. This procedure is repeated until the desired precision in terms of difference between guessed minimum function value and actual function value is reached (for an illustration of the algorithm see also Figure 4.2). Obviously, such an algorithm is only suited for benign functions that are "well behaved" enough (second derivative exists everywhere etc.). A very useful feature of the *variable metric method* is that a good estimate of the error matrix is automatically provided, which contains variances and co-variances for the parameters.

[4] The simplest possible polytope is for example in 2D a triangle and in 3D a tetrahedron

[5] The Hesse matrix is the matrix of second-order partial derivatives of a scalar-valued function (the Jacobi matrix of the gradient vector).

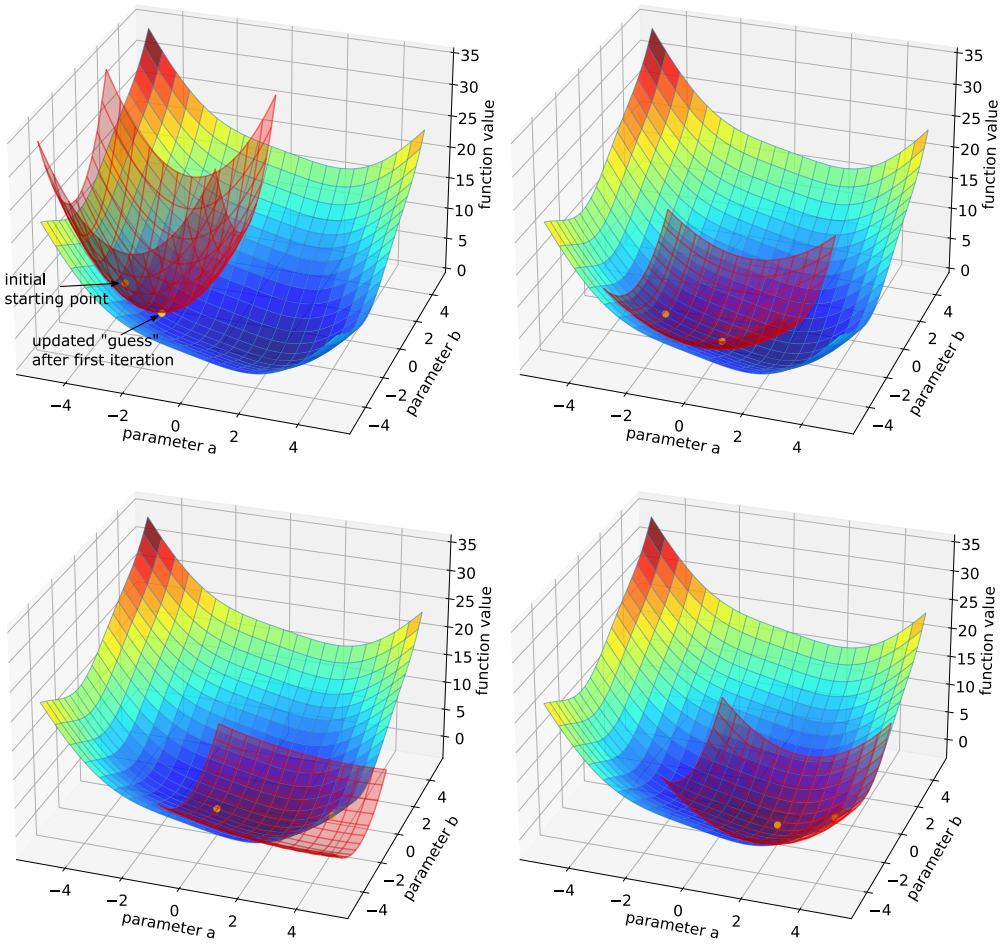

Fig. 4.2.: Illustration of the variable metric method in a 2D parameter space. The to-be-minimized function is locally approximated with a paraboloid, such that the function value and first derivative match at the starting value. Some initial guess (upper left panel: yellow dot on the left) has to be chosen for the second derivative. The vertex of the paraboloid (upper left panel: yellow dot in the vertex of the parabola) forms the starting point for the next iteration (upper right panel). The updated Hesse matrix can be computed based on the difference between vertex and true function value. This procedure is repeated iteratively until the parabola in the final iteration is a very good approximation for the function around the minimum (as long as the function is reasonably well behaved at the minimum).

4.2.2.3 Levenberg–Marquardt algorithm

This widely used algorithm that was first mentioned by Levenberg (1944) and later re-discovered by Marquardt (1963) is very similar to the so-called Gauss-Newton method. In contrast to the previously discussed method, it only uses first-order derivatives instead of first and second-order ones. It is important to note that the Levenberg-Marquardt algorithm, as opposed to the methods mentioned above, is only a minimizer for scalar-valued functions and can only be applied in least-square fits (for example χ^2 minimization when individual summands are represented as a vector). Instead of working with the derivatives of the scalar-valued function, it uses the vector of squared residuals. The general concept of this method is to compute the Jacobi matrix of this vector-valued function via finite differences and use a linear approximation, solve the linear-least-squares problem and thereby approach the smallest sum of squared residuals. Besides not being applicable to all classes of problems (like e.g. general likelihood maximization), it does also not offer a parameter error estimation in a similar way as the variable metric method.

Throughout the software that was developed in the scope of this thesis, the minimizer *Minuit* by James and Roos, 1975, that utilizes the *variable metric method*, was used extensively due to its relative speed and robustness, the possibility of estimating parameter uncertainties and the availability within the *iminuit* Python package.

4.2.3 Parameter uncertainties estimation

In the frequentist framework, there is no PDF in the parameter space which describes the degree of belief in the parameters derived from the data points. Probability is merely interpreted as - like the name suggests - frequency of a certain outcome of a random experiment. Parameter uncertainties are typically addressed using confidence intervals. A confidence interval for a parameter θ is constructed by a computational rule that is defined before the experiment has been conducted and that ensures that the true value of the parameter lies within that interval with a certain predefined probability. Morey et al. (2016) provide a detailed discussion of confidence intervals.

In a Bayesian framework, parameter uncertainties can be discussed in a slightly different way. They can be defined, for example, in terms of quantiles of the posterior distribution (eg. 0.16 to 0.84 for a 68% containment error). In the following, this Bayesian approach will be used to calculate the parameter uncertainties of a χ^2 fit.

4.2.3.1 Parameter uncertainties of a χ^2 fit

Consider the following example of N data points measuring y_i at the points x_i. The data shall be described by a model $f(x_i, \theta)$. For simplicity, it is assumed that f only depends on a single parameter θ. This could later be generalized to a multi-dimensional parameter space where all parameters are kept fix except for one, doing so iteratively for all parameters. All measurements are associated independently with Gaussian uncertainties σ_i. The likelihood function is then given by

$$\begin{aligned}\mathfrak{L}(\theta) &= \prod_{i=1}^{N} \left(\frac{1}{\sigma_i \sqrt{2\pi}} \cdot \exp\left(-\frac{1}{2} \frac{(y_i - f(x_i, \theta))^2}{\sigma_i^2} \right) \right) \\ &= \left(\frac{1}{\sqrt{2\pi}} \right)^N \cdot \left(\prod_{i=1}^{N} \frac{1}{\sigma_i} \right) \cdot \exp\left(-\frac{1}{2} \sum_{i=1}^{N} \frac{(y_i - f(x_i, \theta))^2}{\sigma_i^2} \right). \end{aligned} \tag{4.5}$$

In a next step, it is assumed that f is linear in θ. At first glance, this might not sound very reasonable, especially considering that in a linear-model case the fit itself would be rather trivial. On the other hand, it has to be considered that if N is sufficiently large and the model can be Tailor expanded for each value of θ, even small changes in θ will lead to a substantial change of $\mathfrak{L}$, small enough for only the first-order term in the Tailor polynomial to dominate. It is important to point out that this assumption is not valid for small N or models with very strong non-linearities around the optimal-fit parameter values μ_i. Otherwise Equation 4.5 can be approximated, with $\mu_i + \alpha_i \, \Delta\theta$ as the Tailor expansion of $f(x_i, \theta)$ up to first order in $\Delta\theta$ (which is the deviation from the best-fit parameter) by:

$$\begin{aligned}&\mathfrak{L}(\Delta\theta) = \\ &= \left(\frac{1}{\sqrt{2\pi}} \right)^N \cdot \left(\prod_{i=1}^{N} \frac{1}{\sigma_i} \right) \cdot \exp\left(-\frac{1}{2} \sum_{i=1}^{N} \frac{(y_i - \mu_i - \alpha_i \, \Delta\theta))^2}{\sigma_i^2} \right) \\ &= \left(\frac{1}{\sqrt{2\pi}} \right)^N \cdot \left(\prod_{i=1}^{N} \frac{1}{\sigma_i} \right) \cdot \exp\left(-\frac{1}{2} \sum_{i=1}^{N} \frac{(\delta_i^2 - 2\,\delta_i \, \alpha_i \, \Delta\theta + \alpha_i^2 \, \Delta\theta^2))}{\sigma_i^2} \right) \qquad (4.6) \\ &= \left(\frac{1}{\sqrt{2\pi}} \right)^N \cdot \left(\prod_{i=1}^{N} \frac{1}{\sigma_i} \right) \cdot \exp\left(-\frac{1}{2} \left(\Delta\theta^2 \cdot \sum_{i=1}^{N} \frac{\alpha_i^2}{\sigma_i^2} - 2\,\Delta\theta \cdot \sum_{i=1}^{N} \frac{\delta_i \, \alpha_i}{\sigma_i^2} + \sum_{i=1}^{N} \frac{\delta_i^2}{\sigma_i^2} \right) \right) \\ &= \left(\frac{1}{\sqrt{2\pi}} \right)^N \cdot \left(\prod_{i=1}^{N} \frac{1}{\sigma_i} \right) \cdot \exp\left(-\frac{1}{2\,a^2} \left(\Delta\theta^2 - 2\,b \cdot \Delta\theta + b^2 + c \right) \right) \\ &= \left(\frac{1}{\sqrt{2\pi}} \right)^N \cdot \left(\prod_{i=1}^{N} \frac{1}{\sigma_i} \right) \cdot \exp\left(-\frac{c}{2\,a^2} \right) \cdot \exp\left(-\frac{(\Delta\theta - b)^2}{2\,a^2} \right). \qquad (4.7) \end{aligned}$$

In the last two steps, the sums in the exponent that do not depend on $\Delta\theta$ are first substituted using the variables

$$a = \frac{1}{\sqrt{\sum_{i=1}^{N} \frac{\alpha_i^2}{\sigma_i^2}}}, \quad b = \frac{\sum_{i=1}^{N} \frac{\delta_i \, \alpha_i}{\sigma_i^2}}{\sum_{i=1}^{N} \frac{\alpha_i^2}{\sigma_i^2}}, \quad c = \frac{\sum_{i=1}^{N} \frac{\delta_i^2}{\sigma_i^2}}{\sum_{i=1}^{N} \frac{\alpha_i^2}{\sigma_i^2}} - \left(\frac{\sum_{i=1}^{N} \frac{\delta_i \, \alpha_i}{\sigma_i^2}}{\sum_{i=1}^{N} \frac{\alpha_i^2}{\sigma_i^2}} \right)^2 ,$$

and then brought into the final form by square addition. The above has the shape of a Gaussian in $\Delta\theta = \theta - \theta_0$, as highlighted by the substitutions in the last two lines. θ_0 is the parameter that maximizes the likelihood. In the above $y_i - \mu_i$ has been replaced by δ_i, which can be understood as the deviation of the measurement from the best-fit model in the i^{th} data point. $\alpha_i \, \theta$ is the linear approximation of f at point i.

The exponent of Equation 4.5 is identical to χ^2 except for a factor -0.5. Equations 4.6 to 4.7 indicate that a variation of θ which increases the expression for χ^2 by exactly 1 in either direction, is equivalent with reaching the 1σ boundaries of the Gaussian. If $\mathfrak{L}$ is normalized and interpreted as posterior PDF[6] for θ, then the parameter range for which $\Delta\chi^2 < 1$ represents the 68.3% containment interval around the best-fit value for θ.

4.2.3.2 Parameter uncertainties of a likelihood fit: Wilks' theorem

As shown above, it is relatively easy to state parameter uncertainties if the optimization problem can be formulated as a χ^2 fit. In the general $\log(\mathfrak{L})$ case calculating parameter uncertainties is not straightforward. However, according to Wilks' theorem Wilks, 1938, the following statement is asymptotically true for very large sample sizes (e.g. large number of measurements/data points N):

$$-2 \, \log(\Delta\mathfrak{L}) \xrightarrow[N \to \infty]{} \chi^2 \, . \tag{4.8}$$

Here, $\Delta\mathfrak{L}$ is the likelihood ratio of $\mathfrak{L}(\boldsymbol{\theta})$ with respect to the maximum $\mathfrak{L}(\boldsymbol{\theta}_0)$. This is equivalent to approximating the log-likelihood profile with a parabola around the maximum. Assuming that the above approximations hold, the χ^2 formalism for parameter uncertainties can then also be used for likelihood maximization problems. For a single parameter θ_j, this means that moving the parameter value away from the value that maximizes $\log(\mathfrak{L})$ in any direction, such that $\log(\mathfrak{L})$ decreases by 0.5, corresponds to the bounds of the 1σ confidence interval for that parameter.

[6] Note that in the absence of a prior, the posterior PDF is given by the normalized likelihood (see Section 4.3)

4.3 Bayesian tools for parameter estimation

In the frequentist approach to statistics, probability is merely interpreted as the frequency for which a certain outcome is expected from an experiment probing a model with a random component. Bayesian statistics on the other hand use probability as a measure for the "degree of belief" in certain parameter values. In this framework, it is possible to express the result of an experiment in the form of an (updated) probability density function (PDF) in the parameter space of a model (see also Particle Data Group et al. (2018)). In this context, "updated" means that in Bayesian statistical analyses the starting point is a prior PDF as input, which expresses the current state of knowledge from before the new data have been analyzed. This prior can also be completely uninformed if no prior data that could constrain the model is available.

The fundamental equation of Bayesian inference is given by Bayes' theorem, which states that

$$P(\boldsymbol{\theta}|\boldsymbol{x}) = \frac{P(\boldsymbol{\theta}) \cdot P(\boldsymbol{x}|\boldsymbol{\theta})}{\int P(\boldsymbol{\theta}) \cdot P(\boldsymbol{x}|\boldsymbol{\theta}) \, \mathrm{d}\boldsymbol{\theta}} \,, \tag{4.9}$$

where $P(\boldsymbol{\theta}|\boldsymbol{x})$ is the posterior probability for the parameters $\boldsymbol{\theta}$, given the data $\boldsymbol{x}$, $P(\boldsymbol{\theta})$ is the prior probability, $P(\boldsymbol{x}|\boldsymbol{\theta})$ is the likelihood[7] and the integral in the denominator serves as a normalization factor, summing all possible values for $\boldsymbol{\theta}$. This normalization factor is usually hard to calculate for most practical applications. Therefore, Markov-Chain Monte Carlo (MCMC) methods, that circumvent this issue, are frequently used for mapping out the posterior PDF in the parameter space.

4.3.1 Markov-Chain Monte Carlo techniques

The general term "Monte Carlo methods" describes techniques that use (typically computer-generated pseudo-) random numbers for computations that address random processes or probabilities in nature. In a Markov Chain, the probability of a subsequent state is only influenced by the previous one, which in turn means that only relative properties of the PDF need to be known (Press, 2007). MCMC methods specifically are techniques for generating a set of random numbers that are distributed following a certain PDF that is often not accessible via other methods. The normalization of this PDF does not have to be known explicitly as it is implicitly contained in the set of values drawn using the MCMC. In the framework of Bayesian inference, this implies that the denominator in Bayes' theorem (Equation 4.9), which

[7] This is in fact the same likelihood as is used in the merit function in frequentist analysis, see also Section 4.2.1.2

is particularly hard to obtain, does not have to be computed. One of the most basic algorithms in this class is the algorithm by Metropolis et al. (1953) and Hastings (1970). It can be described in its simplest form by following this list of steps:

- sample from the proposal distribution (for more about this proposal distribution, see below) and add the vector to $\boldsymbol{\theta}_{i+1}$ in order to obtain a candidate point $\boldsymbol{\theta}_{i+1}$
- evaluate the function f at $\boldsymbol{\theta}_{i+1}$ or
- Keep the new value
  1. if $f(\boldsymbol{\theta}_{i+1})/f(\boldsymbol{\theta}_i) > 1$
  2. if a randomly drawn number in the interval $[0, 1]$ exceeds $f(\boldsymbol{\theta}_{i+1})/f(\boldsymbol{\theta}_i)$,

  otherwise set $\boldsymbol{\theta}_{i+i} = \boldsymbol{\theta}_i$

For clarification see also Figure 4.3. This simple algorithm ensures that the resulting

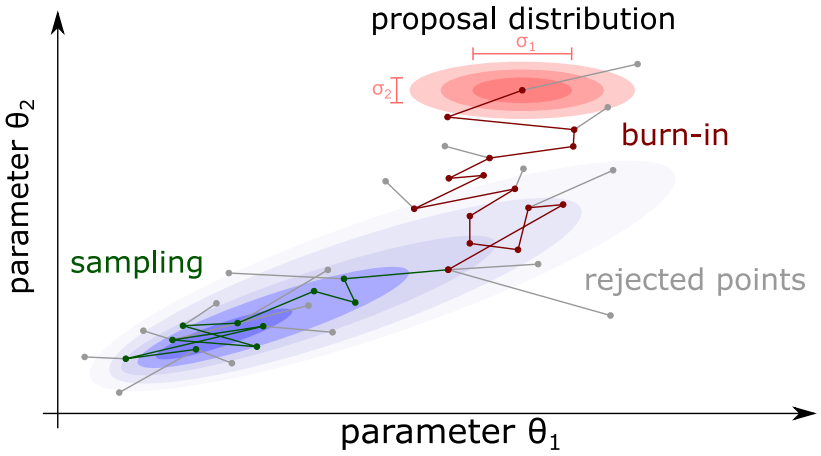

Fig. 4.3.: Illustration of the working principle of the Metropolis-Hastings algorithm. New positions are drawn based on the current/starting position and a proposal distribution (red contours). Those new positions are evaluated according to the rules stated in the text and either accepted or rejected. The algorithm needs to run for a number of iterations (burn-in) before it reaches the region of the extremum. Then, the algorithm samples the PDF and produces a sample of points that are distributed accordingly.

chain of random values reproduces the function f in terms of shape everywhere locally. Finally, this means that the $\boldsymbol{\theta}_i$ will be distributed with a PDF that is a normalized version of f after a long enough "burn-in" phase (see Figure 4.3) and after enough iterations. The most challenging aspect of the Metropolis-Hastings algorithm is the choice of the proposal distribution, especially as the parameter uncertainties in the final distribution are unknown apriori, but should reflect in the choice of $\boldsymbol{\sigma}_j$. This means that the steps - typically drawn from a multivariate

Gaussian distribution where σ_j should match the shape of the posterior PDF - need to be large enough for the entire parameter space to be mapped in a reasonable amount of computing time, but also small enough in order to not propose new values with close to zero likelihood. Especially problematic are PDFs with a high degree of correlation between the parameters, as in this case a simple multivariate Gaussian as proposal distribution is not effective anymore. In this scenario, one would need to sample in the direction of the correlation using larger enough steps while at the same time using smaller steps in the direction perpendicular to that. Apart from such cases, choosing the right proposal distribution in the first place may be difficult as well without knowing anything about the function which is to be probed.

4.3.2 The *emcee* algorithm

The problem of choosing an appropriate proposal distribution is solved in an elegant way in the *emcee* python package Foreman-Mackey et al., 2013, based on an algorithm described by Goodman and Weare (2010). The key feature of this algorithm's performance is unaffected by affine transformations of the parameter space, such as scaling, rotation and skew. This implies in particular that any PDF which can be brought into a radially symmetric shape by applying affine transformations can be sampled with the same efficiency as a Metropolis-Hastings sampler with a symmetric multi-dimensional Gaussian as proposal distribution would do on a symmetrically shaped PDF (see Figure 4.4 for illustration). This behavior is achieved by using a

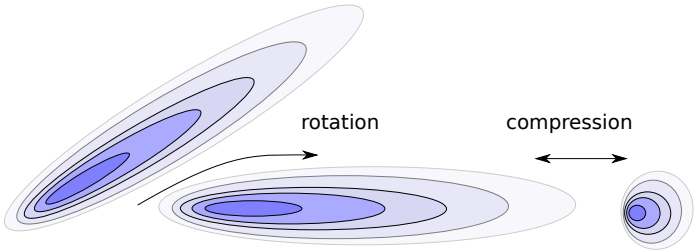

Fig. 4.4.: Example of affine transformations acting on a 2D distribution that causes the distribution to morph into a more symmetric shape. A key property of the *emcee* algorithm is that it uses a mechanism for suggesting new parameter values, that depends on the distribution of walkers on the parameter space, but is invariant under such affine transformations. As a consequence, it samples the tilted, elongated shape on the left with exactly the same efficiency as it would sample the circular shape on the right.

larger number of "walkers" (e.g. 100, but should at least exceed the dimensionality of the parameter space) and their respective positions in the parameter space for proposing new positions. For an illustration of this, see Figure 4.5. This is in contrast

to the Metropolis-Hastings algorithm, where only a single sampler is moved through the parameter space in a random walk. The walkers are first randomly distributed around an initial guess position. Then, one walker is chosen (X_k) and randomly assigned a second walker (X_j) from the remaining walker pool. The new position (Y) for the first walker is then determined along the ray pointing from the second to the first walker using the following PDF:

$$g(z) = \begin{cases} \frac{1}{\sqrt{z}} & \text{if } z \in \left[\frac{1}{a}, a\right], \\ 0 & \text{otherwise}. \end{cases} \tag{4.10}$$

The variable z here is measured in units of distance between the two walkers and a

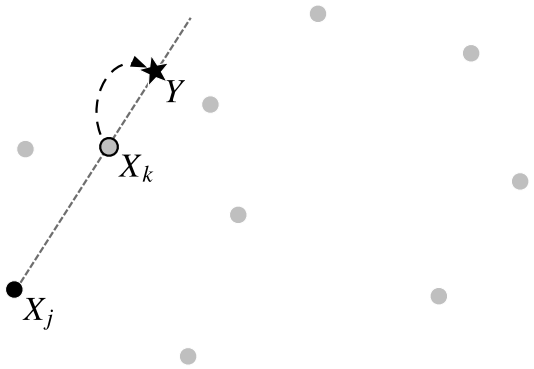

Fig. 4.5.: Illustration of the 'stretch move' performed between two walkers. The goal is to propose a new position Y for the walker at position X_k, which for that purpose is randomly assigned a second walker X_j. The new position is then chosen on the ray pointing from X_j to X_k by drawing from the PDF in Equation 4.10. Image source: Goodman and Weare, 2010

is the only free parameter for optimization. The condition for acceptance or rejection of the new position for the walker is determined in the exact same way as for the Metropolis-Hastings algorithm, namely by evaluating the function in the new point (Y) and comparing it to the old value (X_k). If the likelihood is higher for the new position, it is automatically accepted. Otherwise, it is only kept if a random number from a uniform distribution between 0 and 1 is smaller than the likelihood ratio. This way, the ensemble of walkers quickly "learns" the shape of the PDF and only "reasonable" new positions are proposed as the sampling progresses. The *emcee* algorithm, therefore, performs much better when dealing with models containing highly correlated parameters, something that is common in modeling transit light curves. It was therefore chosen as MCMC sampler for the transit fitter program (Chapter 6).

5

MARMOT - Munich Analyzer for Radial velocity Measurements with b-spline Optimized Templates

> *Scientific success can be measured in the amount of broken equipment.*
>
> **— oral tradition among scientists working on hardware**

In this chapter, the high-level analysis code for Échelle spectrograph data, which has been developed in the scope of this thesis, is described in detail and its performance is demonstrated using bench-mark observations. The program has been named *MARMOT* (**M**unich **A**nalyzer for **R**adial velocity **M**easurements with b-spline **O**ptimized **T**emplates). The main task of the software is to compute precise radial velocity measurements from pre-extracted 1D Échelle spectra.

Although designed to be flexible and easily adaptable to other data formats, *MARMOT* has been designed to plug into the output of *GAMSE* (**G**eneral **A**stronо**M**ical **S**pectra **E**xtractor)[1,2], the spectra extractor that has been developed at the USM under the leadership of Dr. Liang Wang[3]. *GAMSE* provides 1D order-wise spectra from 2D Échelle spectrograph images, including a first, ThAr based, wavelength calibration, and correction of CCD readout bias and stray-light in the image. An overview over the main features of that program, and a detailed description of the calculation and propagation of uncertainties, which has been contributed to *GAMSE* in the scope of this thesis, is summarized in Section 5.1.

The program *MARMOT* itself, which has been developed entirely in the scope of this thesis, is designed to start with those already extracted 1D spectra, which are provided Échelle-order wise. The software then applies barycenter and frequency comb corrections to each frame, computes spectral templates for each order, and

[1] *GAMSE* download : `https://github.com/wangleon/gamse`
[2] *GAMSE* documentation: `https://gamse.readthedocs.io/en/latest/index.html`
[3] Contact information: liangwang@niaot.ac.cn / lwang@mpe.mpg.de

finally calculates the relative shifts between frames in terms of radial velocity. The structure and features of *MARMOT* are described from Section 5.2 onward. Tests to verify the performance of the software, as well as some scientific analyses, are shown in Section 5.10.2 and following.

5.1 *GAMSE*

The program *GAMSE* (Wang et al., in prep.) is designed to extract Échelle spectra from raw 2D images and produces 1D spectra in the format that is required as input for *MARMOT*. The error estimation has been contributed in the context of this thesis. For some instructions on how to use *GAMSE* for processing data, see Appendix 9.6. To highlight the purpose of the individual data reduction steps performed by *GAMSE*, the total light distribution in the focal plane (which is then recorded by a CCD camera) is modeled as

$$S_{\mathrm{raw}}(x,y) = \sum_{o \in \mathrm{orders}} \left[(\Psi_o(x,y,\lambda) + bkg'_o(x,y,\lambda)) \otimes f(\lambda) \right] \cdot \epsilon(x,y) \; + \; bias(x,y)\,. \tag{5.1}$$

Here, x and y are the coordinates on the CCD-chip and $f(\lambda) = star(\lambda) + sky(\lambda)$ is the sum of the intrinsic spectrum of an astrophysical source $star(\lambda)$ and the sky background $sky(\lambda)$.[4] The spectrum gets folded with the 2D mapping function $\Psi_o(x,y,\lambda)$ of the spectrograph, for the o-th order and $bkg'_o(x,y,\lambda)$, the mapping function for scattered light from the optical and mechanical components of the spectrograph. $\epsilon(x,y)$ is the sensitivity of individual pixels to light, and $bias(x,y)$ is the CCD bias that is added by the CCD electronics to all images for technical reasons and needs to be subtracted. Although the background is created by the mapping of stray-light to the CCD chip and therefore also depends on wavelength and the blaze function, it can for practical purposes also be described as an additive component to the spectrograph image:

$$S_{\mathrm{raw}}(x,y) = \left(\sum_{o \in \mathrm{orders}} \left[\Psi_o(x,y,\lambda) \otimes f(\lambda) \right] \; + \; bkg(x,y) \right) \cdot \epsilon(x,y) \; + \; bias(x,y)\,. \tag{5.2}$$

[4] In the data reduction of *FOCES* the sky background is assumed to be negligible since *FOCES* is not equipped with a so-called sky-fiber which removes the possibility to accurately estimate the sky background. For fiber spectrographs in general and *FOCES* in particular, these assumptions hold if the observation target is not too close to the moon, not observed to close to the horizon during twilight or with a lot of moonlight in cloudy conditions.

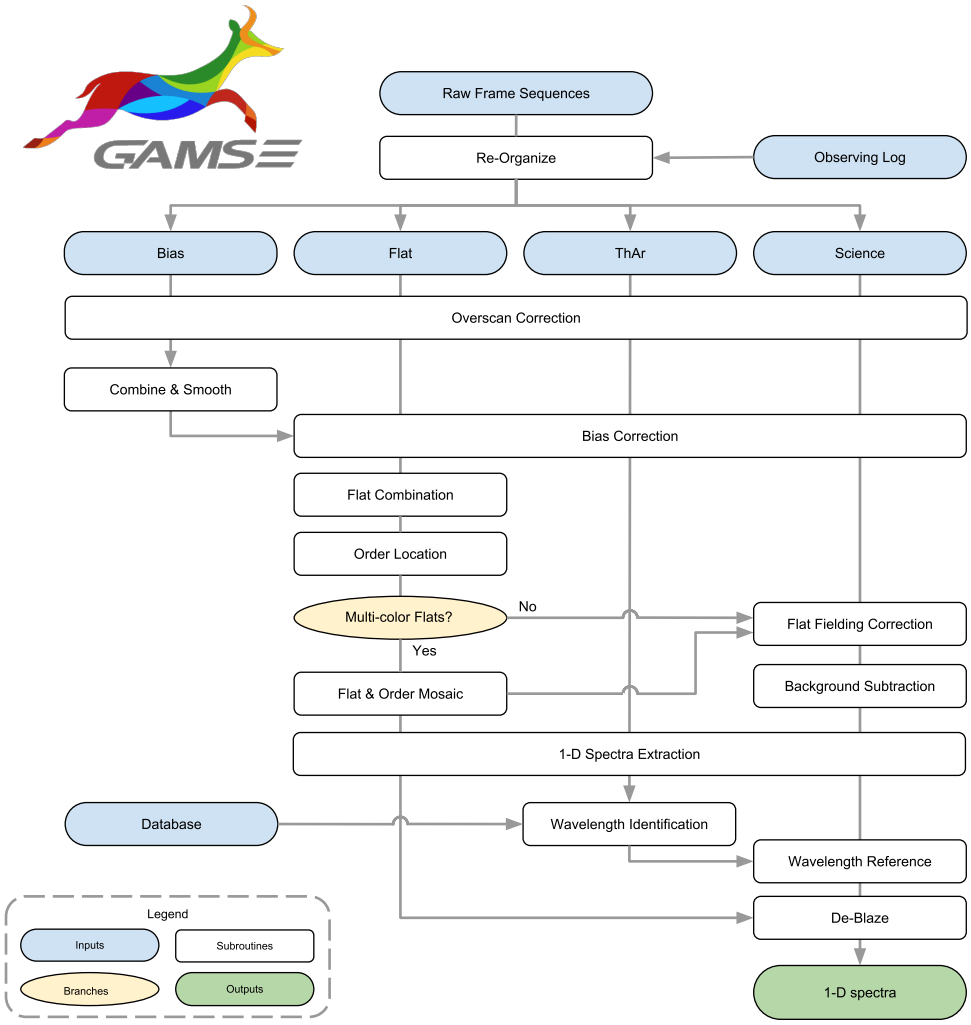

Fig. 5.1.: This flow chart illustrates the data reduction procedure of *GAMSE*. All the individual steps during processing of the four different types of images used by *GAMSE* are shown in the four main columns. The whole program can be controlled by an ini-file. The data is then extracted and calibrated to obtain the final order-wise 1D spectra. Diagram kindly provided by Liang Wang.

The remaining mapping function can be decomposed (approximately[5]) into the slit function $s_o(x, \lambda)$ (main dispersion direction), the decker[6] function $d_o(y, \lambda)$ (cross-

[5]The assumptions that have to be made in order for this decomposition to hold and that are not always met in real Échelle images are the following: a) The x-dependence of the decker function can be converted into a wavelength dependence within the same Échelle order. b) The shape of the slit function does not change in y-direction within the (pixel) height of one Échelle order. c) The lines in the spectrum are - and this is not true for most instruments, including *FOCES* - not tilted against the y-axis.

[6]The entrance of a slit spectrograph is usually of rectangular shape, with the short side of the entrance configuration usually called slit width and the longer side called decker (slit length).

order direction), and the blaze function $blaze_o(\lambda)$ that describes the brightness modulation along the order

$$\Psi_o(x, y, \lambda) \approx s_o(x, \lambda) \cdot d_o(y, \lambda) \cdot blaze_o(\lambda)\,, \tag{5.3}$$

The recorded flux has to be wavelength calibrated and extracted before *MARMOT* can perform the RV estimation. For this purpose, *GAMSE* performs the following steps for its data reduction, (see also Figure 5.1):

- overscan correction
- bias correction
- flat correction
- background subtraction
- 1D spectra extraction
- ThAr-based wavelength calibration
- identification of the physical orders

For further details and an introduction on the ThAr-based wavelength calibration and identification of the physical orders, the reader is referred to Wang et al. (in prep.).

The data reduction requires several different types of calibration images, which are taken during a daily calibration run with various calibration light sources and exposure times. Since fiber-fed spectrographs are decreasingly efficient from the red to the blue part of the spectrum and also some of the light sources used for calibration are relatively dim at blue wavelengths, in order to obtain an optimally illuminated image, a mosaic is created. It is composed of several images, in each of which only a specific portion of the spectrum is optimally illuminated since it is not possible to ideally illuminate for example the blue part of the spectrum without simultaneously saturating the red and green parts. An example of this is shown in Figure 5.2. For a listing of the images taken during a typical calibration run and their naming scheme with a 4 digit postfix see also Table 5.1. In cases when more than one exposure time is needed for the same fiber, light source and image type, this is indicated by separate rows in the table.

Subsequently, a short introduction to the essential steps of the data reduction, which influence the extracted flux and therefore the uncertainty estimation is given. For all following sections of the introduction of *GAMSE*, image descriptions written in italic and a leading capital letter refer to the image type, e.g. *Bias* for an image taken

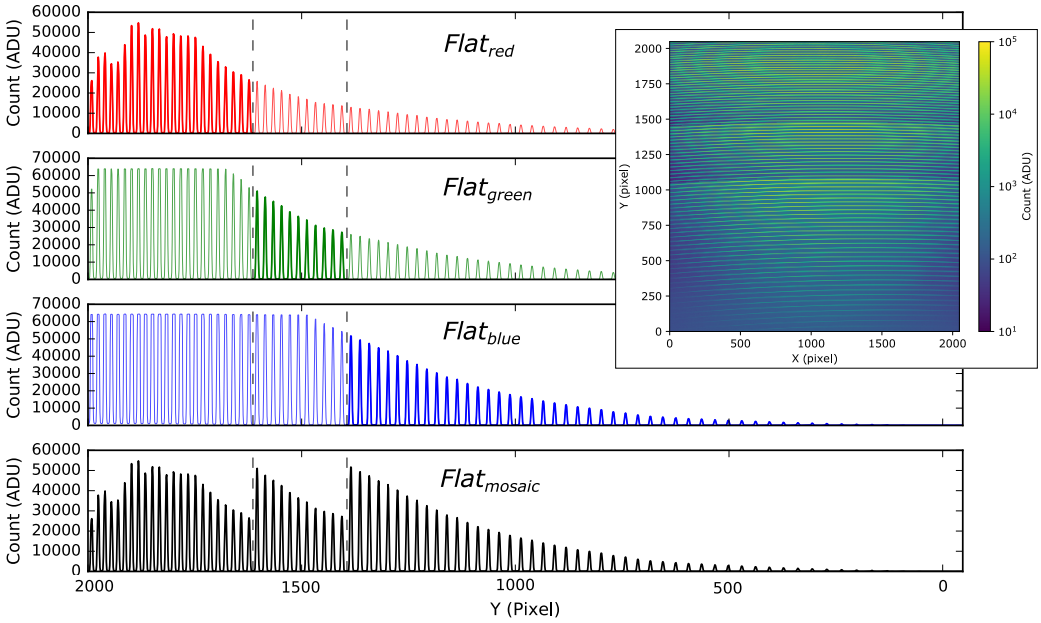

Fig. 5.2.: Schematic figure for a *Mosaic Flat* which consists of 3 different $Flat$ images with increasing exposure time. The plot shows a cut through the center pixel row of the individual $Flat$ images and the *Mosaic Flat* (black). The insert shows as an example the full image of the *Mosaic Flat*. Images kindly provided by Dr. Liang Wang and modified by me.

in the bias configuration. Specific numbers quoted in italic can be changed in the ini-file whereas non-italic numbers are hard-coded in the source code of *GAMSE*.

Tab. 5.1.: Images taken during a typical calibration run of *FOCES*. *name* establishes the naming scheme used in this thesis and the column *code* specifies the name tags in the filenames. The listed exposure times should only be seen as a rough guide since they change with aging light sources and hardware modifications.

name	object in fiber A	object in fiber B	exp. time [s]	code
$Bias$	—	—	0.00002	BIAS
$Flat$	*order identification and sensitivity map*			
$Flat_{S,r}$	Flat,red region	—	30	FLS0
$Flat_{S,g}$	Flat, green region	—	120	FLS1
$Flat_{S,b}$	Flat, blue region	—	480	FLS2
$Flat_{C,r}$	—	Flat, red region	0.3	FLC0
$Flat_{C,g}$	—	Flat, green region	1.2	FLC1
$Flat_{C,b}$	—	Flat, blue region	4.8	FLC2
$ThAr$	*coarse wavelength calibration*			
$ThAr_{C,r}$	—	ThAr, red region	12	THC0
$ThAr_{C,b}$	—	ThAr, blue region	22	THC1
$Comb$	*fine wavelength calibration*			
$Comb_S$	Comb	—		COS0
$Comb_C$	—	Comb		COC0
$Comb/Comb$	Comb	Comb		COCS
$Science$				
$Science$	Star	—		SCI0
$Science_C$	Star	Comb		SCC2
$Science_T$	Star	ThAr		SCT2

5.1.1 Overscan and bias subtraction

For technical reasons, pixels of the CCD cameras are biased with an offset voltage, independent of the exposure time, which is translated during the readout to CCD counts and that has to be subtracted from all frames during data reduction. This bias can also differ slightly from frame to frame, therefore the bias subtraction is handled in two steps. The first step is the so-called overscan correction, which is done independently for each frame (*Bias*, *Science* ...) and uses dedicated areas at the right and left of the CCD chip that are not exposed to light. In this step, half of the pre-readout overscan region of the CCD chip, which coincides with the blue orders of the Échelle pattern (lower half), is averaged and subtracted from the image (for comparison see also Figure 5.3). The standard deviation of all pixels in this region are used to determine the read-out noise for every image. This specific region on the CCD is chosen as reference as all the other overscan regions can be contaminated by spill-over from strongly illuminated parts of the spectrum or incomplete clearing of the pixels from previous exposures. Afterwards, all *Bias* images are combined by averaging pixel-wise while removing hot pixels (e.g. hits by cosmic rays) via pixel-

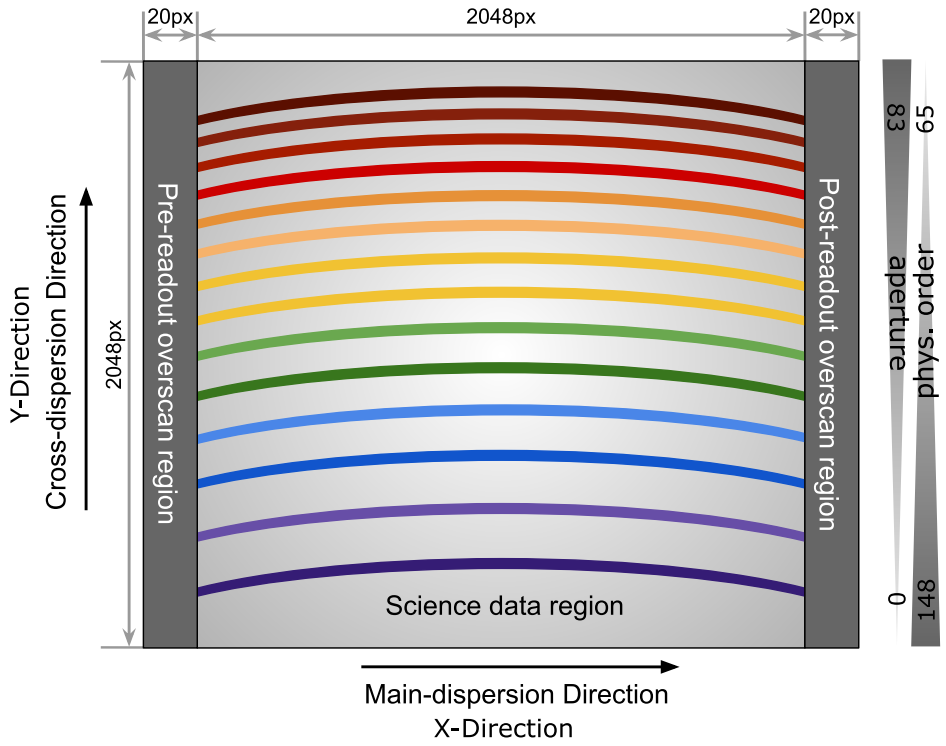

Fig. 5.3.: Schematic view of the Échelle spectrum recorded on the *FOCES* CCD (figure not to scale) including the overscan regions. Image kindly provided by Dr. Liang Wang and modified by me.

wise 10σ-clipping during this process. The images treated this way are still not bias free as the bias values are not perfectly homogeneous over the whole CCD, which can be seen in the saddle-like structure in the upper right panel in Figure 5.4. For further proof see also the deviation from 0 and variation in the mean position of the red histograms in Figure 5.4 lower right panel, which represent the 9 marked areas in Figure 5.4 upper left panel. To correct for this position-dependent effect in all other images, the remaining *Bias* image is smoothed using a 2D Gaussian smoothing kernel (*3 pixel*) creating the so-called (smooth) *Master-Bias*. The histograms in the lower right of Figure 5.4 correspond to the regions in the two images on the left in red and blue that are indicated with a-i. These histograms demonstrate that the remaining noise in the images perfectly follows a Gaussian distribution, both before and after subtracting the *Master-Bias*. Furthermore, the offset of the mean of the distribution is reduced to zero after subtracting the smooth *Master-Bias* for all nine regions. This *Master-Bias* image can be assumed to be stable over the course of one night but should be generated at least once per night.

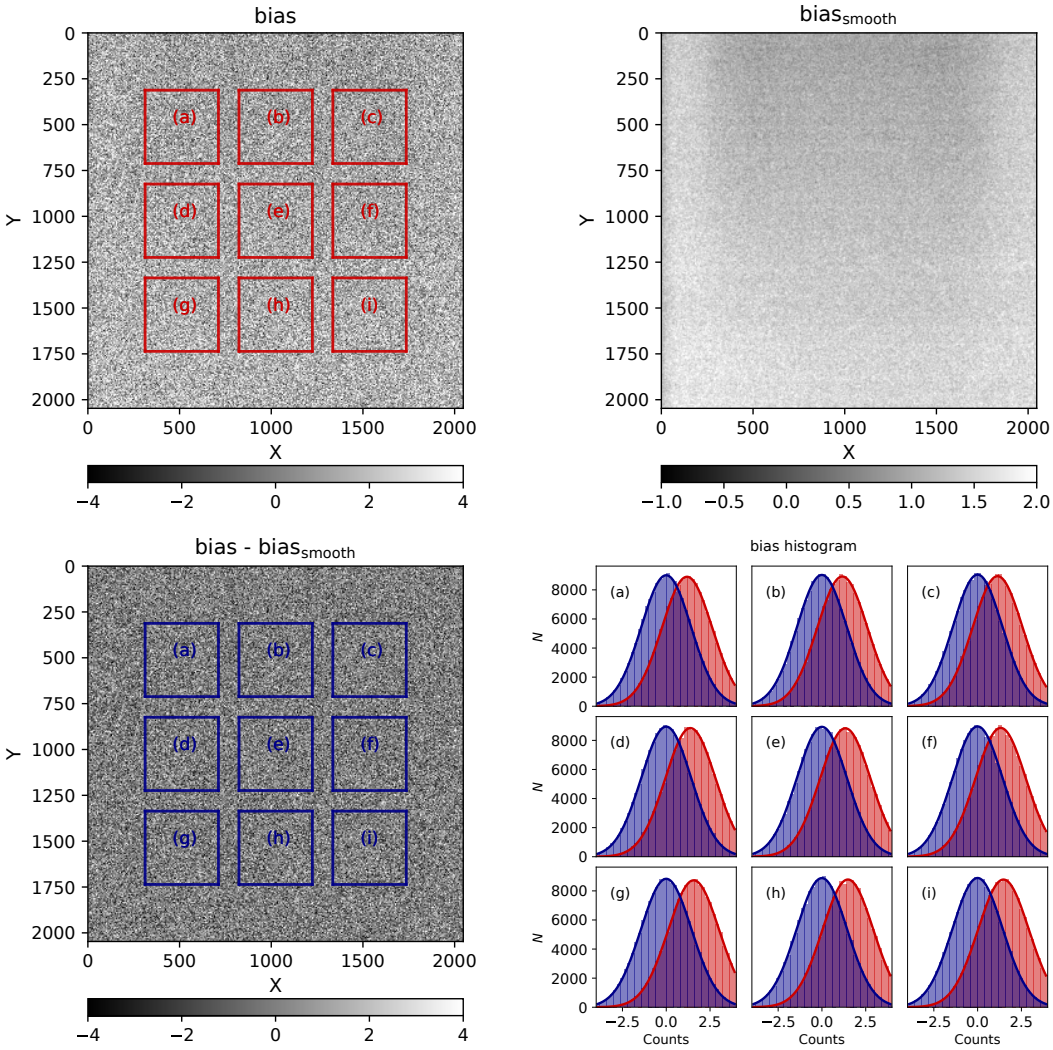

Fig. 5.4.: This figure illustrates the procedure for estimating and subtracting the inhomogeneous part of the CCD. The upper left panel shows the average (excluding hot pixels via pixel-wise sigma clipping) of ten *Bias* frames that are used for generating the *Master-Bias* image. The stacked *Bias* is then smeared with a 2D Gaussian kernel in order to obtain the smooth *Master-Bias* image (upper right), which also shows the characteristic saddle-shape found for the *FOCES* CCD. The lower left panel shows the stacked *Bias* subtracted by the smooth *Master-Bias*. The histograms in the lower right correspond to the regions in the two images on the left in red and blue that are indicated with a-i. These histograms demonstrate that the remaining noise in the images perfectly follows a gaussian distribution, both before (red) and after (blue) subtracting the *Master-Bias* image, and that the offset of the mean of the distribution is reduced to zero after subtracting the smooth *Master-Bias* for all nine regions. Figure kindly provided by Dr. Liang Wang and modified by me.

5.1.2 Flat-field correction

A typical flat-field correction is usually done with a homogeneous illumination of the CCD to eliminate pixel-to-pixel variations. These deviations in *FOCES* arise from two main sources: different pixels respond differently to light illumination due to manufacturing which is on the level of 1% or less in modern science grade CCDs and fluctuations due to fringing especially in the red part of the CCD. To canonically correct for them, a light source or illumination screen would have to be placed inside fiber-fed Échelle spectrographs to homogeneously illuminating the pupil position and hereby bypassing the order structure on the CCD to create a uniform illumination of the camera chip. In highly stabilized spectrographs - like *FOCES* - it is neither possible nor advisable to place such a dedicated flat-field light source inside the spectrograph since this would contradict all aforementioned efforts to stabilize the whole optical setup.
Therefore a modified flat-field approach was taken, utilizing *Flat* images with the typical order-wise structure of an Échelle spectrograph and identifying sensitivity variations from pixel to pixel along the orders. This is done by producing a so-called sensitivity map $\boldsymbol{\epsilon}_{ij}$,

$$\epsilon_{ij} = \frac{\frac{\sum_{k=1}^{N_{\mathrm{flat}}} F_{ij,k}}{N_{\mathrm{flat}}}}{\mathrm{smooth}\left(\frac{\sum_{k=1}^{N_{\mathrm{Flat}}} F_{ij,k}}{N_{\mathrm{flat}}}\right)}\,, \tag{5.4}$$

which is the quotient of the sum of the 'unsmoothed' *Flat* images, divided by the result of a sophisticated smoothing process which is outlined in the following steps:

- **generation** of a dimensionless representation of the cross-order profile which will be called **'decker'-function** $\mathrm{d}_i(\sigma)$, that is valid within the i-th slice. The σ denotes that the decker function generated as described in the following acts as a normalized "shape template" that is subsequently transformed to fit at any given position along each order (see also Figure 5.5).
  - Every i-th pixels cut trough all orders in cross-order direction (y-direction),
  - combine for every x position all profiles of all orders by fitting them with a gaussian function + offset ($a \cdot \exp\left(-(y-\mu)^2/2\sigma^2\right) + b$) and shifting by μ, subtracting b and normalizing/re-scaling them by a and σ,
  - resample the averaged profile with a step size of 0.1 σ between $\pm 4\sigma$,
  - smooth/filter the profile with Savitzky-Golay filter (Savitzky and Golay, 1964) (window length=9, order=5),
  - remove outlier with 3σ-clipping.

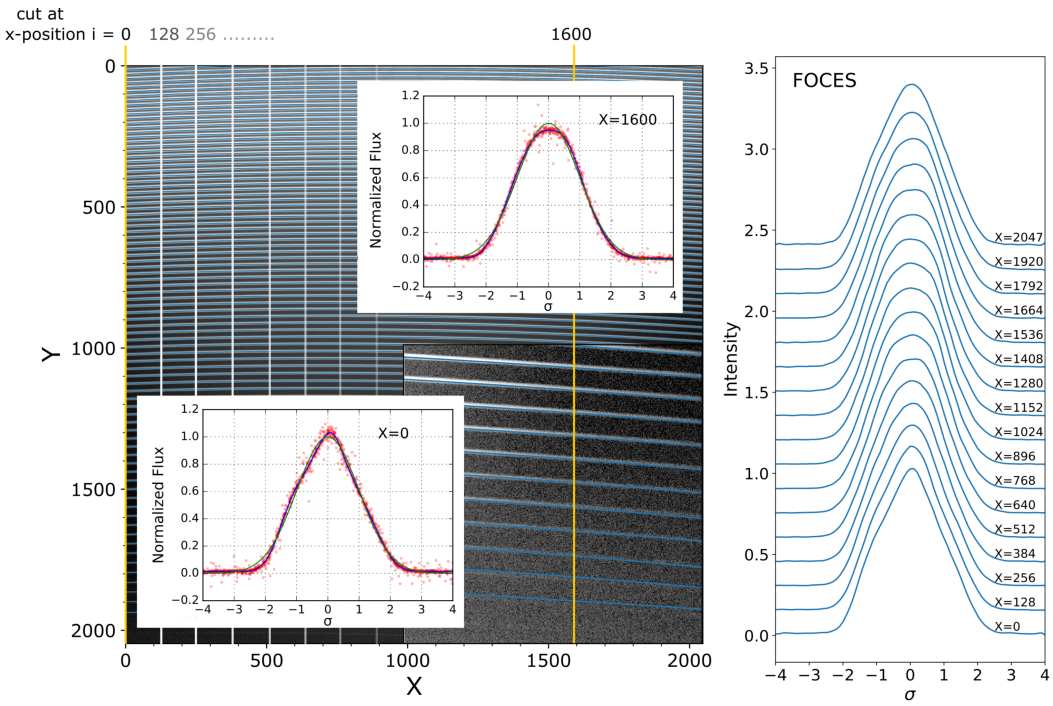

Fig. 5.5.: This combined figure illustrates the procedure used by *GAMSE* for producing the smooth flat that is required for the sensitivity corrections. First the "decker function" is estimated by stacking the cross-order profiles for the 16 columns in the cross-dispersion directions that are highlighted by white and yellow vertical lines. Examples of stacked profiles for different columns are shown in the two inset plots of the left panel. The stacked profiles are then smoothed by applying a Savitzky-Golay filter (blue). Examples for all 16 smoothed profiles are shown on the right. These shapes are then used for reconstructing the *Flat* image by fitting a re-scaled version to the cross-order profile at every 10$^{\text{th}}$ pixel column and interpolating between those. Figure parts kindly provided by Dr. Liang Wang and modified by me.

- **fitting the decker-function to every 10$^{\text{th}}$ cross-order profile** $p_i(y) = A_i \cdot d_i(K_i \cdot y - C_i) + B_i$, with A, K and B as scaling factors on the amplitude, standard deviation of the Gaussian function and background level and in addition C as the shift in the center of the order position. d_i represents the decker-function that changes every i-th pixel; fitting could be performed at every x-position but due to the slow variation of the cross-order profile along the x-axis and for efficiency reasons its is sufficient to perform the fit every 10$^{\text{th}}$ pixel row

- **fitting the scaling coefficients** for an effective smoothing of the order profile (see also Figure 5.6)
  - C, K, B vs. x and for orders contaminated with fringes[7] A vs. x are fitted with a 4$^{\text{th}}$ or lower order polynomial depending on the severity of the fringes
  - orders not affected by fringes: A vs. x are fitted with 7$^{\text{th}}$ order polynomial

- **reconstruction of the smoothed flat field** utilizing the mathematical relation gained in the previous step

The flat image is then divided by the reconstructed smooth flat created as described above in order to obtain the sensitivity map ϵ. All the aforementioned steps are performed on an averaged *Mosaic-Flat* image where all individual *Flats* of one color-type are pixel-wise averaged and in this process 10σ-clipped. Since the red part of a 'Flat' exposure is orders of magnitude brighter than the blue end of the spectrum, 3 separate types of *Flat* (color-type) images with increasing exposure time are taken. Due to that, some regions are intentionally over-exposed in the red part, therefore the colour flats are afterwards stitched together on traces between the orders by always selecting the order from the 3 image types with the best non-saturated S/N-level. The sensitivity correction is applied to all pixels that are above 10% of the brightest pixel value in cross-order direction and that have an SNR greater than 50 (ini-file default value). The reason for that strategy is that the relative errors of that flat-fielding correction increase with decreasing brightness, especially at the edges of the cross-order profile. For small SNR, the contribution of the sensitivity variation between pixels is negligible w. r. t. the photon counting noise. In areas not affected by fringes (blue part of the CCD), the pixel-to-pixel variation of the *FOCES* CCD could be measured using the sensitivity map and was found to be around 0.4%.

5.1.3 Background / stray-light subtraction

Although *FOCES* is already equipped with an intermediate slit for reducing the amount of stray light reaching the CCD it is still not negligible for the scientific analysis. This stray light is produced by mainly scattering on the optical and mechanical components of the spectrograph and leads to a smooth but non-homogeneous background. This background cannot be measured within the orders of the Échelle

[7] In *FOCES* orders containing wavelengths $> 700\,\text{nm}$ are heavily affected by fringes caused by the interference of the CCD coating

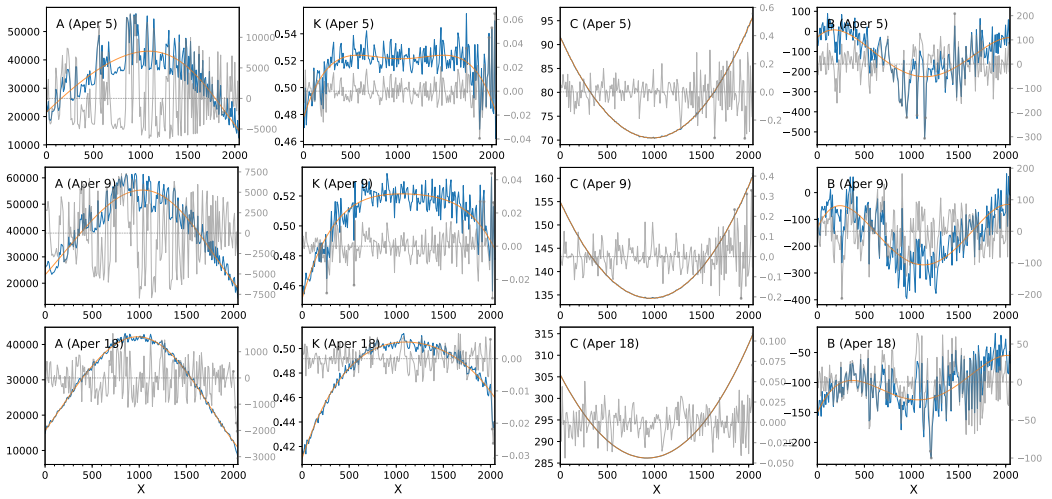

Fig. 5.6.: Polynomial fit to the evolution of the position/scaling parameters used to match the decker function to the cross-order profile at every 10th pixel column. As an example, three Échelle orders (rows) have been picked to show the raw parameter values (blue curves), fitted polynomials (orange curves), and residuals after subtraction (gray curves), for the four parameters A, K, C, B. The term 'Aper' (short for aperture) is by the definition of *GAMSE* an order but not numbered by its physical order number but by its appearance on the CCD e.g. phys. order 65 = Aper 0. Plots kindly provided by Dr. Liang Wang

spectrum but has to be estimated by interpolating the region *between* the orders. To do so, at every x position cuts in the cross-order direction (y-direction) are performed through the image and local minima are identified within the regions between the orders. The identified minima are subsequently interpolated utilizing a cubic spline for a first estimate of the background light which is further treated by a two-step smoothing process starting with a median filter (x=9, y=1) followed by a 2D Savitzky-Golay smoothing (window length=(21, 101), order=3) to obtain a 2D model of the background light. When *FOCES* is operating in the double fiber mode (A=science=star light, B=calibration=(usually) comb light) two distinct stray-light models are obtained (Figure 5.8). The comb stray-light model is created using the calibration image from the daily calibration run in which comb light is fed into fiber B. For the star stray-light model, an exposure taken with only starlight was used. If one or both of these images are not taken during this night, *GAMSE* attempts to find the closest match to the observed star type and closest in time to the observation date single comb image in an *GAMSE* internal data base[8]. To account for brightness differences in the models to the actual $Science$ ($+Comb$) image, the models are fitted using a single parameter as scaling factor for every model. Since the wavelength coverage and shape of the comb light can vary during the course

[8]The database should be regularly reevaluated and extended by all users.

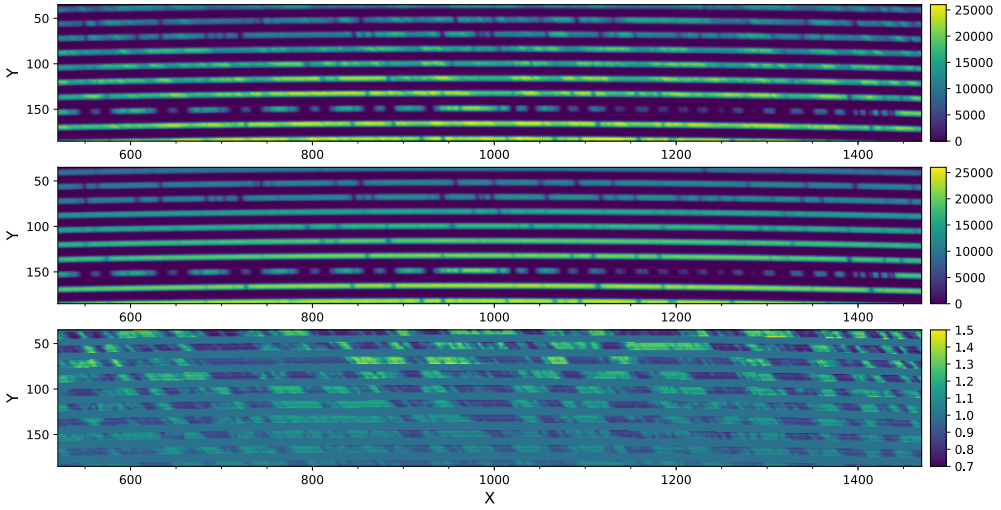

Fig. 5.7.: Comparison of uncorrected, highly fringe affected (upper panel) and flat-field corrected 2D Échelle spectrum (middle panel) of the sun at $\lambda = 760 - 790\mathrm{nm}$ (lower left - upper right) taken with *FOCES*. Lower panel shows the used sensitivity map. Plots kindly provided by Dr. Liang Wang.

of the night quite a bit, it is good practice to always inspect the *GAMSE* quality check plots in the "report"-folder. The aforementioned background subtraction might struggle to remove optical ghost images[9] appropriately. However, since *FOCES* is only weakly affected by this undesirable optical effect with only some minor order ghosts in the blue region of the spectrum, this effect can be neglected.

A flow chart overview of the extraction process of the different 1D data products stored in the *GAMSE* output fits can be found in Figure 5.9.

[9] Contrary to stray-light which is produced by chaotic/non-deterministic light scattering, optical ghosts are undesired deterministic reflections of light which are imaged trough the optical setup. As a result, they can have a quite well-defined shape.

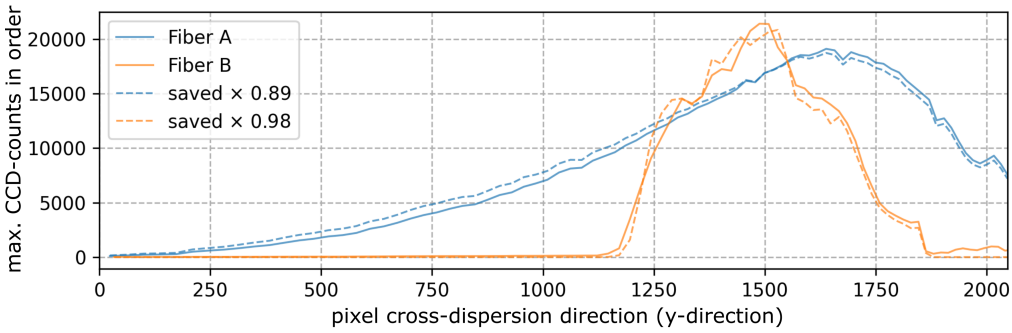

Fig. 5.8.: Illustration of the background estimation procedure used by *GAMSE*. The stray light that diffusely distributes across the CCD chip, also between the orders, is modeled based on special exposures that only illuminate one fiber so that the intensity between the orders can be estimated. The background is then subtracted by fitting the brightness ratio between the single-fiber exposures and the corresponding fiber in the double-fiber science frame for both fibers and subtracting the scaled sum of the background models. The solid lines in the plot show the maximal brightness of the orders in the double-fiber science frame and the dashed lines correspond to the scaled brightness profiles of the single-fiber reference frames.

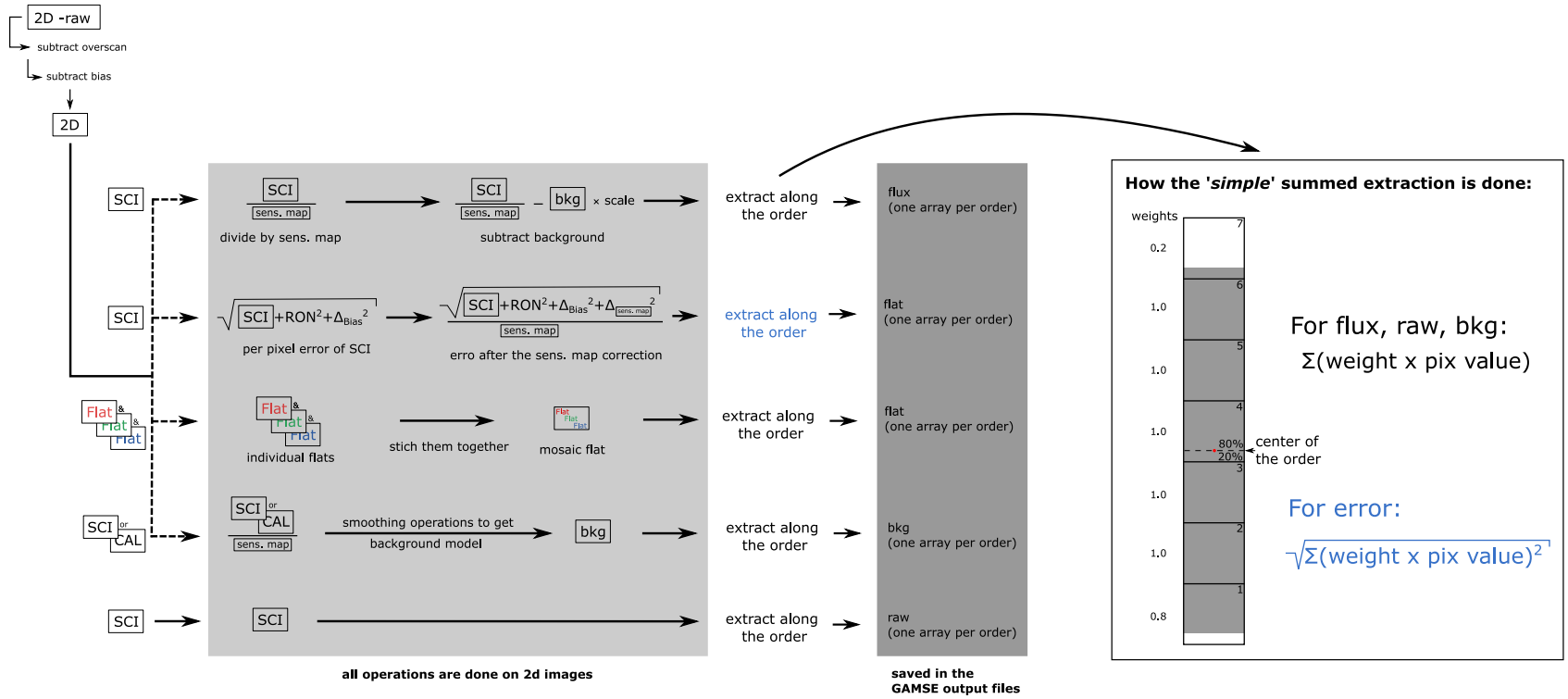

Fig. 5.9.: Visualization of the data reduction performed by the software *GAMSE*

5.1.4 Flux error propagation

The image I_{ij} computed by *GAMSE* before extracting the 1D order-wise spectrum consists of the *Science* frame S_{ij} that is corrected by a sensitivity map ϵ_{ij}, which is a product of the *Flat* image, and subtracted by a scaled background model B_{ij}. The indices *i* and *j* correspond to the x- and y-axis of an image.

$$I_{ij} = \frac{S_{ij}}{\epsilon_{ij}} - bkg_{ij} \cdot s \,. \tag{5.5}$$

The error of the *Science* image is estimated using Gaussian error propagation. This is reasonably well motivated as all the relevant contributions to the error are based on statistical (counting) errors that are independent.

$$\Delta I_{ij} = \sqrt{\left(\frac{1}{\epsilon_{ij}} \cdot \Delta S_{ij}\right)^2 + \left(\frac{S_{ij}}{\epsilon_{ij}^2} \cdot \Delta \epsilon_{ij}\right)^2} \,. \tag{5.6}$$

The background is modeled by a smooth function, the uncertainties of which are highly correlated and can therefore not be treated with Gaussian error propagation. This topic will be further discussed at the end of this section. The errors in the already bias-subtracted *Science* frame S_{ij} that is also affected by readout noise, on top of Poisson noise can be expressed as

$$\Delta S_{ij} = \sqrt{\left(\sqrt{ADU_{ij} \cdot g}\right)^2 + RON^2 + \Delta^2_{\mathrm{Bias}}} \,, \tag{5.7}$$

where ADU_{ij}[10] is the number of photons detected in a given pixel ij, with g as gain[11]. RON is the readout noise of the image and Δ_{Bias} the error introduced by the bias subtraction. The contribution to the total per-pixel error from the overscan subtraction is maximally correlated between pixels (same value for all pixels) and thus does not influence the calculation of RV shifts. It is therefore neglected as it is a very small contributor and would lead to an overestimation of pixel-to-pixel fluctuations. The contribution to the error introduced by the overscan subtraction is a constant value for the entire frame, can therefore not be treated with Gaussian error propagation, and has no significant influence on spectral features. The contribution to the error by the bias subtraction is

$$\Delta_{\mathrm{Bias}} = \frac{RON}{\sqrt{N_{\mathrm{Bias}} \cdot 4\pi\sigma^2_{\mathrm{smooth}}}} \,, \tag{5.8}$$

[10] ADU = **A**nalog-to-**D**igital **U**nits

[11] For *FOCES* and the chosen readout option the gain=1 according to the data sheet of our specific *Andor ikon-L 936* camera model.

where N_{Bias} is the number of bias frames that are combined and σ_{smooth} is the σ of the Gaussian smearing kernel in units of pixels that is applied to the averaged *Bias* frame[12].

The pixel-wise sensitivity correction is based on a stack of *Flat* frames $F_{ij,k}$, where the raw sum is divided by a noise-reduced (smoothed) sum of the frames (with k as the number of frames in that stack).

$$\epsilon_{ij} = \frac{\frac{\sum_{k=1}^{N_{\mathrm{flat}}} F_{ij,k}}{N_{\mathrm{flat}}}}{\mathrm{smooth}\left(\frac{\sum_{k=1}^{N_{\mathrm{Flat}}} F_{ij,k}}{N_{\mathrm{flat}}}\right)} = \frac{\sum_{k=1}^{N_{\mathrm{flat}}} F_{ij,k}}{\mathrm{smooth}\left(\sum_{k=1}^{N_{\mathrm{flat}}} F_{ij,k}\right)}\,. \tag{5.9}$$

The smoothing of the noise reduced *Flat* image (high SNR images) as described above leads to presumably very small and highly correlated uncertainties that are not suited for Gaussian error propagation and therefore not taken into account. The uncertainty of the summed *Flat* images on the other hand is dominating the error of the sensitivity map and can consequently not be ignored in the error estimation.

$$\Delta\epsilon_{ij} = \frac{\Delta\left(\sum_{k=1}^{N_{\mathrm{flat}}} F_{ij,k}\right)}{\mathrm{smooth}\left(\sum_{k=1}^{N_{\mathrm{flat}}} F_{ij,k}\right)} = \frac{\sqrt{\sum_{k=1}^{N_{\mathrm{flat}}} (\Delta F_{ij,k})^2}}{\mathrm{smooth}\left(\sum_{k=1}^{N_{\mathrm{flat}}} F_{ij,k}\right)}\,. \tag{5.10}$$

The uncertainty of the per-pixel values of the *Flat* images $\Delta F_{ij,k}$ are computed in analogy to the error of the science image (Equation 5.6). In case the aforementioned assumption $\Delta F_{ij,k} \approx \sqrt{F_{ij,k}}$ is valid, the relative error of the sensitivity map correction can be expressed as:

$$\frac{\Delta\epsilon_{ij}}{\epsilon_{ij}} = \frac{1}{\sqrt{\sum_{k=1}^{N_{\mathrm{flat}}} (\Delta F_{ij,k})^2}}\,, \tag{5.11}$$

where the noise-reduced smoothed flat image cancels, which simplifies Formula 5.6 to

$$\Delta I_{ij} = \frac{1}{\epsilon_{ij}} \sqrt{\Delta S_{ij}^2 + \left(S_{ij} \cdot \frac{\Delta\epsilon_{ij}}{\epsilon_{ij}}\right)^2}\,. \tag{5.12}$$

The last analysis step performed by *GAMSE* is the extraction of the 1D order-wise spectra from the fully corrected 2D image along the order trace. For this extraction, a certain number of pixels, centered on the order trace is summed along the cross-order direction. As the order trace slowly drifts in the cross-order direction while moving along the Échelle order, in order to avoid aliasing effects, the first and last pixel in the column are added with a weight w_j that depends on the distance to the

[12] The factor $4\pi\sigma_{\mathrm{smooth}}^2$ in the denominator has been found empirically using a toy-MC simulation.

center of the order trace. See also Figure 5.9 on the right for an illustration. The total light flux can thus be expressed as a weighted sum,

$$J_i = \sum_{j=1}^{N} I_{ij} \cdot w_j \,, \tag{5.13}$$

where w_j is the fraction of the pixel that lies within the extraction band. For the flux error one then obtains

$$\Delta J_i = \sqrt{\sum_{j=1}^{N} (\Delta I_{ij})^2 \cdot w_j^2} \,. \tag{5.14}$$

This is the error that is stored with the output spectra of *GAMSE*. Within *MARMOT*, this error is specifically important for the χ^2 fits to the spectra that are performed for wavelength calibration, generating the templates, but also for extracting the radial velocity values (see Section 5.7). These errors can also be used for estimating the uncertainty of the cross-correlation method for radial-velocity measurement via a Monte Carlo approach (see Section 5.8).

The final data product of *GAMSE* is stored in FITS format in a binary table. A schematic view of the output structure can be found in Figure 5.10. 1D spectra of both fibers (A = Science and B = Calibration) are available as rows, order by order, the content of which can be found in Table 5.2.

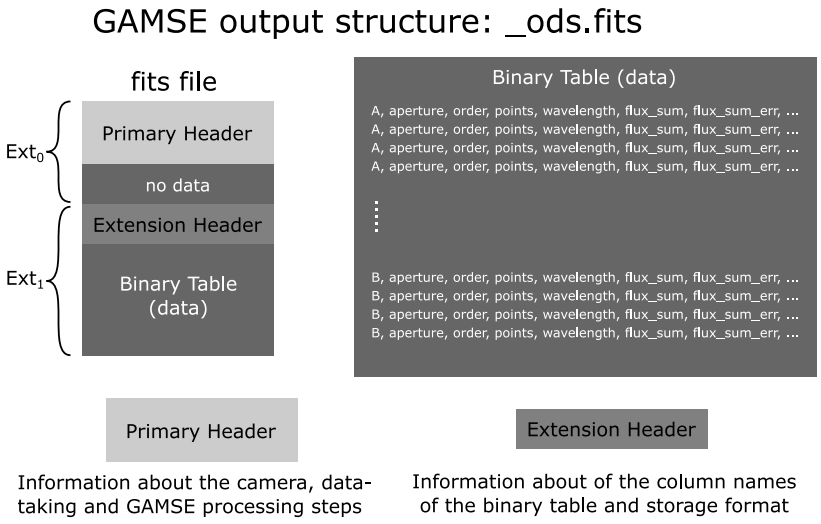

Fig. 5.10.: Schematic overview over the structure of the output fits-file of *GAMSE*. In case only one fiber was recorded only the output for this fiber is stored in the fits-file. The *Primary Header* contains all information about the CCD camera, data taking process, telescope data and information about processing steps performed by *GAMSE*. The first *Extension Header* lists the storage format and names for the individual columns of the binary table.

Tab. 5.2.: Content stored in FITS file as the output of *GAMSE* for every fiber and order of an image. For columns marked with (I/P), the routines are not yet fully implemented, therefore these output arrays are empty.

column name	type	content / comments
fiber	str	fiber type 'A'=science or 'B'=calibration
aperture	int (16-bit)	numerical aperture/order
order	int (16-bit)	physical order of the grating
points	int (16-bit)	number of bins (usually bin=pixel)
wavelength	array float (64-bit)	wavelength for every bin
flux_sum	array float (32-bit)	summed flux values
flux_sum_err	array float (32-bit)	error of the summed flux values
flux_sum_mask	array float (32-bit)	mask for the summed flux values
flux_opt	array float (32-bit)	optimal extraction flux values (I/P)
flux_opt_err	array float (32-bit)	optimal extraction flux error values (I/P)
flux_opt_mask	array float (32-bit)	mask for optimal extraction flux values (I/P)
flux_raw	array float (32-bit)	raw flux
blaze	array float (32-bit)	blaze estimate
flat_sum	array float (32-bit)	summed flat values
flat_raw	array float (32-bit)	raw flat values
flat_bkg	array float (32-bit)	background/stray-light estimation flat
background	array float (32-bit)	background/stray-light estimation flux

5.2 Program structure of *MARMOT*

MARMOT is a software package written in Python 3, where an object-oriented approach has been chosen, in which the classes in the code map the logical structure of the input data onto nested objects (see Figure 5.11 for an illustration), containing a class for every:

- analysis of a science target (`RVAnalysis`),
- every frame contributing to the analysis (`EchelleFrame`),
- every Échelle order in every frame (`EchelleOrder`).

Conceptually, *MARMOT* is a software suite similar to for example the no longer maintained software IRAF[13] but following a purely object-oriented approach in which the data can also be stored in the object itself. *MARMOT* therefore offers methods to conduct individual analysis steps (template creation, RV estimation etc.) which have to be executed and optimized by the user in the form of a script. An example of such a script can be found in Appendix 9.7. The individual steps of the analysis are provided as class methods acting on the different types of objects and thereby manipulating/extending their content (For an example on how to access the data see also Figure 5.12). At any step of the analysis the `RVAnalysis` object can be stored using *pickle*[14] in order to save the progress. In addition, it is possible for computationally intense analysis steps to be executed on multiple CPU cores, which is achieved by processing individual frames on separate cores using the Python package *multiprocessing*[15] and products of the aforementioned procedures can even be stored separately (for example the template generation, see also Section 5.6). Thus, an already existing analysis project created with *MARMOT* can be extended with additional data without reprocessing the whole data set. Important settings for configuring an analysis with *MARMOT* can be provided to the software via an ini-file (an example can be found in Appendix 9.8). Figure 5.13 outlines an exemplary workflow of an analysis with *MARMOT*. This example does not only show a single possible workflow but already highlights some of the available choices up to the user and which depend on data quality and scientific goals.

[13] *IRAF* documentation: `https://iraf-community.github.io/`
[14] *pickle* documentation: `https://docs.python.org/3/library/pickle.html`
[15] *multiprocessing* documentation: `https://docs.python.org/3/library/multiprocessing.html`

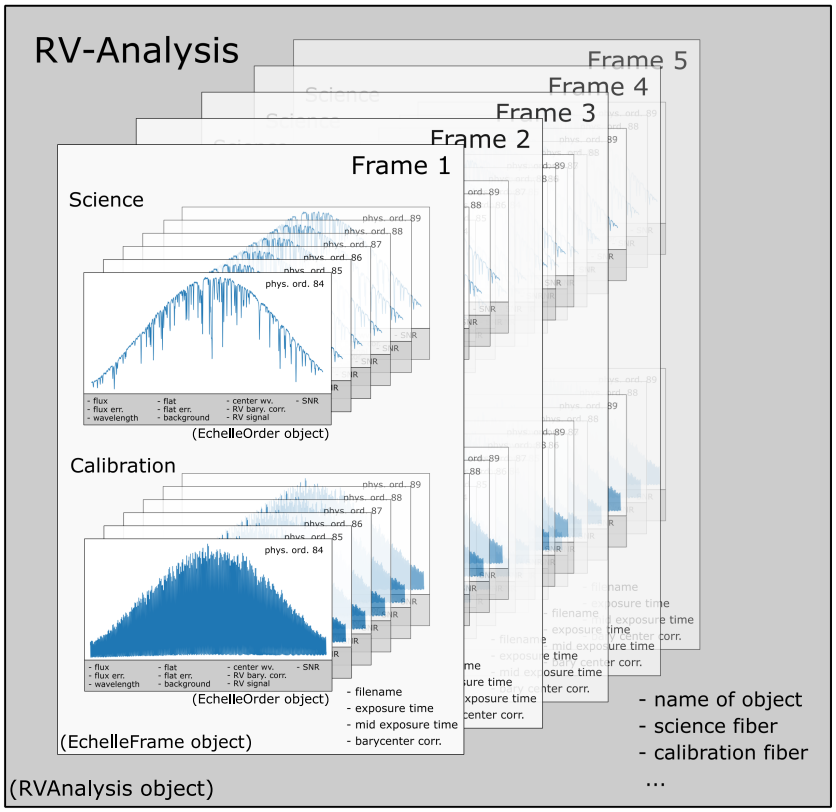

Fig. 5.11.: Illustration of the nested structure of objects used by *MARMOT*. Each analysis session is stored in a single container object (`RVAnalysis`). This in turn consists of a list of container objects for each frame (`EchelleFrame`). The last structural object is one Échelle order (`EchelleOrder`) that stores all the relevant data of the measurements. The listings in the lower right corner of every object (represented by a box) indicate important properties stored within that object.

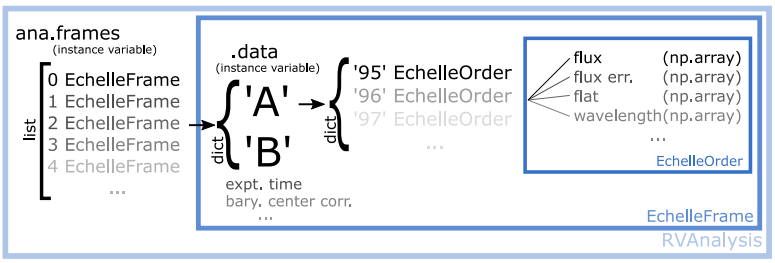

example: ana.frames[2].data['A']['96'].flux

Fig. 5.12.: Illustration of the data organization and structure within the nested objects of *MARMOT*. In this example *ana* is an instance of the `RVAnalysis` class, which stores all the information corresponding to an entire data set. The data structures indicated in the image above refer to python lists and dictionaries and can therefore be accessed as such. `EchelleFrame` can be accessed via their numerical index while `EchelleOrders` and their content can be accessed via the identifier of the fiber and the physical order.

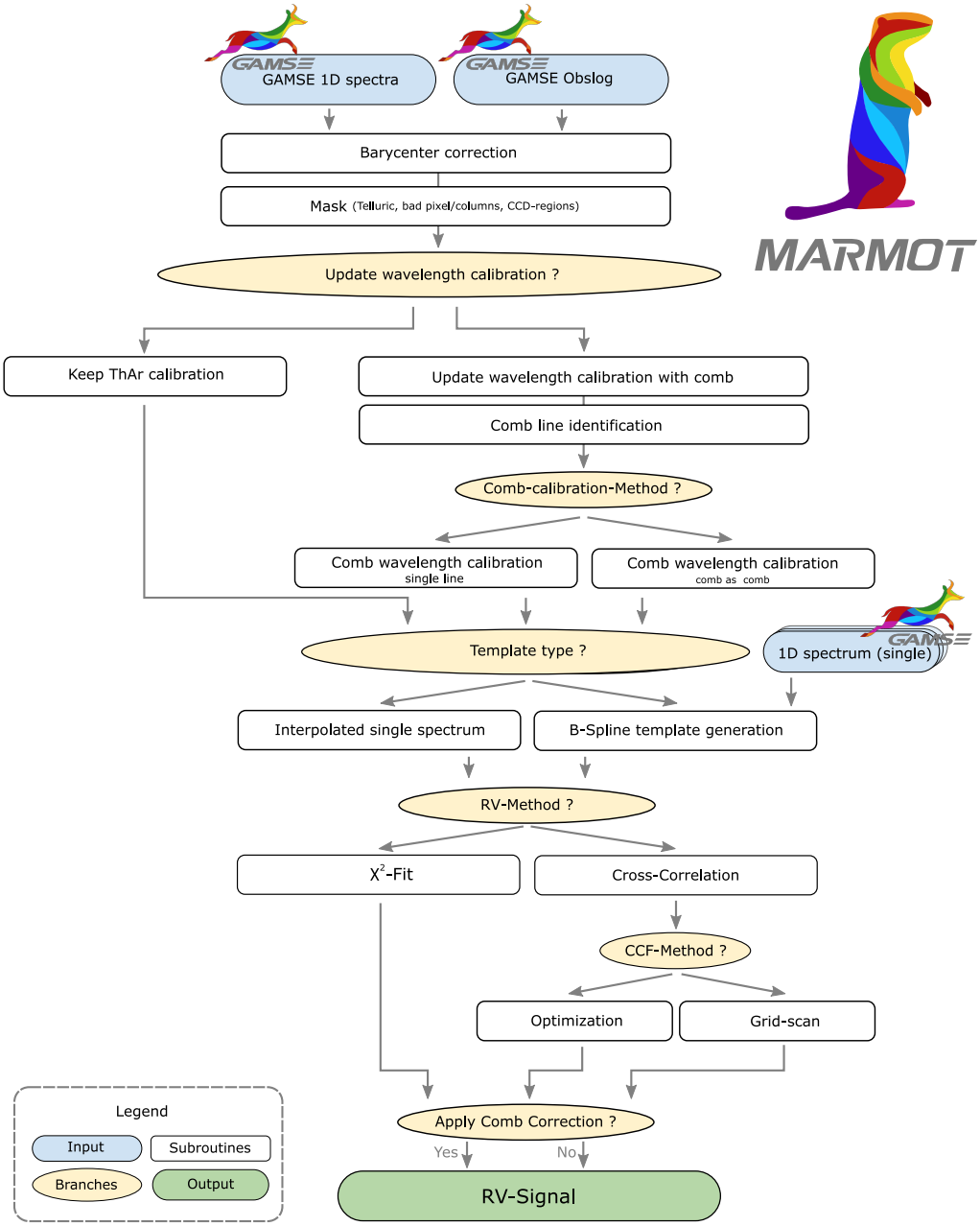

Fig. 5.13.: Possible program flow chart of a radial velocity analysis with the software package *MARMOT*. The program offers a variety of methods for the individual tasks. At the branching points highlighted by yellow ellipses, the user can choose between different options. The choice may depend on the shape and quality of the spectrum and on how much computing time the user is willing to invest.

5.3 Overview over the essential functions of *MARMOT*

MARMOT comprises routines for all analysis steps from order-wise 1D Échelle spectra to exposure-wise, comb calibrated radial velocity measurements. One of the main aspects of the program is that it allows to use simultaneously recorded data from a laser frequency comb for precise contemporaneous wavelength calibration. It is designed in a modular way, such that different steps of the RV determination can be exchanged flexibly and tailored to the specific problem. There are three main features implemented in *MARMOT* that offer different options:

- the *wavelength calibration* can be refined by using LFC data (Section: 5.4);
- the *template spectrum* for the observed star can be generated either by an interpolation of a single observed spectrum or by a combined B-spline fit (inspired by Zechmeister et al. (2018)) of several observed spectra (Section: 5.6);
- the *RV shift* between the observed and the template spectrum can be obtained either by calculating a cross-correlation function (CCF) and locating its maximum or by performing a χ^2 fit of the template to the data (Section: 5.7).

In addition, *MARMOT* offers a function to remove excessive comb calibration light from the science fiber in the case of optical cross-talk between the science and calibration channel[16] (Section: 5.5). Furthermore, it is possible to mask regions in the data which are strongly affected by telluric absorption lines or otherwise not suited for RV calculation from the analysis, using exclusion masks (see also Appendix 9.8).

To test all the aforementioned options *MARMOT* is equipped with a function to utilize existing theoretical calculated spectra and to adapt them to reassemble *FOCES* spectra including sampling them with the resolution of *FOCES*, options for different physical smearing kernels (like for micro-turbulence) and even creation of these file in the *GAMSE* output format.

Besides that, *MARMOT* offers a number of auxiliary functions such as the calculation of barycenter velocity correction for each frame using the Python package *barycorrpy*[17,18] by Wright and Eastman (2014) (see also Kanodia and Wright (2018)) and getting astronomical information like relative moon position and phase or height above the horizon.

[16] This only ever happens when the comb light was set far too bright.

[17] *barycorrpy* download: `https://github.com/shbhuk/barycorrpy`

[18] It is worth noting that *barycorrpy* is downloading data from a US government website, which might fail as these websites might be geo-blocked depending on the user's country of access.

In the following chapters, the utilities for wavelength calibration, spectral template generation and RV-shift calculation, as well as the FFT-based method for removing frequency-comb lines from the science data will be presented in more detail. Many of the auxiliary features of *MARMOT* that either serve the data preparation or utilities helping the user visualizing the data are purely technical and serve no physical reasoning, thus they are only mentioned in the detailed software documentation of *MARMOT* on the internal web page of the Wendelstein group where a comprehensive overview of all function is provided.

5.4 Laser frequency comb based wavelength calibration

During the daily calibration run, ThAr spectra are recorded at least once a night, either before or after the science data, which enables *GAMSE* to perform and provide at least a coarse wavelength calibration. This is done by taking the ThAr spectrum and assigning the same wavelength solution to every science exposure. This implies that intra-night drifts of the instrument are not accounted for. Along with science light, the user of *FOCES* has the option to request simultaneous comb calibration during data taking. As it is described in detail in Chapter 3.2.1, in *FOCES*, the science light, typically from a star, and the light from the LFC are fed into the spectrograph simultaneously[19] using a multi-fiber slit assembly (Kellermann et al., 2019). The purpose of the simultaneously recorded LFC spectra is to enable frame-by-frame corrections that account for intra-night drifts in the system and thereby improve the RV accuracy and precision. This light, which enters the spectrograph through a separate fiber is mapped to the CCD in its own separate set of Échelle rows and is afterwards extracted by *GAMSE* as 1D order-wise spectrum and is hereafter called "calibration" or "B-fiber" spectrum, while the spectrum extracted from the fiber that is connected to the telescope is referred to as "science" or "A-fiber" spectrum. Assuming that the changes in the B-fiber are a good representation of shifts occurring in the A-fiber, intra-night drifts of the whole instrumental setup can be corrected. For a study on this assumption see also Section 3.2.3.2.

[19]The comb spectrum does not cover the entire wavelength range of *FOCES*. The highlighted Échelle orders in Appendix 9.5 mark therefore orders where comb light is available.

For this purpose, different methods are available which can be categorized into two groups which offer different options to the user:

- individual comb line correction (`calc_comb_corr`),
- updated and refined wavelength calibration which offers two options:
  - canonical wavelength calibration using comb lines (`apply_comb_wv_cal`),
  - fitting the comb as comb (`apply_comb_wv_cal`, Option: `CombAsComb`).

All methods above have in common that they require the determination of the line centroid and identification of the aforementioned comb modes. For this reason, the following section provides an overview of the techniques accomplishing this, implemented in *MARMOT* before breaching into the description of the different comb correction options.

5.4.1 Comb line determination and identification

As described in Chapter 2.4.2, the frequency of each comb line is exactly defined by

$$f_n = n\, f_{\mathrm{rep}} + f_{\mathrm{CEO}}. \tag{5.15}$$

Both f_{frep} and f_{CEO} are referenced by a Rubidium atomic frequency standard and therefore known with extreme precision. This implies that the "true" wavelength of each comb line can be exactly predicted by:

$$\lambda_{i,\mathrm{air}} = \frac{\lambda_i}{n_{\mathrm{air}}} = \frac{c}{n_{\mathrm{air}}\, f_n}, \tag{5.16}$$

with the refractive index of air, n_{air} and the vacuum speed of light c. The first task of *MARMOT* is therefore twofold by firstly the determination of the center of every comb line and secondly by assigning and identifying the individual frequency comb mode number n to the aforementioned comb lines.

5.4.1.1 Comb line centroid determination

The centroid determination of the comb lines is not trivial, due to several different factors such as:

- the overall envelope functions,
- background photons beneath the comb lines,
- sampling of a single comb line with only 5-7 pixels.

Envelope function

The first problem arising is that the comb light is modulated with several different envelope functions such as for example the blaze function of the spectrograph or even the spectral flattening function in the comb itself. These envelope effects distort the shape of every comb line in a slightly different way. Hereby moving the centroid of each comb line in a different manner which has an adverse effect especially when these functions change with time.

Floor of background photons

The second problem mentioned above is the underlying background which is mainly caused by two effects: spontaneous emission of photons during the process of spectral broadening, where visible light is created from the initial infrared comb spectrum in the PCF (see also Chapter 2.4.2.3) and the fact that the tails of the resolution function of neighboring lines overlap to some extent. This floor of photons can change due to alignment effects, which themselves can be triggered by environmental changes inside the comb itself or for example due to aging of the PCF. Like the envelope effect, this can detrimentally change the estimated center position of the comb lines over time and in order to allow for an accurate and unbiased centroid measurement the background light and the envelope effect, have to be removed.

To remove these effects in a first step local minima (for the background) and maxima (for the envelope) in the spectrum are identified. Thereafter a spline with a low number of equally spaced knots (ten for the background, five for the envelope) is fitted to those data points. This is done in an iterative process, where after each iteration lower/upper outliers are excluded from the fit via sigma clipping for the envelope/background estimation (see also Figure 5.14 upper and middle panel). The comb spectrum is then, background subtracted and subsequently normalized by the envelope function determined in this way.

In case of the background, it has been found that sometimes its shape shows structures that are difficult to remove with a spline fit. This is usually the case when periodic structures with relatively high frequency appear in the comb spectrum. This effect is probably related to the type, alignment and aging effects in the PCF that is used for broadening the spectrum of the comb but is still under further investigation by the comb manufacturer *Menlo Systems*. In those cases, one can switch to a procedure where local minima are identified, a Gaussian smearing is applied and the resulting values are interpolated using a cubic spline (see also Figure 5.14,

lowest panel). In contrast to the previously mentioned effects, the varying intensities between neighboring comb lines, which can either be intrinsic or a result of sampling onto the CCD pixels, are not corrected by *MARMOT*. This is intentional, as correcting intrinsic effects of the comb would bias the fitted centroid position of the comb lines. Since it is not possible to disentangle the intrinsic brightness differences from the ones introduced by the CCD sampling, the following approach was chosen.

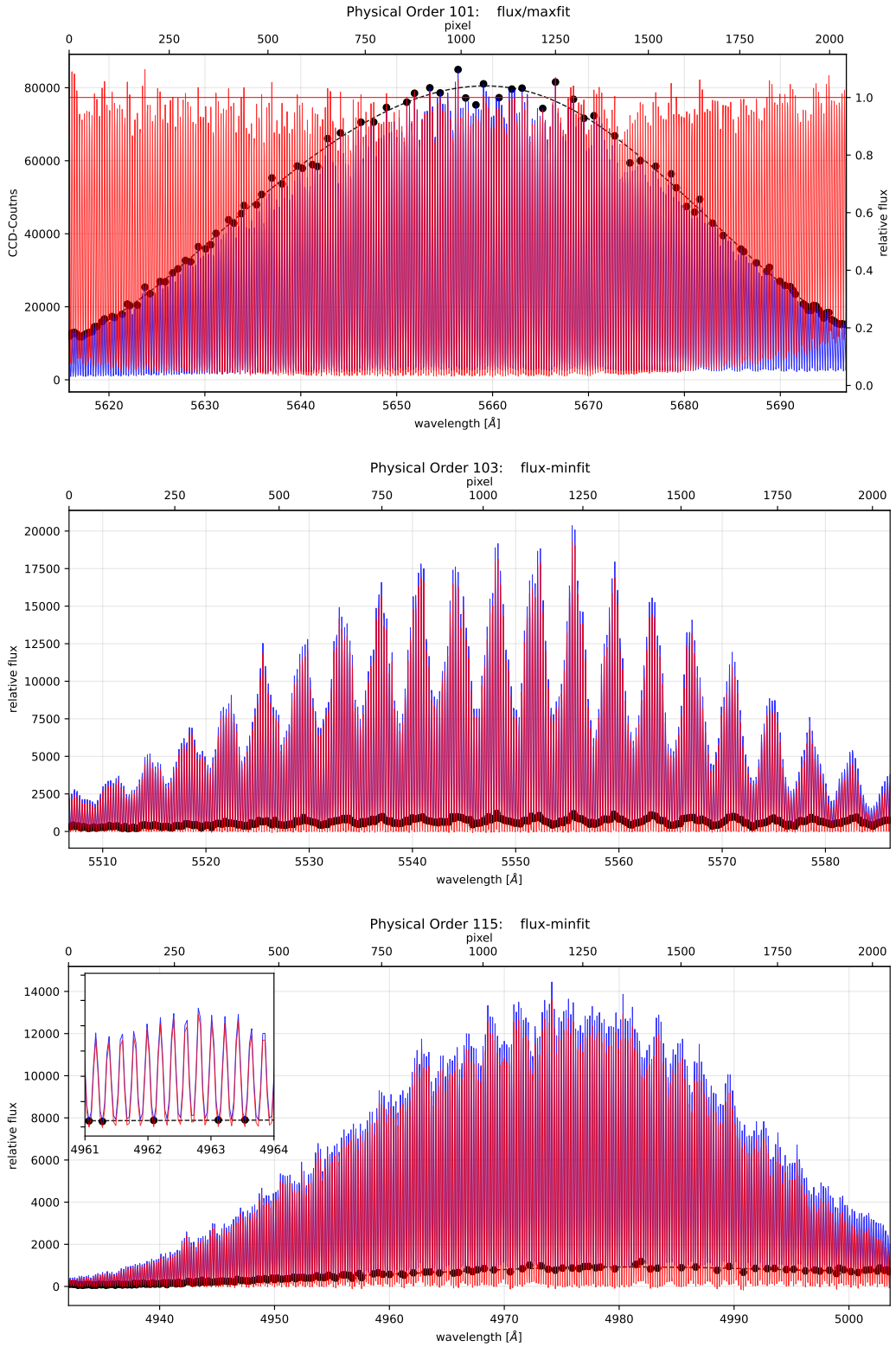

Fig. 5.14.: Upper panel: Blaze function removal of a comb spectrum. Middle & Lower panel: Illustration of the background removal methods. While the middle panel gives an example for the background removal with the Gauss smearing method, in the lower panel the spline fit is utilized. A zoomed inset where the individual comb lines can be resolved is shown in the top left corner.

Sampling of a comb line

The third challenge which was mentioned above is that a single comb line is only sampled by a maximum of 5-7 pixels (minima between the comb peaks) depending on its position in the spectrum. As discussed before this also leads to wings of neighboring comb lines overlapping and together with the sampling effect on the CCD results in a distortion of the lines which can even change over time, with changes of the refractive index in the spectrograph due to temperature and pressure changes. This ultimately leads to errors in the centroid estimation. A natural solution would be to fit a sloped background to every comb line (which was done during the calibration run of the FOCES-LFC in La Silla at the HARPS spectrograph (Probst et al., 2020)). However, this is not advised or suitable since this would lead in some places of the CCD to an under-constrained fit (with zero or less free parameters for the fit; 5 or less data points and 5 parameters : Gaussian: amplitude, center, sigma, line: slope, y-intercept). To solve this problem *MARMOT* offers two solutions:

- by either estimating and removing the background as mentioned before, followed by a single line fit with a Gaussian function or
- by performing a combined and simultaneous fit of three neighboring lines together with a parabola as background estimator and only taking the resulting parameters from the middle line.

Note that it is still possible to subtract the background as in the first option before performing the triple peak centroid estimation). The fit function (with 12 fit parameters) evaluated in pixel coordinates x can be described as:

$$F_{\mathrm{fit}}(\boldsymbol{\mu}, \boldsymbol{A}, \boldsymbol{\sigma}, \boldsymbol{p}, x) = \sum_{i=1}^{3} A_i \, \exp\left(-\frac{(x-\mu_i)^2}{2\,\sigma_i^2}\right) + \sum_{j=0}^{2} p_j \, x^j \,, \tag{5.17}$$

where μ_i are the centroids of the comb lines in pixel coordinates, A_i and σ_i are the amplitudes and widths of the Gaussian functions used to describe the comb lines, and p_j are the polynomial coefficients of the parabola. An example of such a fit can be found in Figure 5.15. The information about the line parameters (A_2, μ_2, σ_2) is afterwards stored for each comb mode in each `EchelleOrder` object of each `EchelleFrame` for the analysis of a scientific target.

5.4.1.2 Comb mode identification

For the comb line identification, *MARMOT* expects the 1D spectra that are fed into the analysis to be at least rudimentary wavelength-calibrated. This calibration does not

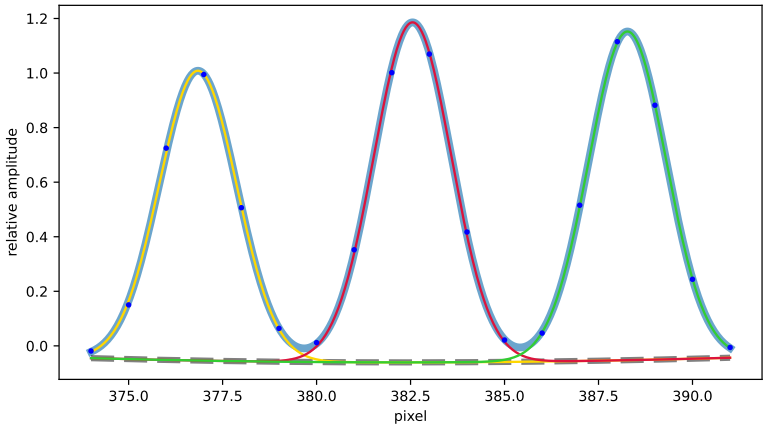

Fig. 5.15.: Illustration of the triple-Gauss fit for comb line centroid determination identification. Only the information of the middle peak is used for further calculations.

need to be extremely precise but should allow to unequivocally identify the individual modes of the LFC in order for this next step of the calibration process to work. Each centroid-estimated comb line in the spectrum is assigned to a theoretically predicted mode if it lies within $0.3\times$ the distance between the comb lines from a theoretical mode. This, naturally, requires the initial calibration to be at least precise down to about one pixel or approximately $2100\,\mathrm{m\,s^{-1}}$, which is easily achievable with a ThAr based calibration. In principle, even a precision down to only about 5 pixels would already work, but the 0.3-criterion has proven to work equally well, with the additional advantage that the probability of accidentally picking up noise in regions with a very weak comb intensity is greatly reduced. Finally, comb lines within a certain region of interest (typically between pixel 200 and 1800) have been individually fitted, their precise centroid position in pixel coordinates, as well as the exact nominal wavelength of the corresponding comb mode, are known.

5.4.2 LFC wavelength calibration and correction

The following section will give an overview of the main 3 options implemented in *MARMOT* on how to correct the science spectrum utilizing the simultaneously recorded comb light in the calibration fiber.

The first and more ad-hoc method for frame-to-frame correction of the RV measurements computes the average RV drift of the calibration spectrum by evaluating the differences between centroid positions for all comb lines. The drift that is found in the calibration data this way is then subtracted from the RV measurements that are based on the spectrum of the science fiber.

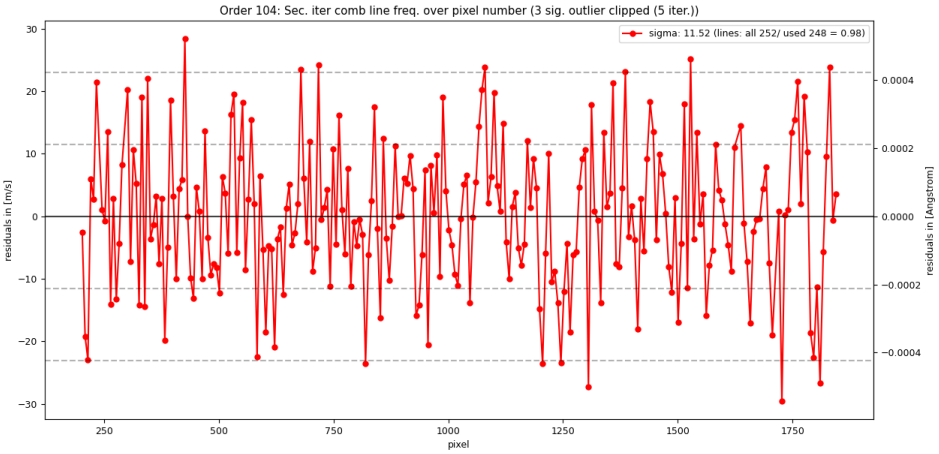

Fig. 5.16.: Example of the residuals after subtracting the 5th order polynomial fit from the location of individual comb lines. The remaining scatter for single lines is about 12 m/s RMS.

The second category of options uses the precise knowledge of the exact nominal position of each comb line for a frame-by-frame, order-by-order improved wavelength calibration. Such a re-calibration automatically adjusts for drifts in the spectra of different frames and therefore corrects the final RV measurements. For the `apply_comb_wv_cal` method, this is achieved by fitting a 5th order polynomial to the center points of the comb mode's "true" wavelength vs. fitted pixel value) using again the minimizer of MINUIT. Finally, the resulting 5th polynomial is evaluated at each pixel, resulting in a refined wavelength calibration, unique for each frame, as shown in Figure 5.16). The other approach that has been explored in this thesis regarding LFC-based wavelength calibration is fitting a joint model for the entire comb spectrum (Option `CombAsComb` in `apply_comb_wv_cal`). Thereby, every peak of the more than 200 comb lines in an Échelle order is modeled by a Gaussian, while the additional pedestal/background is modeled with a polynomial. The blaze function is computed and removed before the fit, in order to prevent a high degree of degeneracy in the parameters, especially the amplitudes of individual comb lines and the blaze function. In this model, only the amplitudes of individual lines and those of the background model are actual free parameters. The location of the lines is defined by the wavelength calibration that is modeled as a polynomial $\lambda(x, \boldsymbol{p}_{wl})$, as in the previous method. Therefore, it provides the actual sought-after set of parameters. Also, the evolution of the line widths along the order is modeled by a polynomial

$\sigma(x, \boldsymbol{p}_{lw})$ reducing the number of free parameters significantly. The full model can be expressed as

$$
\begin{aligned}
&F_{\mathrm{fit}}(\boldsymbol{A}, \boldsymbol{p}_{\mathrm{wl}}, \boldsymbol{p}_{\mathrm{lw}}, \boldsymbol{p}_{\mathrm{bkg}}, x) = \\
&= \sum_{i=1}^{N} A_i \, \exp\left(-\frac{(\lambda_i - \lambda(x, \boldsymbol{p}_{wl})^2}{2\,\sigma(x, \boldsymbol{p}_{lw})^2} \right) \qquad + \sum_{l=0}^{N_{\mathrm{bkg}}} p_{\mathrm{bkg},l} \, (x - x_0)^l \\
&= \sum_{i=1}^{N} A_i \, \exp\left(-\frac{(\lambda_i - \sum_{j=0}^{N_{\mathrm{wl}}} p_{\mathrm{wl},j} \, (x - x_0)^j)^2}{2\,(\sum_{k=0}^{N_{\mathrm{lw}}} p_{\mathrm{lw},k} \, (x - x_0)^k)^2} \right) \quad + \sum_{l=0}^{N_{\mathrm{bkg}}} p_{\mathrm{bkg},l} \, (x - x_0)^l \,, \qquad (5.18)
\end{aligned}
$$

where A_i and λ_i are amplitude and nominal wavelength of each comb line. Only A_i is a free parameter of the model, the λ_i are an intrinsic physical property of the frequency comb. The other free parameters of the model are the coefficients of the three polynomials that are used to describe the background from spontaneous emission ($p_{\mathrm{bkg},l}$), the evolution of the line widths along the order ($p_{\mathrm{lw},k}$) and the coefficients of the polynomial which describes the wavelength calibration in terms of a mapping between pixels and wavelength ($p_{\mathrm{wl},j}$), which are the sought-after variables.

Although the fit usually converges and provides a good solution for the wavelength calibration, it is very computationally expensive, which is the reason why this method was not applied to larger data sets. An example plot of a comb spectrum fitted with this model is shown in Figure 5.17.

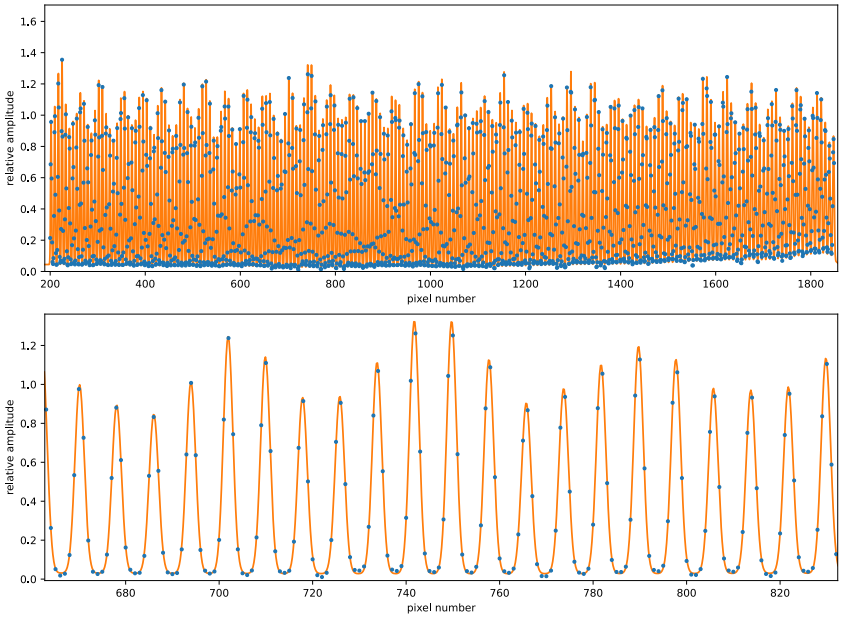

Fig. 5.17.: Upper panel: Full frequency-comb model fit to LFC spectrum. Lower panel: Enlarged excerpt of the fit.

5.5 Cleaning comb light contaminated science spectra

As is demonstrated in Section 5.10.2, the LFC-based re-calibration of stellar spectra leads to a great improvement in the accuracy of the RV measurements. However, in the rare case when the light intensity in the calibration fiber is much stronger than in the science fiber, this way of calibrating may also lead to problems. Diffraction effects in a rectangular slit are unavoidable and therefore the tail of the diffraction pattern of neighboring orders leak into the adjacent order to some degree. If the LFC is attenuated correctly, then this effect only has a minor impact on the science data. However, in case the LFC is too bright, then the residual light in the science spectrum can even be visible directly by eye, as is shown in the blue spectrum of Figure 5.18. This may have adverse effects when analyzing the data using either the CCF or the template fit method and ultimately bias the RV measurement. In order to deal with

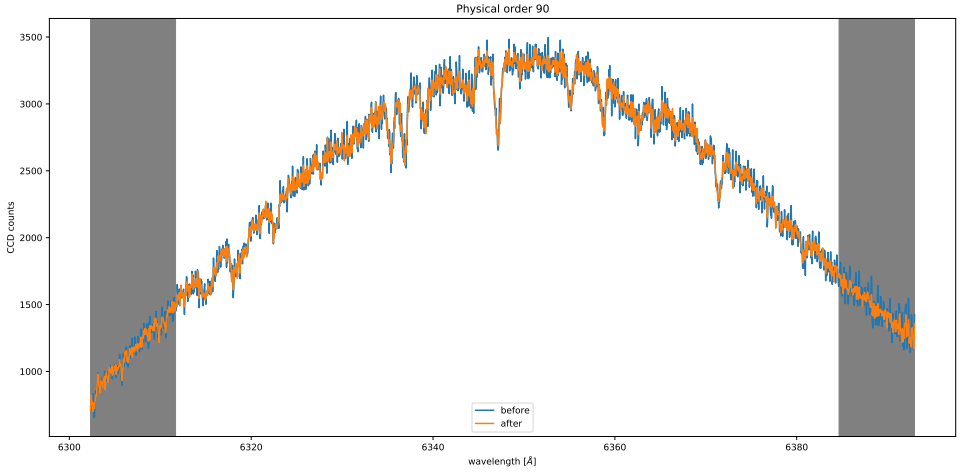

Fig. 5.18.: Example of a spectrum before (blue) and after (yellow) the removal of the comb light that leaked into the star spectrum. The influence of the comb structure is clearly visible in the blue spectrum.

such data an fast Fourier transform (FFT)-based technique has been implemented into *MARMOT* that allows to remove these patterns (`fft_comb_remove_all`). This method exploits the fact that the LFC spectrum is highly periodical and therefore also the residual spill-over effects into adjacent orders are as well. Consequently, this implies that any contamination of the stellar spectra caused by the LFC should be clearly visible in the Fourier spectrum.

In a first step, the spectrum is converted from wavelength to frequency, as this is where the features in the FFT are expected to be strictly periodic. After that, the FFT is computed for both the science and the corresponding calibration spectrum, an

example of that can be seen in Figure 5.19. The main peak stems from the frequency

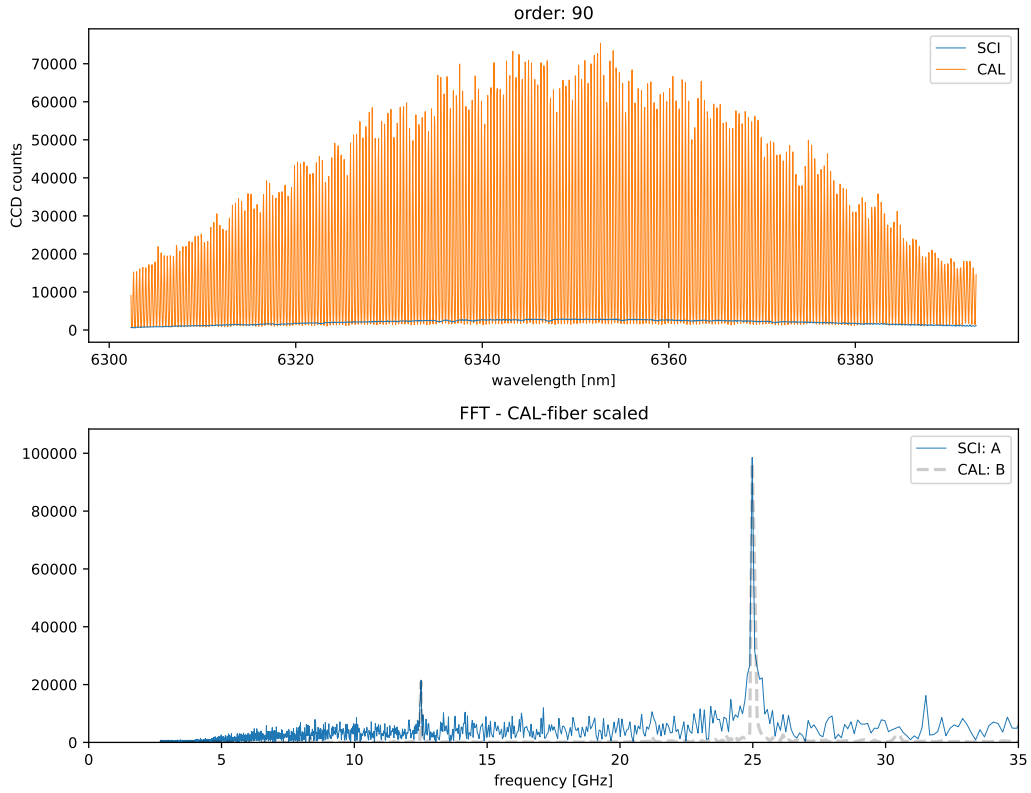

Fig. 5.19.: Upper panel: Spectrum from neighboring orders to highlight that the comb light was set far too bright due to a user error.
Lower panel: FFT spectrum of both fibers scaled so that the highest peaks match in height for better visualization.

spacing of the comb lines which is 25GHz for our particular comb. The strategy that is used for removing spill-over effects from the LFC in *MARMOT* is to eliminate the frequency component that corresponds to the LFC line spacing entirely from the Fourier spectrum - set to zero - and transform/convert back into wavelength space. The regions that are to be removed from the Fourier spectrum are not identified in the science spectrum but instead in the corresponding (closest) calibration Échelle order where they can be guaranteed to be the strongest feature above a certain frequency. Thus identified regions are subsequently set to zero in the FFT of the science spectrum. See Figure 5.20 for an illustration of the process and the yellow spectrum in Figure 5.18 for an example of the spectrum after comb removal.

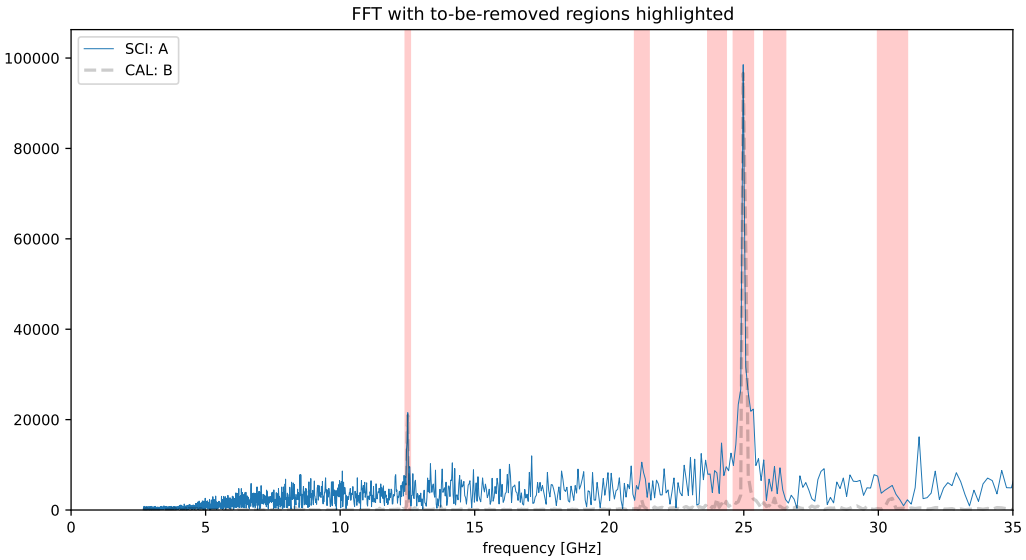

Fig. 5.20.: Science and the calibration FFT spectrum of the same physical order scaled so that the highest peaks match in height for better visualization. Regions in the spectrum to be removed are shaded red.

5.6 Template generation

One of the goals that are pursued with *MARMOT* is to accommodate different techniques for computing the radial velocity changes of stars, namely using a CCF as well as a χ^2 fit. It is therefore advantageous not to use discrete spectral templates but instead to generate and store spectral templates as parametric functions. This way, they can be evaluated for any given RV or wavelength shift, which makes using them in a fit much easier.

The simplest way of obtaining such a template spectral function is to use a sample spectrum with high SNR and just interpolate the data points. However, no matter if a linear or higher-order interpolation is used, the template will not be a fully realistic representation of the stellar spectrum, which is then inevitably affected by the binning induced by the CCD pixel structure. Additionally, statistical fluctuations are also "baked into" the template function this way. Higher order-like cubic-spline-interpolation might even amplify the noise structure in the data. This can lead to biases and aliasing effects when extracting the radial velocity shift, independently of whether the signal is extracted using the CCF or using a χ^2 fit further down in the processing. This is partially solved by stacking several sample spectra. However, a certain degree of smearing due to radial velocity changes between measurements is unavoidable.

A better solution was found in fitting the data points of one or several measured spectra with a smooth function. A high-order polynomial is not suited for this purpose, as in reaching the required level of complexity, the high powers in the function render it unstable. Further computational issues arise from the high degree of correlation between the polynomial coefficients that render the approach even more numerically unstable. *MARMOT* uses so-called cubic B-splines, which are cubic splines that are defined by control points that guide the shape of the function. The wavelength coordinates of the control points are chosen to lie on a uniform grid, while the corresponding flux coordinates form the parameters of the fit. The grid is thereby deliberately chosen in such a way that the control points do not coincide with the pixels. This grid is equally spaced in wavelength, but with a larger spacing than the pixel width. It was found that using $N_{\mathrm{knots}} = N_{\mathrm{pix}}/\sqrt{2}$ ensures that the B-spline is able to follow any physical structure in the spectrum while at the same time suppressing the small-scale pixel-to-pixel noise.

The B-spline parameterization, which is just another mathematical factorization of a normal cubic spline, has the advantage of being computationally cheap by minimizing the correlation between the parameters. This stems from the fact that therein the spline is described as a sum of (in the equally spaced case) symmetric basis splines of minimal width (roughly looking like Gaussian peaks, but with tails decaying to exactly 0 after the third knot) that sit at each knot. Furthermore, using a linear interpolation between pixel values for the control points as an initial guess for the fit grants reasonably fast convergence for a typical fit of the template that has more than 1000 free parameters).

In order to further suppress the influence of noise in the spectrum from a single frame, several frames can be simultaneously fitted to collectively represent one template model. This requires the introduction of further parameters into the model that allow to compensate for the following two effects: a) The envelope function may vary due to different exposure times (linearly scaling the amount of CCD counts) or different zenith angles during the exposure (changing the apparent color of the star and therefore causing a relative difference between the intensities at both ends of the spectrum). b) The barycenter motion of both observer and star leads to an RV-induced shift of the spectra between frames. Those two effects are treated in the template model through an individual envelope function (second-order polynomial) that is multiplied on top of each frame's spectrum (a) and a linear scale that is multiplied to the wavelength axis for each frame before inserting to the B-spline, compensating for the RV drift (b).

The χ^2 function for the fit is then defined as:

$$\chi^2(\boldsymbol{\Delta}, \boldsymbol{b}, \boldsymbol{p}) = \\ = \sum_{m=0}^{N_{\mathrm{frames}}} \sum_{i=0}^{N_{\mathrm{pix}}} \frac{\left[f_{i,m} - Bspl(\lambda_{i,m} \cdot (1 + \Delta_m/c), \boldsymbol{b}) \cdot \sum_{j=0}^{2} p_{j,m} \left(\lambda_{i,m} \cdot (1 + \Delta_m/c)^j \right] \right.^2}{(\Delta f_{i,m})^2}, \tag{5.19}$$

where $\boldsymbol{\lambda}$ and $\boldsymbol{f}$ represent the wavelength and flux arrays for each participating frame, $\boldsymbol{b}$ are the coefficients of the B-spline $Bspl$, $\boldsymbol{\Delta}$ is the radial velocity correction for each frame, $\boldsymbol{p}$ are the polynomial coefficients, and c is the speed of light. As mentioned before, the model in this χ^2 function serves two purposes: the spectra from the different frames are scaled and reshaped by multiplying a 2^{nd} order polynomial and they are shifted by applying a multiplicative scaling to their wavelength axis. This ensures that RV shifts between the individual frames are automatically computed and corrected by the fit. The other purpose that is simultaneously fulfilled by the fit is to describe the structure of absorption lines in the spectrum by adjusting the B-spline parameters. The resulting template for each order is then stored as a Python function object for use in a fit or CCF.

Due to the high dimensionality of the parameter space, making a good initial guess for the parameters is crucial in order to enable the fit to converge in a reasonable amount of time. The optimization itself is done utilizing the Python package *iminuit*[20], which is a wrapper around the MINUIT.

Figure 5.21 shows an example of this procedure using five frames and the B-spline method. The inset panels show, side-by-side, the initial guess and the final result of the fit. The initial guess for the B-spline parameters is, as described above, obtained by interpolating the data points of the first frame and evaluating at the wavelength coordinates of the control points. Additionally, the barycenter correction for the observatory is already applied to the wavelength axis of the data points for each frame and the spectra are scaled in such a way that their fitted blaze functions match in their maxima.

Please note that a similar approach as the one described here (fitting B-splines) is also used by the software package SERVAL (Zechmeister et al., 2018) from which inspiration was drawn for *MARMOT*.

[20] *iminuit* documentation: `https://iminuit.readthedocs.io`

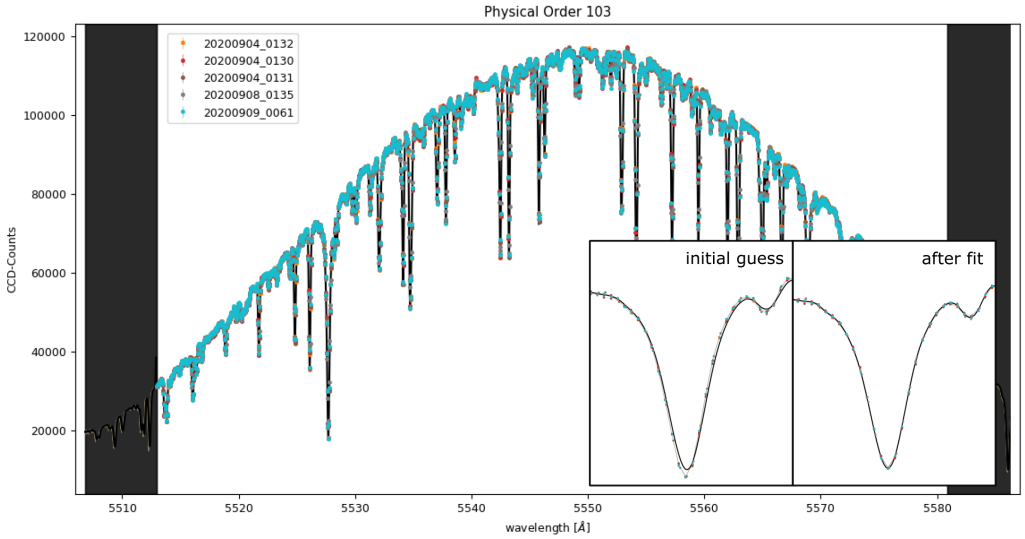

Fig. 5.21.: Illustration of the method of generating spectral templates using the B-spline method. For the generation of this template, data from five frames recorded during three different nights are simultaneously fitted with a model that uses a B-spline to describe the overall spectral shape but also matches the spectra in terms of RV shifts and intensity. The zoomed insets show the data together with the initial guess (left) and after the final fit (right). The shaded regions in the plot mark regions that will later be excluded for the RV signal determination.

5.7 Calculating radial velocity shifts of stellar spectra

MARMOT currently offers two different methods for extracting RV shifts from stellar spectra. Both need a spectral template for each Échelle order as input, in order to match it to the spectra of the individual measurements. The procedure for creating these templates is described in Section 5.6. They are available as Python function objects and can thus be evaluated at any given wavelength within the corresponding order. Using a smooth function instead of a discrete grid has the advantage that no adverse effects like aliasing etc. are expected to arise, as long as such problems have been eliminated during the template construction. Another advantage is that this way of storing the templates grants the necessary flexibility for performing either a cross-correlation-function (CCF) based or a χ^2-fit based RV evaluation without the need of modifying the templates.

5.7.1 Fit-based radial velocity extraction

The goal of the fit-based RV extraction method is to achieve a nearly perfect match between the template and the data points for all the individual frames. The fit

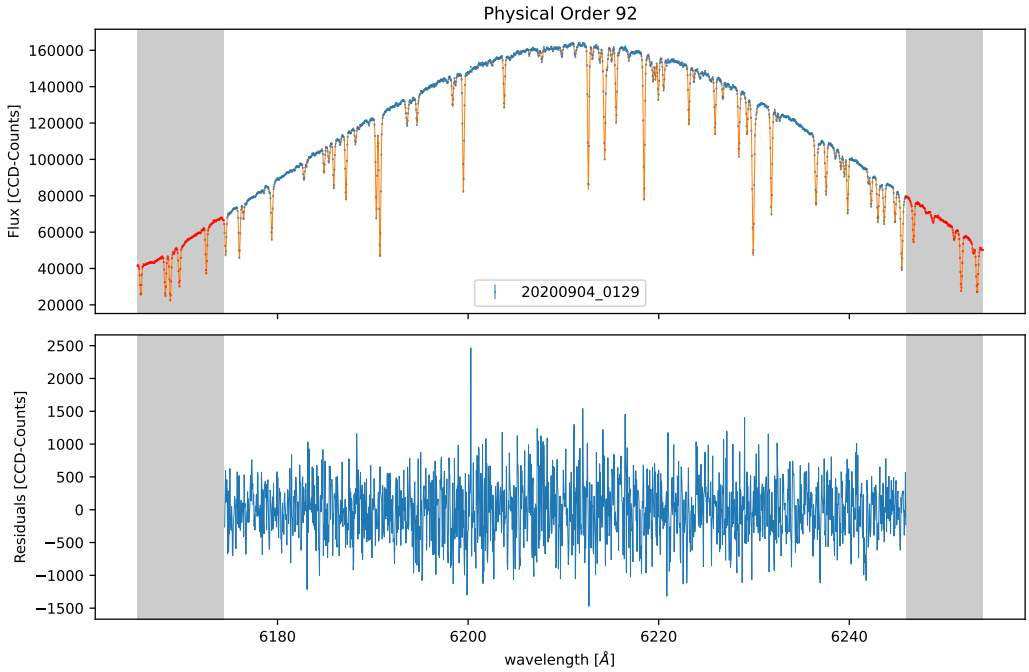

Fig. 5.22.: Example of the fit method used for measuring the radial velocity in a certain Échelle order.

is therefore allowed to scale and deform the flux values of the template using a 3rd order polynomial, for compensating effects like atmospheric transmission at different zenith angles and varying exposure times. In addition, the fit also applies a multiplicative shift to the wavelength axis, which of course is the RV shift that is the actual goal of the entire exercise. The following shows the function that is used to fit the data points of a single order of a single frame.

$$F_{\mathrm{fit}}(\Delta_{\mathrm{RV}}, \boldsymbol{p}, \lambda) = F_{\mathrm{template}}\left(\lambda \frac{\Delta_{\mathrm{RV}}}{c}\right) \sum_{j=0}^{3} p_j \, \lambda^j \,, \tag{5.20}$$

where Δ_{RV} is the radial velocity change between frames and the p_j are the polynomial coefficients. The minimizer of *iminuit* is also used for the fit here, allowing to not only store the best-fit RV shift value, but also the error of the fit. This can then be used in order to compute the weighted average of the individual order-wise values for each frame. The uncertainty of this value is then derived as the error of the weighted average. This method will be refered to as 'χ^2 fit' in the following sections.

The χ^2-based RV-extraction method has the advantage that local deviations of the data from the template spectrum can be easily quantified, for example in terms of

standard deviations of the error in the data. This can be exploited when activating the `remove_tellurics` option in the `rv_fit` method of the `RVAnalysis` class in *MARMOT*. The method will then run the fit twice, while masking regions that deviate by more than 3σ after the first fit, before fitting a second time.

5.7.2 CCF-based radial velocity extraction

The second method provided by *MARMOT* calculates the CCF between the template and the data for each order. For this method, it is important that the spectra are deblazed before computing the CCF, as otherwise, the shape of the blaze function would also influence the maximum of the CCF. This is done using a similar method as already described in Section 5.4.1.1, thereby also normalizing the spectra with respect to the highest occurring values, as an example see also Figure 5.23. While computing the CCF, a constant shift is applied between template and data. In contrast to that, an RV shift would act as linear scaling of the wavelength axis. Therefore, the spectrum and the template need to be evaluated in $\log(\lambda)$ for the CCF. In order to find the optimal value of the CCF, two different methods are available in

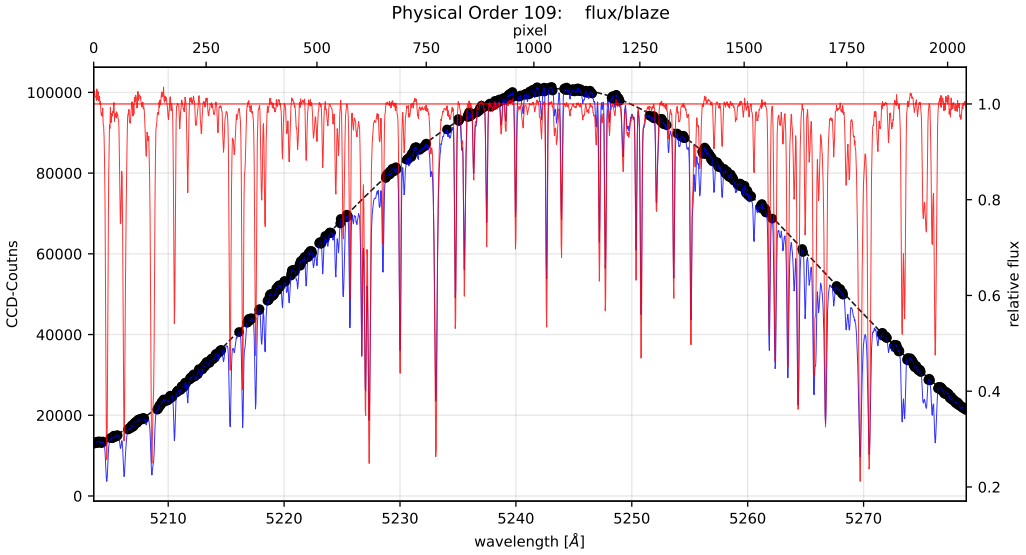

Fig. 5.23.: Example of a blaze function removal on a star spectrum. The first and last 200 pixels are usually excluded from any further calculation to prevent them from adversely affecting the RV measurements.

MARMOT: grid-scan type of approach, where the CCF is evaluated on a grid with an RV resolution of about 50 m/s. The peak in the resulting discretely mapped CCF is then fitted with the sum of a Gaussian and a first-order polynomial. The position of the center of the Gaussian is then interpreted as the optimal CCF value.

Alternatively as a second option, a minimizer, (provided by the *scipy* Python package[21] is used on the negative CCF, yielding the maximum value of the CCF that is then subsequently used. An example plot illustrating the method is shown in Figure 5.24. Both approaches have been found to perform comparably well and will in the following be referred to as 'CCF fit' and 'CCF opt'.

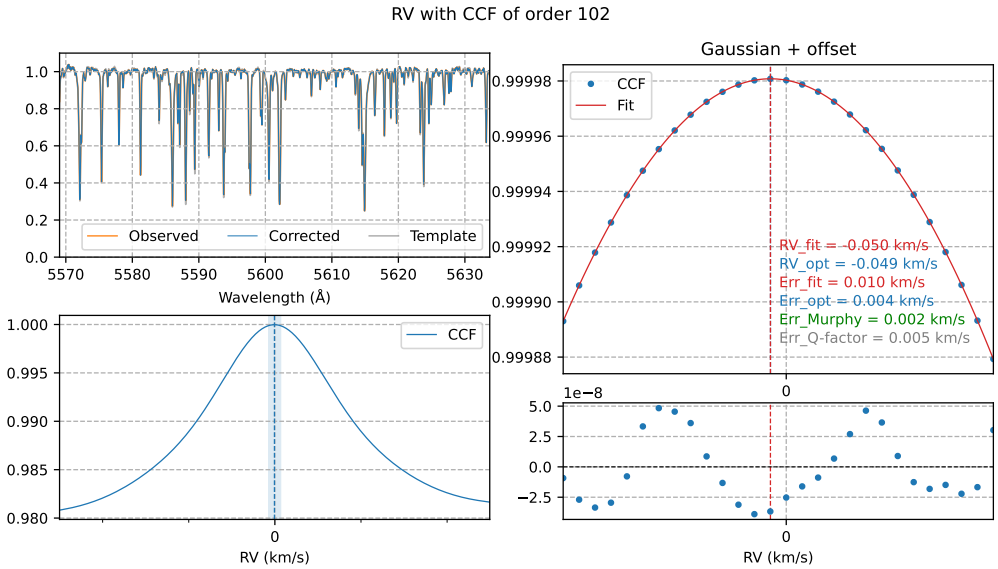

Fig. 5.24.: Example of the CCF method used for measuring the radial velocity in a certain Échelle order. The right side shows a zoom-in on the same peak of the CCF that is shown in the lower left (blue shaded area). The peak is fitted with a Gaussian function within the zoomed-in region. The plotting routine for this graph was provided by Dr. Liang Wang and modified by me.

5.8 Considerations regarding the error estimation

Not only is any measurement by itself of little value without a proper estimation of its uncertainty, but furthermore, the radial velocities computed by *MARMOT* are used as input for fitting models of orbital motion. It is therefore of even greater importance that the error estimation provided by *MARMOT* produces reliable and justified values as otherwise not only the uncertainties of the model parameters but also the parameter values themselves might get biased in the process. As already briefly mentioned in the previous section, the χ^2-fit-based RV extraction method offers a relatively straightforward way of computing such an error estimate (see Chapter 4). The cross-correlation based, on the other hand, although showing similar good

[21] *scipy* download and documentation: `https://www.scipy.org/`

performance during the tests (see Section 5.10), does not offer an obvious strategy for estimating the uncertainty of the cross-correlation function (CCF) maximum. In this thesis, several strategies have been examined that are meant to serve this purpose.

5.8.1 Standard deviation between orders

The first method does not at all attempt to directly estimate the uncertainty associated with the CCF but rather exploits the fact that usually several Échelle orders are analyzed individually, but then averaged for a single measurement and frame. If the error of a single order is assumed to be unknown, all individual values have to be given equal weights. But in this case, the error of the mean can be calculated according to

$$\Delta\overline{RV} = \sqrt{\frac{\sum_{i=1}^{N}\left(RV_i - \overline{RV}\right)^2}{N\left(N-1\right)}}. \tag{5.21}$$

This method, although starting with the probably wrong assumption, that all Échelle orders can and should be given equal weights, has the advantage of being relatively robust against underestimating the errors. If the radial velocity measurements of individual orders contain some degree of uncertainty, this will inevitably reflect in the scatter between those measurements. On the other hand, this way no weighted averaging can be performed, which should lead to less accurate measurements in cases where some orders have a higher signal-to-noise ratio and more spectral features as opposed to other orders. Uncertainties from worse orders might spoil the average and also lead to larger error bars.

The other methods that are suggested in the following are therefore all attempts to assign an individual error that corresponds to the actual precision of the CCF for a certain order. This way a weighted average $\overline{x}$ and the uncertainty of the weighted average $\Delta\overline{x}$ can be computed.

$$\overline{x} = \frac{\sum_i w_i x_i}{\sum_i w_i}\,,\ \Delta\overline{x} = \frac{1}{\sqrt{\sum_i w_i}}\,,\ \text{with } w_i = \frac{1}{\Delta x_i^2}\,. \tag{5.22}$$

5.8.2 Monte Carlo error estimation

Fundamentally, the accuracy with which the CCF can be calculated depends on the number, depth and steepness of spectral lines as well as the signal-to-noise ratio in the data for a given spectral order. All these factors lead to a propagation of flux

uncertainties into some degree of error in the radial velocity measurement. If the spectral shape and the uncertainties in the spectral bins are known, it is possible to draw random representations of such spectra. By drawing random representations and subsequently computing the CCFs and calculating the standard deviation it is possible to obtain a relatively good estimation of the radial velocity error due to random fluctuations (mostly from photon noise) in the spectra. The disadvantage of this method is that in order to obtain a reasonable accuracy on those uncertainties, about 100 random representations need to be drawn, significantly increasing the required computing time, as each of the samples needs to be processed with the CCF.

The observed spectra already contain noise and therefore fluctuate from bin to bin. As adding additional noise on top does not represent the actual situation in the real data, for *MARMOT* a different strategy has been chosen. The spectral templates use smooth functions (B-splines) for representing the observed spectral shape, based on several exposures, further decreasing the influence of noise. Those spectral templates are re-scaled to the observed flux in each CCD frame. Then, Poisson-distributed random numbers are generated for each bin for the sample spectra. Alternatively, Gaussian random numbers can be generated, inserting the bin-wise flux errors in the observed spectrum as σ. Both methods are not 100% accurate. Generating Poisson-distributed random flux values assumes that the error is dominated by photon noise, while the Gaussian errors include also other contributions to the total bin-wise uncertainties which include readout noise and flat-fielding correction errors, among other contributions (see also Section 5.1.4). On the other hand, the Gaussian variant is less accurate for small photon counts and in case other errors are subdominant. Overall, the method of using Gaussian errors has been chosen as default as it should perform slightly better in the high S/N regime where the Poisson distribution is very similar to the Gaussian shape. However, for low SNR data, the Poisson noise option has to be chosen since the Gaussian error could produce negative values which are physically not possible.

5.8.3 Q-factor method

Another method for estimating the CCF error that is implemented in *MARMOT* uses a technique described by Bouchy et al. (2001) and Artigau et al. (2018), which tries to estimate the theoretical photon-noise-limited uncertainty of RV measurements. This

approach separates the effect of the spectral shape and photon counts by introducing a so-called Q-factor

$$\Delta V_{\mathrm{RMS}} = \frac{c}{Q\sqrt{N_{e^-}}}\,, \tag{5.23}$$

where N_{e^-} is the total number of photo-electrons/CCD-counts in the observed spectrum and c is the vacuum speed of light. The definition of Q can be found in Bouchy et al. (2001).

$$Q = \frac{\sqrt{\sum_i W_i}}{\sqrt{\sum_i A_{0,i}}}\,,\ \text{with}\ W_i = \frac{\lambda_i^2 \left(\frac{\Delta A_{0,i}}{\Delta \lambda_i}\right)^2}{A_{0,i}}\,. \tag{5.24}$$

Here, $A_{0,i}$ is the number of photon counts in the i^{th} spectral bin and λ_i the corresponding wavelength. $(\Delta A_{0,i})/(\Delta \lambda_i)$ is the numerical derivative. For this approach to correctly describe the theoretical limits, the absolute number of photo-electrons contributing to the Échelle order needs to be known, taking into account all the backgrounds that have been subtracted and the flat-fielding that is performed eventually. One disadvantage of this method is that it has no way of taking into account other imperfections in the spectrum, like spikes or telluric lines, that might influence the CCF. The previous method using MC-generated sample spectra also shares some of these problems, as the spectral template and not the actual measured spectrum is used. With these problems in mind, the next idea has been developed and tested.

5.8.4 Modified "Murphy"

The last option available in *MARMOT*, was first used in this form in the context of this thesis but is heavily inspired by the considerations originally studied by Murphy et al. (2007). The idea behind this method is that ideally the peak in the CCF can be approximated by a perfect parabola around its maximum. Noise in the spectra on the other hand imprints some remaining structure onto the residuals after subtracting the fitted peak. Also, this structure has a characteristic "frequency" that depends on the bin-size of the input spectrum and possibly also on additional structure/noise in the spectra (see also Figure 5.24 as reference). This problem is reminiscent of fitting a line to noisy data as is discussed by Murphy et al. (2007) where the following solution is proposed:

$$\Delta V = c \cdot \frac{\mathrm{FWHM}}{\mathrm{S/N}\sqrt{n}}\,. \tag{5.25}$$

For the CCF-peak fit, c is a to-be-determined[22] proportional constant, FWHM can be interpreted as the width of the line or peak (within the window of the fit). In

[22] Values around 30 show a good agreement with the other methods.

this case, S/N is the relative scale of the amplitude of the residuals of the fit with respect to the amplitude of the signal, and for n the position of the peak in the FFT is used. The reason for the last adaptation is that in the original publication, n is the number of pixels on which the line is sampled and that are affected by statistically independent Poisson fluctuations. This concept does not exist in this form for the CCF, since it is evaluated on a more or less arbitrary grid, which, if chosen fine enough, is independent from the structure of the noise in the residuals. The peak in the FFT is simply used as estimator for the characteristic scale on which the residuals fluctuate. One might argue that this estimate is rather crude, but on the other hand, n only appears in the square root, resulting in a rather small effect on the final result, even if the estimation is not perfect. An illustration of the method and the extraction of the relevant parameters from the CCF can be found in Figure 5.25.

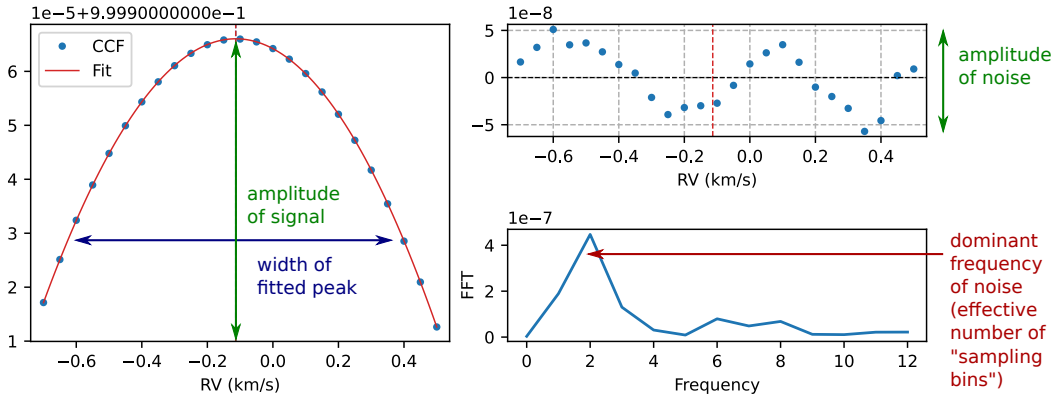

Fig. 5.25.: Illustration of the method *modified* "*Murphy*" and the extraction of the relevant parameters from the CCF.

The different methods for error estimation and propagation that have been implemented in *MARMOT* and that are outlined above have also been tested on artificial stellar spectra. The details of the generation process of these spectra are described in the next section. The results of the comparison of the different methods are shown at the end of Section 5.10.1.

5.9 Simulating realistic Échelle spectra

To test the performance of the pipeline and as an option for future feasibility studies on upcoming scientific targets, *MARMOT* offers the option to adopt simulated spectra to match realistically data recorded with *FOCES*. This section describes the generation process with its different options. In order to produce mock spectra that

are as realistic as possible, high resolution artificially generated stellar spectra, at least one real exposure taken with *FOCES* as well as one comb spectrum is required. The later 2 are necessary to extract the spectrograph-related parameters. *MARMOT* is capable of performing the following list of adoptions:

- adding RV shifts,
- adding physical effects like Macro turbulence,
- resolution adoption,
- introducing the *FOCES* specific blaze imprint and
- adjustment for noise.

Figure 5.26 illustrates the individual steps listed above. One additional option which

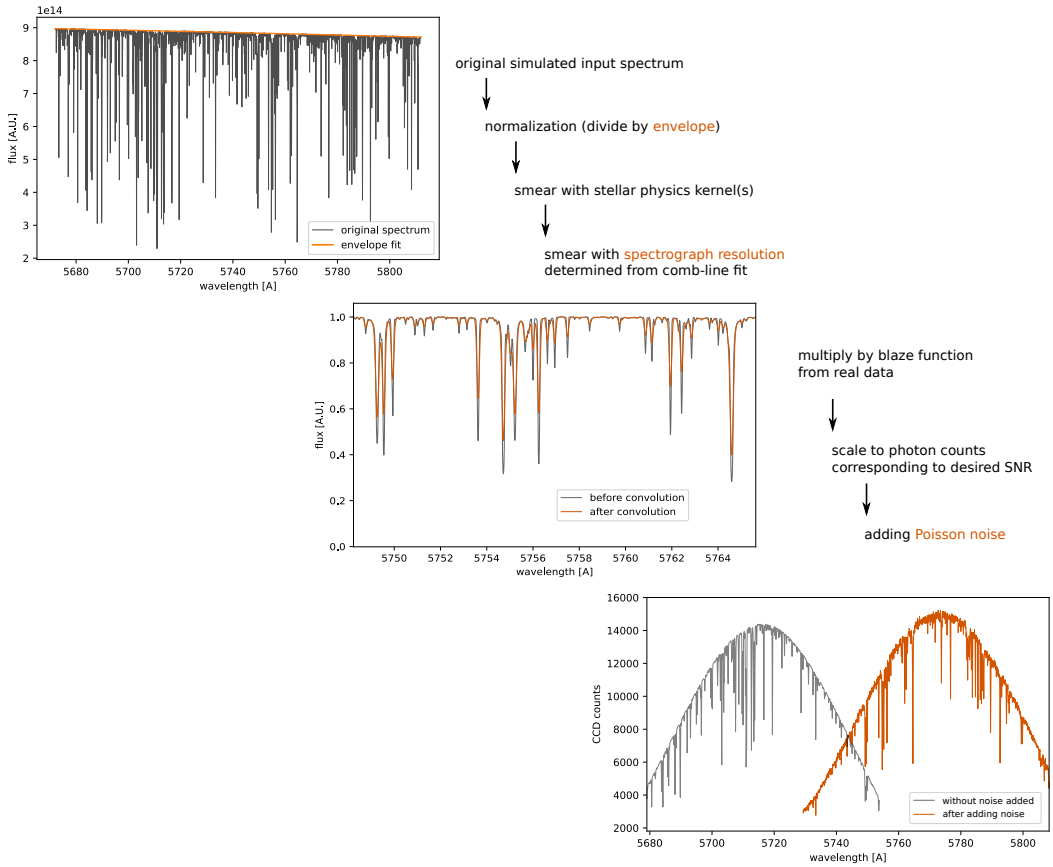

Fig. 5.26.: Illustration of the individual steps for creating realistic synthetic Échelle spectra in *MARMOT*.

is currently under development is the possibility to apply telluric features. This will be possible by adding realistic telluric spectra generated with *MOLECFIT*[23] and if

[23] *MOLECFIT* download and documentation: `https://www.eso.org/sci/software/pipelines/skytools/molecfit`

desired randomly adjusted in their intensity. The telluric library and the program have the possibility to simulate different atmospheric water content and atmospheres which need to be checked and adopted by the user.

5.9.1 Synthetic input spectra

Spectra generated with the PHOENIX (Husser et al., 2013b) simulation code serve as input for generating the mock Échelle spectra. In a first step, the user has to manually download simulated spectra[24] according to the type of star which is of interest. This mainly refers to the following parameters:

- surface temperature,
- surface gravity,
- metallicity,
- alpha element abundances.

After reading this as input spectrum, in a first step the region of interest is extracted from the spectrum, flattened and normalized by removing the black body envelope[25]. For the normalization, the local maxima of the spectrum are fitted with a polynomial. This fit is repeated iteratively in order to remove eventual dips that are not part of the overall black-body shape but due to absorption lines through outlier detection. The region of interest can either be provided by the user or is automatically chosen based on the real data set that is used for extracting the parameters of the spectrograph.

5.9.2 Adding an RV shift

At this point, if specified by the user an artificial radial velocity shift (non-relativistic approximation) can be introduced by multiplying the wavelength axis by

$$\lambda' = \left(1 + \frac{\Delta v}{c}\right) \cdot \lambda \tag{5.26}$$

After this step, the spectral data points are interpolated and stored as a Python function object that can be evaluated for arbitrary wavelengths.

[24] *PHOENIX*-database download: `https://phoenix.astro.physik.uni-goettingen.de/?page_id=15`

[25] In a later step the blaze function of every order is imprinted on the simulated spectrum. The blaze function is thereby extracted from a real stellar spectrum and it is not trivially possible to disentangle the blaze of the spectrograph from the black body envelope. To avoid adding the black body function of the star two times (one from the simulated spectrum and one from the blaze function) the initial black body envelope needs to be removed.

5.9.3 Adding other optional physical effects

Additional physical effects that lead to the broadening of spectral lines can be folded into the spectrum at this point. The effects to select from are:

- macro turbulence,
- doppler broadening and
- broadening due to stellar rotation.

All those effects ultimately work via the Doppler effect and influence the spectrum with a magnitude that is proportional to the wavelength. The spectral function is therefore evaluated on a fine logarithmic grid, before applying the convolution with the corresponding kernel. Thereafter, the resulting spectrum is again interpolated in order for it to be available as an analytic function.

5.9.4 Adjusting to the resolution of the spectrograph

Now that all the astrophysical effects have been included in the data, the next step is to introduce the instrumental effects. Here, instead of creating a complicated model that describes the mapping of the spectra onto CCD pixels including effects like the blaze function etc., it was decided to directly extract those properties from real measurements. For matching the resolution, a measurement of the laser frequency comb spectrum is used. A good estimator for the actual resolution of the instrument is the comb line width, which is as function available via a polynomial fit of line width vs. wavelength. The synthetic spectrum is subsequently evaluated on a new grid for each order, that is generated such that each bin is exactly 0.1 sigma of the resolution at that wavelength. Doing so the following folding with a Gaussian with a sigma of 10 results in exactly the right distribution of the flux to mimic the mapping trough *FOCES* and onto its CCD.

5.9.5 Introducing the blaze function

Next, the blaze function is extracted from real data. This time, science observations should be used as input. The observations should contain an object of similar temperature and spectral type as the spectrum one intends to simulate. The blaze function is fitted in the usual way (see Section 5.4.1.1 for more information) for each order and multiplied onto the normalized spectra of each order. At this point, it is possible to choose the simulated signal strength (in units of SNR) by scaling the

blaze functions of all orders in such a way that the global maximum matches the desired SNR.

5.9.6 Simulating random noise

The final step, if desired by the user, is to introduce random photon noise in the spectra to adjust for different SNR scenarios. In general, photons are assumed to arrive at a constant rate, but with random arrival times. If a CCD pixel is exposed to such a stream of photons for a fixed amount of time, the number of collected photons is governed by the Poisson statistic with

$$P_\lambda(k) = \frac{\lambda^k}{k!}\,\mathrm{e}^{-k}\,, \tag{5.27}$$

where k is the number of detected photons and λ the expectation value. Therefore, Poisson-distributed random numbers are drawn using the previously calculated bin content as expectation value λ.

5.9.7 Example study on the influence of higher SNR templates

As an example for future applications of the simulation feature in *MARMOT*, a brief analysis of possible beneficial effects and an overall cost-benefit analysis of higher SNR templates to strategically optimize observation procedures is presented. For dim or time-critical objects, it might not be feasible to observe spectra with optimal SNR values every time but it could be advantageous to have higher SNR data at least for the template. This test is addressing whether there is and if so, how big the improvement of the measurement precision is when dealing with lower SNR data but fitting with a template that has been generated using three dedicated higher SNR frames. For this test, the mock data sample of 100 artificial Sun-like stellar spectra with an SNR of 25 has been used.

The results of this small study can be found in Table 5.3. From this, it can be concluded that utilizing higher SNR templates improves the performance of all RV-estimation methods, but beyond a SNR of 50 to 100, the improvements are not significant and do for most cases not justify the additional telescope time.

Tab. 5.3.: A study on possible benefits of utilizing higher SNR B-spline templates performed on SNR=25 mock data.

SNR template	25	50	100	200	400
std. (CCF opt.) [m/s]	15.84	12.24	12.30	11.97	12.19
std. (CCF fit) [m/s]	13.84	11.35	10.69	10.53	10.65
std. (χ^2 fit) [m/s]	13.73	10.59	9.97	9.70	9.59

5.10 Performance verification of *MARMOT*

MARMOT offers a variety of different methods at several steps of the analysis. This section presents a selection of tests that have been performed on mock and real data sets in order to compare those different methods as well as benchmark the performance limitations of the software. Subsequently, the spectra are used to test the influence of:

- varying SNR,
- different methods for determining RV shifts and
- different template generation methods

on the RV precision.

5.10.1 Verification on simulated spectra

Using mock data generated with the methods described in the preceding sections, it is possible to compare the performance of the different available analysis options and combinations of such. For this test, sets of 100 mock data frames for different SNR (25, 50, 100, 200 and 400) were generated utilizing artificial spectra chosen from the *PHOENIX* database with stellar parameters ($\mathrm{T_{eff}} = 5800\mathrm{K}$, $log(g) = 4.5$, $\mathrm{Fe/H} = 0$, $\alpha/\mathrm{M} = 0$) as close as possible to the Sun. All the subsequently presented results are generated using only the Échelle orders also employed in analyses of real data sets[26](84 to 114). The obtained standard deviation between the individual results is used as indicator for the accuracy that can be achieved.

Tab. 5.4.: Comparison of the different methods for determining RV shifts with mock data generated with different degrees of SNR. For the analysis, the B-Spline template was used.

RV shift: 0 m/s, template: B-spline					
SNR	25	50	100	200	400
std. (CCF opt.) [m/s]	15.84	6.33	2.80	1.48	0.65
std. (CCF fit) [m/s]	13.84	6.19	2.65	1.45	0.65
std. (χ^2 fit) [m/s]	13.73	5.88	2.61	1.40	0.59

Tab. 5.5.: Comparison of the different methods for determining RV shifts with mock data generated with different degrees of SNR. For the analysis, a single-frame interpolated template was used.

RV shift: 0 m/s, template: single-frame interpolated					
SNR	25	50	100	200	400
std. (CCF opt.) [m/s]	19.22	6.03	2.90	1.42	0.62
std. (CCF fit) [m/s]	16.93	5.99	2.79	1.40	0.62
std. (χ^2 fit) [m/s]	126.7	65.33	27.78	7.50	2.20

5.10.1.1 Comparison of the different RV-estimation techniques

Tables 5.4 and 5.5 summarize the performance of the analysis with *MARMOT* for various analysis configurations in terms of SNR and RV-extraction method. For the template generation, 3 randomly selected spectra out of the 100 frames included in one data set have been used to generate a B-spline template for Table 5.4 (for details on template generation see Section 5.6). A random spectrum was selected as template for the single-frame interpolation of Table 5.5. The data presented here are the result of non-RV-shifted mock data. An artificial RV-shift of 123 m/s was applied to a second data set to reassemble typical overall RV-shifts. The obtained results are comparable to the values presented here and can be found in Appendix 9.9. In all those examples the individual Échelle orders of each frame have been combined by simply calculating the mean of the obtained RV-shifts. Other methods of combining individual Échelle orders have also been explored. The details of that are outlined in the next section.

In summary, it can be stated that the standard deviation is roughly inversely proportional to the SNR in all cases when using the B-spline templates, which would also be expected from theory. Generally, no significant difference between RV-extraction methods can be observed with the B-spline templates. The results for the interpo-

[26] Some orders are usually excluded due to their high telluric contamination while others are excluded due to their intense absorption lines like for example the H-α region.

lated single-frame templates, however, show large variations between the individual RV-extraction methods. This is to be expected, since using only a single frame as template introduces more randomness into the effective RV-shift of the template. On the other hand, the RMS between the frames is comparable to the B-spline case for the CCF-based RV-extraction methods. For the χ^2-fit, the results are generally worse, especially for lower SNR data and with the interpolated template.

As it is demonstrated in the next section, when real data is analyzed, the difference between the χ^2-fit method and the CCF methods is not merely as large when moving from the B-spline templates to single-frame interpolated templates. The reason for this behavior might be that for the simulated data the B-spline templates reconstruct a near-perfect spectral model. In real data on the other hand the observational conditions, like atmospheric transmission, induce small differences that could possibly reduce the difference in how much better the B-spline template describes the data when compared to the interpolated template. Another reason could be that the SNR in the data set that is described in the next section is actually between 200 and 400, where the difference reduces, even when using mock data. In conclusion, it is always recommended to use B-spline templates, although the computational effort for generating those is significantly larger compared to the simple interpolation.

5.10.1.2 Comparison of different error propagation methods

The artificial spectra were also utilized for a comparison of the different methods for the error estimation and propagation that are described in Section 5.8. Again sets of 100 artificial spectra with no intrinsic RV shift (0m/s) and SNRs of 25, 50, 100, 200 and 400 were processed with the B-spline method. The frame-wise average radial velocity and error estimates have been compared for the different RV-calculation methods (χ^2 fit, CCF fit, CCF opt.), different error calculation methods (χ^2 fit, MC - CCF fit, MC - CCF opt., Murphy, Q-factor)[27] entering the weighted average, and averaging without weights. (Only reasonable combinations are chosen for this analysis.) Out of the 100 artificial frames, three key values have been computed for each configuration:

- **scatter between frames**
  mean of the residuals
- **mean error**
  mean of the errors bars of every data point

[27] For both MC methods 50 samples were drawn for the error estimation in each Échelle order.

- $\boldsymbol{\chi^2_{\mathrm{DoF}}}$
  estimator for the accuracy of the error estimations compared to the scatter between the data points

Ideally, the scatter between frames should be as small as possible and be matched by the average error estimate for the frames. χ^2_{DoF} should then be proximately unity. The results of this test are shown in Table 5.6. The key conclusions that can be deduced from this table can be summarized as:

- The *Modified Murphy* errors estimation method yields reasonable values, considering the somewhat arbitrariness of the method. The overall performance is the least optimal among the different methods but also the fastest so it is only recommended for quick-look analysis.
- The Q-Factor method leads to a slight overestimation of the order-wise and therefore also per-frame error, resulting in a χ^2_{DoF} on the order of 0.5. The resulting precision is not significantly worse than using the *Minuit* errors, the Monte-Carlo errors, and are also comparable to the mean without individual order-wise weights and the standard deviation between orders as error estimates.
- Overall the χ^2-fit method shows the best results, both, in terms of scatter between frames and also in terms of the error estimate and χ^2_{DoF}.
- Weighted averaging produces the smallest scattering between frames, when using the best-performing order-wise error estimation methods and especially at low SNR.
- Especially at high SNR, but also in general, the simple mean/standard deviation method performs surprisingly well and yields results that are comparable to those where weighted averaging has been applied.

The smallest scatter is found for the weighted averaging methods, especially at low SNR. The simple mean/standard deviation between orders method, on the other hand, shows the most robust performance with reasonable values for both, scatter between orders as well as χ^2_{DoF} across all signal to noise ratios. This behavior could also be observed when analyzing real data, where additional sources of uncertainty (e.g. atmospheric and instrumental effects), apart from pure photon statistics enter the (order-wise) measurements. Therefore weighted averaging leads to somewhat underestimated errors as well as no improvement to the residual scatter. For this reason, the tests on 51 Pegasi that are presented in the next section use the simple mean/standard deviation method throughout the analyses. At lower SNR, between 25 and 50 however, it is expected that using the weighted average instead of simple mean/standard deviation hint be the better choice, as statistical errors dominate in this regime.

Tab. 5.6.: Comparison of the performance of different methods of calculating and propagating errors. The study has been performed on artificial spectra with varying SNR and is based on 100 artificial exposures for each set. The numbers refer to RV statistics after combining individual Échelle orders.

source value	source error	w. avg.	scatter [m/s]	mean err. [m/s]	$\chi^2/N.D.F.$
SNR 25					
χ^2 fit	χ^2 fit	Yes	10.95	9.25	1.41
CCF fit	MC - CCF fit	Yes	13.98	8.77	2.55
CCF opt.	MC - CCF opt	Yes	12.16	9.71	1.57
CCF opt.	Murphy	Yes	18.62	27.38	0.52
CCF opt.	Q-factor	Yes	12.99	14.56	0.80
χ^2 fit	-	No	14.29	13.55	1.21
CCF fit	-	No	14.49	13.96	1.18
CCF opt.	-	No	16.20	15.33	1.23
SNR 50					
source value	source error	w. avg.	scatter [m/s]	mean err. [m/s]	$\chi^2/N.D.F.$
χ^2 fit	χ^2 fit	Yes	5.00	4.64	1.16
CCF fit	MC - CCF fit	Yes	5.94	4.86	1.51
CCF opt.	MC - CCF opt	Yes	5.74	5.31	1.17
CCF opt.	Murphy	Yes	8.67	8.44	1.22
CCF opt.	Q-factor	Yes	5.77	7.66	0.57
χ^2 fit	-	No	6.27	6.04	1.18
CCF fit	-	No	5.69	5.41	1.12
CCF opt.	-	No	5.99	5.86	1.14
SNR 100					
source value	source error	w. avg.	scatter [m/s]	mean err. [m/s]	$\chi^2/N.D.F.$
χ^2 fit	χ^2 fit	Yes	2.20	2.33	0.89
CCF fit	MC - CCF fit	Yes	2.59	2.48	1.09
CCF opt.	MC - CCF opt	Yes	2.59	2.78	0.87
CCF opt.	Murphy	Yes	3.51	3.07	1.38
CCF opt.	Q-factor	Yes	2.56	3.88	0.44
χ^2 fit	-	No	2.53	2.69	1.02
CCF fit	-	No	2.60	2.92	0.85
CCF opt.	-	No	2.68	2.99	0.87
SNR 200					
source value	source error	w. avg.	scatter [m/s]	mean err. [m/s]	$\chi^2/N.D.F.$
χ^2 fit	χ^2 fit	Yes	1.29	1.17	1.23
CCF fit	MC - CCF fit	Yes	1.48	1.25	1.39
CCF opt.	MC - CCF opt	Yes	1.39	1.45	0.91
CCF opt.	Murphy	Yes	2.12	1.59	1.91
CCF opt.	Q-factor	Yes	1.46	1.95	0.56
χ^2 fit	-	No	1.38	1.28	1.32
CCF fit	-	No	1.42	1.39	1.19
CCF opt.	-	No	1.46	1.40	1.21
SNR 400					
source value	source error	w. avg.	scatter [m/s]	mean err. [m/s]	$\chi^2/N.D.F.$
χ^2 fit	χ^2 fit	Yes	0.51	0.58	0.78
CCF fit	MC - CCF fit	Yes	0.56	0.63	0.80
CCF opt.	MC - CCF opt	Yes	0.59	0.78	0.58
CCF opt.	Murphy	Yes	0.75	1.18	0.41
CCF opt.	Q-factor	Yes	0.55	0.97	0.32
χ^2 fit	-	No	0.55	0.63	0.81
CCF fit	-	No	0.61	0.69	0.82
CCF opt.	-	No	0.62	0.70	0.81

5.10.2 Verification on observed data

The performance of *MARMOT* and its ability to accurately determine RV measurements of *FOCES* data has been examined by evaluating a data set of 51 Pegasi observations, which were recorded in autumn 2020. This star is well known for its planetary companion 51 Peg b (Mayor and Queloz, 1995) with an orbital period of 4.23 days and an RV amplitude of about 56 m/s.

In order to directly obtain a comparison of the *FOCES* data set to the already well established orbital parameters of this exoplanet system, a combined fit is performed, including numerous measurements from four major instruments (*ELODIE* (Naef et al., 2004; Birkby et al., 2017), *LICK* (Butler et al., 2006; Birkby et al., 2017), *HIRES* (Birkby et al., 2017) and *HARPS* (Birkby et al., 2017)).

The Python package *RadVel*[28] (Fulton et al., 2020) has been used for the task of fitting the physical model. In order to avoid the possibility of *FOCES* data points influencing the orbital parameters, error bars of *FOCES* were artificially increased by a factor 100 for the fit. Thus, the orbital parameters obtained through the fit are essentially determined by those archival measurements with only the vertical offset of the *FOCES* data set being optimized during fitting. Finally, residuals of the *FOCES* data points provide a realistic estimate for the performance of the *MARMOT* pipeline. The overall performance of the RV determination methods is presented in Table 5.7. For this comparison the frame-wise mean values of the order-wise relative RVs were computed. The standard error of the mean is used for the frame-wise error bars. The best RV results are obtained when combining the wavelength calibration information of the LFC with the B-spline template. The different RV extraction methods

- 'CCF opt.' = CCF optimization,
- 'CCF fit' = iterative Gaussian fit to CCF grid scan and
- 'χ^2 fit' = χ^2 fit of a template

all showing similar performances with a residual RMS of ~ 3.5 m/s. Figure 5.27 presents the RV curve (*FOCES* data points in yellow, all other instruments in varying shades of green) and the residuals. This demonstrates that the targeted RV precision of few m/s for the whole instrument setup, including both pipelines *GAMSE* and *MARMOT*, is clearly satisfied.

[28] *RadVel* documentation: `https://radvel.readthedocs.io/`

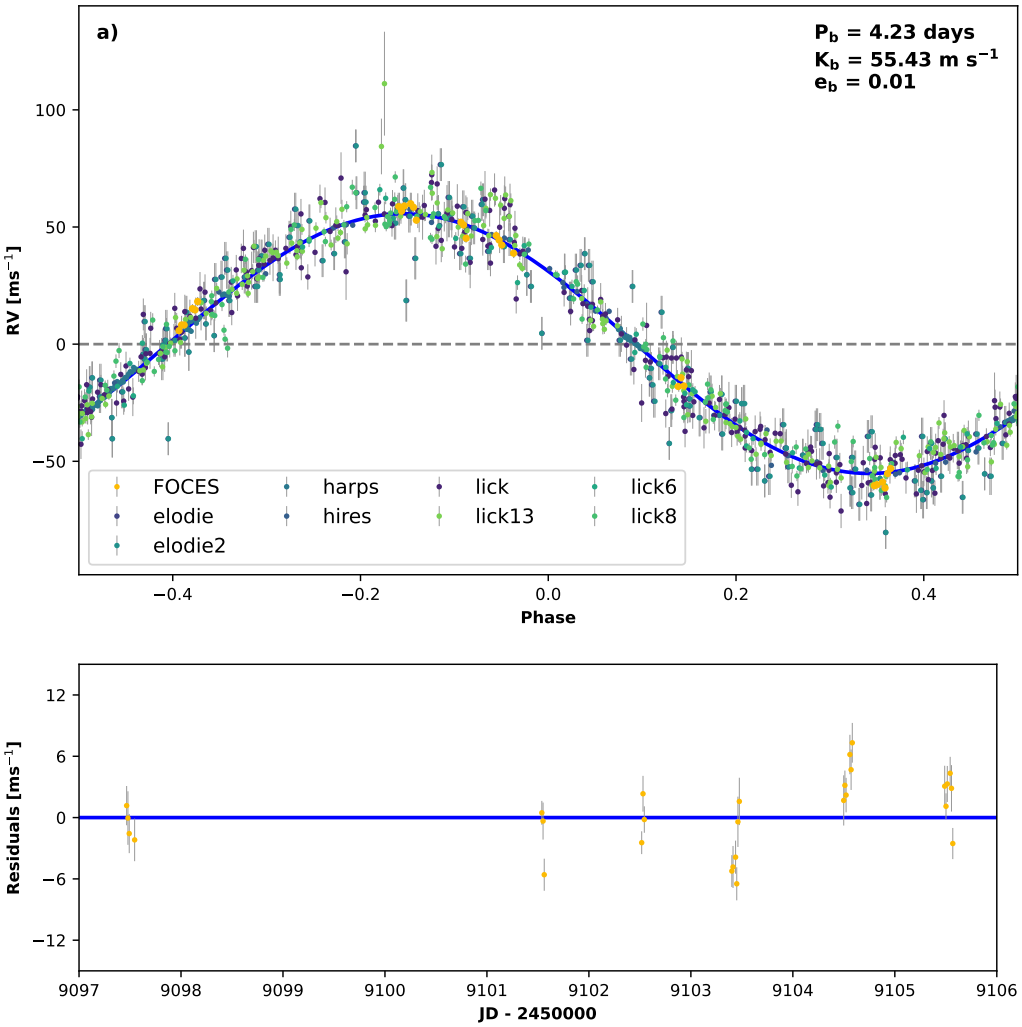

Fig. 5.27.: *FOCES* RV-measurements of 51 Pegasi b, obtained with *MARMOT*, simultaneously fitted to a physical model with measurements from four major instruments. Top: RV curve of 51 Peg, phase-folded. Yellow data points: *FOCES* data, obtained with comb correction, B-spline template and CCF optimization; other points: literature data; blue solid line: best-fitting RV curve to all data (error bars for *FOCES* data points up-scaled by a factor 100 for the fit, not in the plot). Bottom: Residuals of *FOCES* data to best fit, not phase-folded.

Further possible combinations of methods and their respective performance are shown in Table 5.7. Those include ThAr instead of LFC calibrated data and utilizing an interpolated spectrum of a single exposure instead of the B-spline template. In case a single interpolated spectrum of the star is used as a template, the RMS of the CCF methods is still remarkably good (~ 5 m/s), while the precision of the χ^2 fit is noticeably declining at 8.45 m/s. A possible explanation for this behavior might be that the shape of the template does not represent the actual spectral shape as

Tab. 5.7.: Comparison of the overall measurement residuals of the 51 Pegasi b data set, obtained with different configurations of *MARMOT*. The fit has been performed including data from *ELODIE*, *HARPS*, *HIRES* and *LICK* in addition to *FOCES* data.

method	template	WL. calib.	residual RMS [m/s]
CCF opt.	B-spline	comb	3.57
CCF fit	B-spline	comb	3.64
χ^2 fit	B-spline	comb	3.54
CCF opt.	single	comb	5.53
CCF fit	single	comb	4.52
χ^2 fit	single	comb	8.45
CCF opt.	B-spline	ThAr	14.5
CCF fit	B-spline	ThAr	14.5
χ^2 fit	B-spline	ThAr	14.2
CCF opt.	single	ThAr	15.8
CCF fit	single	ThAr	15.5
χ^2 fit	single	ThAr	13.3

well in this particular case. When the RV-determination is executed on frames with ThAr-calibrated wavelength solutions, the results for both template methods are similar while still yielding a slight advantage in the B-spline version. In these cases, the effect of the imperfect wavelength calibration is clearly dominating and leading to values to residuals of around 13.3-15.8 m/s. The results stated in Table 5.7 are illustrated in Figure 5.28

It can be concluded from Table 5.7 that the largest improvement can be attributed to the LFC-based refined wavelength calibration of the spectra, thereby eliminating shift of the whole instrumental setup and thereby reducing the measurement errors by up to 75%. Using fitted B-splines as templates instead of interpolated single frames can lead to an improvement of about 50%.

In conclusion, these tests demonstrate the capabilities of the upgraded high-resolution spectrograph *FOCES* in combination with the data reduction software *GAMSE* and the newly developed RV-analysis software *MARMOT*. Although some further optimizations, including an improved treatment of the residual influence of telluric absorption lines, are still under development, *FOCES* in its current configuration reaches an RV-precision in the few m/s-regime. The benefit of utilizing the B-Spline method to generate templates introduced in *MARMOT* and the simultaneous LFC-based wavelength calibration were demonstrated to have a decisive influence on accuracy of the RV measurements.

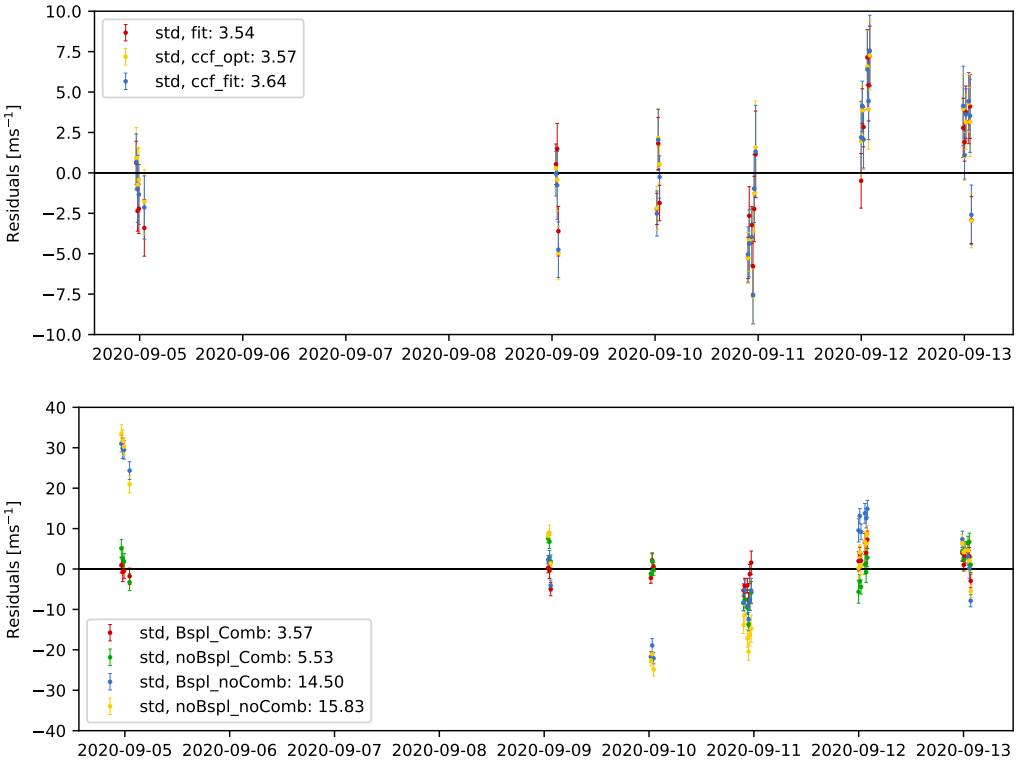

Fig. 5.28.: Upper panel: Comparison of the residuals for the three different RV extraction methods utilizing B-spline templates and comb-corrected spectra. Lower panel: Residuals for four different combinations of wavelength calibration and template generation applying the CCF-fit method.

6 The Multi-Transit Fitter data analysis tool

> *Nothing in life is to be feared. It is only to be understood.*
>
> — **Marie Curie**

This chapter summarizes the Multi-Transit Fitter (*multranfit*) Python package for analyzing photometric light curves of exoplanets transiting in front of their stars. This software package was developed in the scope of this thesis to combine photometric data from different wavelength bands and even different instruments into a single fit utilizing a transit model describing the exoplanet system. The *multranfit* package uses a maximum likelihood approach for this fit and also offers the possibility of introducing parameter priors as well as utilizing Markov-Chain Monte Carlo sampling for determining the posterior distribution in the parameter space. The packages were subsequently extended with additional functionality and are now able to perform the following tasks:

- detrending of light curves,
- fitting of a multi-transit data set including parameter and uncertainty estimation either via:
  - likelihood maximization fit utilizing the minimizer MINUIT (James and Roos, 1975) or
  - Markov-Chain-Monte-Carlo sampling of the posterior probability distribution,
- period estimation from single transits (contribution by Jana Steuer, currently under development).

6.1 Structure of the package

The *multranfit* Python package uses object-oriented Python 3, with the main features and analysis methods combined in the *TransitFitter* class. Only some auxiliary

functions are kept outside of the main object, like for example the class for parsing the configuration file that contains the instructions that define the analysis steps. The actual physical transit model is not part of the *multranfit* package but has to be provided externally. By default *multranfit* utilizes the physical model described by Mandel and Agol (2002), which is implemented via the Python package *batman*[1] (Kreidberg, 2015). *batman* provides a computationally efficient model/parameterization for transiting exoplanets, including stellar limb darkening.

The program flow is controlled by an analysis script, in which the user has the possibility to customize the analysis to the specific needs of the observed data. This might be necessary, in particular when a model other than the default *batman* model is used for computing transit light curves. Appendix 9.10 provides an example script for typical applications. An overview of the structure and basic program flow of *multranfit* is given in Figure 6.1.

multranfit currently offers three different options for detrending (*simple*, *sysrem*, *SARS*) to be executed before the fit is performed (see also Section 6.2 for more information). If desired, different detrending methods can be applied individually for every light curve. The transit parameters and their corresponding priors can be initialized via a configuration file, an example for which can be found in Appendix 9.10. Since the combination of orbital and limb-darkening parameters can be highly degenerated, special emphasis was given to options for the treatment of the limb-darkening parameters, which the user can choose from, which will be discussed in Section 6.3.2.2. Note that there is only a single set of physical parameters describing the star, planet and its orbit, while the limb darkening may differ between wavebands and therefore a separate set of parameters is needed for each instrument/band. The final step of the analysis executes a likelihood fit, and, depending on the settings in the configuration file, Markov-Chain Monte Carlo (MCMC) sampling. The program output includes the raw and folded light curves, including the best fit orbital parameters and 1-, 2-, 3-σ error bands, as well as the corner plot, in case the MCMC sampling has been activated. All provided information in terms of data and settings, as well as the fit results and the entire MCMC samples, are stored directly in the *TransitFitter*-object.

[1] *batman* documentation: `https://lweb.cfa.harvard.edu/~lkreidberg/batman/`

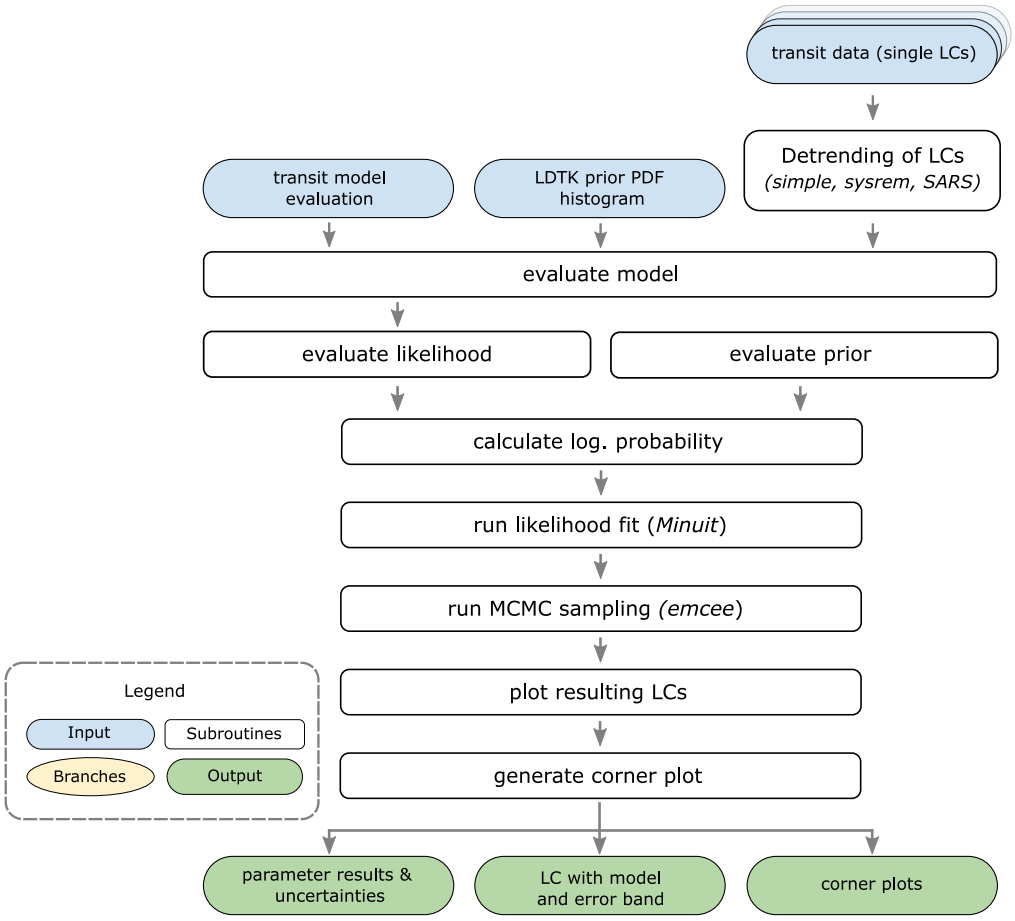

Fig. 6.1.: Diagram summarizing the structure and depicting a possible program flow of the *multranfit* Python package for fitting transit light curves (LC), observed in different filter bands and with different instruments, simultaneously.

6.2 Detrending: Implementation of the algorithms *sysrem* and *SARS*

The main purpose of *multranfit* is the simultaneous fitting of transit light curves, from both earth- and space-based instruments. All optical instruments that observe from the ground have one problem in common: atmospheric extinction. This phenomenon depends on zenith angle, wavelength and current atmospheric conditions such as the amount of water vapor in the atmosphere. Furthermore, the sky may have different regional and time-dependent absorption depending on the sky position due to fast-moving high-altitude clouds. This implies that on top of statistical fluctuations, which are associated with photon noise, systematic effects related to the state of the atmosphere imprint on the data and significantly influence the uncertainties. Since

photon noise is a property of the amount of light detected, only larger telescopes or longer exposures can reduce this error component. The uncertainties introduced by the changing atmosphere, however, can be corrected as long as it is possible to measure these changes independently, for example with several reference stars in the field of view during the observation.

For such a situation, Tamuz et al. (2005) suggested the iterative algorithm (*sysrem*) that was later extended by Ofir et al. (2010) (Simultaneous Additive and Relative Sysrem (SARS)). Those algorithms attempt to account for color-dependent effects that cause some stars to be more affected by changes in air mass than others. While the more elaborate algorithms are superior for a large enough number of simultaneously imaged stars and sufficiently small statistical errors, too few stars and noisy data can adversely affect these algorithms. Therefore, and in addition to the aforementioned algorithms, a much simpler correction method (*simple*) has been implemented as a last option for detrending. All three options are described in detail in the following paragraphs.

simple correction method

The main idea for this detrending of the light curves (inspired by Jana Steuer & Dr. Christian Obermeier and also implemented in *AstroImageJ*, (Collins et al., 2017)) is to compute the average brightness of the N simultaneously imaged stars for M frames and use this value for correcting the light curve data points $x_{0,j}$ of the star exhibiting the transit.

$$x'_{0,j} = \frac{x_{0,j}}{\sum_{i=1}^{N} x_{i,j}}\,,\ j = 1, .., M. \tag{6.1}$$

The shortcomings of this method are that stars of different spectral types may react differently to changes in atmospheric transmission, due to changes in air mass or weather phenomena over the field of view. These adverse effects are partially solved by the *sysrem* and especially by the *SARS* algorithm for cases where enough reference stars are in the field of view. Another effect that cannot be corrected adequately in this way are residual constant offsets from improper bias or background subtraction. Those are additive biases, in contrast to changes in atmospheric transmission that cause multiplicative changes to the flux.

sysrem correction method

For a data set with N stars observed with M exposures, Tamuz et al. (2005) propose to model the average-subtracted (averaging over the exposures) stellar magnitudes (= residuals) r_{ij} by

$$r_{ij} = m_{ij,\mathrm{measured}} - m_{i,\mathrm{true}} = a_j\, c_i + \mathrm{noise}\,, \tag{6.2}$$

where the a_j denote the M airmasses, c_i the N individual color coefficients. These coefficients can be estimated by iteratively applying the following two expressions.

$$c_i = \frac{\sum_{j=1}^{M} \left(\frac{r_{ij}\, a_j}{\sigma_{ij}^2} \right)}{\sum_{j=1}^{M} \left(\frac{a_j^2}{\sigma_{ij}^2} \right)}, \quad a_j = \frac{\sum_{i=1}^{N} \left(\frac{r_{ij}\, c_i}{\sigma_{ij}^2} \right)}{\sum_{i=1}^{N} \left(\frac{c_i^2}{\sigma_{ij}^2} \right)}, \tag{6.3}$$

with σ_{ij}, the statistical uncertainties of the i$^{\mathrm{th}}$ star in the j$^{\mathrm{th}}$ exposure. The advantage of this method is that neither the airmasses of each exposure, nor the color-dependent scaling coefficient of the systematic effect on each star need to be known a-priori, only $m_{i,\mathrm{true}}$ is expected to be constant over time.

SARS correction method

As it is stated by Ofir et al. (2010), the *sysrem* algorithm only removes effects that are linear in stellar brightness and fails to compensate for effects that stem for example from improper subtraction of the background for some exposures. In order to incorporate this effect, the authors suggest to extend the model by a term that depends on the absolute brightness of the star $x_{ij} = 10^{0.4(m_{i,j} - m_{\mathrm{rel}})}$. Thereby, $m_{i,j}$ denote the magnitude of the stars in each frame and m_{rel} serves as an arbitrary scaling factor for avoiding overly small or large values.

$$r_{ij} = A_j\, x_{ij}\, C_{A,i} + R_j\, C_{R,i} + \mathrm{noise}\,, \tag{6.4}$$

where A_j and $C_{A,i}$ are the coefficients describing an additive effect and R_j and $C_{R,i}$ describe a relative effect. The algorithm then consists of iteratively evaluating the following expressions:

$$A_j = \frac{\sum_{i=1}^{N}\left(\frac{r_{ij}\,x_{ij}\,C_{A,i}}{\sigma_{ij}^2}\right) - R_j\sum_{i=1}^{N}\left(\frac{C_{R,i}\,x_{ij}\,C_{A,i}}{\sigma_{ij}^2}\right)}{\sum_{i=1}^{N}\left(\frac{x_{ij}^2\,C_{A,i}^2}{\sigma_{ij}^2}\right)}\,, \tag{6.5}$$

$$R_j = \frac{\sum_{i=1}^{N}\left(\frac{r_{ij}\,C_{R,i}}{\sigma_{ij}^2}\right) - A_j\sum_{i=1}^{N}\left(\frac{C_{R,i}\,x_{ij}\,C_{A,i}}{\sigma_{ij}^2}\right)}{\sum_{i=1}^{N}\left(\frac{C_{R,i}^2}{\sigma_{ij}^2}\right)}\,, \tag{6.6}$$

$$C_{A,i} = \frac{\sum_{j=1}^{M}\left(\frac{r_{ij}\,x_{ij}\,A_j}{\sigma_{ij}^2}\right) - C_{R,i}\sum_{j=1}^{M}\left(\frac{A_j\,x_{ij}\,R_j}{\sigma_{ij}^2}\right)}{\sum_{j=1}^{M}\left(\frac{x_{ij}^2\,A_j^2}{\sigma_{ij}^2}\right)}\,, \tag{6.7}$$

$$C_{R,i} = \frac{\sum_{j=1}^{M}\left(\frac{r_{ij}\,R_j}{\sigma_{ij}^2}\right) - C_{A,i}\sum_{j=1}^{M}\left(\frac{A_j\,x_{ij}\,R_j}{\sigma_{ij}^2}\right)}{\sum_{j=1}^{M}\left(\frac{R_j^2}{\sigma_{ij}^2}\right)}\,. \tag{6.8}$$

Both algorithms have been tested, alongside non-preprocessed data before running the *multranfit* code. Figure 6.2 shows an example that highlights the necessity and performance of the described algorithms. Which algorithm is best suited in practice for a particular case depends on the signal-to-noise ratio in the data set, as well as the number of reference stars and needs to be decided on a case-by-case basis.

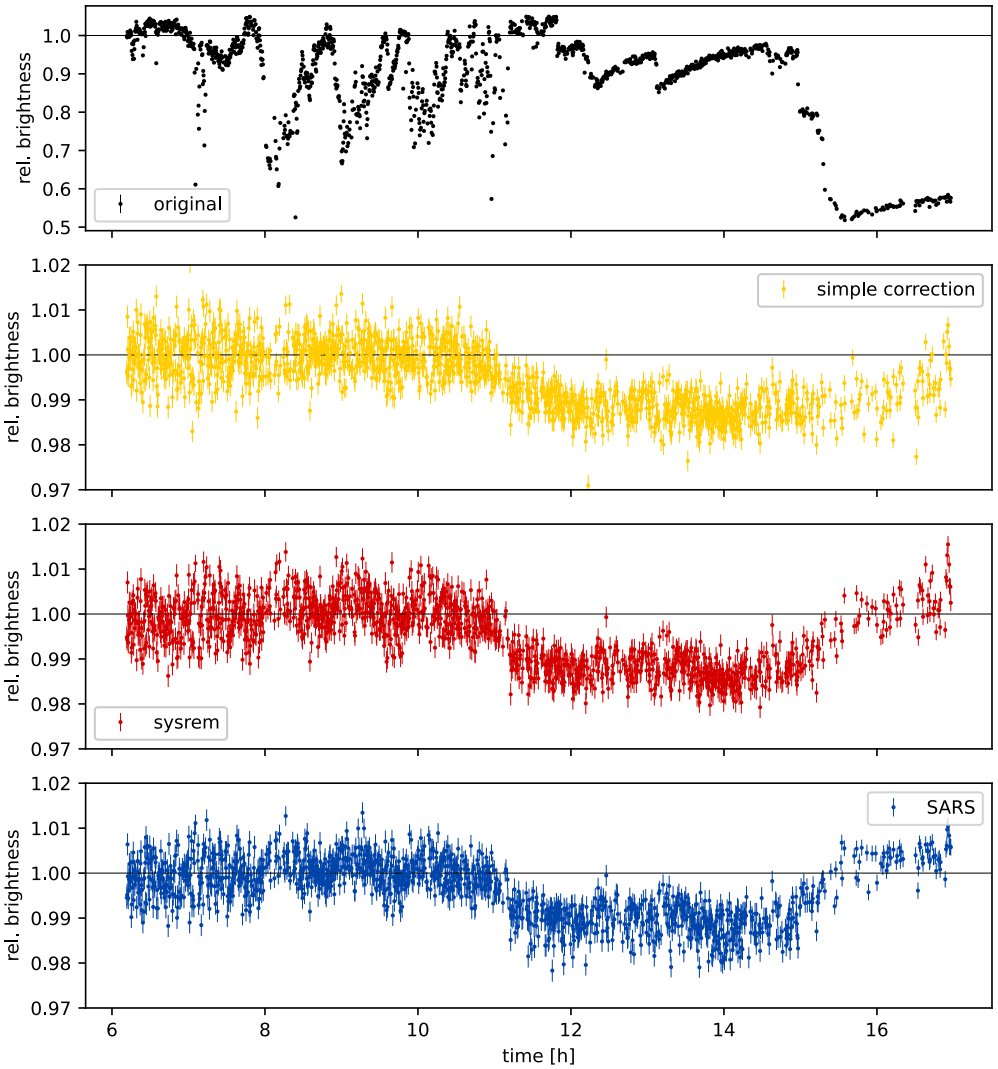

Fig. 6.2.: Detrending example for TOI-1823 and all three options utilizing only four reference stars for the trend estimation. 3KK-data taken on the 12/2/2021 with the g-filter. Photometric data extraction kindly provided by Jana Steuer.

6.3 Parametric model fit of transiting exoplanets

This section describes the core functionality of the *multranfit* software package, which is fitting a parametric model describing the planetary system experiencing transits to a set of light curves from observations. The observational data can originate from one or several instruments, without the need of being contemporary and can include an arbitrary number of transits. *multranfit* does not include the transit model itself but requires to be provided with such a model as an external code/module. Such a model typically consists of two major parts that will be described in the following two subsections. One part describes the planetary orbit and size (physical model), while the second part is a parametrization of the surface brightness profile of the star, also called limb darkening. The last part of this section describes the actual fitting procedure employed by *multranfit*, from the construction of the likelihood and the inclusion of limits/priors to the minimization/Markov-Chain Monte Carlo sampling and error estimation.

6.3.1 Physical model of transiting exoplanets

The parametrization of transit light curves must describe two aspects of the planetary system. The first is the parametrization of the orbital dynamics of the system and the second is the transit itself. For the orbit, either a more physical parametrization can be chosen that contains the stellar mass directly, or a more phenomenological parametrization in which the orbital period P replaces the mass[2]. Other important parameters are the semi-major axis a, the eccentricity e, the longitude of the periastron ω (orientation of the ellipse relative to the observer) and inclination i of the orbital plane w.r.t. the direction towards the observer. For modeling the actual transit itself, the radius of the planet relative to the stellar radius $R_{\rm p}$ is most important, followed by the limb darkening which is needed as input in order to calculate a light curve.

Although *multranfit* is kept flexible in that regard, in the scope of this thesis one particular physical transit model implementation was used: the Python package *batman* (BAsic Transit Model cAlculatioN, Kreidberg (2015)). This package offers simple use and a relatively efficient calculation of transit light curves from planetary and orbital parameters, based on the analytical model by Mandel and Agol (2002). *batman* uses an efficient integration scheme that exploits the inherent rotational symmetry of typical limb-darkening models by dividing the area that is obscured by

[2]Combining Keppler's third law and Newtonian gravity

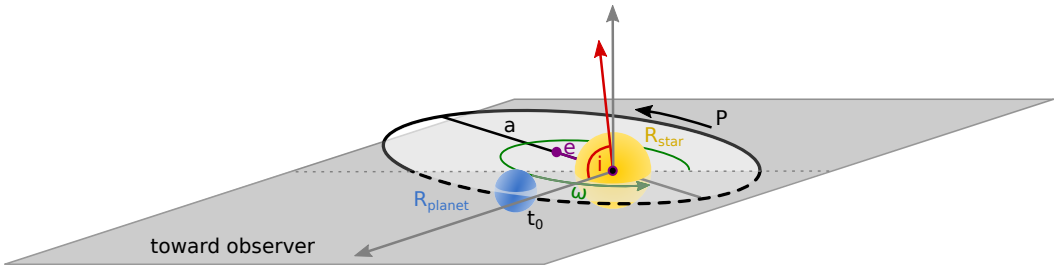

Fig. 6.3.: Illustration of the orbital parameteritzation utilized by the *batman* package. Note that $R_{\rm star}$ and $R_{\rm planet}$ are not directly used in the parametrization, but only their ratio denoted $R_{\rm p}$.

the planet into ring segments. As the brightness gradient is larger towards the edge of the stellar disk, the rings also have variable width, following a $\cos^{-1}(x)$ scaling, where x is the distance from the center of the stellar disk in units of stellar radii (Kreidberg, 2015).

The transit model of *batman* is based on the following parameters (also illustrated in Figure 6.3):

- t_0 time of inferior conjunction
- P orbital period
- $R_{\rm p}$ planet radius (in units of stellar radii)
- a semi-major axis (in units of stellar radii)
- i orbital inclination
- e eccentricity
- w longitude of periastron
- $\boldsymbol{u}$ limb darkening coefficients

The number of limb-darkening parameters depends on the chosen limb-darkening model, a topic that is discussed in detail in the next section.

6.3.2 Stellar limb darkening

Limb darkening is an optical effect in stellar atmospheres that causes the central part of a star to appear brighter to an observer than the edge of the stellar disk (for an illustration see also Figure 6.4). The cause of this effect, which varies with wavelength, is that the light received at a distance is not entirely emitted directly at the surface of a star, but generated at a certain depth. Depending on the angle under which the stellar surface appears to the observer, the distance through the atmosphere and therefore the mean free path on which the light is not reabsorbed varies, too. The functional dependence of brightness versus distance from the center is usually approximated with an analytic expression. Those so-called limb-darkening

models can be either left free during the fit of a transit, be pre-calculated using stellar atmospheric simulations, or be determined using actual data from similar stars.

6.3.2.1 Parameterization of stellar limb darkening

It has already been shown by Schwarzschild (1906) that limb darkening can be parametrized as a polynomial in $\cos i$, where i is the angle to the surface normal under which the stellar surface is observed (see Figure 6.4). In the following, the brightness relative to the center of the star will be described with $F(i)$. Schwarzschild (1906) demonstrates that the following linear model already gives a reasonable approximation for measurements on the Sun:

$$F(i) = \frac{1 + 2\,\cos i}{3}\,. \tag{6.9}$$

Common limb-darkening models are the linear (the above falls under this class)

$$F(i) = 1 - a(1 - \cos i)\,,\ a \in [0, 1]\,, \tag{6.10}$$

the quadratic model

$$F(i) = 1 - u_1\,(1 - \cos i) - u_2\,(1 - \cos i)^2\,,\ u_1 \in [0, 2]\,, u_2 \in [-1, 1]\,, \tag{6.11}$$

or the nonlinear model with four coefficients

$$F(i) = 1 - \sum_{n=1}^{4} c_n\,(1 - \cos i^{n/2})\,,\ \sum_{n=1}^{4} c_n \in [0, 1] \tag{6.12}$$

(Espinoza and Jordán, 2015; Espinoza and Jordán, 2016). The parametrization is illustrated in Figure 6.4, which shows a photograph of the Sun during a Venus transit with the characteristic dimming towards the edge. The parametrization can be converted into a function of the distance from the center of the star r, relative to the stellar radius R.

$$\frac{r}{R} = \sin i \Rightarrow \cos i = \sqrt{1 - \left(\frac{r}{R}\right)^2}\,. \tag{6.13}$$

The decision, which parametrization/model to apply is mainly driven by the quality of the data set. Noisy data and a high dimensional parameter model lead to an excessive amount of free parameters and ultimately reduces the validity of the resulting best-fit parameter sets. For all following examples, it was decided to utilize

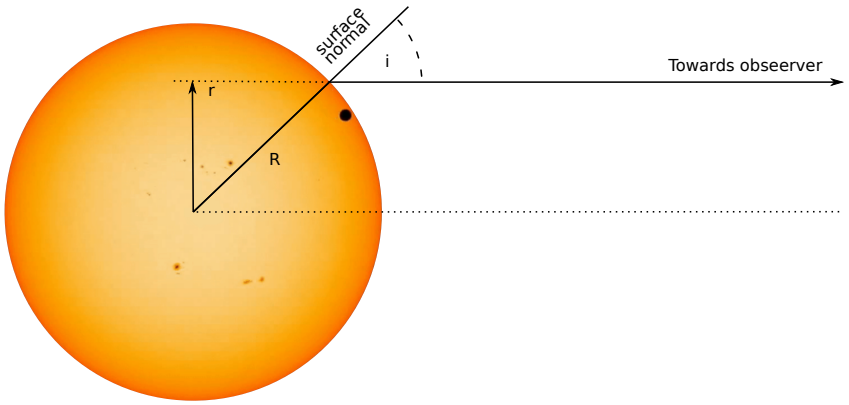

Fig. 6.4.: Limb darkening parametrization illustrated with an actual photograph of the Sun during the Venus transit in 2012 that highlights the effect. Photograph credit: NASA/Goddard Space Flight Center/SDO.

the quadratic limb-darkening model that is fully described by two parameters but already provides enough flexibility to adequately describe the data with the given signal-to-noise ratio.

6.3.2.2 Stellar limb darkening prior estimated by LDTk

More important than the actual limb-darkening parametrization itself is to impose reasonable constraints on the parameters, especially when dealing with noisy data. No matter what parametrization is used to describe the stellar limb darkening, a large fraction of the parameter space is usually non-physical. In fact, if the properties of the star, in terms of size and spectral type are known, the limb darkening can be estimated using stellar models. This allows for a quite precise prediction of the limb darkening. Through relatively tight constraints on the limb-darkening parameters in the form of a statistical prior, they can be converted from free parameters into valuable input that allows for a more precise estimation of the planetary orbital parameters of the system. A tool for converting simulations of stellar atmospheres into a limb-darkening parameter prior already exists in the form of the Python package *LDTk* (Limb Darkening Toolkit) authored by Parviainen and Aigrain (2015).

In *LDTk*, stellar limb darkening is parametrized as a function of

$$\mu = \sqrt{1 - \left(\frac{r}{R}\right)^2} = \cos i \,, \tag{6.14}$$

where $\frac{r}{R}$ is the normalized distance from the center of the stellar disk and i is the angle between the direction to the observer and the direction from the center of the

star to the observed spot on its surface. The following limb-darkening models are supported by *LDTk*:

- *Linear* $1 - C(1-\mu)$
- *Quadratic* $1 - C_1(1-\mu) - C_2(1-\mu)^2$
- *Nonlinear* $1 - \sum_{n=1}^{4} c_n(1-\mu^{n/2})$
- *General* $1 - \sum_{n=1}^{N} c_n(1-\mu^n)$

To estimate the limb-darkening parameters, *LDTk* utilizes the stellar atmosphere simulations generated by *PHOENIX* (Hauschildt and Baron, 1999; Husser et al., 2013a), a stellar simulation software. The University of Göttingen provides a freely accessible database of FITS files generated with this code[3], where *LDTk* utilizes the *'Specific intensity spectra'*. Each file provided by the database is simulated with a certain set of stellar parameters:

- T surface temperature of the star
- $\log(g)$ surface gravity
- z metallicity

The individual files contain intensity spectra spaced along 78 stellar radia in units of μ over a wavelength range of 50 nm to 2600 nm, with an 0.1 nm grid. By multiplying these intensity spectra with the throughput of the instrument curve (e.g. filter of the camera and/or quantum efficiency curve of the detector), limb darkening parameters estimation can be tailored to the specific instrument used for the observation of interest. The individual spectra that have been weighted in this way are then integrated for all 78 values of μ, resulting in a limb darkening profile for the given stellar type and throughput of the instrument.

Since stellar parameters are never known with infinite precision, *LDTk* provides an option to account for this uncertainty. To accommodate for this circumstance, the original *LDTk* package expects an uncertainty range (interpreted as σ of a Gaussian) for all three parameters and will subsequently download all available *PHOENIX* spectra within a $2n\sigma$ cube in the parameter space, using $n = 3$ as default. *LDTk* subsequently performs an interpolation within the grid of stellar parameters, providing limb-darkening curves with 78 radial data points for arbitrary values of T, $\log(g)$ and z, as a linear combination of the surrounding grid points. The interpolation utilizes the *qhull*[4] algorithm (Barber et al., 1996) that is available within *scipy*[5]. For an illustration of the whole process see Figure 6.5. This way, with *LDTk* it is not only possible to find the best-fit parameters for a given stellar spectral

[3] PHOENIX data download: `http://phoenix.astro.physik.uni-goettingen.de/`
[4] *qhull* project webpage: `http://www.qhull.org/`
[5] *scipy* project webpage: `https://docs.scipy.org`

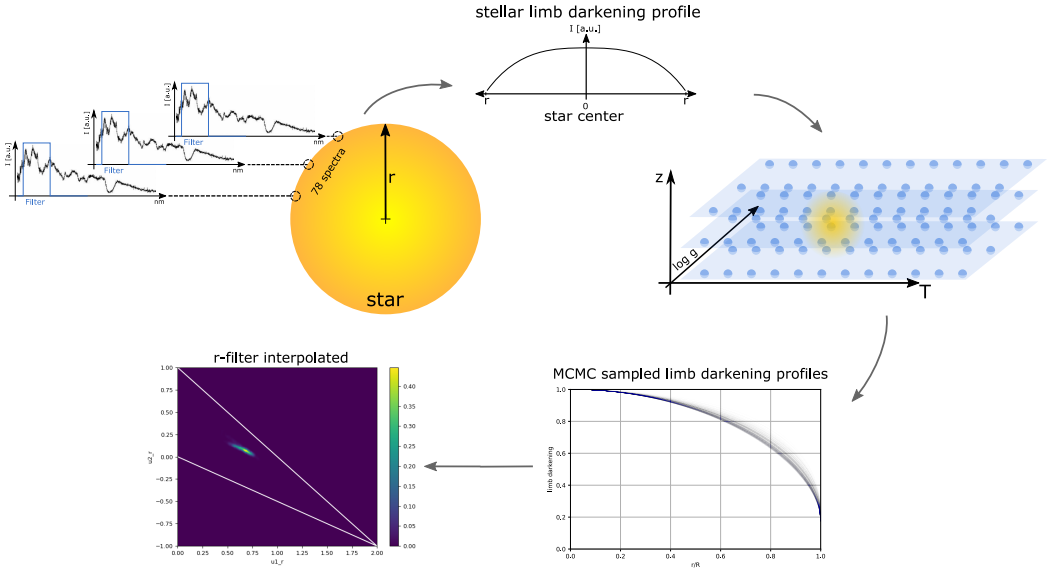

Fig. 6.5.: Illustration of the process performed by *LDTk*. To the simulated PHOENIX intensity spectra of an observation, a specific filter is applied before the whole individual spectra are summed up resulting in an intensity profile recreating the limb darkening profile of the chosen stellar type. To account for uncertainties in the stellar parameters T, $\log(g)$ and z, this is done for all available simulated spectra within the provided uncertainty ranges, creating a grid of limb darkening profiles in T, $\log(g)$, z space. By interpolating between grid points it is possible to derive limb-darkening profiles, also for stellar parameters not covered by the grid structure (points between the grid). Note: Every dot in the grid shown on the right represents one stellar limb darkening profile for one specific stellar parameter combination. Random combinations of stellar parameters are drawn, based on the provided means and standard deviations. Limb-darkening profiles are generated with the help of the interpolation function and fitted with the limb-darkening parametrization. This leads to the histogram of limb-darkening parameters shown in the lower left.

type and limb-darkening model, but also to determine the parameter uncertainty of the limb-darkening model that arises from the uncertainty on the input parameters. This is achieved by the authors utilizing Monte-Carlo sampling from the stellar parameter space and fitting the resulting profile with the desired limb-darkening parametrization. This way, the uncertainty in the space of stellar parameters is converted into a probability distribution in the space of limb-darkening parameters. The original version of *LDTk* then computes the covariance matrix based on this distribution, which can be handed on to a transit-fitting software as prior for the limb-darkening parameters.

For *multranfit* and in the scope of this thesis, the code of *LDTk* has been modified to directly provide an interpolated function of the probability density function in the limb-darkening parameter space to the transit fitter code. This is done by directly

taking the output histogram that results from the aforementioned Monte-Carlo sampling and convert it into a function object, also via *qhull* interpolation (Barber et al., 1996).

An example of such a histogram for the parameters of the *Quadratic* model can be found in Figure 6.6. From this histogram, it can be concluded that in some cases the description of parameter uncertainties and correlation in terms of a covariance matrix only (which would show as a simple ellipse), as it is done in the original version of the package, may not be adequate for describing the actual limb-darkening parameter distribution, since features like asymmetry and curving of the PDF cannot be described with a bivariate Gaussian.

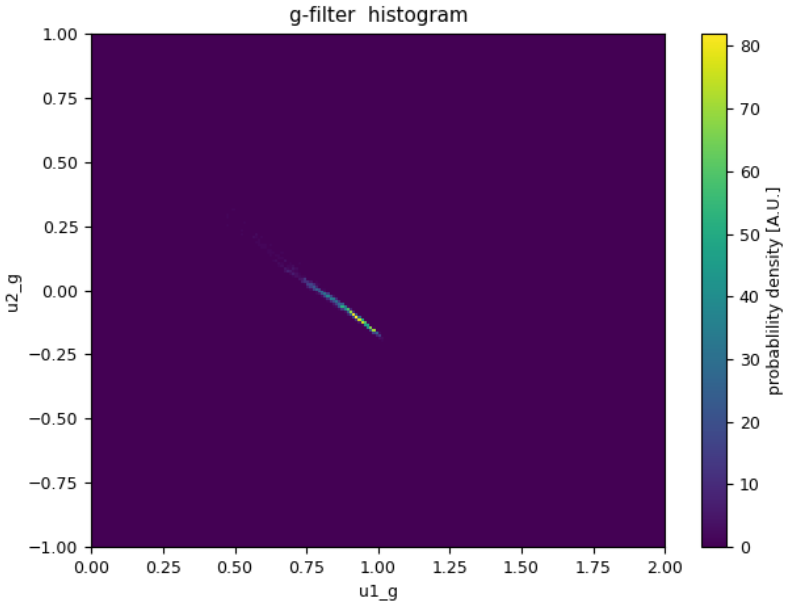

Fig. 6.6.: Example of a limb-darkening parameter prior distribution that has been obtained with the modified *LDTk* code. This example shows the probability distribution for the two parameters of the *Quadratic* limb-darkening model. It is obvious from the plot that a description of the parameter uncertainty and correlation in terms of a covariance matrix may not be precise enough for describing the distribution.

For numerical stability and/or testing purposes, it might be advantageous to artificially increase the freedom given to the limb-darkening parameters. This can be realized by applying a simple Gaussian smearing kernel to the parameter histogram. An example of this is shown in Figure 6.7, where only a mild smearing kernel of 0.012 was applied to the histogram. To still ensure that unphysical regions are excluded from the parameter space, the following two minimal conditions need to be applied to the limb-darkening models:

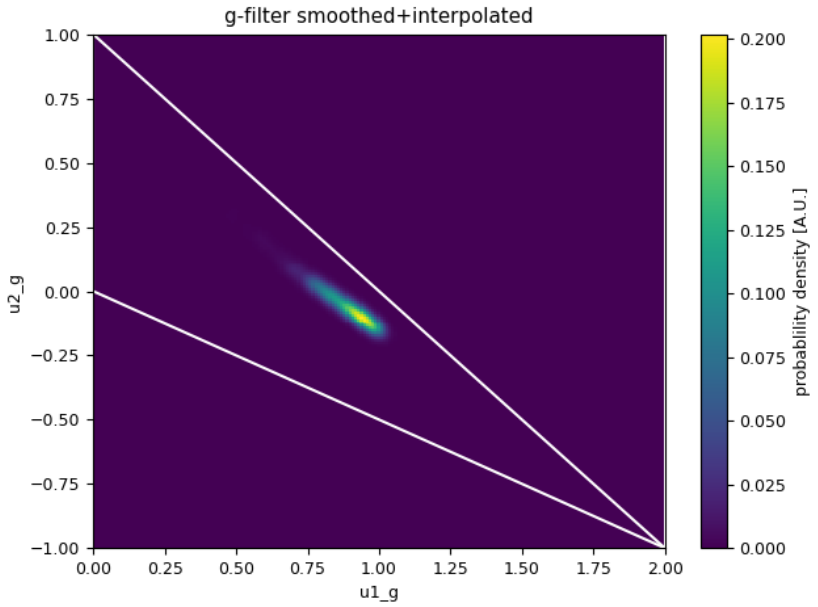

Fig. 6.7.: Example of a smeared limb-darkening parameter prior distribution that has been obtained with the modified *LDTk* code. Parameter combinations outside the triangle bounded by the white lines provide unphysical values.

- The brightness of the stellar disk needs to be positive everywhere.
- The brightness should never decrease when moving from the edge of the disk to the center (Kipping, 2013).

For the *Quadratic* model, which is mostly used for describing limb darkening in the scope of this thesis, this translates into the following three conditions (Kipping, 2013):

- $u_1 + u_2 < 1$
- $u_1 > 0$
- $u_1 + 2\,u_2 > 0\,.$

6.3.3 Likelihood formulation and Bayesian parameter estimation

The data provided to *multranfit* is in the form of normalized light curves, unit-less flux values with Gaussian error bars and attributed timestamps. The likelihood for the fit and MCMC sampling is formulated as a Gaussian likelihood:

$$\ln \mathfrak{L} = -\sum_{i=1}^{N_{\mathrm{ch}}} \sum_{j=1}^{M_i} \left[\frac{1}{2} \ln \left(2\,\pi\,(\Delta f_{i,j})^2 \right) + \frac{(f_{\mathrm{m},ij} - f_{\mathrm{d},ij})^2}{2\,(\Delta f_{i,j})^2} \right]. \tag{6.15}$$

The first part ensures the normalization of a Gaussian distribution. The log-likelihood values are summed over all wavebands/instruments/channels N_{ch} and overall data points within the light curves M_i. $f_{\mathrm{m},ij}$ and $f_{\mathrm{d},ij}$ are the flux values in the model (evaluated at certain parameter values) and data respectively, with attributed measurement errors $\Delta f_{i,j}$. The underlying assumption here is that the uncertainty, when producing the data from the model, follows independent Gaussian distributions for all data points with attributed standard deviations that are the estimated measurement errors. This is appropriate as long as the errors attributed to the model in this fashion can be assumed to be independent of the parameter value. An exception would be very large relative uncertainties on the measurements, similar in magnitude to the actual measured value, a scenario that usually does not occur for transit light curves.

In the next step, the log-likelihood ($\ln \mathfrak{L}$) value is added to the log-prior ($\ln P$), which is also evaluated at the given parameter values. The resulting *log-probability* function can then be negated and handed to a minimization algorithm or directly to an MCMC sampler for finding the best parameter values and the corresponding uncertainty regions in a Bayesian fashion. The following prior distributions are available within *multranfit* and can be assigned individually for each parameter:

- *none* no prior, $\Delta \ln P = 0$,
- *fix* parameter is not varied at all,
- *unif* $\Delta \ln P = 0$ if $x \in [x_1, x_2]$, $\Delta \ln P = -\infty$ else,
- *gaus* $\Delta \ln P = \ln(\frac{1}{\sqrt{2\,\pi}\,\sigma^2}) - \frac{(x-x_0)^2}{2\,\sigma^2}$,
- *LDTk* evaluating interpolated function, only for limb darkening.

The orbital parameters, during the fitting of transit light curves, are often highly correlated, especially when dealing with noisy data. The transit duration can for example be altered by changing either the inclination i or by changing the semi-major axis a of the orbit. In case of highly eccentric orbits also the argument of the periastron ω strongly influences the duration of the transit. The same holds true for the limb-darkening parameters that determine the steepness of ingress and egress of the transit in a very similar fashion as a change in inclination would do. A simplified assessment of parameter correlations, like expressing them in terms of a covariance matrix, might not be sufficient. Directly determining the posterior PDF of the entire parameter set via MCMC sampling provides more detailed information about those parameter correlations, as well as the capability of accurately marginalizing over certain parameters, in order to obtain reliable confidence ranges for other parameters.

When running *multranfit*, it is recommended to always perform a likelihood maximization first before starting the MCMC sampling in order to optimize the sampling starting point. For the minimization of $-\ln \mathfrak{L}$, *multranfit* uses the Python package *iminuit*[6], which is a wrapper around the MINUIT optimization framework (James and Roos, 1975). MINUIT, apart from being fast, reliable and widely used in particle physics, also has the advantage that it provides an error estimate for the best-fit parameters and can provide the covariance matrix as well. More details are provided in Chapter 4.2.2.

Within the scope of this thesis, *multranfit* was used in several analyses of multi-band/multi-instrument data sets from observations of transiting exoplanets. In those observational campaigns, the 3KK multi-band imager of the 2.1 m telescope at the Wendelstein Observatory (see Chapter 1.3) was the primary instrument of choice. In some cases, these observations were carried out as part of a larger collaboration, in a joint effort including space-based instruments and data from different telescopes around the globe.

The results from three of those analyses are presented in Chapter 7.2, in order to highlight the capabilities and performance of *multranfit*. The lead of the observational campaigns and the photometric data analysis was prosecuted by Dr. Christian Obermeier and Jana Steuer. In both cases, only the joint multi-band/multi-instrument fits to the pre-processed light curves was contributed in the scope of this thesis. Both analyses are presented in dedicated scientific papers, see also Obermeier et al. (2020) and H. Kellermann (in prep.).

[6] *iminuit* documentation: `https://iminuit.readthedocs.io`

Part IV

Results and Conclusion

7 Scientific Results

> *Have no fear of perfection; you'll never reach it.*
>
> — **Salvador Dali**

A large fraction of this thesis is dedicated to the description of technical details regarding the development of instruments and methods in hardware and software, as well as the results from evaluating the performance of those methods. Often the transition from evaluation and commissioning to scientific operations is a gradual process. Therefore, this chapter summarizes the first scientific results that could already be achieved by exploiting the newly developed hardware and software. The results fall into two categories, a first radial-velocity-based study of the 51 Pegasi exoplanet system utilizing the upgraded *FOCES* and the newly developed *MARMOT* software, and the discovery/confirmation of the transiting exoplanets Wendelstein-1b and Wendelstein-2b, as well as TOI-1823.

7.1 First observations of 51 Pegasi b with the upgraded *FOCES*

The star 51 Pegasi, well-known for its planetary companion 51 Peg b (Mayor and Queloz, 1995) was observed with *FOCES* as one of the first astrophysical targets during commissioning in autumn 2020. Good quality data could be obtained from

Tab. 7.1.: Observation dates and number of images observed with *FOCES* at the Wendelstein Observatory of the known exoplanetary host system 51-Pegasi.

51 Pegasi b	
date	no. of frames (SCC2)
2020/09/04	4
2020/09/08	3
2020/09/09	3
2020/09/10	6
2020/09/11	4
2020/09/12	6
Total number of images:	26

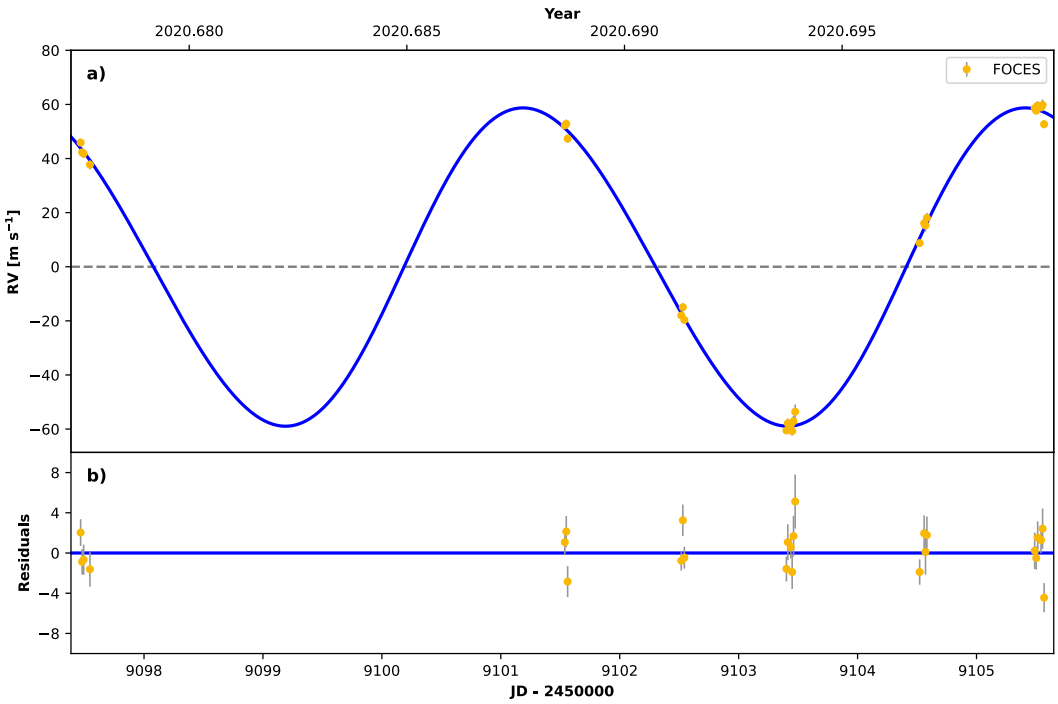

Fig. 7.1.: RV measurements with best-fit orbital model and residuals. The RV measurements have been obtained with *MARMOT*, employing LFC calibration and B-Spline templates as input for the χ^2-fit method. The orbital model fit has been conducted using *RadVel*.

a total of six observational nights (summary in Table 7.1). These data were first processed using *GAMSE* (see Chapter 5.1) and then further analyzed with the RV-analysis package *MARMOT*. The resulting RV-curve after LFC wavelength calibration, utilizing the B-Spline template method and performing a χ^2 RV fit can be found in Figure 7.1. The plot also features the fit of an orbital model using *RadVel*.

By utilizing the MCMC method to obtain estimates for the parameter uncertainties, an orbital period of $4.22^{+0.03}_{-0.03}$ days, a velocity semi-amplitude of $58.84^{+0.86}_{-0.56}$ m/s and an eccentricity of $0.04^{+0.04}_{-0.02}$ could be obtained. The residual RMS after subtracting the fit is 2.04 m/s, with a χ^2/N_{DoF} of 1.6. The results of the fit, besides literature values and the results of a joint fit, including publicly available archival data from several instruments as well as the aforementioned data set of *FOCES*, are summarized in Table 7.2. Note that the time of the pericenter passage T_0 and the argument of the periastron ω (argument of the periastron) are not shown deliberately[1].

[1] T_0 can be chosen arbitrarily at any pericenter passage and should be chosen such that it matches the time window in which the data were recorded. In case of a nearly circular orbit ($e \approx 0$) the value of the argument of the periastron ω is not very meaningful either.

Tab. 7.2.: Comparison of the results of a *FOCES*-only fit, literature values from (Wang and Ford, 2011) and results from a joint fit including archival data from several instruments.

51 Peg orbital parameters					
parameter			*FOCES*	literature	joint fit
period	P_b	[days]	$4.22^{+0.03}_{-0.03}$	$4.2308^{+3.7\times10^{-5}}_{-3.7\times10^{-5}}$	$4.2307883^{+1.6\times10^{-6}}_{-1.6\times10^{-6}}$
vel. semi amp.	K_b	[ms^{-1}]	$58.84^{+0.86}_{-0.56}$	$55.65^{+0.53}_{-0.53}$	$55.72^{+0.11}_{-0.11}$
eccentricity	e_b		$0.04^{+0.04}_{-0.02}$	$0.0069^{+0.0066}_{-0.0069}$	$0.0098^{+0.0013}_{-0.0013}$

The *FOCES* data set was analyzed utilizing the MCMC sampler included in *RadVel* which, on top of the parameter estimation, allows to provide parameter uncertainties. The corner plot generated from the corresponding MCMC sample is shown in Figure 7.2. The fit and MCMC sampling were repeated, combining archival data and the *FOCES* data set, the results of which are also shown in Table 7.2 and plotted in Figure 7.3. The corresponding corner plot of the MCMC samples is shown in Figure 7.4. The error estimates in both cases, *FOCES* data only, as well as for the joint fit should be interpreted with caution at this stage, since it is possible that still unknown *systematic* uncertainties are not yet sufficiently taken into account for the fit.

Literature values for this exoplanet system yield an orbital period of $4.2308^{+3.7\times10^{-5}}_{-3.7\times10^{-5}}$ days, a velocity semi-amplitude of $55.65^{+0.53}_{-0.53}$ m/s and an eccentricity of $0.006^{+0.0069}_{-0.0066}$ (Wang and Ford, 2011). While the other parameters agree within error margins, the deviation of the velocity semi amplitude derived from *FOCES* data set, is larger with respect to literature values than the statistical error margin. This discrepancy can probably be explained by the fact that the error bars attributed to *FOCES* data points describe only statistical uncertainties and do not yet include systematic errors. Such systematic errors can for example be caused by the presence of telluric absorption lines in the spectrum that influences the radial velocity measurement, especially for varying air mass and changing atmospheric conditions between nights. The short duration of the observations and sparse sampling (only six observational nights) spread throughout less than two orbital periods can further enhance the effect on the fitted velocity semi amplitude. The magnitude of the deviation of the measured velocity semi amplitude is comparable in magnitude to the residual RMS that was already found in the same data set when comparing *FOCES* data to a fit that only considered archival measurements from other instruments to determine the orbital parameters (see Chapter 5.10.2). Further analysis of possible sources of systematic error contributions is part of current and ongoing investigations.

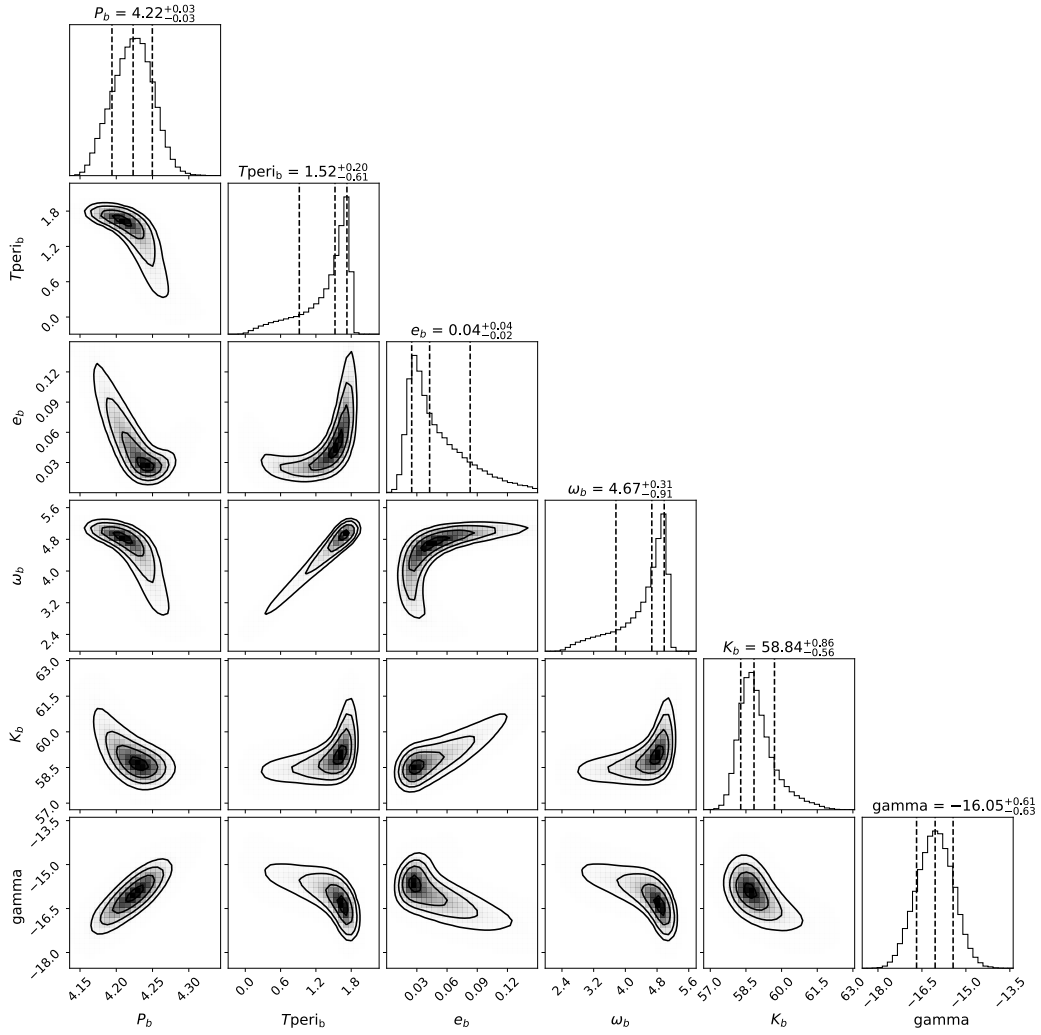

Fig. 7.2.: Corner plot for MCMC sampling of *FOCES* 51 Peg data with *RadVel*. Note: The timestamps of the data points have been biased with a constant offset, bringing them close to zero. This avoids problems with the MCMC-sampling. The constant offset has been added back to the data points and to $T_{\mathrm{peri_b}}$. 'gamma' describes the absolute RV offset in *FOCES* data with respect to the center of mass of the 51 Pegasi system.

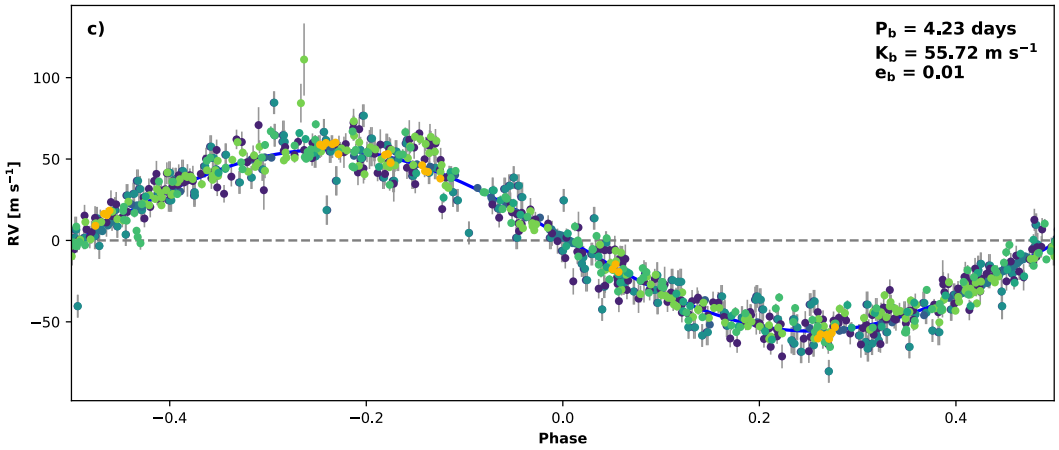

Fig. 7.3.: Phase folded RV curve with model curve and orbital parameters. The RV measurements for *FOCES* have been obtained with *MARMOT*, employing LFC calibration and B-Spline templates as input for the χ^2-fit method. The other data points are measurements from *ELODIE* (Naef et al., 2004; Birkby et al., 2017), *LICK* (Butler et al., 2006; Birkby et al., 2017), *HIRES* (Birkby et al., 2017) and *HARPS* (Birkby et al., 2017). The orbital model fit has been conducted using *RadVel* and fitting all data points simultaneously.

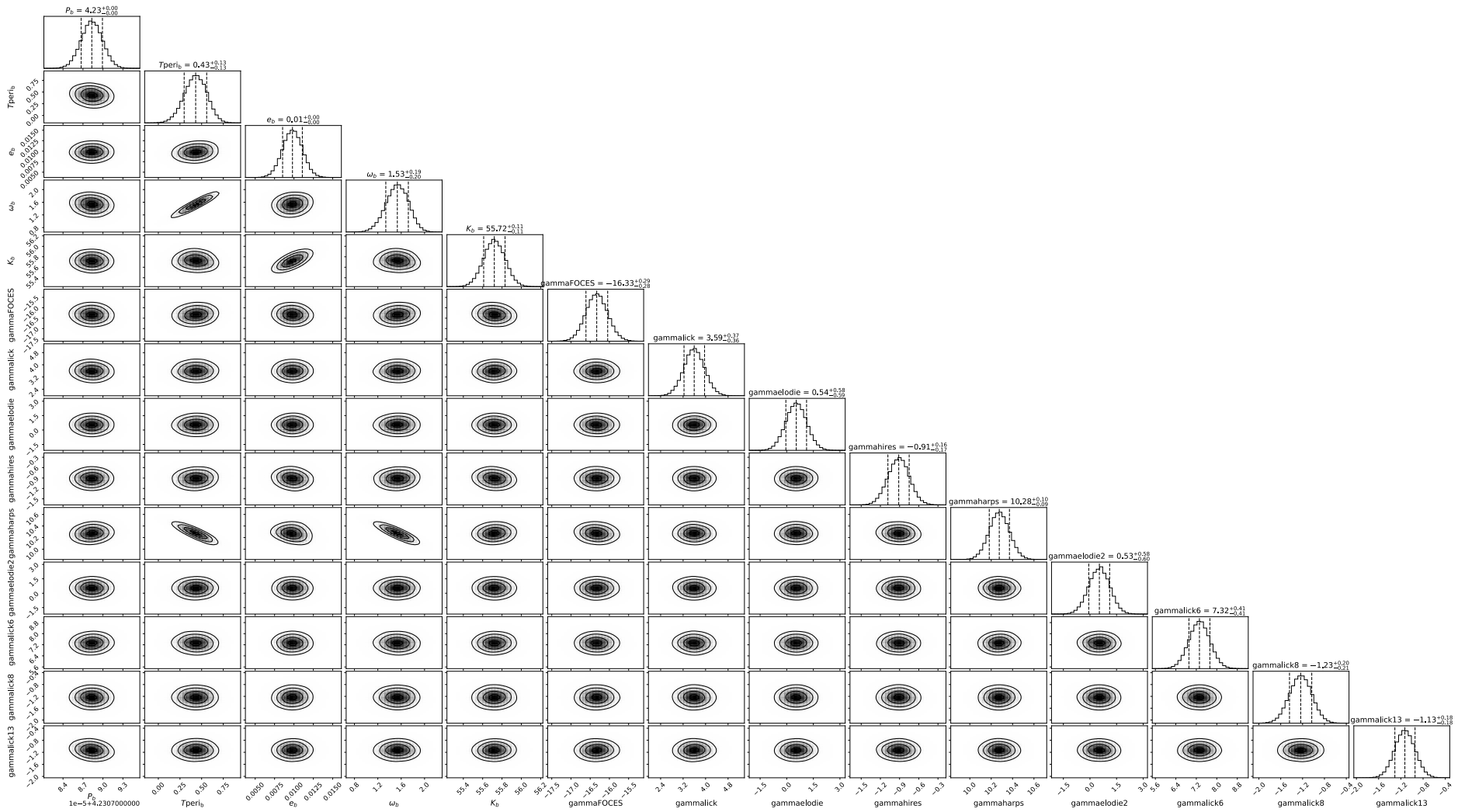

Fig. 7.4.: Corner plot for MCMC sampling of *FOCES* and literature data of 51 Peg with *RadVel*. Note: The timestamps of the data points have been biased with a constant offset, bringing them close to zero. This avoids problems with the MCMC-sampling. The constant offset has been added back to the data points and to T_{peri_b}. The 'gamma' parameters describe the absolute RV offset in the data of different instruments data with respect to the center of mass of the 51 Pegasi system.

7.2 Discovery and verification of exoplanet systems utilizing *multranfit*

In this section, three analyses of transit light curve data sets will be presented. The observations were carried out with the 3KK multi-band imager (see Chapter 1.3), as well as other ground-based telescopes and space-based instruments. The observational campaigns and the photometric data analysis were led by Dr. Christian Obermeier (Wendelstein-1b & Wendelstein-2b) and Jana Steuer (TOI-1823). In both cases, only the joint multi-band/multi-instrument fits to the pre-processed light curves were contributed in the scope of this thesis. Both analyses led to dedicated scientific publications (Obermeier et al., 2020; H. Kellermann, in prep.).

7.2.1 Wendelstein-1b (PP140-14711) and Wendelstein-2b (PP127-21645)

Wendelstein-1b and Wendelstein-2b were exoplanet candidates selected of a sample created by the Pan-Planets survey that was performed by the Pan-STARRS1 telescope with a wide-field, high-resolution camera, located at the Haleakala Observatory, Hawaii (Chambers et al., 2016). This survey, which covered a field-of-view of 42 x 42 degrees, was specifically targeted at finding planets around the coolest spectral types of main-sequence stars, K and M.

Many of the candidates found by the Pan-Planets survey, as well as the numerous candidates detected by recent satellite missions (mainly Kepler and TESS), have a high probability of being false positives. This may still be the case, even with a reasonably significant detection of periodic dimming in the light curve. The problem rather is that other periodic features in light curves, such as the ones caused by eclipsing binaries, can be mistaken for transiting exoplanets. In order to obtain a large enough and unbiased data set of exoplanets for drawing statistical conclusions with regards to planet formation, it is important to find a reasonably fast and scalable solution for confirming the aforementioned candidates.

The traditional method for follow-up observations for confirming such candidates is measuring the radial velocity of the host star. Such a measurement requires the availability of a stabilized high-resolution spectrograph and a significant amount of observation time, as at least an entire orbit needs to be covered. However, even the largest telescopes to date struggle with a radial velocity follow-up of the faint stars ($V_{mag} > 18$) which were observed by Pan-Planets and Kepler.

To contribute a possible solution to this problem, Obermeier et al. (2020) proposes a mainly photometric approach by which simultaneous observations of the same transit in a variety of different wavelength bands should be performed. This way, it is possible to distinguish eclipsing binaries from transiting exoplanets with multi-band observations, as eclipsing binaries that both emit light with somewhat different spectra show discrepancies between wavelengths, while transiting planets produce an achromatic effect regarding the transit depth. A similar effect is also expected from grazing eclipsing binaries that have a relatively high probability of occurring for geometrical reasons (similar stellar radii) and that can therefore produce similar transit depths like those expected from actual transiting planets. The concept of using multi-band observations including also NIR was first suggested by Rosenblatt (1971), pointing out that due to changing limb-darkening profiles the transit depths of grazing binaries increase with increasing wavelengths. Another scenario that can lead to eclipsing binaries mimicking transiting exoplanets is a third star blended within the PSF of the instrument and decreasing the observed relative depth of the occultation so that the light curve resembles more a planetary transit than an eclipsing binary. Here, multi-band observations can also be utilized for probing such a scenario, as long as the stars have different temperatures and therefore emission spectra, again leading to different depths of the light curves in different filters. An overview of the false positive scenarios that are outlined above can be found in Figure 7.5.

The measurement campaign under the lead of Dr. Christian Obermeier had the goal of demonstrating that such observations can be carried out with 2 m class telescopes and moderate investment in terms of observation time. The candidates now known as Wendelstein-1b (PP140-14711) and Wendelstein-2b (PP127-21645) were chosen for this demonstration which turned out successfully and led to the publication by Obermeier et al. (2020).

These two candidates were initially followed up using the 64-megapixel Wide-Field-Imager (Kosyra et al., 2014) attached to the 2.1 m telescope at the Wendelstein Observatory. With its FOV of 0.5 x 0.5 degree and a pixel scale of 0.2 arcsec/pixel it was possible to record full transits in the i-filter-band. Additional observations performed with the 3KK imager opened the possibility for multi-band photometry in in total five filter bands (g', r', z',H, Ks). Table 7.3 and 7.4 give an overview of the data obtained and used for this multi-band analysis. Figure 7.6 shows the contributing wavelength filter bands. The combined multi-band fit to this set of observations (Figure 7.7 and 7.8) and herein especially the measurement of the transit depth and shape in all five wavelength bands (see also Table 7.5 and 7.6) reinforced the exoplanet hypothesis for this two planet candidates substantially. Subsequently

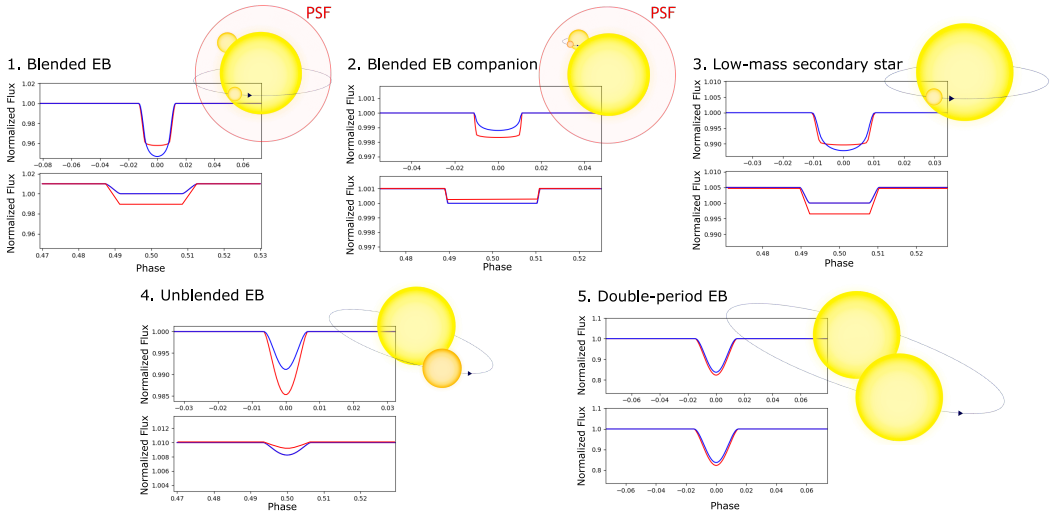

Fig. 7.5.: Compilation of exemplary scenarios that can lead to false-positive detections of exoplanet transits. Each scenario is shown alongside schematic primary (top curve) and secondary (bottom curve) transits. The blue light curves represent the expected behavior if a short wavelength filter is used, while the red light curves indicate the expected behavior for long wavelength filters in comparison. In scenario 5, the secondary transit can be easily mistaken for another primary transit with half of the true orbital period. Figure originally created by Dr. Christian Obermeier, modified and kindly provided by Jana Steuer.

measurements with HIRES, the spectrograph of the 10 m Keck telescope in Hawaii (Vogt et al., 1994), and HPF, the Habitable-zone Planet Finder (Mahadevan et al., 2012), a fiber-fed near-infrared spectrograph mounted on the 1 m Hobby-Eberly Telescope in Texas, confirmed the planets' status of both targets.

Tab. 7.3.: Observation dates, filter bands and number of images observed with 3KK and the WWFI imager at the Wendelstein Observatory of Wendelstein-1b (PP140-14711).

Wendelstein-1b			
date	filter	number of frames	instrument
2015/08/02	i'	182	WWFI
2017/08/07	Ks, r', z'	452	3KK
2017/08/14	Ks, r', z'	350	3KK
2018/06/03	H, g', z'	266	3KK
2018/07/29	H, g', z'	247	3KK
Total number of images:		1497	

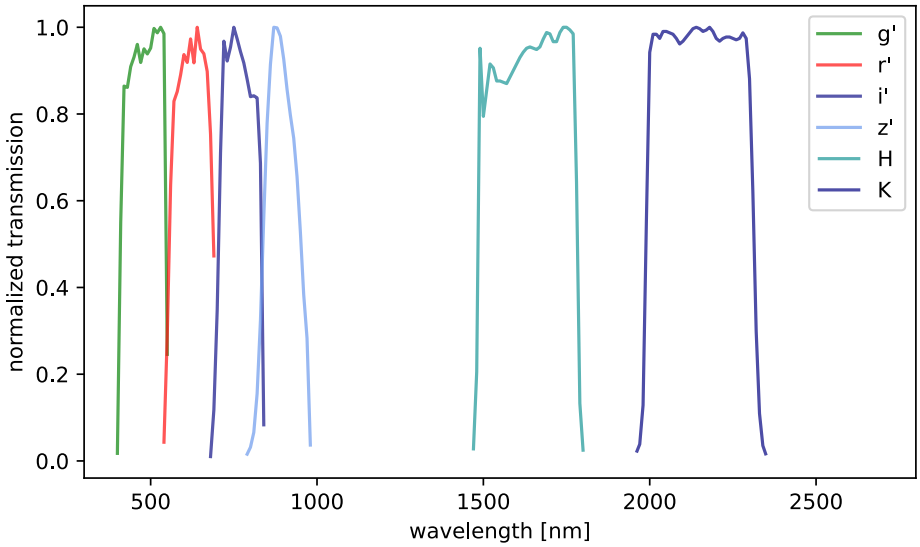

Fig. 7.6.: Normalized filters used in the multi-band fit of Wendelstein 1b & 2b. These are also the filters that were provided to *LDTk* in order to compute the limb darkening prior.

Tab. 7.4.: Observation dates, filter bands and number of images observed with 3KK and the WWFI imager at the Wendelstein Observatory of Wendelstein-2b (PP127-21645).

Wendelstein-2b			
date	filter	number of frames	instrument
2015/07/15	i'	106	WWFI
2015/08/06	i'	252	WWFI
2017/08/17	Ks, r', z'	471	3KK
2017/10/13	Ks, r', z'	170	3KK
2018/06/02	H, g', z'	220	3KK
2018/07/30	H, g', z'	232	3KK
Total number of images:		1451	

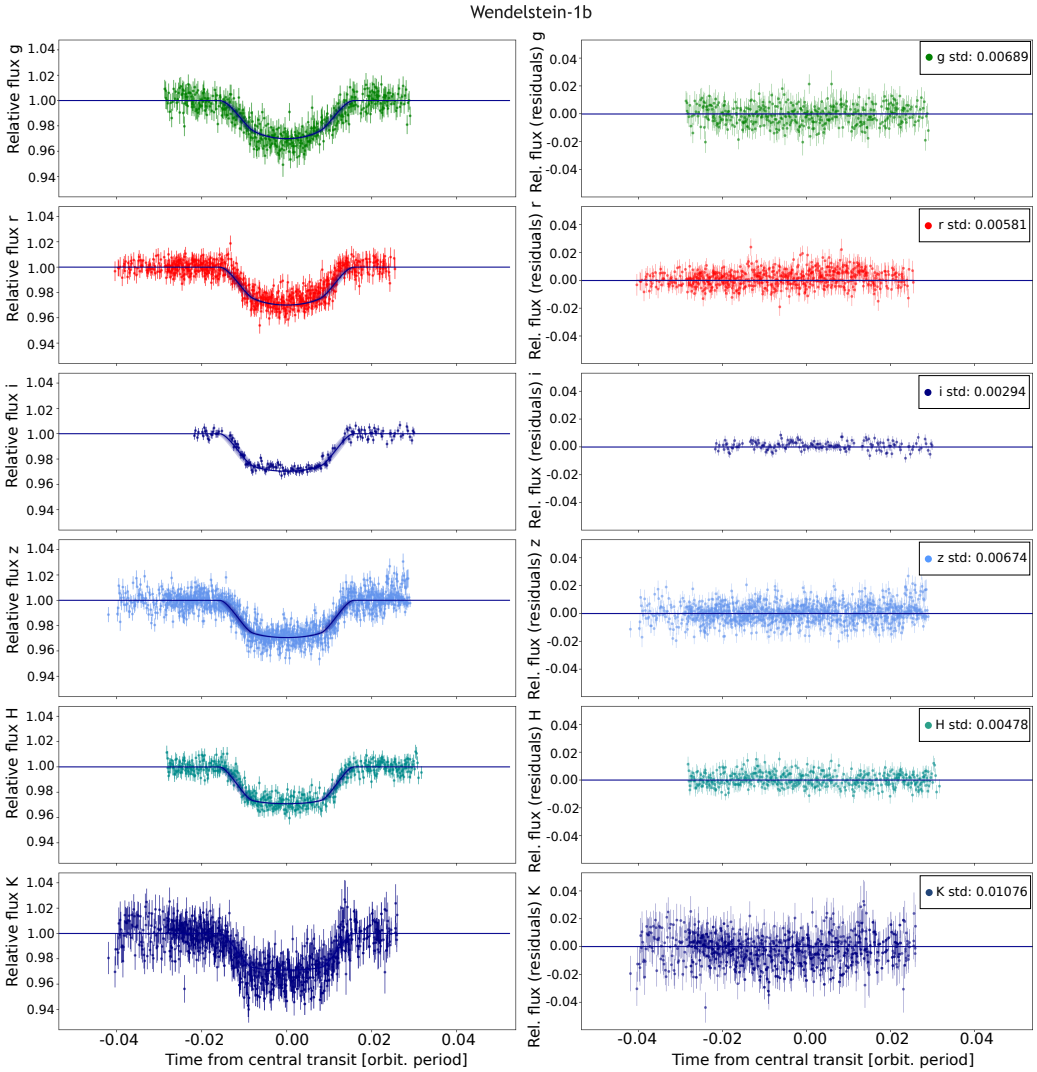

Fig. 7.7.: Left panel: Simultaneous fit of the transit light curves of Wendelstein-1b recorded with the Wendelstein Observatory's WWFI and 3KK, in the photometric bands g', r', i', z', H, Ks. The best-fit curve, as well as 1σ, 2σ and 3σ error bands, are shown alongside the data. Right panel: Residuals after subtracting the best-fit curve.

Tab. 7.5.: Orbital parameters and uncertainties determined from the posterior distribution of Wendelstein-1b, based on multi-band photometry. ΔF denotes the flux drop for the corresponding band. u_1 and u_2 represent the quadratic limb darkening coefficients for each photometric band.

Wendelstein-1b		
Parameter		Result
t_0	[BJD_TDB]	2455367.738464 $\pm$ 0.000014
P	[d]	2.663416 $\pm$ 0.000001
R_P	[R_*]	0.1698 $\pm$ 0.0010
a	[AU]	0.0282 $\pm$ 0.0015
i	[deg]	86.12 -0.39 +0.43
e		$<$ 0.056
	$u_{1,\mathrm{g'}}$	0.89 $\pm$ 0.02
	$u_{2,\mathrm{g'}}$	-0.07 $\pm$ 0.02
	$u_{1,\mathrm{r'}}$	0.68 $\pm$ 0.01
	$u_{2,\mathrm{r'}}$	0.07 $\pm$ 0.01
	$u_{1,\mathrm{i'}}$	0.50 $\pm$ 0.01
	$u_{2,\mathrm{i'}}$	0.15 $\pm$ 0.01
	$u_{1,\mathrm{z'}}$	0.41 $\pm$ 0.02
	$u_{2,\mathrm{z'}}$	0.17 $\pm$ 0.02
	$u_{1,\mathrm{H}}$	0.23 $\pm$ 0.02
	$u_{2,\mathrm{H}}$	0.22 $\pm$ 0.02
	$u_{1,\mathrm{Ks}}$	0.18 $\pm$ 0.02
	$u_{2,\mathrm{Ks}}$	0.20 $\pm$ 0.02
	$\Delta F_{g'}$	0.0223 $\pm$ 0.0009
	$\Delta F_{r'}$	0.0257 $\pm$ 0.0006
	$\Delta F_{i'}$	0.0269 $\pm$ 0.0003
	$\Delta F_{z'}$	0.0269 $\pm$ 0.0010
	ΔF_H	0.0275 $\pm$ 0.0007
	ΔF_{Ks}	0.0281 $\pm$ 0.0011

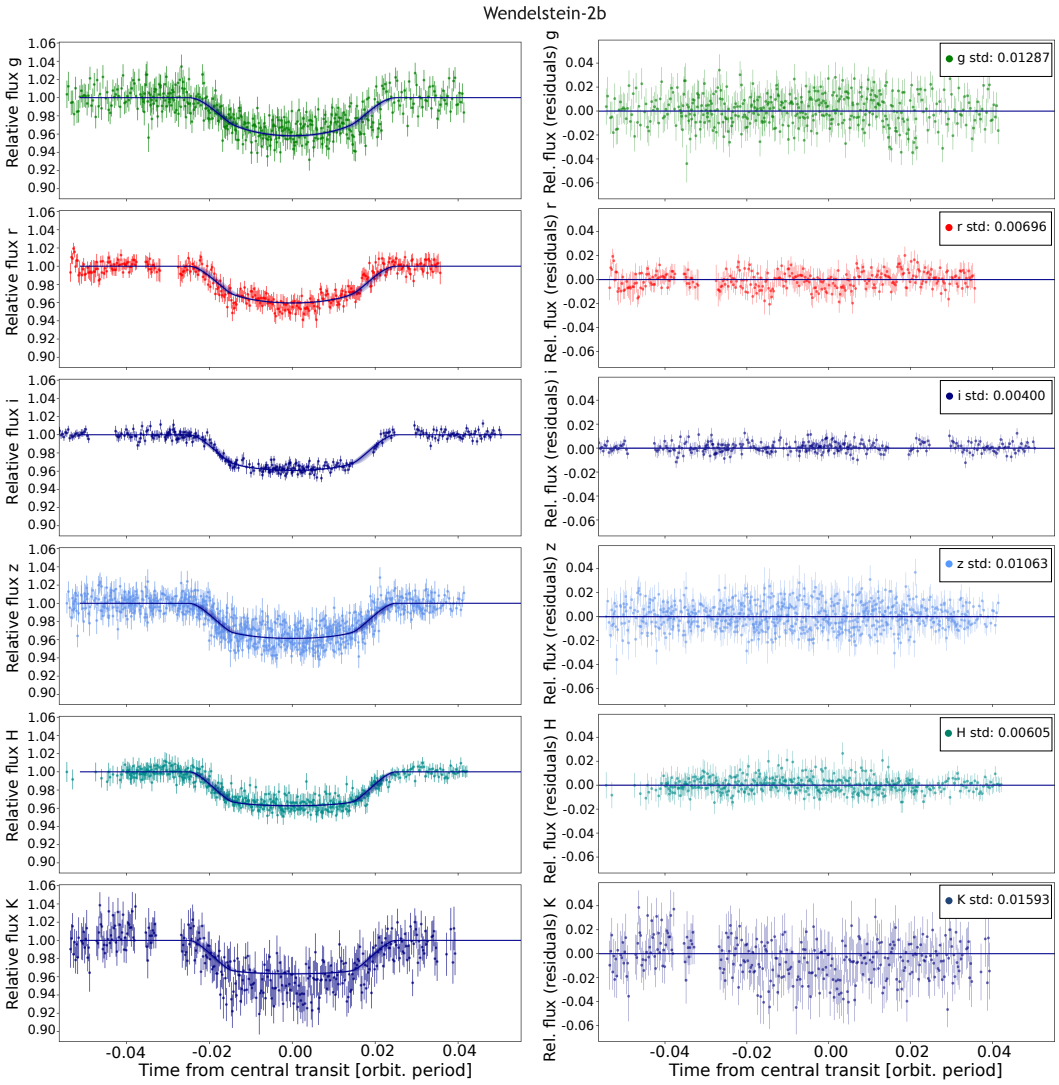

Fig. 7.8.: Left panel: Simultaneous fit of the transit light curves of Wendelstein-2b recorded with the Wendelstein Observatory's WWFI and 3KK, in the photometric bands g', r', i', z', H, Ks. The best-fit curve, as well as 1σ, 2σ and 3σ error bands, are shown alongside the data. Right panel: Residuals after subtracting the best-fit curve.

Tab. 7.6.: Orbit parameters and uncertainties determined from the posterior distribution of Wendelstein-2b, based on multi-band photometry. ΔF denotes the flux drop for the corresponding band. u_1 and u_2 represent the quadratic limb darkening coefficients for each photometric band.

Wendelstein-2b		
Parameter		Result
t_0	[BJD_TDB]	2455679.254400 ± 0.000013
P	[d]	1.7522239 ± 0.0000008
R_P	[R_*]	0.176 ± 0.004
a	[AU]	0.0234 ± 0.0015
i	[deg]	87.87 +0.98 -1.04
e		< 0.057
	$u_{1,\mathrm{g'}}$	0.96 ± 0.02
	$u_{2,\mathrm{g'}}$	-0.13 ± 0.02
	$u_{1,\mathrm{r'}}$	0.70 ± 0.01
	$u_{2,\mathrm{r'}}$	0.04 ± 0.01
	$u_{1,\mathrm{i'}}$	0.54 ± 0.01
	$u_{2,\mathrm{i'}}$	0.10 ± 0.01
	$u_{1,\mathrm{z'}}$	0.46 ± 0.02
	$u_{2,\mathrm{z'}}$	0.12 ± 0.02
	$u_{1,\mathrm{H}}$	0.21 ± 0.02
	$u_{2,\mathrm{H}}$	0.24 ± 0.02
	$u_{1,\mathrm{Ks}}$	0.18 ± 0.02
	$u_{2,\mathrm{Ks}}$	0.18 ± 0.02
	$\Delta F_{g'}$	0.0355 ± 0.0014
	$\Delta F_{r'}$	0.0397 ± 0.0011
	$\Delta F_{i'}$	0.0359 ± 0.0004
	$\Delta F_{z'}$	0.0355 ± 0.0009
	ΔF_H	0.0366 ± 0.0011
	ΔF_{Ks}	0.0375 ± 0.0022

7.2.2 TOI-1823 b

The Wendelstein observatory is part of a collaboration among instruments that carry out follow-up observation campaigns of exoplanet candidates in the photometric data collected with the TESS satellite (see also Chapter 1.3). The TOI-1823 observations were triggered by a single transit event recorded in sector 15 of the TESS observational schedule, in August 2019. According to the Revised TESS Input Catalog (Stassun et al., 2019), TOI-1823 is a high proper motion star with 0.82 ± 0.05 solar radii at a distance of 71.65 ± 0.11 parsecs. The target in question is a K dwarf with a temperature of $T_{\text{eff}} = 4760 \pm 117$ K and a brightness of $V_{mag} = 10.728 \pm 0.01$.

As already introduced in Chapter 1.3, TESS scans the sky in a stripe-like pattern with an observation period of one strip of 27 days. Due to the design of the satellite mission, a certain portion of the observation strips overlap resulting in higher observational coverage of these regions. As a result of its location in the sky, TOI-1823 was recorded in four non-consecutive TESS sectors (14, 15, 21 and 22) and transits could be detected in sectors 15 (August 2019) and 22 (March 2020). An additional hint for a possible transit egress could be found at the very edge of the sector 21 time window but was first excluded from further analysis steps since this light curve region is usually not reliable enough (originating mainly from pointing instabilities) and therefore ignored. From the two significant transit events, a maximum orbital period for the planet of 194.1 days could be concluded. Due to the gaps in the observation, also integer fractions of this value, 97.05 d, 64.7 d, 48.525 d, 38.82 d or 32.35 d could not be excluded from TESS data alone. Shorter periods could be excluded due to the observation length of a TESS strip. The third hint for a transit, as well as an estimate of the orbital period based on a single transit fitted with *multranfit*, triggered a campaign led by Jana Steuer that probed the 38.82 day period, initially using the 43 cm telescope at the Wendelstein Observatory. These observations yielded another hint of an incomplete transit, which was the starting point for a joint observational campaign with several other institutes to finally verify the 38.82 d period and to determine the properties and orbital parameters of the planet candidate.

It was possible to realize a combined observation with seven different instruments on three observation sites (Wendelstein Observatory in Germany, Teide Observatory on Tenerife, Spain, and the Xinglong Observatory in China), as well as two satellite missions (TESS and the Near Earth Object Surveillance Satellite, NEOSSat). A detailed breakdown of the contributing instruments, that were included in the final

Tab. 7.7.: Observation dates, filter bands and number of images for each instrument contributing to the TOI-1823 parameter estimation.

Tess TOI-1823				
date	filter	number of frames	site	instrument
15/8-27/8/2019	$f_{T.}$	7992	satellite	TESS
29/8-9/9/2019	$f_{T.}$	7887	satellite	TESS
20/2-4/3/2020	$f_{T.}$	8843	satellite	TESS
1/5/2021	V	748	Xinglong	85cm China
1/5/2021	R	746	Xinglong	85cm China
1/5/2021	I	748	Xinglong	85cm China
12/2/2021	g	821	Wendelstein	3KK (FWT)
12/2/2021	i	1418	Wendelstein	3KK (FWT)
12/2/2021	$f_{N.}$	1139	satellite	NEOSSat
12/2/2021	$g_{S.}$	687	Teide	WiFSIP (STELLA)
Total number of images:		31029		

analysis which is presented in the following figures, can be found in Table 7.7.[2] While the devices TESS and 3KK were already introduced in Section 1.3, the following paragraph will briefly introduce the additional contributing instruments.

The Wide Field STELLA Imaging Photometer (WiFSIP) installed at the 1.2 m STELLA telescope (Strassmeier et al., 2010) located at the Izana Observatory in Tenerife (Spain) was able to contribute two transit observations. This imager utilizes a large-format CCD with a pixel scale of 0.32 arcsec/pixel and a usable field-of-view (FoV) of 22 x 22 arcmin. The 85cm-telescope at the Xinglong Observatory in China (Bai et al., 2018) captured the transit in three different wavelength bands, (R, I, g) with a FOV of 32 x 32 arcmin and a pixel scale of 0.93 arcsec/pixel. Even though the micro-satellite NEOSSat (Hildebrand et al., 2008) developed by the Canadian Space Agency with a FOV of 0.85 x 0.85 degrees is not capable of continuous observation, it was possible to detect the transit clearly in its observation bursts. Due to its operation mode, observations are interrupted by the Earth eclipse, the South Atlantic Anomaly flybys, and momentum desaturation which limit the pointing of the satellite at a section of the sky to 53 min at a time leading to non-continuous transit light curves. Figure 7.9 illustrates the different filter bands in which observations could be obtained. All pre-processed light curves with reasonable data quality gathered in this observation campaign were subsequently fitted with *multranfit*. Figure 7.10 shows the phase-folded transit light curve with the best-fit curve and error band of the model obtained with MCMC sampling. Figure 7.11 depicts the residuals after subtracting the model from the data. Due to the large degeneracy of the parameter

[2]Data from observations with the 43 cm telescope of the Wendelstein Observatory, as well as from the 65 cm telescope of the Xinglong Observatory were not included in the fit as the level of noise in the data is not expected to lead to a helpful contribution.

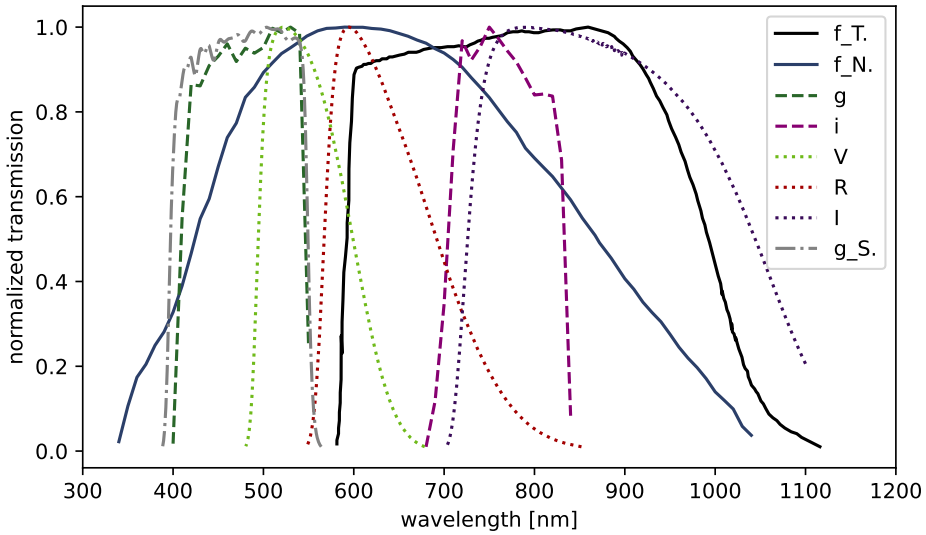

Fig. 7.9.: Filters used in the multi-band/multi-instrument fit of TOI-1823. Normalized filter curves for each instrument/band contributing to the fit are shown. These are also the filters that were provided to *LDTk* in order to compute the limb darkening prior. The indicated filter types and their corresponding instruments can be found in Table 7.7.

space, the eccentricity was fixed at zero[3]. Therefore ω does not yield any information and was fixed likewise. The parameter results with uncertainties in terms of median and symmetric 68% confidence intervals are presented in Table 7.8.

These results clearly confirm the 38.82 d period and a depth of 10.331 ± 0.001 mmag. Its size could be calculated to 7.58 ± 0.46 Earth radii, putting it into the size range of Saturn. Contributions of the Automated Planet Finder (APF) spectrograph at the Lick Observatory on Mt. Hamilton in California (USA) could narrow the mass down to $59 \pm 9\, M_E$. This implies a bulk density of $0.747 \pm 0.114\ g/cm^3$, which is comparable to Saturn's density rendering a false positive detection of the planet highly unlikely.

[3]This assumption was confirmed to be valid by radial velocity observations performed by Dr. Paul Dalba utilizing the APF.

Tab. 7.8.: Orbital parameters and uncertainties determined from the posterior distribution of TOI-1823, based on multi-band photometry. u_1 and u_2 represent the quadratic limb darkening coefficients for each photometric band.

TOI-1823			
parameter	value	uncertainty	uncertainty
t_0 [BJD]	2458909.24659	+0.00036	-0.00036
P [d]	38.81362	+0.00005	-0.00005
R_p [R_*]	0.0847	+0.0004	-0.0004
a [AU]	55.296	+0.794	-0.361
i [deg]	89.901	+0.108	-0.070
e	fix		
ω [deg]	fix		
$u_{1,\,(\mathrm{Tess})}$	0.512	+0.035	-0.031
$u_{2,\,(\mathrm{Tess})}$	0.104	+0.029	-0.028
$u_{1,\,(\mathrm{NEOSSat})}$	0.732	+0.029	-0.027
$u_{2,\,(\mathrm{NEOSSat})}$	0.043	+0.026	-0.028
$u_{1,\,(\mathrm{3KK,\,g})}$	0.952	+0.051	-0.038
$u_{2,\,(\mathrm{3KK,\,g})}$	-0.111	+0.039	-0.048
$u_{1,\,(\mathrm{3KK,\,i})}$	0.552	+0.035	-0.029
$u_{2,\,(\mathrm{3KK,\,i})}$	0.117	+0.026	-0.029
$u_{1,\,(\mathrm{85cm,\,V})}$	0.792	+0.056	-0.042
$u_{2,\,(\mathrm{85cm,\,V})}$	-0.002	+0.038	-0.047
$u_{1,\,(\mathrm{85cm,\,R})}$	0.616	+0.066	-0.057
$u_{2,\,(\mathrm{85cm,\,R})}$	0.096	+0.042	-0.042
$u_{1,\,(\mathrm{85cm,\,I})}$	0.426	+0.054	-0.044
$u_{2,\,(\mathrm{85cm,\,I})}$	0.140	+0.027	-0.037
$u_{1,\,(\mathrm{WiFSIP})}$	0.668	+0.096	-0.089
$u_{2,\,(\mathrm{WiFSIP})}$	0.098	+0.083	-0.109

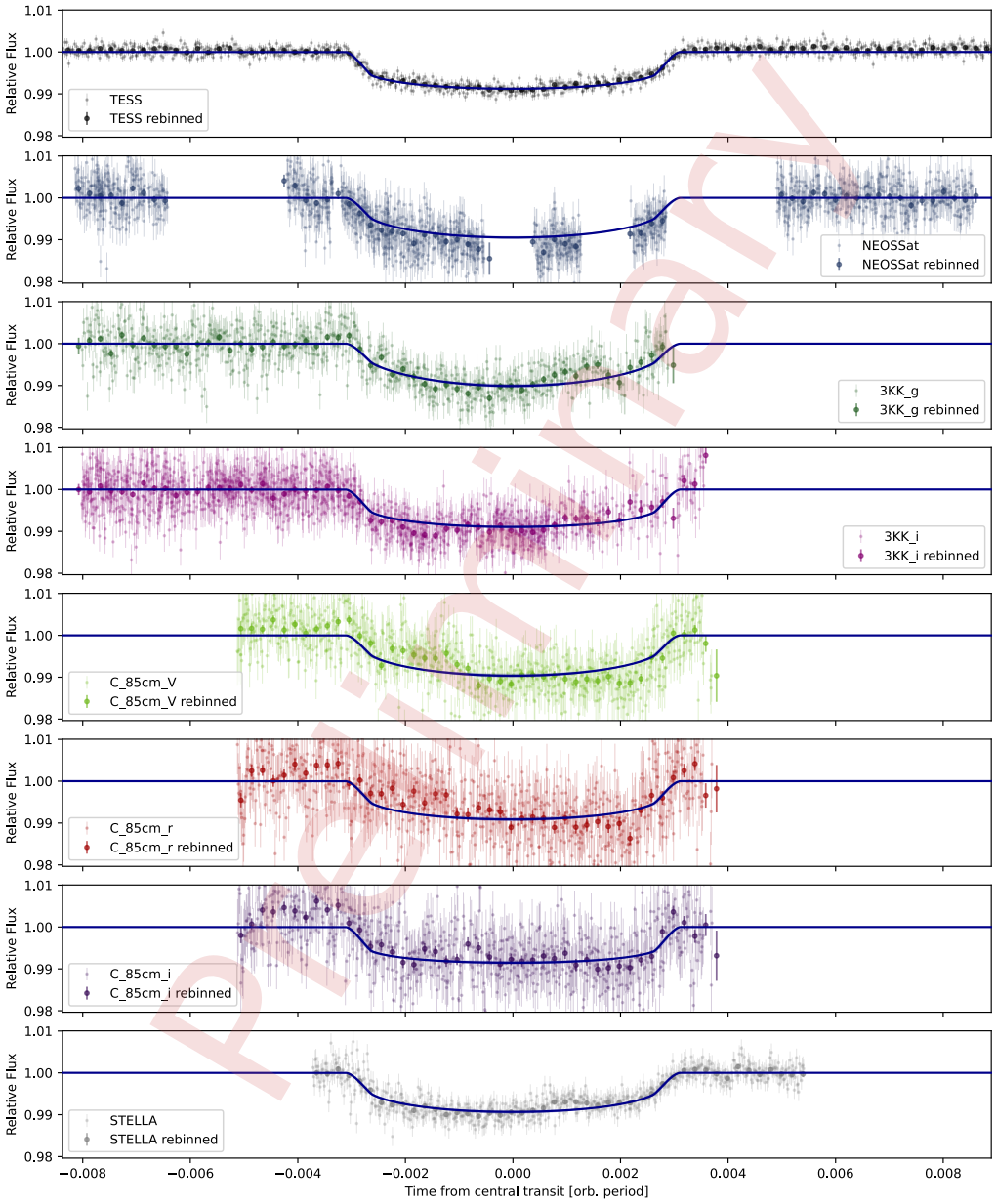

Fig. 7.10.: Simultaneous fit of the transit light curves of TOI-1823 with light curves contributing from TESS, NEOSSat, WiFSIP, 3KK and the 85 cm telescope in China recorded in the wavelength bands $f_{T.}$, V, R, I, g, i, $f_{N.}$, $g_{S.}$

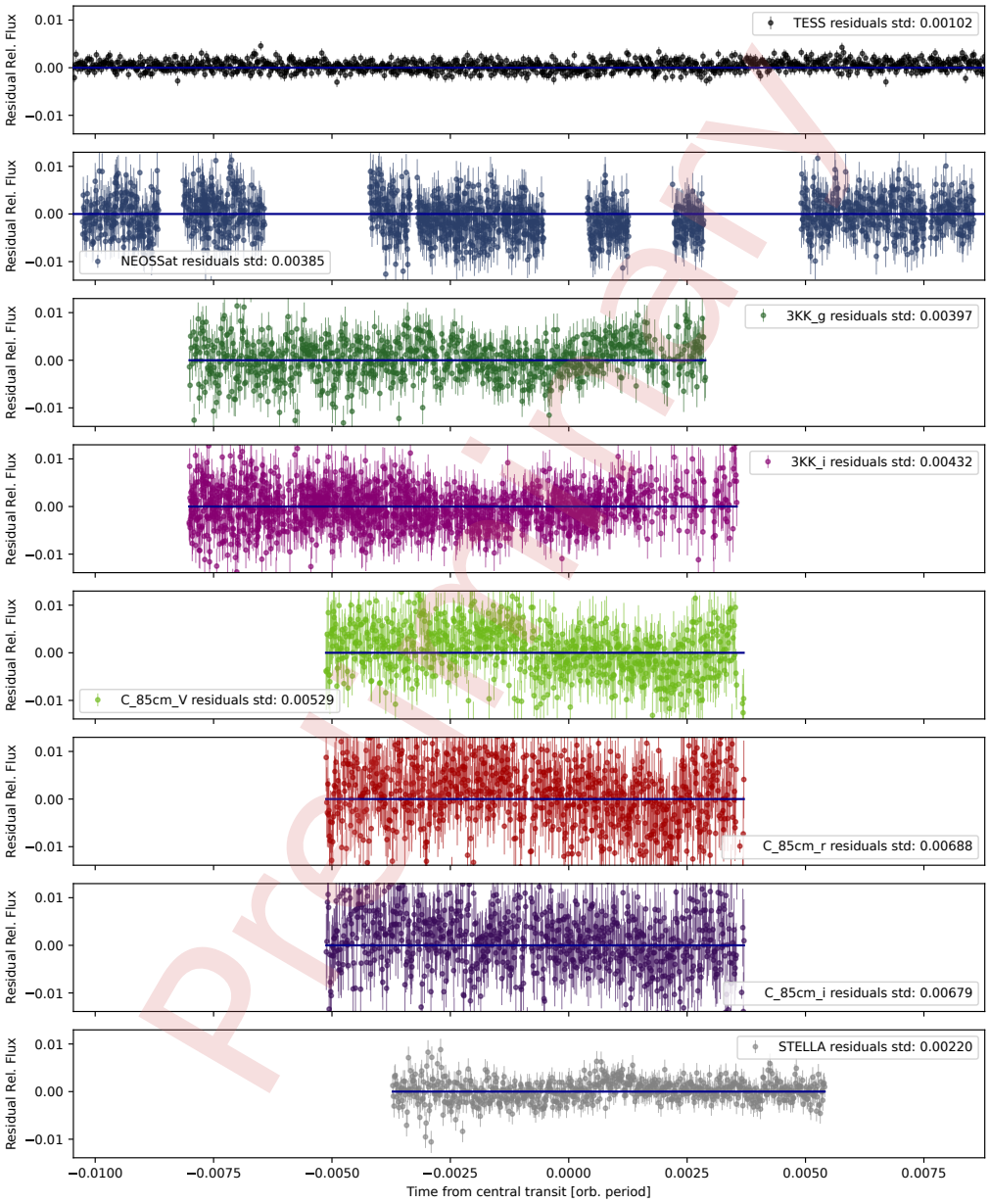

Fig. 7.11.: Residuals after subtracting the best-fit curve for TOI-1823.

Conclusion and Outlook

8

> *One never notices what has been done; one can only see what remains to be done.*
>
> — **Marie Curie**

The work that led to this thesis was dedicated to improving the capabilities, in terms of instrumentation at the Wendelstein observatory, as well as in terms of analysis software available to the USM, in hunting for exoplanets with both, the radial-velocity as well as the transit method. These developments are demonstrated by re-observations of known systems, as well as the confirmation/discovery of new exoplanet candidates.

The most important developments that are presented in this thesis are:

- Design, assembly, qualification and installation at the Wendelstein Observatory of a *4-fiber-slit assembly* as entrance aperture for the *FOCES* high resolution Échelle spectrograph, that enables simultaneous calibration using a laser frequency comb or other calibration light sources.
- Design, assembly and installation at the Wendelstein observatory, of a calibration unit for *FOCES* that allows to select, combine and attenuate light from different sources that can then be used for various calibration measurements with *FOCES*. Most prominently these calibration light sources also include an optical laser frequency comb.
- Assembly of the *FOCES* spectrograph at the Wendelstein observatory, inside its new insulated pressure vessel and installation of the hardware components for temperature and pressure stabilization.
- Development and implementation of different methods for fiber-mode scrambling within the optical fibers feeding *FOCES*, including a mechanical fiber shaker.
- Development of a software framework (*MARMOT*) for analyzing pre-extracted 1D Échelle spectra, utilizing simultaneously recorded calibration spectra. The main features comprise LFC-based wavelength re-calibration or RV-corrections, spectral template generation utilizing b-splines, radial velocity extraction using both, a χ^2 fit or cross-correlation function, as well as barycentric corrections

and fitting of externally provided physical models. The framework also includes tools to evaluate the performance/stability of the spectrograph, as well as to generate realistic artificial spectra to be used for tests of different analysis methods.

- Development of software tools (*multranfit*) to simultaneously fit transit light curves recorded in different wavelength bands and various instruments, all within a Bayesian framework that allows to introduce sophisticated priors for nuisance parameters linked to for example limb darkening.

With those improvements and new tools, it was possible to confirm/detect three new exoplanet systems, Wendelstein-1b and Wendelstein-2b (lead by Dr. Christian Obermeier), as well as TOI-1823 b, the latter in a joint effort together with different ground and space-based observatories (lead by Jana Steuer). Wendelstein-1b and 2b were both candidates from the Pan-Planets survey that could not unequivocally be identified as planets using a single wavelength. Using however simultaneous observations with the 3KK multi-channel optical and near-infrared imager at the Wendelstein observatory it was possible to largely preclude false-positive detections. These results highlight the value to conduct multi-band/multi-instrument observations of exoplanet transits and the availability of software tools for simultaneously fitting the recorded light curves.

The performance of the new upgraded *FOCES* spectrograph with its simultaneous LFC-based wavelength calibration and the new analysis software *MARMOT* were demonstrated by observing the well-known exoplanet hosting system 51 Pegasi b. Based on observations that were carried out in autumn 2020, the different RV-extraction methods of *MARMOT* could be compared and the capabilities of the LFC-based wavelength calibration were tested. With these studies it could be demonstrated that utilizing the B-spline based spectral templates and applying the LFC-based wavelength re-calibration, an RV precision of around 3.6 m/s could be reached consistently with both the χ^2 fit-based and the CCF-based method. The achieved performance of *FOCES* is thus already within the targeted range for our 2 m-class telescope, although further tuning and optimizations in hardware and software might still improve this first benchmark.

In the following, an overview of possible future hardware and software optimizations/improvements is given:

- For an even better fiber-mode scrambling and a more homogeneous near field pattern of the fiber that guides the science light from the telescope to the spectrograph, replacing the standard multimode optical fiber with an octagonal-cross-section optical fiber is already scheduled. These fibers are

known for quickly "losing their memory" on any spatial mode pattern at the input ruling them insensitive to guiding errors or clouds passing the FoV of the telescope during an observation.

- The new so-called *First-Ring* currently under construction will offer a much sturdier and more reliable light coupling to the transport fiber of *FOCES* increasing the long-term repeatability of the light input thus removing one of the largest contributors to long-term systematic uncertainties of RV measurements.
- Due to its exposed position at the top of the mountain and its geographic location in the south of Germany, the Wendelstein observatory is frequently subject to lightning strikes with the potential of damaging the electronic devices associated with *FOCES*. These damages are not only an expensive nuisance as repairing/replacing the hardware is demanding in terms of money and manpower, and leads to a loss of observation time, but can also jeopardize the long-term continuity of the RV-measurements. This is specifically relevant for planets with long orbital periods, where wavelength calibration stability needs to be maintained over months or years.
- One of the current limiting factors to the RV precision that can be achieved with *FOCES* is the influence of telluric absorption lines and the resulting RV shifts. In the context of this thesis, some techniques for mitigating this effect have already been implemented and tested, with the main focus on identifying and excluding affected regions in the spectra. More extensive studies, founded on a larger and more diverse data set could help optimizing this technique even more. Furthermore, a promising idea that has already been tested briefly within the context of this thesis but was not followed up sincerely due to a lack of time, could be further explored. This idea foresees to include a flexible telluric absorption spectral template into the fit as separate component with independent scaling and RV-shift.
- Finally, extending the capabilities of *multranfit* with the option of simultaneously fitting transit light curves and RV measurements is a natural next step. Such a combined analysis has the capability of constraining the physical properties of an exoplanet much more tightly. For example, this way one of the model parameters that can be determined in a joint fit is the average density of the exoplanet, enabling conclusions about its composition.

Part V

Appendix

Appendix 9

9.1 Appendix I – LFC source comb

The particular LFC design that is used as the source comb inside the *astro-comb* of *FOCES* is the so-called *figure-9*-laser configuration, patented by *Menlo Systems* (Hänsel et al., 2013). This laser design is an advancement of the widely used *figure-8*-laser fiber laser (see for example Paschotta, 2008). A schematic drawing of this type of mode-locked, stabilized femtosecond fiber laser is depicted in Figure 9.1.

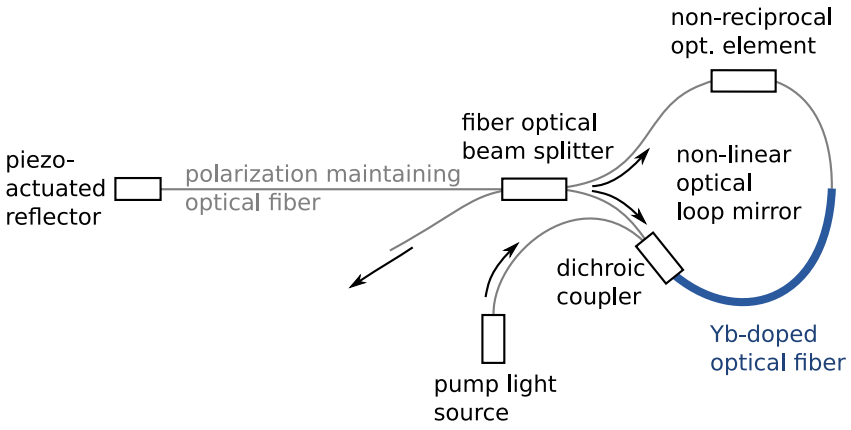

Fig. 9.1.: Schematic illustration of the basic design and most important components of a *figure-9*-laser forming the source comb of FOCES-LFC. This illustration is based on drawings in Hänsel et al. (2013).

In the traditional laser designs, a gain medium is arranged inside a laser cavity that in its simplest form consists of two mirrors, with one mirror being partially transparent and thus acting as output window for the laser beam. The same fundamental principle is also utilized in fiber lasers, where either traditional mirrors or fiber-optical loop mirrors form the laser resonator and special doped optical fibers act as gain medium. Lasers can generally be operated in two different modes, constant wave or pulsed mode. Pulsation is achieved by techniques that favor the pulsed (high intensity) components over weaker field strengths. These techniques are called mode-locking and can either be reached by externally modulating the round-trip gain of the system (active mode-locking) or by utilizing non-linear optical elements, such as Kerr lenses (in combination with specifically designed aperture) that automatically

give preference to high-intensity components (passive mode-locking). Frequency combs are femtosecond lasers by nature, implying some form of ultra-fast passive mode-locking to be implemented into the design.

The resonators of fiber lasers used in frequency combs (e.g. *figure-8/figure-9*-laser) are based on fiber-loops (Figure 9.1 fiber loop on the right side) or specifically in the case of the *figure-9* design as a combination of a fiber loop and a piezo-actuated reflector. The gain medium is thereby a fiber amplifier (in case of the *FOCES* LFC a Ybtterbium (Yb) doped fiber) placed inside the fiber loop which can be pumped via a dichroic fiber coupler.

To create a frequency comb the pulsed mode needs to be favored over the cw-mode. Passive mode-locking in such a laser can be achieved by combining a so-called *non-linear optical loop mirror (NOLM)* with a beam splitter. A NOLM is a optical fiber loop that introduces a phase shift depending on the power/field strength as a result of non-linear optical effects occurring in the loop. Preferred amplification of fast pulses can be evoked by asymmetrically placing the gain fiber inside the fiber loop (Figure 9.1 blue marked Ybtterbium (Yb) doped fiber). Two copies of a pulse traveling from the beam splitter in opposing directions through the fiber loops are thereby affected differently by non-linear-optical effects inside the fiber, depending on their direction of propagation. The pulse propagating counter-clockwise passes the gain fiber first and thus travels at higher intensity over a longer distance through the rest of the fiber loop, thereby accumulating a higher non-linear-optical phase shift compared to its counterpart traveling in the other direction (only amplified at the end of its round-trip). The two copies of the laser pulse arrive at the beam splitter with a certain phase shift, which affects the splitting ratio. The properties of the fiber-optical beam splitter need to be chosen such that a larger fraction of the pulsed component is guided towards the upper light path in Figure 9.1 (left side) and thus towards the second reflector. The other (lower) light path is coupled out of the resonator and therefore lost for future amplification. This way the round-trip gain of the pulsed mode is higher, soon causing this mode to dominate the entire operation of the laser.

By additionally introducing a *non-reciprocal* optical element into the NLOM, a persistent phase shift, depending on the direction in which light passes through, is achieved. This improves the self-starting capabilities of the system, as already small differences in intensity at low power density lead to a notable difference in round-trip gain, once the initial phase difference is different from zero.

Altogether, these properties of the laser ensure that the peak of a pulse gets amplified more efficiently on each round trip, leading to mode-locking of the laser and the

generation of a femtosecond pulse train. By means of the piezo-actuated reflector the round-trip length and therefore the pulse-repetition frequency of the laser f_{rep} can be adjusted and stabilized.

9.2 Appendix II – Technical drawing of the 4-fiber ferrule

Figure 9.2 provides a technical drawing of the 4-fiber ferrule that is described in Chapter 3.

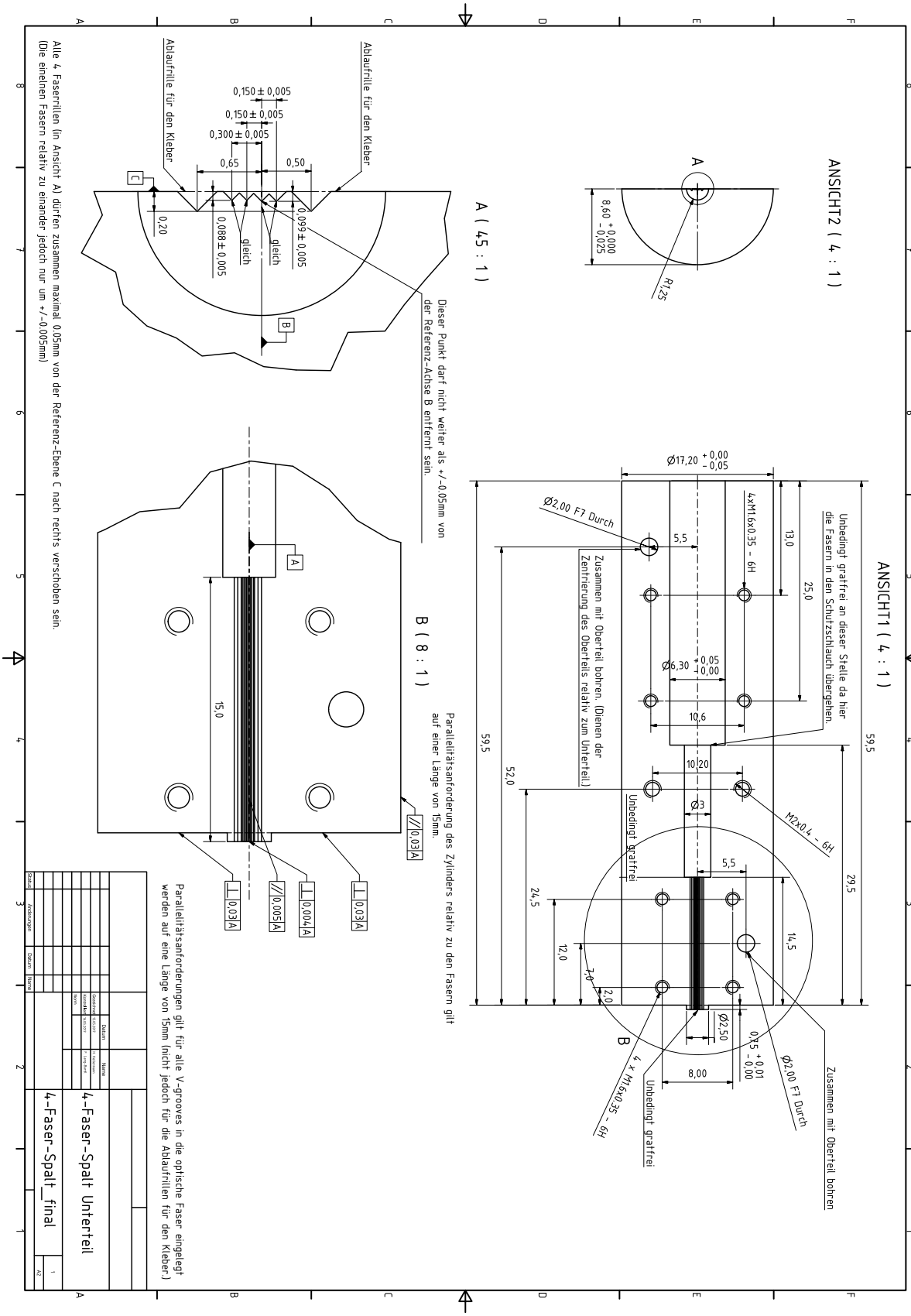

Fig. 9.2.: Technical drawing of the 4-fiber-ferrule.

9.3 Appendix III – Lightning protection

Being located on an exposed position on the very top of the Wendelstein mountain, lightning strikes to the observatory happen relatively frequently and proper over-voltage protection is crucial to avoid damages to the instruments. Therefore, all instruments related to *FOCES* are connected to the power grid through professional lightning protection sockets (power sockets from *Brennenstuhl*). Any additional electrical connections between devices are avoided where possible. USB connections were replaced by commercial fiber connections via USB-to-fiber converters (*Lindy*: 42702). All electrical devices are connected to the power grid in a star-shaped pattern. The main power supply for the CCD camera of *FOCES* is installed inside a full metal enclosure (58 x 38 x 41 cm) which is protected via an inline voltage filter with over-voltage protection and an additional over-voltage protection connector strip inside the box (see also Figure 9.3). The metal enclosure is coupled to the pressure vessel by means of a woven copper mesh tube. As an additional benefit of this setup, variations in the exhaust heat of the main power supply of the camera in this approach do not influence the highly stabilized optical setup of the spectrograph.

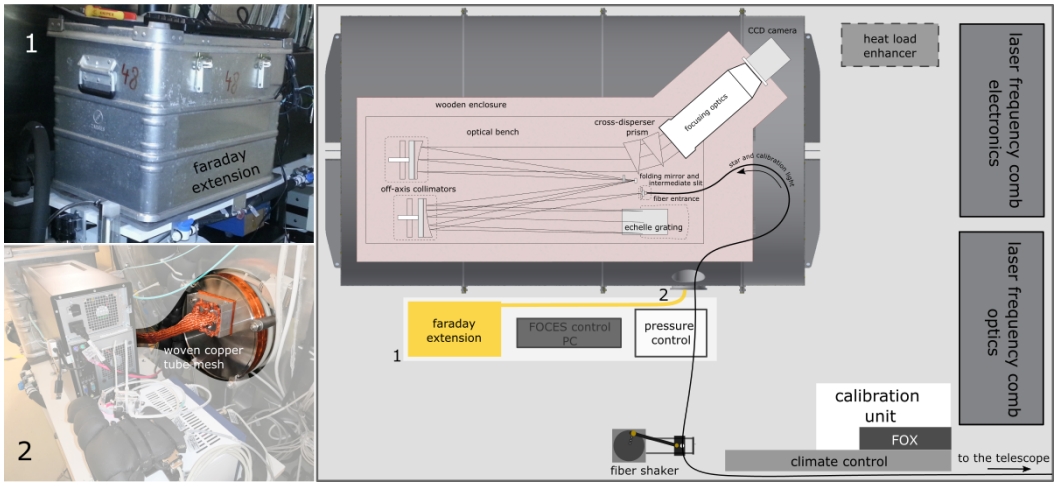

Fig. 9.3.: Illustration of the lighting protection for the main power supply of the *FOCES* camera which is housed in the so-called Faraday extension. (Note: The *FOCES* tank itself is not a faraday cage because of the cable connections entering e.g. heating mats.)

9.4 Appendix IV – FOX the mini-spectrograph for in-situ exposure time measurements

Scientific spectra recorded with *FOCES* usually have an exposure time in the order of 30-60 min[1]. To optimize the light intake of every exposure, an in-situ measurement of the already accumulated photons on the CCD during data taking is of great benefit. For radial velocity measurements, it is crucial to assign the correct observation time to the recorded RV signal. Clouds passing the FoV during data taking and/or guiding errors can modulate the usually assumed uniform photons per second, shifting the assigned mean observation time of the spectrum and thus introducing additional uncertainties. An in-situ measurement and documentation, (ideally spectrally distinct) of the photon arrival profile can solve this problem. To overcome this obstacle a small prism-spectrograph, named FOX, was installed (mechanical design and construction by Nils Baisert (see also Baisert (2017)). The whole setup of this auxiliary spectrograph consists of two parts:

- the light pick-up unit inside the spectrograph situated directly below the optical grating (Figure 9.4 upper part and lower right panel)
- and the actual mini-spectrograph itself (Figure 9.4 lower left panel).

The Échelle grating of *FOCES* is by design overfilled i.g. parts of the light are lost at the grating due to a too large footprint of the light beam arriving at the grating (Figure 9.4 upper part). This formerly lost light is with the new setup redirected and used for exposure time monitoring and for the measurement of the photon arrival statistic. The two hardware components of FOX are connected via an optical fiber whichs end face in addition acts as entrance aperture for this mini-spectrograph. This is done to aim for maximal efficiency since higher resolution (smaller entrance aperture) is not beneficial in this case.

In the lower left panel of Figure 9.4 the simple optical design of FOX is shown equipped with a *FLI* Hyperion HPx695 interline CCD camera. For the collimation and refocusing of the light beam two 60 mm achromatic lenses are utilized.

[1]For RV measurements with *FOCES* an exposure time of not more than 30 min is recommended due to the cooling and heating cycles of the AC.

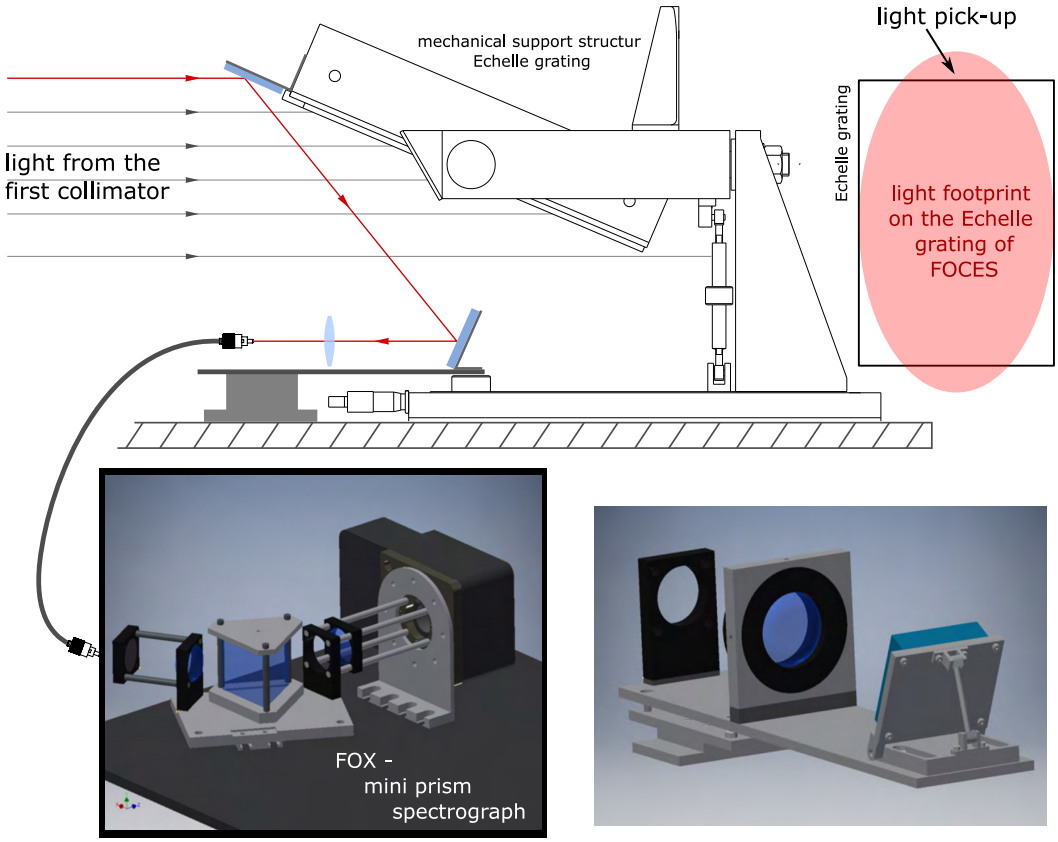

Fig. 9.4.: Upper panel: Schematic illustration of the light pick-up of FOX in *FOCES* situated directly below the Échelle grating. The upper right panel depicts the light footprint on the Échelle grating. Lower panel: On the left and 3d rendering of the simple design of the prism spectrograph FOX is shown while the right side depicts the light pick-up installed in *FOCES*. Both lower images are taken from Baisert (2017) and modified by me.

9.5 Appendix V – Overview of the Échelle orders of *FOCES*

Table 9.1 lists for every Échelle order of *FOCES* the wavelength range which its covers. Marked in red are the orders where also comb light can be provided. The blue rows indicate orders which will be available for the comb calibration after the upgrade of the LFC with a new PCF design in the near future.

Tab. 9.1.: List containing for every Échelle order the wavelength range of the *FOCES* spectrograph. Red: comb light is available for calibration in this wavelength range. Blue: comb light will be available after the upgrade of the LFC with a novel PCF design.

Phy. Order	center WL [angstom]	center WL [nm]	diff-WL [angstom]	diff-WL [nm]	start WL [angstom]	end WL [angstom]
65	8789.98	879.00	124.59	12.46	8726.39	8850.98
66	8656.81	865.68	122.74	12.27	8594.16	8716.90
67	8527.61	852.76	120.94	12.09	8465.88	8586.82
68	8402.21	840.22	119.20	11.92	8341.37	8460.57
69	8280.44	828.04	117.50	11.75	8220.47	8337.97
70	8162.16	816.22	115.85	11.59	8103.03	8218.88
71	8047.21	804.72	114.25	11.43	7988.89	8103.14
72	7935.45	793.55	112.70	11.27	7877.92	7990.62
73	7826.75	782.68	111.18	11.12	7770.00	7881.18
74	7720.99	772.10	109.71	10.97	7664.99	7774.70
75	7618.05	761.81	108.28	10.83	7562.78	7671.06
76	7517.81	751.78	106.88	10.69	7463.26	7570.14
77	7420.19	742.02	105.53	10.55	7366.32	7471.85
78	7325.06	732.51	104.21	10.42	7271.87	7376.08
79	7232.35	723.24	102.92	10.29	7179.81	7282.73
80	7141.95	714.20	101.67	10.17	7090.05	7191.72
81	7053.78	705.38	100.44	10.04	7002.51	7102.95
82	6967.77	696.78	99.24	9.92	6917.11	7016.35
83	6883.82	688.38	98.07	9.81	6833.76	6931.83
84	6801.88	680.19	96.94	9.69	6752.39	6849.33
85	6721.86	672.19	95.83	9.58	6672.94	6768.77
86	6643.71	664.37	94.74	9.47	6595.34	6690.08
87	6567.35	656.74	93.68	9.37	6519.52	6613.20
88	6492.72	649.27	92.64	9.26	6445.43	6538.07
89	6419.78	641.98	91.63	9.16	6373.00	6464.63
90	6348.45	634.85	90.64	9.06	6302.18	6392.82
91	6278.69	627.87	89.67	8.97	6232.92	6322.59
92	6210.45	621.05	88.72	8.87	6165.16	6253.88
93	6143.68	614.37	87.80	8.78	6098.86	6186.66
94	6078.33	607.83	86.89	8.69	6033.97	6120.86
95	6014.35	601.44	86.01	8.60	5970.44	6056.45
96	5951.71	595.17	85.14	8.51	5908.24	5993.38
97	5890.35	589.04	84.29	8.43	5847.32	5931.61

Phy. Order	center WL [angstom]	center WL [nm]	diff-WL [angstom]	diff-WL [nm]	start WL [angstom]	end WL [angstom]
98	5830.25	583.03	83.45	8.35	5787.65	5871.10
99	5771.37	577.14	82.64	8.26	5729.18	5811.82
100	5713.66	571.37	81.84	8.18	5671.88	5753.72
101	5657.09	565.71	81.06	8.11	5615.71	5696.77
102	5601.64	560.16	80.28	8.03	5560.65	5640.93
103	5547.26	554.73	79.54	7.95	5506.65	5586.19
104	5493.93	549.39	78.80	7.88	5453.69	5532.49
105	5441.61	544.16	78.07	7.81	5401.75	5479.82
106	5390.28	539.03	77.36	7.74	5350.78	5428.14
107	5339.91	533.99	76.67	7.67	5300.76	5377.43
108	5290.47	529.05	75.99	7.60	5251.67	5327.66
109	5241.94	524.19	75.32	7.53	5203.48	5278.80
110	5194.29	519.43	74.65	7.47	5156.17	5230.82
111	5147.50	514.75	74.01	7.40	5109.71	5183.72
112	5101.55	510.16	73.37	7.34	5064.08	5137.45
113	5056.41	505.64	72.75	7.28	5019.26	5092.01
114	5012.06	501.21	72.14	7.21	4975.22	5047.36
115	4968.48	496.85	71.54	7.15	4931.95	5003.49
116	4925.65	492.57	70.94	7.09	4889.43	4960.37
117	4883.56	488.36	70.36	7.04	4847.63	4917.99
118	4842.18	484.22	69.79	6.98	4806.54	4876.33
119	4801.49	480.15	69.23	6.92	4766.14	4835.37
120	4761.49	476.15	68.67	6.87	4726.42	4795.09
121	4722.14	472.21	68.13	6.81	4687.35	4755.48
122	4683.44	468.34	67.60	6.76	4648.92	4716.52
123	4645.37	464.54	67.07	6.71	4611.12	4678.19
124	4607.92	460.79	66.56	6.66	4573.92	4640.48
125	4571.06	457.11	66.06	6.61	4537.32	4603.38
126	4534.79	453.48	65.55	6.56	4501.31	4566.86
127	4499.09	449.91	65.06	6.51	4465.86	4530.92
128	4463.94	446.39	64.58	6.46	4430.96	4495.54
129	4429.34	442.93	64.11	6.41	4396.60	4460.71
130	4395.28	439.53	63.63	6.36	4362.78	4426.41
131	4361.73	436.17	63.17	6.32	4329.47	4392.64
132	4328.70	432.87	62.72	6.27	4296.66	4359.38
133	4296.16	429.62	62.27	6.23	4264.35	4326.62
134	4264.10	426.41	61.83	6.18	4232.52	4294.35

Phy. Order	center WL [angstom]	center WL [nm]	diff-WL [angstom]	diff-WL [nm]	start WL [angstom]	end WL [angstom]
135	4232.52	423.25	61.40	6.14	4201.16	4262.56
136	4201.41	420.14	60.98	6.10	4170.26	4231.24
137	4170.75	417.08	60.55	6.06	4139.82	4200.37
138	4140.53	414.05	60.14	6.01	4109.81	4169.95
139	4110.75	411.08	59.73	5.97	4080.24	4139.97
140	4081.39	408.14	59.33	5.93	4051.09	4110.42
141	4052.45	405.25	58.93	5.89	4022.35	4081.28
142	4023.92	402.39	58.54	5.85	3994.02	4052.56
143	3995.79	399.58	58.16	5.82	3966.08	4024.24
144	3968.05	396.81	57.78	5.78	3938.53	3996.31
145	3940.69	394.07	57.40	5.74	3911.37	3968.77
146	3913.70	391.37	57.03	5.70	3884.57	3941.60
147	3887.09	388.71	56.67	5.67	3858.14	3914.81
148	3860.83	386.08	56.31	5.63	3832.06	3888.37

9.6 Appendix VI - GAMSE short manual and ini-file

The whole *GAMSE* program can be customized and controlled via a ini-file and can be called with three different options:

- *gamse config*
  creating a config-file with the preset parameters which can subsequently be modified by the user
- *gamse list*
  creating an type of log-file listing all the observed data found by *GAMSE*
- *gamse reduce*
  starts the reduction software (*gamse config* and *gamse list* need to be called before)
- *gamse show 'path/and/filename/of/the/1dimage'*
  opens the wavelength-calibrated 1D spectrum in question extracted by *GAMSE*; to open more than one spetrum list the filename comma separated

The following is an example of a typical ini-file for *GAMSE* used for *FOCES*:

```
[data]
telescope   = Fraunhofer
instrument  = FOCES
rawdata     = ./rawdata
statime_key = FRAME
exptime_key = EXPOSURE
direction   = xb+
fibermode   = double
fiberoffset = 9

[reduce]
midproc     = midproc
report      = report
onedspec    = onedspec
mode        = normal
oned_suffix = ods
fig_format  = png
ncores      = max

[reduce.bias]
bias_file     = ${reduce:midproc}/bias.fits
cosmic_clip   = 10
maxiter       = 5
smooth        = yes
smooth_method = gaussian
smooth_sigma  = 3
smooth_mode   = nearest

```

```
[reduce.trace]
minimum    = 8
scan_step  = 100
separation = 500:26, 1500:15
filling    = 0.3
align_deg  = 2
display    = no
degree     = 3

[reduce.flat]
slit_step       = 128
q_threshold     = 50
param_deg       = 7
mosaic_maxcount = 50000

[reduce.wlcalib]
search_database  = yes
database_path    = /path/to/wlcalib
linelist         = thar.dat
use_prev_fitpar  = no
window_size      = 13
xorder           = 3
yorder           = 4
maxiter          = 6
clipping         = 2.3
q_threshold      = 10
auto_selection   = yes
rms_threshold    = 0.006
group_contiguous = yes
time_diff        = 120

[reduce.background]
subtract      = yes
ncols         = 9
distance      = 2
yorder        = 6
database_path = /path/to/background

[reduce.extract]
upper_limit = 4.5
lower_limit = 4.5
```

9.7 Appendix VII – *MARMOT* analysis script

```
# !/usr/bin/env python3
# -*- coding: iso-8859-1 -*-
'''
    Copyright 2021 Hanna Kellermann

    Using Ipython:
    run filename.py path+config_file.ini
    run transit_fit_batman_ldtk.py /path/to/the/data/config_file.ini

    Not using IPython:
    python filename.py path+config_file.ini
'''

import os, sys
import numpy as np
from marmot import RVAnalysis
import pickle
import matplotlib.cm
import matplotlib.pyplot as plt

cmap = matplotlib.cm.get_cmap('Spectral')
matplotlib.use('TkAgg')


def main(inifile=None):
    # if inifile is None:
    inifile = sys.argv[1]

    # Creation of an analysis object
    ana = RVAnalysis(ini_filepath=inifile, vlevel=3)

    # In case already processed data should be extended or reprocessed
    # ana = pickle.load(open(os.path.join('/path/to/the/data/','filename.p'), "rb"))

    ########################################################
    ## Start Analysis
    ########################################################

    ### Reading the data ###
    ana.load_files(multicore=ana.multicore)

    plt.close('all')

    # Identify single/double frames
    ana.single_double_list()

    # Set the specified mask regions
    ana.set_masks(path=ana.datainf['mpath'], filename=ana.datainf['maskfile'],
                  fiber=ana.scifiber)
    select_use_frames = ana.select_template_frames(plot=True, mode='single', quantity=3)

```

```
    # Only new files should be processed
    use_frames = []
    for f in ana.double_frames:
        for day in ana.days:
            if ana.frames[f].filename.find(day) > -1:
                use_frames.append(f)

    ana.double_frames = use_frames

    # Option to save the progress (recommended at this point)
    pickle.dump(ana,
                open(os.path.join(ana.datainf['opath'], ana.datainf['analyproj']), "wb"))

    # Applying the comb calibration
    ana.apply_comb_wv_cal(orders=ana.order_list, pixrange=[200, 1850],
                          use_frames=ana.double_frames,
                          which='cal', CombAsComb=False, plotwv=False,
                          multicore=ana.multicore)
    pickle.dump(ana,
                open(os.path.join(ana.datainf['opath'], ana.datainf['analyproj']), "wb"))

    # Template creation
    ana.create_templates(ana.scifiber, orders=ana.order_list, plot=False,
                         use_frames=select_use_frames[0],
                         opath=ana.datainf['opath'], ofilename=ana.datainf['star_templ'],
                         multicore=ana.multicore)
    ana.save_pickle_template(opath=ana.datainf['opath'],
                             ofilename=ana.datainf['star_templ'])

    # RV-shift calculation
    # Option 1
    ana.rv_fit(fiber='A', order_list=ana.order_list, fitrange=[200, 1850],
               use_frames=ana.double_frames,
               plot=False, opath=ana.datainf['opath'], show=False,
               multicore=ana.multicore, remove_tellurics=True)
    # Option 2
    #ana.rv_ccf(fiber='A', order_list=ana.order_list, fitrange=[200, 1850],
    #           use_frames=ana.double_frames, plot=False, opath=ana.datainf['opath'],
    #           show=False, multicore=ana.multicore, iter=5, mc_samples=50)

    # Save whole analysis
    pickle.dump(ana,
                open(os.path.join(ana.datainf['opath'], ana.datainf['analyproj']), "wb"))

    return ana


if __name__ == '__main__':
    ana = main()
```

9.8 Appendix VIII – *MARMOT* auxiliary files

MARMOT configuration file

```
# Start of Config File
[technical-information]
multicore = 15

[observatory]
latitude = 47.703618
longitude = 12.012222
altitude = 1842

[data-analysis]
analyname = name-of-analysis
dpath = /path/to/data/

mpath = /path/to/Maskregion/
maskfile = Mask-regions.ini

opath = /path/to/output/folder/
star_templ= template_filename.p
analyproj = project_filename.p

scifiber = A
calfiber = B
# name of the target as it can be found in the data header
starname = name-of-target-header
# name of the target as it can be found in 'SIMBAD Astronomical Database'
aliasname = name-of-star-simbad

[days]
# add individual date(s)
aidate  = 202?-??-??, 202?-??-??, 202?-??-??
# all days between start and (including) end date
listdate = 202?-??-??, 202?-??-??
# exclude/remove individual date(s)
exdate = #202?-??-??

[orders]
# add individual order(s)
aiorders = ???, ???, ???
#add all orders between start and (including) end order
listorders = ???,???
#exclude/remove this order(s) from list
exorders = ??,??,??,??

[rv-fitting]
t0  = 2459101.872143599
per = 4.23079           # orbital period
ecc = 0.01              # eccentricity
w   = 54.1              # longitude of periastron (in degrees)
k   = 55.65             # RV-amplitude
```

```
50
51 [param-prior]
52 # Please specify the folloing priors:
53 # values 1 for prior function; e.g. 0.0 (as lower limit)
54 # values 2 for prior function; e.g. 0.2 (as lower limit)
55 # example:
56 # ecc  = 0.0, 0.2
57 per = 4.2, 4.3
58 ecc = 0., 0.5
59 k   = 40.0, 80.0
60
61 # End of Config File
```

MARMOT mask file

```
1  # Start of Config File
2  [wavelength_bands]
3  # (start-wl, end-wl) in ANGSTROM
4  tellurics  = (6276,6320);(6511,6520);(7593,7700);(7865,7930);(7023,7028);
5               (7037,7040);(7160,7400);(7958,8046);(8100,8380);(8925,9850);
6
7  [pixel-region]
8  # (start x_pix, end x_pix) in pixel
9  # masks column
10 mask_pix_x = (??,150);(1900,2048)
11
12 # (xstart, xend, ystart, yend) in pixel
13 # masks rectangular region
14 mask_pix_xy= (50,70,2000,2048);(5939,5952,6867,6960);(6276,6320,6472,6484)
15
16 [order]
17 # (order, start pix, end pix) order = physical order
18 order_mask = (100,0,50);(100,2000,2048)
19
20 # End of Config File
```

9.9 Appendix IX – RV-extraction methods comparison to mock data.

The data presented in the two following lists (9.2 and 9.3) are the result of the mock data analysis intruded in Section 5.10.1, implying an artificial RV-shift of 123 m/s to reassemble typical overall RV-shifts for the data analysis evaluation. The results presented here are comparable to the values presented in Section 5.10.1.

Tab. 9.2.: Comparison of the different methods for determining RV shifts with mock data generated with different degrees of SNR and shifted by 123 m/s versus the template used. Here the B-Spline template has been used.

RV shift: 123 m/s, template: B-spline template					
SNR	25	50	100	200	400
mean (CCF opt.) [m/s]	121.9	116.7	123.3	122.0	123.1
std. (CCF opt.) [m/s]	15.91	6.38	2.63	1.47	0.66
mean (CCF fit) [m/s]	121.1	116.6	123.5	122.0	123.1
std. (CCF fit) [m/s]	12.57	6.33	2.59	1.45	0.67
mean (χ^2 fit) [m/s]	124.0	115.9	123.1	122.2	123.0
std. (χ^2 fit) [m/s]	13.13	5.85	2.38	1.44	0.63

Tab. 9.3.: Comparison of the different methods for determining RV shifts with mock data generated with different degrees of SNR and shifted by 123 m/s versus the template used. The single-frame interpolated template has been used here.

RV shift: 123 m/s, template: single-frame interpolated					
SNR	25	50	100	200	400
mean (CCF opt.) [m/s]	109.6	120.0	115.5	116.2	116.4
std. (CCF opt.) [m/s]	18.8	6.59	2.52	1.40	0.64
mean (CCF fit) [m/s]	111.1	121.6	117.0	117.4	123.1
std. (CCF fit) [m/s]	16.91	6.58	2.55	1.41	0.67
mean (χ^2 fit) [m/s]	607.5	430.8	225.2	147.7	123.0
std. (χ^2 fit) [m/s]	73.69	10.43	2.29	1.40	0.63

9.10 Appendix X – *multranfit* analysis script

multi transit fitter analysis script

```
#!/usr/bin/env python
# coding=utf-8
'''
    Copyright 2020 Hanna Kellermann

    Using Ipython:
    run filename.py path+config_file.ini
    example:
    run transit_fit_batman_ldtk.py /path/to/the/data/config_file.ini

    Not using IPython:
    python filename.py path+config_file.ini
'''
import numpy as np
import matplotlib
#try:
#    matplotlib.use('TkAgg')
#except:
#    matplotlib.use('QT4Agg')
#matplotlib.use('TkAgg')
from matplotlib import pyplot as plt
#plt.switch_backend('agg')
#import matplotlib.pyplot as plt
import os
from os.path import join

import math as mt
import astropy.io.fits
import pandas as pd
import batman
import time
import sys
import radvel
from astropy.time import Time
import ldtk
from ldtk import LDPSetCreator, TabulatedFilter

from os.path import join
from scipy.stats import norm
from scipy.stats import uniform

from emcee import EnsembleSampler
import emcee
import iminuit
import corner
import time
import astropy.constants as const
import configparser
from copy import deepcopy
```

```
import pickle
import importlib

from multranfit import TransitFitter
from multranfit.TransitFitter import *

from multranfit import ReadinConfigFile
from multranfit.ReadinConfigFile import *

import time

start = time.time()
################################################################################
# 1. Defining a transit model (for a single wl band) based on the batman package
################################################################################
def batman_model(para,time):
    params = batman.TransitParams()
    params.t0  = para[0]                # time of inferior conjunction
    params.per = para[1]                # orbital period
    params.rp  = para[2]                # planet radius (in units of stellar radii)
    params.a   = para[3]                # semi-major axis (in units of stellar radii)
    params.inc = para[4]                # orbital inclination (in degrees)
    params.ecc = para[5]                # eccentricity
    params.w   = para[6]                # longitude of periastron (in degrees)
    params.u   = [para[7], para[8] ]    # limb darkening coefficients [u1, u2]
    #print(params.u)
    params.limb_dark = "quadratic"      # limb darkening model

    m = batman.TransitModel(params,time) #,nthreads=4) #initializes model
    flux = m.light_curve(params)         #calculates light curve

    return flux


#################################
# 2. Reading the data
#################################
anfang=time.time()

confipars = TransConfigParser(sys.argv[1])

dataPath   = confipars.readinPath(str('data'))
filterPath = confipars.readinPath(str('filter'))
outputPath = confipars.readinPath(str('output'))
limbdPath  = confipars.readinPath(str('limbcache'))

if not os.path.exists(outputPath):
    os.makedirs(outputPath)
#####################################
### Reading of the tranist files ###

# Check which files should be read
filtername = []
filename   = []
labels     = []
```

```
print('Reading the transit-files .... ')
for files in confipars.config['transit-files']:
    files = str(files)
    # Checks if the user specified a filter for each filename
    try:
        para  = str(confipars.config['transit-files'][files])
        para  = list(filter(None, para.split('#')[0].split(',')))
        filtername.append(str(para[0].strip()))
        filename.append(  str(para[1].strip()))
        labels.append(    str(para[2].strip()))
    except:
        print('Error 10:  For \'', files,'\' in [\'transit-files\'] either filter or '
              'filename are missing or they are not seperated by a \',\'')
        sys.exit()

# Reading in of the transit files
err_scale = 1

t_all = []
f_all = []
e_all = []

for files in filename:
    print(join(dataPath,files))
    data = np.loadtxt(join(dataPath,files)).transpose()
    t_all.append(np.sort(data[0])                          )
    f_all.append(data[1][np.argsort(data[0])]              )
    e_all.append(data[2][np.argsort(data[0])] * err_scale)

t_all = np.array(t_all)
f_all = np.array(f_all)
e_all = np.array(e_all)


################################################
# 3. Initialisation of the parameters and prioes
################################################

# Per definition of the python package BATMAN this parameters are named like this
para_names  =  ['t0', 'per', 'rp', 'a', 'inc', 'ecc', 'w']

para0   = []
scatter = []

prior_type  = []
prior_mean  = []
prior_sigma = []

print('Reading the parameters and their priors .... ')
para0, scatter                    = confipars.readinParam(para_names,
                                                          parameter='parameters',
                                                          prior='param-prior',
                                                          para_array=para0,
                                                          scatter_array=scatter)
prior_type,prior_mean,prior_sigma = confipars.readinPrior(para_names, prior='param-prior',
```

```
                                                        prio_type_array=prior_type,
                                                        prio_mean_array=prior_mean,
                                                        prio_sigma_array=prior_sigma)

# calculating proper offset and setting t0 to 0
# using the t0 from config file:
# Option 1:  with t0 set to literature value
t_offs = para0[0]
# Option 2: with t0 set to the first filter channel in data
# t_offs = t_all[0][np.argmin(f_all[0])]

for i in range(len(t_all)):
    t_all[i] -= t_offs
para0[0] = 0.0


##############################################################
# 4. Initialisation of the Limbdarkening Parameters & Priors
##############################################################
# Check if the user wants to specify its own limbdarkening parameters
ldtk_prior = bool
ldtk_prior = confipars.readinBool(str('limbdarkening'),str('ldtk_prior'))

# Creating a list of the limbdarkening parameters for each filter
para_filter = []
LDPfilters  = []
print('Reading the filter curves .... ')
for filters in filtername:
    filters = str(filters)
    if filters.casefold()=='kepler' and ldtk_prior:
        para_filter.append('u1_'+filters)
        para_filter.append('u2_'+filters)
        if ldtk_prior:
            LDPfilters.append(ldtk.filters.kepler)
    elif filters.casefold()=='tess'and ldtk_prior:
        para_filter.append('u1_'+filters)
        para_filter.append('u2_'+filters)
        if ldtk_prior:
            LDPfilters.append(ldtk.filters.tess)
    else:
        # Reading the limb darkening parameter specified by the user
        para_filter.append('u1_'+filters)
        para_filter.append('u2_'+filters)
        if ldtk_prior:
            fname = 'Filter_'+filters+'.txt'
            filtervalues = np.loadtxt(join(filterPath,fname),skiprows=1).transpose()
            LDPfilters.append(TabulatedFilter(filters, filtervalues[0], filtervalues[1]))

# Extends the parameter names by the limbdarkening parameters for each filter
para_names = para_names+para_filter


###############################################
### Reading or Creating the limdarkening ###
### parameters and priors                ###
```

```
215
216 priors = None
217 ldtk_ps = None
218 if not ldtk_prior:
219     print('Reading the limbdarkening coefficients .... ')
220     para0, scatter = confipars.readinParam(para_filter,  parameter='param-limbdarkening',
221                                            prior='prior-limbdarkening', para_array=para0,
222                                            scatter_array=scatter)
223     prior_type,prior_mean,prior_sigma = confipars.readinPrior(para_filter,
224                                                               prior='prior-limbdarkening',
225                                                               prio_type_array=prior_type,
226                                                               prio_mean_array=prior_mean,
227                                                               prio_sigma_array=prior_sigma)
228     smear_lim = confipars.readinFloat(str('limbdarkening'),str('smear_limbdark'))
229
230 else:
231     print('Estimating the limbdarkening coefficients .... ')
232     begin = time.time()
233     star_para = []
234     for name in ['star_temp', 'star_logg', 'star_ z']:
235         # Checks if the user specified the correct parameters names
236         try:
237             para  = str(confipars.config['limbdarkening'][str(name)])
238             para  = list(filter(None, para.split('#')[0].split(',')))
239         except:
240             print('Error 11: In \'limbdarkening\' is ', name,' not specified!')
241             sys.exit()
242         # Checks if mean and scatter of the parameter are given by the user
243         try:
244             para = [float(x) for x in para]
245             star_para.append(tuple(para))
246         except:
247             print('Error 12:  For ', name,' in \'limbdarkening\' either mean or sigma is '
248                   'missing or they are not seperated by a \',\'')
249             sys.exit()
250
251     ldtk_prior_recompute = confipars.readinBool(str('limbdarkening'),str('ldtk_prior_recompute'))
252     ldtk_prior_profile = confipars.readinBool(str('limbdarkening'),str('ldtk_prior_profile'))
253     ldtk_prior_fix = confipars.readinBool(str('limbdarkening'),str('ldtk_prior_fix'))
254     smear_lim = confipars.readinFloat(str('limbdarkening'),str('smear_limbdark'))
255
256     plot_limb = confipars.readinPlot(str('general-plotting'),str('plot_limb'))
257     ########################################
258     # Estimate the limbdarkening if needed #
259     ########################################
260
261     # If requested by user a recalculation is done
262     if ldtk_prior_recompute or not( os.path.exists('ldtk.pkl') ):
263         print('Calculating the Limb Darkening Priors ...')
264         sc = LDPSetCreator(teff=star_para[0], logg=star_para[1], z=star_para[2],
265                            filters=LDPfilters, cache=limbdPath)
266         ps = sc.create_profiles(nsamples=int(confipars.readinFloat(str('limbdarkening'),
267                                                                    str('lim_samples'))))
268         qc,qe = ps.coeffs_qd(do_mc=True, n_mc_samples=int(confipars.readinFloat(
269             str('limbdarkening'),str('lim_mcmc'))))
```

```
270
271         # Start the search for the limbdarkening
272         if plot_limb[0]:
273             histos = ps._gen_coef_profiles(plot=plot_limb[0],  show=plot_limb[1],
274                                            filterid=filtername,
275                                            savepath=join(outputPath,plot_limb[2]),
276                                            smear=smear_lim)
277         else:
278             histos = ps._gen_coef_profiles(filterid=filtername,
279                                            savepath=join(outputPath, plot_limb[2]),
280                                            smear=smear_lim)
281
282         ldtk_file = open('ldtk.pkl', 'wb')
283         pickle.dump(histos, ldtk_file)
284     # else the precalculated values of a previous run are loaded
285     else:
286         sc = LDPSetCreator(teff=star_para[0], logg=star_para[1], z=star_para[2],
287                            filters=LDPfilters, cache=limbdPath)
288         ps = sc.create_profiles(nsamples=100)
289         qc,qe = ps.coeffs_qd(do_mc=True,
290                              n_mc_samples=int(confipars.readinFloat(str('limbdarkening'),
291                                                                     str('lim_mcmc'))))
292         print('Loading the Limb Darkening Priors ...')
293         ldtk_file = open('ldtk.pkl', 'rb')
294         histos = pickle.load(ldtk_file)
295
296         if plot_limb[0]:
297             histos = ps._gen_coef_profiles(plot=plot_limb[0], show=plot_limb[1],
298                                            filterid=filtername,
299                                            savepath=join(outputPath, plot_limb[2]),
300                                            precomp_histos=histos, smear=smear_lim)
301         else:
302             histos = ps._gen_coef_profiles(filterid=filtername,
303                                            savepath=join(outputPath, plot_limb[2]),
304                                            precomp_histos=histos, smear=smear_lim)
305
306     if ldtk_prior_profile and not ldtk_prior_fix:
307         ldtk_ps=ps
308
309     for i, name in enumerate(para_filter):
310         para0.append(qc.flatten()[i])
311         if ldtk_prior_fix:
312             prior_type.append('fix')
313             prior_mean.append( np.nan)
314             prior_sigma.append(np.nan)
315             scatter.append(    np.nan)
316         else:
317             prior_type.append('gaus')
318             prior_mean.append(qc.flatten()[i])
319             prior_sigma.append(qe.flatten()[i])
320             scatter.append(qe.flatten()[i]*0.1)
321
322     print('Limb estimation time: ', (time.time()-begin)/60.,'[min]')
323
324
```

```
##################################
# 5. Creating the fitter object
##################################
# N_para = number of parameters for ONE light curve (changes with limb-darkening-model)
# N_LD   = number of parameters for the limb-darkening-model (quadratic = 2)
# lc_time= TIME   of all different data sets of light curves
# lc_data= FLUX   of all different data sets of light curves
# lc_errs= ERRORS of all different data sets of light curves

##################################
### General plotting settings ###
folding = confipars.readinBool(str('general-plotting'),str('phase_fold'))

multifig = confipars.readinBool(str('general-plotting'),str('multifig'))

### Reading the colors for the plots  ###
plot_colors = []
try:
    colors = str(confipars.config['general-plotting']['plot_colors'])
    #colors  = list(filter(None, colors.split('#')[0].split(',')))
    colors  = list(colors.split(','))
    for col in colors:
        plot_colors.append(str((col.replace('\"','')).replace('\'','').strip()))
    # Check if number of colors and filter is the same
    if len(plot_colors)!=len(filtername):
        print('Error 13: To few or to many colors for the different filters are specified!')
except:
    print('Error 14: The colors for the plot are not specified please do so under '
          '[\'general-plotting\'] in plot_colors!')
    sys.exit()


##########################################
### Ininialise the TransitFitter Object ###
rebin = int(confipars.readinFloat(str('general-plotting'),str('rebin')))

TF = TransitFitter(model=batman_model, p0=para0, N_para=len(prior_mean), N_LD=2,
                   lc_time=t_all, lc_data=f_all, lc_errs=e_all, ldtk_ps=ldtk_ps,
                   print_lvl=1, labels=labels)
TF.set_prior(prior_type, np.array(prior_mean), np.array(prior_sigma), p_name=para_names)


pure_plot = confipars.readinPlot(str('general-plotting'),str('plot_pure'))
if pure_plot[0]: TF.plot_all(labels=labels, colors= plot_colors, mode='PURE',fold=folding,
                             show=pure_plot[1], savepath=join(outputPath,pure_plot[2]),
                             multifig=multifig)

########################################
###         Fit with Minuit         ###
if confipars.readinBool(str('minuit-fit'),str('fit_minuit')):

    print('Fit/Estimate the parameters with Minuit .... ')
    TF.run_Fit()
    #TF.run_Fit()
```

```
380
381     ##############################################
382     ### Estimate the Period of a singe transit ###
383     if confipars.readinFloat(str('simulation'),str('per')):
384         print ('\nEstimate the Period of a singe transit ...')
385         sim_per = confipars.readinFloat(str('simulation'),str('per'))
386         sim_ink = confipars.readinFloat(str('simulation'),str('ink'))
387         M_star  = confipars.readinFloat(str('simulation'),str('M'))
388         R_star  = confipars.readinFloat(str('simulation'),str('R'))
389
390         pseudo_per = para0[1]
391         pseudo_a   = para0[3]
392         print(pseudo_per,pseudo_a)
393
394         a_per         = TF.p0[TF.p_name.index('a')]/TF.p0[TF.p_name.index('per')]
395         per_real_days = (const.G.value*M_star*const.M_sun.value)/\
396                         (4*np.pi**2*(a_per*(R_star*const.R_sun.value/(24*3600)))**3)/\
397                         (24*3600)
398         a_real        = pseudo_a/pseudo_per*per_real_days
399         ink_real      = -((pseudo_a/a_real*(90-TF.p0[TF.p_name.index('inc')]))-90)
400
401         print('\nAssuming a/per= '+str(a_per)+'\n'+'M_star= '+str(M_star)+' M_sol'+
402               '\n'+'R_star= '+str(R_star)+' R_sol')
403         print('the predicted period is: %.2f days'% per_real_days)
404         print('Simulated was          : %.2f days'% sim_per)
405         print('\n')
406         print('the predicted inklination is: %.5f °'% ink_real)
407         print('Simulated was               : %.5f °'% sim_ink)
408
409     fit_plot = confipars.readinPlot(str('general-plotting'),str('plot_fit'))
410     if fit_plot[0]:
411         fig, axs =TF.plot_all(labels=labels, colors=plot_colors, mode='PURE', fold=folding,
412                               show=pure_plot[1], xphase=folding, alpha=0.2, marker='.',
413                               elinewidth=0.4, returnfig=True, multifig=multifig)
414
415         TF.plot_all(labels=labels, colors= plot_colors, mode='FIT', fold=folding,
416                     show=fit_plot[1], savepath=join(outputPath,fit_plot[2]),
417                     xphase=folding, rebin=rebin, fig=fig, axs=axs, marker='o',
418                     elinewidth=1.2, smooth=True, multifig=multifig)
419
420     res_plot = confipars.readinPlot(str('general-plotting'),str('plot_res'))
421     if res_plot[0]:
422         TF.plot_all(labels=labels, colors= plot_colors, mode='RESIDUALS',fold=folding,
423                     show=fit_plot[1], savepath=join(outputPath,res_plot[2]),
424                     xphase=folding, multifig=multifig)
425     f0 = TF.fitObj
426
427     print('\n\n ### Fit parameter results ### ')
428     for i,n in enumerate(para_names):
429         if n == 't0':
430             print("%4s: %.5f  (+/-%.9f)"%(n, f0.values[n]+t_offs, f0.errors[n]))
431         if n == 'per':
432             print("%4s: %.5f  (+/-%.9f)"%(n, f0.values[n]       , f0.errors[n]))
433         else:
434             print("%4s: %.5f  (+/-%.4f)"%(n, f0.values[n]       , f0.errors[n]))
```

```
435
436 end = 0.0
437 ######################################
438 ###         Fit with MCMC           ###
439 if confipars.readinBool(str('mcmc-fit'),str('fit_mcmc')):
440     print('\nFit/explore the parameter space with MCMC .... ')
441     walker = int(confipars.readinFloat(str('mcmc-fit'), str('nwalkers')))
442     iterat = int(confipars.readinFloat(str('mcmc-fit'), str('iterations')))
443     burnin = int(confipars.readinFloat(str('mcmc-fit'), str('burn_in')))
444     print('With:  \n', walker,'walkers\n', iterat,'iterat\n', burnin,'burnin\n' )
445
446     TF.run_MCMC(nwalkers=walker, iterations=iterat, burn_in=burnin, start_rnd=scatter)
447
448     ####################################
449     ###    Plot EMCEE and residuals   ###
450     mcmc_plot = confipars.readinPlot(str('general-plotting'),str('plot_mcmc'))
451     t_eval    = confipars.readinFloat(str('general-plotting'),str('t_eval'))
452     if mcmc_plot[0]:
453         fltrname = labels
454         if folding:
455             fltrname = labels
456         fig, axs =TF.plot_all(labels=fltrname, colors=plot_colors, mode='PURE',
457                               fold=folding, show=pure_plot[1], xphase=folding, alpha=0.2,
458                               marker='.', elinewidth=0.4, returnfig = True,
459                               multifig=multifig)
460         TF.plot_all(labels=fltrname, colors= plot_colors, mode='MCMC', smooth=True,
461                     fold=folding, show=mcmc_plot[1], savepath=join(outputPath,mcmc_plot[2]),
462                     xphase=folding, rebin=rebin, fig=fig, axs=axs, marker='o',
463                     elinewidth=1.2, t_eval=t_eval, multifig=multifig)
464
465         res_plot = confipars.readinPlot(str('general-plotting'),str('plot_res'))
466         if res_plot[0]:
467             fltrname = [labels[i]+" residuals" for i in range(len(labels))]
468             if folding:
469                 fltrname = [labels[i]+" residuals" for i in range(len(labels))]
470             TF.plot_all(labels=fltrname, colors= plot_colors, mode='RESIDUALS',
471                         fold=folding, show=res_plot[1],
472                         savepath=join(outputPath, 'MCMC_'+res_plot[2]), xphase=folding,
473                         multifig=multifig)
474
475     ####################################
476     ###   Print the MCMC parameters   ###
477
478     best_m  = TF.best_params()
479     best_err= TF.best_params_errs()
480     print('\n\n ### MCMC parameter results ###')
481     for i,n in enumerate(para_names):
482         if i == 0:
483             print("%s: %.9f  (-%.9f +%.9f)"%(n, best_err[i][0]+t_offs,
484                                               best_err[i][1], best_err[i][2]))
485         if i == 1:
486             print("%s: %.9f  (-%.9f +%.9f)"%(n, best_err[i][0]       ,
487                                               best_err[i][1], best_err[i][2]))
488         else:
489             print("%s: %.5f  (-%.4f +%.4f)"%(n, best_err[i][0]       ,
```

```
                                            best_err[i][1], best_err[i][2]))

    mcmc_end = time.time()

    end =  time.time()
    #print((end-start)/60.)
    ########################################
    ### Create and Save the Corner Plot ###
    corner_plot = confipars.readinPlot(str('general-plotting'),str('plot_corner'))
    if corner_plot[0] and confipars.readinBool(str('mcmc-fit'),str('fit_mcmc')):
        print('\nCreating the corner plot ....')
        TF.corner_plot(join(outputPath,corner_plot[2]))

    file_sample = (confipars.config['mcmc-fit']['save_sample'].replace('\"','')).\
        replace('\'','').strip()
    pickle.dump(TF.samples, open(join(outputPath,file_sample),'wb'))

##############################################
### Estimate the Period of a singe transit ###
if confipars.readinFloat(str('simulation'),str('per')):
    print ('\nEstimate the Period of a singe transit ...')
    sim_per = confipars.readinFloat(str('simulation'),str('per'))
    sim_ink = confipars.readinFloat(str('simulation'),str('ink'))
    M_star  = confipars.readinFloat(str('simulation'),str('M'))
    R_star  = confipars.readinFloat(str('simulation'),str('R'))

    pseudo_per = para0[1]
    pseudo_a   = para0[3]
    print(pseudo_per,pseudo_a)

    a_per         = TF.best_params()[TF.p_name.index('a')]/TF.best_params()[TF.p_name.index('per')]
    per_real_days = (const.G.value*M_star*const.M_sun.value)/\
                    (4*np.pi**2*(a_per*(R_star*const.R_sun.value/(24*3600)))**3)/(24*3600)
    a_real        = pseudo_a/pseudo_per*per_real_days
    ink_real      = -((pseudo_a/a_real*(90-TF.best_params()[TF.p_name.index('inc')]))-90)

    print('\nAssuming a/per= '+str(a_per)+'\n'+'M_star= '+str(M_star)+' M_sol'+'\n'+
          'R_star= '+str(R_star)+' R_sol')
    print('the predicted period is: %.2f days'% per_real_days)
    print('Simulated was          : %.2f days'% sim_per)
    print('\n')
    print('the predicted inklination is: %.5f °'% ink_real)
    print('Simulated was               : %.5f °'% sim_ink)
    np.savetxt(str(filename[0])+'_mcmc_params.txt', [per_real_days,sim_per,ink_real,sim_ink])

################################################
#####Theoretical RV curve ######################
if confipars.readinFloat(str('simulation'),str('per')):
    current_date=float(Time.now().jd)

    def RV_calc(P,R,rho,M):
        return 28.4*(P/365)**(-1/3)*((4/3*np.pi*(R*637100000)**3*rho)/(1.898*10**(30)))*(M)**(-2/3)

    per=float(per_real_days)
    R_st=float(R_star)
```

```
    rho_pl=float(5.5)
    M_st=float(M_star)
    ecc=float(TF.best_params()[TF.p_name.index('ecc')])
    t0=float(TF.best_params()[TF.p_name.index('t0')])
    w=float(TF.best_params()[TF.p_name.index('w')])
    K=RV_calc(per,R_st,rho_pl,M_st)
    t=[current_date, current_date+2*float(per)]

    # model
    time_base = t[0]
    params = radvel.Parameters(1,basis='per tp e w k')
    params['per1']  = radvel.Parameter(value=float(per))
    params['tp1']   = radvel.Parameter(value= t0)
    params['e1']    = radvel.Parameter(value= ecc)
    params['w1']    = radvel.Parameter(value=np.radians(w))
    params['k1']    = radvel.Parameter(value=K)

    mod = radvel.RVModel(params, time_base=time_base)
    mod.params['dvdt'] = radvel.Parameter(value=0)
    mod.params['curv'] = radvel.Parameter(value=0)
    mod.params['gamma'] = radvel.Parameter(value=0)

    ti = np.linspace(t[0], t[0-1], 250)

    plt.plot(ti, mod(ti))
    plt.xlabel('Time (JD)')
    plt.ylabel('RV [m/s]')
    plt.savefig(str(outputPath)+'/RV_plot.png')

################################################################################
################################################################################
###                                   END                                    ###
################################################################################
################################################################################
```

List of Figures

List of Tables

Bibliography

Andrae, Rene, Tim Schulze-Hartung, and Peter Melchior (Dec. 2010). “Dos and don’ts of reduced chi-squared”. en. In: *arXiv:1012.3754 [astro-ph, physics:physics, stat]*. arXiv: 1012.3754 (cit. on p. 112).

Artigau, Étienne, Lison Malo, René Doyon, et al. (Apr. 2018). “Optical and Near-infrared Radial Velocity Content of M Dwarfs: Testing Models with Barnard’s Star”. en. In: *The Astronomical Journal* 155.5, p. 198 (cit. on p. 167).

Avila, G., Burwitz V., Guirao C., and J. Rodreguez (2011). *CAOS: Club of Aficionados in Optical Spectroscopy*. en-US (cit. on pp. 40, 41).

Bai, Chunhai, Jianning Fu, Taoran Li, et al. (2018). *Upgraded Photometric System of The 85-cm Telescope at Xinglong Station*. arXiv: 1804.08565 [astro-ph.IM] (cit. on p. 218).

Baisert, Nils (2017). “The development of an instrument to in situ measure the exposure of the Wendelstein Echelle spectrograph”. Masterthesis (cit. on pp. 234, 235).

Baranne, A. and M. Duchesne (June 1972). “Le spectrographe coudé "Echel.E.C.152" (Montage à pupille blanche pour caméra électronique).” fr. In: *Auxiliary Instrumentation for Large Telescopes*, pp. 241–245 (cit. on p. 63).

Barber, C. Bradford, David P. Dobkin, and Hannu Huhdanpaa (1996). “The Quickhull algorithm for convex hulls”. In: *Acm Transactions on Mathematical Software* 22.4, pp. 469–483 (cit. on pp. 194, 196).

Beaulieu, J.-P., D. P. Bennett, P. Fouqué, et al. (Jan. 2006). “Discovery of a cool planet of 5.5 Earth masses through gravitational microlensing”. In: *Nature* 439.7075. Bandiera_abtest: a Cg_type: Nature Research Journals Number: 7075 Primary_atype: Research Publisher: Nature Publishing Group, pp. 437–440 (cit. on p. 16).

Beaulieu, J. P., D. M. Kipping, V. Batista, et al. (Dec. 2010). “Water in the atmosphere of HD 209458b from 3.6–8 μm IRAC photometric observations in primary transit”. In: *Monthly Notices of the Royal Astronomical Society* 409.3, pp. 963–974 (cit. on p. 10).

Birkby, J. L., R. J. de Kok, M. Brogi, H. Schwarz, and I. A. G. Snellen (Mar. 2017). “Discovery of Water at High Spectral Resolution in the Atmosphere of 51 Peg b”. In: *AJ* 153.3, 138, p. 138. arXiv: 1701.07257 [astro-ph.EP] (cit. on pp. 179, 207).

Bouchy, F., F. Pepe, and D. Queloz (Aug. 2001). “Fundamental photon noise limit to radial velocity measurements”. en. In: *Astronomy & Astrophysics* 374.2, pp. 733–739 (cit. on pp. 167, 168).

Bourrier, V., D. Ehrenreich, M. Lendl, et al. (Mar. 2020). “Hot Exoplanet Atmospheres Resolved with Transit Spectroscopy (HEARTS) - III. Atmospheric structure of the misaligned ultra-hot Jupiter WASP-121b”. en. In: *Astronomy & Astrophysics* 635. Publisher: EDP Sciences, A205 (cit. on p. 10).

Brucalassi, Anna, Tobias Feger, Frank Grupp, et al. (2012). “Pressure and temperature stabilization of an existing Echelle spectrograph III”. In: *Ground-based and Airborne Instrumentation for Astronomy IV*. Ed. by Ian S. McLean, Suzanne K. Ramsay, and Hideki Takami. Vol. 8446. International Society for Optics and Photonics. SPIE, pp. 865 –873 (cit. on pp. 70, 101).

Brucalassi, Anna, Frank Grupp, Hanna Kellermann, et al. (2016). “Stability of the FOCES spectrograph using an astro-frequency comb as calibrator”. In: *Ground-based and Airborne Instrumentation for Astronomy VI*. Ed. by Christopher J. Evans, Luc Simard, and Hideki Takami. Vol. 9908. International Society for Optics and Photonics. SPIE, pp. 1767 –1775 (cit. on pp. 71, 101).

Brucalassi, Anna, Frank Grupp, Florian Lang, et al. (2013). “Pressure and temperature stabilization of an existing Échelle spectrograph IV”. In: *Techniques and Instrumentation for Detection of Exoplanets VI*. Ed. by Stuart Shaklan. Vol. 8864. International Society for Optics and Photonics. SPIE, pp. 531 –538 (cit. on pp. 71, 101).

Butler, R. P., J. T. Wright, G. W. Marcy, et al. (July 2006). “Catalog of Nearby Exoplanets”. In: *ApJ* 646.1, pp. 505–522. arXiv: astro-ph/0607493 [astro-ph] (cit. on pp. 179, 207).

Chambers, K. C., E. A. Magnier, N. Metcalfe, et al. (Dec. 2016). “The Pan-STARRS1 Surveys”. In: *arXiv e-prints*, arXiv:1612.05560, arXiv:1612.05560. arXiv: 1612.05560 [astro-ph.IM] (cit. on p. 209).

Charbonneau, David, Timothy M. Brown, Adam Burrows, and Greg Laughlin (Mar. 2006). “When Extrasolar Planets Transit Their Parent Stars”. In: *arXiv:astro-ph/0603376*. arXiv: astro-ph/0603376 (cit. on p. 10).

Charbonneau, David, Timothy M. Brown, David W. Latham, and Michel Mayor (Jan. 2000). “Detection of Planetary Transits Across a Sun-like Star”. en. In: *The Astrophysical Journal* 529.1. Publisher: American Astronomical Society, pp. L45–L48 (cit. on p. 9).

Chauvin, G., A.-M. Lagrange, C. Dumas, et al. (Oct. 2004). “A giant planet candidate near a young brown dwarf - Direct VLT/NACO observations using IR wavefront sensing”. en. In: *Astronomy & Astrophysics* 425.2. Number: 2 Publisher: EDP Sciences, pp. L29–L32 (cit. on p. 6).

Collins, Karen A., John F. Kielkopf, Keivan G. Stassun, and Frederic V. Hessman (Jan. 2017). “ASTROIMAGEJ: IMAGE PROCESSING AND PHOTOMETRIC EXTRACTION FOR ULTRA-PRECISE ASTRONOMICAL LIGHT CURVES”. en. In: *The Astronomical Journal* 153.2. Publisher: American Astronomical Society, p. 77 (cit. on p. 186).

Deacon, N. R., J. E. Schlieder, and S. J. Murphy (Apr. 2016). “A nearby young M dwarf with a wide, possibly planetary-mass companion”. In: *Monthly Notices of the Royal Astronomical Society* 457.3, pp. 3191–3199 (cit. on p. 6).

Delcourt, Enguerran, Nessim Jebali, Loïc Bodiou, et al. (June 2020). “Self-phase modulation and four-wave mixing in a chalcogenide ridge waveguide”. In: *Opt. Mater. Express* 10.6, pp. 1440–1450 (cit. on p. 55).

Drever, R. W. P., J. L. Hall, F. V. Kowalski, et al. (June 1983). “Laser phase and frequency stabilization using an optical resonator”. In: *Applied Physics B* 31.2, pp. 97–105 (cit. on p. 54).

Espinoza, Néstor and Andrés Jordán (Apr. 2015). “Limb darkening and exoplanets: testing stellar model atmospheres and identifying biases in transit parameters”. In: *Monthly Notices of the Royal Astronomical Society* 450.2, 1879–1899 (cit. on p. 192).

– (Jan. 2016). “Limb darkening and exoplanets – II. Choosing the best law for optimal retrieval of transit parameters”. In: *Monthly Notices of the Royal Astronomical Society* 457.4, 3573–3581 (cit. on p. 192).

Eversberg, Thomas and Klaus Vollmann (2015). *Spectroscopic Instrumentation: Fundamentals and Guidelines for Astronomers*. en. Astronomy and Planetary Sciences. Berlin Heidelberg: Springer-Verlag (cit. on pp. 40–42, 68).

Fahrenschon, Vanessa (2021). “Stabilization of a high-resolution spectrograph and performance verification by measurements of the Rossiter-McLaughlin effect”. in prep. PhD thesis (cit. on p. 106).

Fahrenschon, Vanessa, Hanna Kellermann, Liang Wang, et al. (2020). “Environmental stability achieved for the Manfred Hirt Planet Spectrograph”. In: *Ground-based and Airborne Instrumentation for Astronomy VIII*. Ed. by Christopher J. Evans, Julia J. Bryant, and Kentaro Motohara. Vol. 11447. International Society for Optics and Photonics. SPIE, pp. 740 –759 (cit. on pp. 71, 101).

Feger, Tobias (2012). “Fieber feed and spectrograph stability at the FOCES spectrograph”. Masterthesis (cit. on pp. 43, 75, 85).

Feger, Tobias, Anna Brucalassi, Frank U. Grupp, et al. (2012). “A testbed for simultaneous measurement of fiber near and far-field for the evaluation of fiber scrambling properties”. In: *Ground-based and Airborne Instrumentation for Astronomy IV*. Ed. by Ian S. McLean, Suzanne K. Ramsay, and Hideki Takami. Vol. 8446. International Society for Optics and Photonics. SPIE, pp. 1278 –1291 (cit. on pp. 43, 70).

Fletcher, R. (Jan. 1970). “A new approach to variable metric algorithms”. In: *The Computer Journal* 13.3, pp. 317–322 (cit. on p. 115).

Foreman-Mackey, Daniel, David W. Hogg, Dustin Lang, and Jonathan Goodman (Feb. 2013). “emcee: The MCMC Hammer”. en. In: *Publications of the Astronomical Society of the Pacific* 125.925. Publisher: IOP Publishing, p. 306 (cit. on p. 122).

Fulton, Benjamin J., Erik A. Petigura, Sarah Blunt, and Evan Sinukoff (Mar. 2018). “RadVel: The Radial Velocity Modeling Toolkit”. en. In: *Publications of the Astronomical Society of the Pacific* 130.986. Publisher: IOP Publishing, p. 044504 (cit. on p. 13).

Fulton, BJ, Sarah Blunt, Spencer Hurt, et al. (May 2020). *California-Planet-Search/radvel: Version 1.4.0* (cit. on p. 179).

Glebocki, R. and P. Gnacinski (Mar. 2005). “VizieR Online Data Catalog: Catalog of Stellar Rotational Velocities (Glebocki+ 2005)”. In: *VizieR Online Data Catalog*, pp. III/244 (cit. on p. 15).

Goodman, Jonathan and Jonathan Weare (Jan. 2010). “Ensemble samplers with affine invariance”. en. In: *Communications in Applied Mathematics and Computational Science* 5.1, pp. 65–80 (cit. on pp. 122, 123).

Griffin, R. and R. Griffin (Jan. 1973). “Accurate wavelengths of stellar and telluric absorption lines near lambda 7000 Angstroms”. In: MNRAS 162, p. 255 (cit. on p. 45).

Grupp, Frank (Dec. 2003). “The nature of the fiber noise with the FOCES spectrograph. Nature, modeling and a way to achieve S/N > 400”. In: *Astronomy & Astrophysics - ASTRON ASTROPHYS* 412, pp. 897–902 (cit. on p. 40).

Grupp, Frank, Anna Brucalassi, Florian Lang, et al. (2011). “Pressure and temperature stabilization of an existing chelle spectrograph II”. In: *Techniques and Instrumentation for Detection of Exoplanets V*. Ed. by Stuart Shaklan. Vol. 8151. International Society for Optics and Photonics. SPIE, pp. 477 –485 (cit. on pp. 70, 101).

Grupp, Frank, Shaoming Hu, and Liang Wang (Aug. 2009). “Modeling the image distortion of echelle spectrographs with T&P changes”. In: *Techniques and Instrumentation for Detection of Exoplanets IV*. Ed. by Stuart B. Shaklan. Vol. 7440. Society of Photo-Optical Instrumentation Engineers (SPIE) Conference Series, 74401G (cit. on pp. 70, 101).

Grupp, Frank, Thomas Udem, Ronald Holzwarth, et al. (2010). “Pressure and temperature stabilization of an existing Echelle spectrograph”. In: *Ground-based and Airborne Instrumentation for Astronomy III*. Ed. by Ian S. McLean, Suzanne K. Ramsay, and Hideki Takami. Vol. 7735. International Society for Optics and Photonics. SPIE, pp. 2528 –2537 (cit. on pp. 70, 101).

H. Kellermann J. Steuer, P. Dalba (in prep.). “Period Estimation and Redetection of the TESS Single Transit Planetary Candidate TOI-1823”. In: (cit. on pp. 199, 209).

Hastings, W. K. (Apr. 1970). “Monte Carlo sampling methods using Markov chains and their applications”. In: *Biometrika* 57.1, pp. 97–109 (cit. on p. 121).

Hatzes, A P (2019). *The Doppler Method for the Detection of Exoplanets*. 2514-3433. IOP Publishing (cit. on p. 15).

Hauschildt, P. H. and E. Baron (Sept. 1999). “Numerical solution of the expanding stellar atmosphere problem.” In: *Journal of Computational and Applied Mathematics* 109, pp. 41–63 (cit. on p. 194).

Hildebrand, A. R., E. F. Tedesco, K. A. Carroll, et al. (Jan. 2008). “The Near Earth Object Surveillance Satellite (NEOSSat) Mission Will Conduct an Efficient Space-Based Asteroid Survey at Low Solar Elongations”. In: *Asteroids, Comets, Meteors 2008*. Vol. 1405, p. 8293 (cit. on p. 218).

Howell, Steve B., Charlie Sobeck, Michael Haas, et al. (Apr. 2014). “The K2 Mission: Characterization and Early Results”. en. In: *Publications of the Astronomical Society of the Pacific* 126.938. Publisher: IOP Publishing, p. 398 (cit. on p. 17).

Husser, T.-O., S. Wende-von Berg, S. Dreizler, et al. (May 2013a). “A new extensive library of PHOENIX stellar atmospheres and synthetic spectra”. In: *Astronomy and Astrophysics* 553, A6 (cit. on p. 194).

Husser, T.-O., S Wende-von Berg, S Dreizler, et al. (2013b). “Astrophysics A new extensive library of PHOENIX stellar atmospheres”. In: *A&A* 553, A6 (cit. on p. 171).

Hänsel, Wolfgang Dr, Ronald Dr Holzwarth, Ralf Doubek, and Michael Dr Mei (Sept. 2013). “Laser with non-linear optical loop mirror”. en. Pat. EP2637265A1 (cit. on p. 229).

Jahns, Jürgen (2001). *Photonik: Grundlagen, Komponenten und Systeme*. de. Oldenbourg (cit. on pp. 34, 37, 55).

Jahns, Jürgen and Stefan Helfert (July 2012). *Introduction to Micro- and Nanooptics*. en. John Wiley & Sons (cit. on p. 28).

James, F. and M. Roos (Dec. 1975). “Minuit - a system for function minimization and analysis of the parameter errors and correlations”. en. In: *Computer Physics Communications* 10.6, pp. 343–367 (cit. on pp. 117, 183, 199).

Kanodia, Shubham and Jason Wright (Jan. 2018). “Python Leap Second Management and Implementation of Precise Barycentric Correction (barycorrpy)”. In: *Research Notes of the AAS* 2.1, p. 4 (cit. on p. 147).

Karlsson, Magnus (1994). *Nonlinear propagation of optical pulses and beams*. en. Doktorsavhandlingsar vid Chalmers tekniska högskola N.S 1051. OCLC: 832388181. Göteborg: Chalmers Univ. of Technology (cit. on p. 56).

Kellermann, Hanna (2015). “Entwicklung und Test von Kalibrierungs- und Optimierungsoptionen für den hochauflösenden Echelle- Spectrographen FOCES”. Masterthesis (cit. on pp. 42, 94).

Kellermann, Hanna, Frank Grupp, Anna Brucalassi, et al. (Sept. 2015). “A new fiber slit assembly for the FOCES spectrograph”. In: *Techniques and Instrumentation for Detection of Exoplanets VII*. Ed. by Stuart Shaklan. Vol. 9605. Society of Photo-Optical Instrumentation Engineers (SPIE) Conference Series, 96051R (cit. on pp. 71, 73).

Kellermann, Hanna, Frank Grupp, Anna Brucalassi, et al. (2016). “Multi-fiber coupling through a miniature lens system into the FOCES spectrograph”. In: *Ground-based and Airborne Instrumentation for Astronomy VI*. Ed. by Christopher J. Evans, Luc Simard, and Hideki Takami. Vol. 9908. International Society for Optics and Photonics. SPIE, pp. 1832 –1838 (cit. on pp. 71, 73).

Kellermann, Hanna, Liang Wang, Vanessa Fahrenschon, et al. (Sept. 2019). “First results of the 4-fiber upgrade of the high-resolution comb calibrated spectrograph FOCES”. In: *Society of Photo-Optical Instrumentation Engineers (SPIE) Conference Series*. Vol. 11117. Society of Photo-Optical Instrumentation Engineers (SPIE) Conference Series, 111171O (cit. on pp. 71, 73, 148).

Kellermann, Hanna, Liang Wang, Vanessa Fahrenschon, et al. (2020). “Verification observations of the Manfred Hirt Planet Spectrograph”. In: *Ground-based and Airborne Instrumentation for Astronomy VIII*. Ed. by Christopher J. Evans, Julia J. Bryant, and Kentaro Motohara. Vol. 11447. International Society for Optics and Photonics. SPIE, pp. 922 –931 (cit. on p. 71).

Kipping, David M. (Nov. 2013). “Efficient, uninformative sampling of limb darkening coefficients for two-parameter laws”. In: *Monthly Notices of the Royal Astronomical Society* 435.3, pp. 2152–2160 (cit. on p. 197).

Kitchin, C. R. (Jan. 1995). *Optical Astronomical Spectroscopy*. en. Google-Books-ID: TJioMnL 6SPEC. CRC Press (cit. on p. 25).

Koch, David G., William J. Borucki, Gibor Basri, et al. (Apr. 2010). “*KEPLER MISSION* DESIGN, REALIZED PHOTOMETRIC PERFORMANCE, AND EARLY SCIENCE”. en. In: *The Astrophysical Journal* 713.2, pp. L79–L86 (cit. on p. 18).

Kosyra, R., C. Gössl, U. Hopp, et al. (Nov. 2014). “The 64 Mpixel wide field imager for the Wendelstein 2m telescope: design and calibration”. In: *Experimental Astronomy* 38, pp. 213–248. arXiv: 1408.2519 [astro-ph.IM] (cit. on p. 210).

Kraft, Robert P. (Nov. 1967). “Studies of Stellar Rotation. V. The Dependence of Rotation on Age among Solar-Type Stars”. In: *The Astrophysical Journal* 150, p. 551 (cit. on p. 14).

Krecker, Kerstin, Maximilian Fabricius, Ralf Bender, et al. (2020). “Multifocal station for the Wendelstein 2m Fraunhofer Telescope”. In: *Ground-based and Airborne Instrumentation for Astronomy VIII*. Ed. by Christopher J. Evans, Julia J. Bryant, and Kentaro Motohara. Vol. 11447. International Society for Optics and Photonics. SPIE, pp. 1338 –1345 (cit. on p. 71).

Kreidberg, Laura (Nov. 2015). “batman: BAsic Transit Model cAlculatioN in Python”. In: *Publications of the Astronomical Society of the Pacific* 127, p. 1161 (cit. on pp. 184, 190, 191).

Lang-Bardl, Florian, Klaus Hodapp, Shane Jacobson, et al. (July 2010). “3kk: the Optical-NIR Multi-Channel Nasmyth Imager for the Wendelstein Fraunhofer Telescope”. In: *Ground-based and Airborne Instrumentation for Astronomy III*. Vol. 7735. International Society for Optics and Photonics, 77353Q (cit. on pp. 20, 21).

Levenberg, Kenneth (1944). “A method for the solution of certain non-linear problems in least squares”. en. In: *Quarterly of Applied Mathematics* 2.2, pp. 164–168 (cit. on p. 117).

Lissauer, Jack J., Geoffrey W. Marcy, Stephen T. Bryson, et al. (Mar. 2014). “VALIDATION OFKEPLER’S MULTIPLE PLANET CANDIDATES. II. REFINED STATISTICAL FRAMEWORK AND DESCRIPTIONS OF SYSTEMS OF SPECIAL INTEREST”. In: *The Astrophysical Journal* 784.1, p. 44 (cit. on p. 6).

Mahadevan, Suvrath, Lawrence Ramsey, Chad Bender, et al. (2012). “The habitable-zone planet finder: a stabilized fiber-fed NIR spectrograph for the Hobby-Eberly Telescope”. In: *Ground-based and Airborne Instrumentation for Astronomy IV. Proceedings of the SPIE, Volume 8446, article id. 84461S, 14 pp. (2012)*. Vol. 8446. Society of Photo-Optical Instrumentation Engineers (SPIE) Conference Series, 84461S (cit. on p. 211).

Mandel, Kaisey and Eric Agol (Dec. 2002). “Analytic Light Curves for Planetary Transit Searches”. en. In: *The Astrophysical Journal* 580.2, pp. L171–L175 (cit. on pp. 9, 184, 190).

Marquardt, Donald W. (June 1963). “An Algorithm for Least-Squares Estimation of Nonlinear Parameters”. In: *Journal of the Society for Industrial and Applied Mathematics* 11.2. Publisher: Society for Industrial and Applied Mathematics, pp. 431–441 (cit. on p. 117).

Mayor, Michel and Didier Queloz (Nov. 1995). “A Jupiter-mass companion to a solar-type star”. en. In: *Nature* 378.6555, pp. 355–359 (cit. on pp. 179, 203).

McCullough, P. R., N. Crouzet, D. Deming, and N. Madhusudhan (July 2014). “WATER VAPOR IN THE SPECTRUM OF THE EXTRASOLAR PLANET HD 189733b. I. THE TRANSIT”. en. In: *The Astrophysical Journal* 791.1. Publisher: American Astronomical Society, p. 55 (cit. on p. 10).

Metropolis, Nicholas, Arianna W. Rosenbluth, Marshall N. Rosenbluth, Augusta H. Teller, and Edward Teller (June 1953). “Equation of State Calculations by Fast Computing Machines”. In: *The Journal of Chemical Physics* 21.6. Publisher: American Institute of Physics, pp. 1087–1092 (cit. on p. 121).

Miles-Páez, Paulo A., Stanimir Metchev, Kevin L. Luhman, Massimo Marengo, and Alan Hulsebus (Nov. 2017). “The Prototypical Young L/T-Transition Dwarf HD 203030B Likely Has Planetary Mass”. en. In: *The Astronomical Journal* 154.6. Publisher: IOP Publishing, p. 262 (cit. on p. 6).

Mizuno, Hiroshi (Aug. 1980). “Formation of the Giant Planets”. In: *Progress of Theoretical Physics* 64.2, pp. 544–557 (cit. on p. 6).

Moffat, A. F. J. (Dec. 1969). “A Theoretical Investigation of Focal Stellar Images in the Photographic Emulsion and Application to Photographic Photometry”. In: *A&A* 3, p. 455 (cit. on p. 42).

Morey, Richard D., Rink Hoekstra, Jeffrey N. Rouder, Michael D. Lee, and Eric-Jan Wagenmakers (Feb. 2016). “The fallacy of placing confidence in confidence intervals”. en. In: *Psychonomic Bulletin & Review* 23.1, pp. 103–123 (cit. on p. 117).

Morton, Timothy D., Stephen T. Bryson, Jeffrey L. Coughlin, et al. (May 2016). “FALSE POSITIVE PROBABILITIES FOR ALLKEPLEROBJECTS OF INTEREST: 1284 NEWLY VALIDATED PLANETS AND 428 LIKELY FALSE POSITIVES”. In: *The Astrophysical Journal* 822.2, p. 86 (cit. on p. 6).

Murphy, M. T., Th. Udem, R. Holzwarth, et al. (Sept. 2007). “High-precision wavelength calibration of astronomical spectrographs with laser frequency combs”. In: *Monthly Notices of the Royal Astronomical Society* 380.2, pp. 839–847 (cit. on p. 168).

Naef, D., M. Mayor, J. L. Beuzit, et al. (Jan. 2004). “The ELODIE survey for northern extra-solar planets. III. Three planetary candidates detected with ELODIE”. In: *A&A* 414, pp. 351–359. arXiv: `astro-ph/0310261 [astro-ph]` (cit. on pp. 179, 207).

Nave, Gillian, Florian Kerber, Elizabeth A. Den Hartog, and Gaspare Lo Curto (2018). "The dirt in astronomy's genie lamp: ThO contamination of Th-Ar calibration lamps". In: *Observatory Operations: Strategies, Processes, and Systems VII*. Ed. by Alison B. Peck, Robert L. Seaman, and Chris R. Benn. Vol. 10704. International Society for Optics and Photonics. SPIE, pp. 80 –92 (cit. on p. 48).

Nelder, J. A. and R. Mead (Jan. 1965). "A Simplex Method for Function Minimization". en. In: *The Computer Journal* 7.4, pp. 308–313 (cit. on p. 115).

Obermeier, C., J. Steuer, H. Kellermann, et al. (July 2020). "Following the TraCS of exoplanets with Pan-Planets: Wendelstein-1b and Wendelstein-2b". In: *Astronomy & Astrophysics* 639, A130 (cit. on pp. 199, 209, 210).

Ofir, Aviv, Roi Alonso, Aldo Stefano Bonomo, et al. (May 2010). "The SARS algorithm: detrending CoRoT light curves with Sysrem using simultaneous external parameters". In: *Monthly Notices of the Royal Astronomical Society: Letters* 404.1, pp. L99–L103 (cit. on pp. 186, 187).

Osterbrock, Donald E., Jon P. Fulbright, and Thomas A. Bida (1997). "Night-Sky High-Resolution Spectral Atlas of OH Emission Lines for Echelle Spectrograph Wavelength Calibration. II". In: *Publications of the Astronomical Society of the Pacific* 109.735, pp. 614–627 (cit. on p. 45).

Particle Data Group, M. Tanabashi, K. Hagiwara, et al. (Aug. 2018). "Review of Particle Physics". In: *Physical Review D* 98.3. Publisher: American Physical Society, p. 030001 (cit. on p. 120).

Parviainen, Hannu and Suzanne Aigrain (Nov. 2015). "LDTk: Limb Darkening Toolkit". In: *Monthly Notices of the Royal Astronomical Society* 453.4. arXiv: 1508.02634, pp. 3822–3827 (cit. on p. 193).

Paschotta, Rüdiger (2008). *Encyclopedia of Laser Physics and Technology*. English. Wiley-VCH; Weinheim; Germany (cit. on pp. 44, 45, 51, 56, 229).

Pepe, Francesco, David Ehrenreich, and Michael R. Meyer (Sept. 2014). "Instrumentation for the detection and characterization of exoplanets". In: *Nature* 513.7518, pp. 358–366 (cit. on p. 97).

Perryman, Michael (2018). *The Exoplanet Handbook*. 2nd ed. Cambridge: Cambridge University Press (cit. on p. 10).

Petigura, Erik A., Andrew W. Howard, and Geoffrey W. Marcy (Nov. 2013). "Prevalence of Earth-size planets orbiting Sun-like stars". en. In: *Proceedings of the National Academy of Sciences* 110.48. Publisher: National Academy of Sciences Section: Physical Sciences, pp. 19273–19278 (cit. on p. 18).

Pfeiffer, M. J., C. Frank, D. Baumueller, K. Fuhrmann, and T. Gehren (June 1998). "FOCES - a fibre optics Cassegrain Echelle spectrograph". In: *Astron. Astrophys. Sup.* 130, pp. 381–393 (cit. on pp. 63–65).

Pound, R.V. (1947). "Frequency Stabilization of Microwave Oscillators". In: *Proceedings of the IRE* 35.12, pp. 1405–1415 (cit. on p. 54).

Press, William H., ed. (2007). *Numerical recipes: the art of scientific computing*. en. 3rd ed. OCLC: ocn123285342. Cambridge, UK ; New York: Cambridge University Press (cit. on pp. 112, 114, 115, 120).

Probst, Rafael A. (July 2015). "Laser frequency combs for astronomy". PhD thesis (cit. on pp. 49, 52, 54, 55, 59).

Probst, Rafael A., Dinko Milaković, Borja Toledo-Padrón, et al. (June 2020). "A crucial test for astronomical spectrograph calibration with frequency combs". In: *Nature Astronomy* 4.6, pp. 603–608 (cit. on pp. 49, 153).

Ramsey, Lawrence W. (Jan. 1988). "Focal ratio degradation in optical fibers of astronomical interest." In: *Fiber Optics in Astronomy*. Ed. by Samuel C. Barden. Vol. 3. Astronomical Society of the Pacific Conference Series, pp. 26–39 (cit. on p. 40).

Ranalli, P, D Hobbs, and L Lindegren (2018). "Astrometry and exoplanets in the Gaia era: a Bayesian approach to detection and parameter recovery". en. In: p. 16 (cit. on p. 16).

Ricker, George R., Joshua N. Winn, Roland Vanderspek, et al. (Oct. 2014). "Transiting Exoplanet Survey Satellite". In: *Journal of Astronomical Telescopes, Instruments, and Systems* 1.1. Publisher: International Society for Optics and Photonics, p. 014003 (cit. on p. 19).

Rosenblatt, F. (Feb. 1971). "A Two-Color Photometric Method for Detection of Extra solar Planetary Systems". In: *Icarus* 14, pp. 71–93 (cit. on p. 210).

Russell, Philip (2003). "Photonic Crystal Fibers". In: *Science* 299.5605, pp. 358–362 (cit. on p. 55).

Samoudi, Bousselham (Jan. 2017). "Realisation of the metre by using a femtosecond laser frequency comb: Applications in optical frequency metrology". In: *International Journal of Metrology and Quality Engineering* 8, p. 16 (cit. on p. 52).

Savitzky, Abraham. and M. J. E. Golay (1964). "Smoothing and Differentiation of Data by Simplified Least Squares Procedures." In: *Analytical Chemistry* 36.8, pp. 1627–1639 (cit. on p. 133).

Schlagintweit, Florian (2015). "Construction and test of a fiber pick-off for the high-resolution Echelle spectrograph FOCES at the 2m Fraunhofer telescope". Masterthesis (cit. on pp. 93, 95).

Schneider, J., C. Dedieu, P. Le Sidaner, R. Savalle, and I. Zolotukhin (Aug. 2011). "Defining and cataloging exoplanets: the exoplanet.eu database". en. In: *Astronomy & Astrophysics* 532. Publisher: EDP Sciences, A79 (cit. on pp. 6, 7, 9, 15).

Schwarzschild, K. (1906). "Ueber das Gleichgewicht der Sonnenatmosphäre". ger. In: *Nachrichten von der Gesellschaft der Wissenschaften zu Göttingen, Mathematisch-Physikalische Klasse* 1906, pp. 41–53 (cit. on p. 192).

Sharma, A. B., Seppo J. Halme, and M. M. Butusov (1981). *Optical fiber systems and their components : an introduction / A.B. Sharma, S.J. Halme, M.M. Butusov*. English. Springer-Verlag Berlin ; New York (cit. on p. 41).

Shrader, Douglas, Jonathan Moffett, Graeme Plant, Barry Sturman, and J. V. Sullivan (2010). "Hollow Cathode Lamps - Yesterday, Today and Tomorrow". In: *Atomic Absorption*. Agilent Technologies, Application Note (cit. on p. 47).

Stassun, Keivan G., Ryan J. Oelkers, Martin Paegert, et al. (Sept. 2019). "The Revised TESS Input Catalog and Candidate Target List". In: *The Astronomical Journal* 158.4, p. 138 (cit. on p. 217).

Steffen, Jason H., Darin Ragozzine, Daniel C. Fabrycky, et al. (May 2012). "Kepler constraints on planets near hot Jupiters". In: *Proceedings of the National Academy of Sciences* 109.21, pp. 7982–7987 (cit. on p. 6).

Steinmetz, Tilo, Tobias Wilken, Constanza Araujo-Hauck, et al. (2008). "Laser Frequency Combs for Astronomical Observations". In: *Science* 321.5894, pp. 1335–1337 (cit. on pp. 49, 54).

Strassmeier, Klaus, Thomas Granzer, Weber Michael, et al. (Jan. 2010). "The STELLA robotic observatory on tenerife". In: *Advances in Astronomy* 2010 (cit. on p. 218).

Stürmer, Julian, Christian Schwab, Stephan Grimm, et al. (July 2016). "Optimal non-circular fiber geometries for image scrambling in high-resolution spectrographs". In: *Advances in Optical and Mechanical Technologies for Telescopes and Instrumentation II*. Ed. by Ramón Navarro and James H.Editors Burge (cit. on p. 43).

Swain, M. R., G. Tinetti, G. Vasisht, et al. (Oct. 2009). "WATER, METHANE, AND CARBON DIOXIDE PRESENT IN THE DAYSIDE SPECTRUM OF THE EXOPLANET HD 209458b". en. In: *The Astrophysical Journal* 704.2. Publisher: American Astronomical Society, pp. 1616–1621 (cit. on p. 6).

Tamuz, O., T. Mazeh, and S. Zucker (Feb. 2005). "Correcting systematic effects in a large set of photometric light curves". In: *Monthly Notices of the Royal Astronomical Society* 356.4, pp. 1466–1470 (cit. on pp. 186, 187).

The Nobel Prize in Physics (2005). en-US (cit. on p. 48).

Trifonov, Trifon (June 2019). *The Exo-Striker: Transit and radial velocity interactive fitting tool for orbital analysis and N-body simulations*. ascl: 1906.004 (cit. on p. 114).

Turnbull, Margaret C., Tiffany Glassman, Aki Roberge, et al. (May 2012). "The Search for Habitable Worlds. 1. The Viability of a Starshade Mission". en. In: *Publications of the Astronomical Society of the Pacific* 124.915. Publisher: IOP Publishing, pp. 418–447 (cit. on p. 7).

Udem, Thomas (Dec. 2002). "Die Messung der Frequenz von Licht mit modengekoppelten Lasern". habilitation thesis (cit. on pp. 49, 51).

Vogt, S. S., S. L. Allen, B. C. Bigelow, et al. (June 1994). "HIRES: the high-resolution echelle spectrometer on the Keck 10-m Telescope". In: *Instrumentation in Astronomy VIII*. Ed. by D. L. Crawford and E. R. Craine. Vol. 2198. Society of Photo-Optical Instrumentation Engineers (SPIE) Conference Series, p. 362 (cit. on p. 211).

Vovk, I., Strzys, M., and Fruck, C. (2018). "Spatial likelihood analysis for MAGIC telescope data - From instrument response modelling to spectral extraction". In: *A&A* 619, A7 (cit. on p. 114).

Wang, Ji and Eric B. Ford (Dec. 2011). “On the eccentricity distribution of short-period single-planet systems”. In: *Monthly Notices of the Royal Astronomical Society* 418.3, pp. 1822–1833 (cit. on p. 205).

Wang, Liang, Frank Grupp, Hanna Kellermann, Ulrich Hopp, and Ralf Bender (2017). “Line profile analysis of the laser frequency comb in FOCES”. In: *Techniques and Instrumentation for Detection of Exoplanets VIII*. Vol. 10400. Proc. SPIE, p. 104001V (cit. on p. 71).

Wang, Liang, Frank Grupp, Hanna Kellermann, et al. (2016). “A new generation of spectral extraction and analysis package for Fiber Optics Cassegrain Echelle Spectrograph (FOCES)”. In: *Software and Cyberinfrastructure for Astronomy IV*. Vol. 9913. Proc. SPIE, 99133O (cit. on p. 71).

Wang, Liang, Hanna Kellermann, Frank Grupp, Ulrich Hopp, and Ralf Bender (in prep.). “GAMSE: A Data Reduction Software for Echelle Spectrographs”. In: (cit. on pp. 126, 128).

Wilks, S. S. (Mar. 1938). “The Large-Sample Distribution of the Likelihood Ratio for Testing Composite Hypotheses”. EN. In: *Annals of Mathematical Statistics* 9.1. Publisher: Institute of Mathematical Statistics, pp. 60–62 (cit. on p. 119).

Withnall, R. (2005). “SPECTROSCOPY | Raman Spectroscopy”. In: *Encyclopedia of Modern Optics*. Ed. by Robert D. Guenther. Oxford: Elsevier (cit. on p. 51).

Wolszczan, A. and D. A. Frail (Jan. 1992). “A planetary system around the millisecond pulsar PSR1257 + 12”. In: *Nature* 355, pp. 145–147 (cit. on p. 16).

Wright, J. T. and J. D. Eastman (Sept. 2014). “Barycentric Corrections at 1 cm/s for precise Doppler velocities”. en. In: *Publications of the Astronomical Society of the Pacific* 126.943. arXiv: 1409.4774, pp. 838–852 (cit. on p. 147).

Zechmeister, M., A. Reiners, P. J. Amado, et al. (Jan. 2018). “Spectrum radial velocity analyser (SERVAL): High-precision radial velocities and two alternative spectral indicators”. en. In: *Astronomy & Astrophysics* 609, A12 (cit. on pp. 147, 161).

Zhang, Zichen, Zheng You, and Daping Chu (Oct. 2014). “Fundamentals of phase-only liquid crystal on silicon (LCOS) devices”. In: *Light: Science & Applications* 3.10, e213–e213 (cit. on p. 58).

Danksagung

An dieser Stelle möchte ich die Gelegenheit nutzen, um all den Menschen meine Dankbarkeit auszudrücken, die es mir durch ihre Geduld und Unterstützung ermöglicht haben, diese Arbeit zu schreiben.

Mein Dank geht zuallererst an Prof. Dr. Ralf Bender, der mir als mein Doktorvater überhaupt erst die Möglichkeit gegeben hat, meine Arbeit an der Uni-Sternwarte der LMU anzufertigen. Darüber hinaus möchte ich selbstverständlich meinem Betreuer innerhalb des Projekts, Dr. Frank Grupp, für seinen Rat und all seine Unterstützung zu jeder noch so seltsamen Uhrzeit und die aufmunternden Worte danken, mit denen er mir tagein, tagaus zur Seite gestanden hat.

Ausdrücklich möchte ich mich auch bei Dr. Ulrich Hopp und Dr. Arno Riffeser für die detaillierten und ausführlichen Anmerkungen und Kommentare zur Arbeit selbst bedanken. Arno, ich weiß nicht, wie du das machst, aber dir fallen selbst Inkonsistenzen bei benutzten Formelzeichen viele Seiten später und inkorrekt eingesetzter Mathe-Modus von LaTeX in einzelnen Indizes auf. Vielen Dank für deine Hilfe!

Bei Dr. Claus Gössel und Dr. Jan Snigula möchte ich mich für jeden Rat und beantworteten Hilferuf bei Software-Fragen und Problemen bedanken und bei Florian Lang-Bardl für all die Unterstützung in mechanischen Fragen und jedes aufmunternde Wort, wenn‘s mal wieder nicht so lief.

Nicht zuletzt geht mein Dank auch an Michael Schmidt und Christoph Ries – unsere beiden Nachtbeobachter – die bei Anruf immer sofort aufgesprungen und in den Keller gespurtet sind, falls bei *FOCES* mal wieder irgendwo der Wurm drin war.

Ady Karasz (gestorben am 12. Februar 2018), wo auch immer du jetzt bist, vielen Dank für deine Freundschaft und die vielen verlässlichen und präzisen Arbeiten aus deiner Feinmechanik-Werkstatt. Ich und hoffentlich wir alle werden dich nicht vergessen!

Dr. Tilo Steinmetz und Dr. Yuanjie Wu – herzlichsten Dank für all die Hilfe, jedes Handauflegen bei unserem Astro-Kamm und all die gemeinsam getrunkenen Tassen Tee zum Aufwärmen auf dem Wendelstein, nachdem wir uns von der Klimaanlage steife Finger geholt haben.

Tausend Dank an Dr. Christian Obermeier und Mihael Kodric für jeden gemeinsamen Kaffee, all das Korrekturlesen, die gemeinsam geschliffenen Fasern, jedes verflixte Software-Problem und all die stundenlangen Diskussionen. Mihael, behalte dir immer deine besondere Fähigkeit bei, dass Probleme sich schon allein dadurch lösen, dass man sie dir in aller Ausführlichkeit erklärt. Das ist mehr wert als Gold!

Ebenfalls geht mein Dank an Dr. Liang Wang für all deinen Einsatz auch lange nach deiner offiziellen Zeit in München, all die gemeinsam durchprogrammierten Nächte (zumindest für einen von uns war schließlich immer Nacht) und jede Übersetzung der chinesischen Speisekarte ohne die ich sicher aufgeschmissen gewesen wäre.

Natürlich möchte ich mich auch bei den beiden Exoplaneten/Hardware-Damen bedanken: Vanessa Fahrenschon und Jana Steuer. Ohne die unendlich vielen durchjustierten Tage und Nächte, all die gemeinsamen Nudeln mit Soße am Berg und das wochenlange Finetuning an unendlich vielen Kleinigkeiten mit Vanessa wäre das alles nicht möglich gewesen. Allerliebster Dank geht auch an Jana Steuer, zwar erst spät zum Projekt dazugestoßen, aber ohne dein unermüdliches Korrekturlesen und all deine aufmunternden Worte, hätte ich diese Arbeit nicht zu Ende bringen können.

Zu guter Letzt geht mein Dank an meine Familie. Danke für euer Verständnis, für all die verpassten Familien-Events, weil ich mal wieder am Berg war, für die Fähigkeit, zu wissen, wann man mal nicht nachfragen sollte, wie es gerade läuft und für die Erkenntnis, dass eine Doktorarbeit auch nur ein Doktorarbeit ist – und dass Kuchen backen zeitweise viel wichtiger sein kann. Und als allerletzes geht mein Dank an Christian Fruck. Was ich dir alles schulde, kann ich nicht in Worte fassen. Daher sage ich es kurz: DANKE! . . . Danke für einfach alles!